Project and development of an optical particle counter for Martian atmosphere: Analysis, design, test and instrument integration

Ph.D. in Industrial Engineering (XXXIV cycle)

Candidate: Giuseppe Mongelluzzo
Tutor: Dr. Francesca Esposito

Al mio micione.
Nel mio cuore, quando mi sveglio,
sei ancora appoggiato alle mie gambe.

INDEX

1. Introduction 1

1.1 The role of dust in Martian climatology 8
1.2 The ExoMars programme, the Dust Complex Suite, and the scientific payload developed by INAF-OAC: GIADA, MEDUSA, DREAMS and MicroMED 16
1.2.1 The ExoMars Programme 16
1.2.2 GIADA 18
1.2.3 MEDUSA 19
1.2.4 The DREAMS Experiment 21
1.2.5 MicroMED 21

2. The fluid dynamic design of MicroMED 40

2.1 CFD analysis of MicroMED's Elegant Breadboard 42
2.1.1 CFD model 42
2.1.2 Validation of the model 61
2.1.3 Results and discussion 64
2.1.4 Undesired phenomena individuated during the analysis 76
2.2 CFD analysis of MicroMED's Flight Model design 79
2.2.1 Geometry variations 79
2.2.2 CFD model 80
2.2.3 Results 81

3. Integration, test and qualification phases of the MicroMED OPC 74

3.1 MicroMED's Flight Model integration 90
3.2 Functional and performance tests on MicroMED 93
3.2.1 INAF – OAC premises 93
3.2.2 Functional tests 106
3.2.3 MicroMED performance tests 111
3.2.4 Bimodal histograms 119
3.2.5 MicroMED performance tests in presence of wind – test campaign at the AWTS II simulator 128
3.2.6 Dust concentration as measured by MicroMED 138
3.2.7 Test campaigns in terrestrial desert 149
3.3 MicroMED's space qualification 153
3.3.1 Vibration test procedure 153
3.3.2 Thermal Vacuum test procedure 157
3.4 MicroMED's calibration procedure 166
3.4.1 Test conditions 166
3.4.2 Test results and discussion 166

4. The terrestrial version of MicroMED 159

4.1 The design of MicroMED's terrestrial version 171
4.1.1 CFD Model 172
4.1.2 Input data for runs 172
4.1.3 Results and discussion 173

4.2 Proposed MicroMED terrestrial adaptations / designs 180
4.2.1 First design solution 180
4.2.2 Second design solution 184
4.2.3 Comparison between the two proposed designs 188
4.2.4 Quick summary of the results of the re-design of MicroMED for terrestrial applications 191

5. The Safeair® instrument 191

5.1 Safeair ® description 194
5.1.1 CFD Model and input data for runs 196
5.1.2 Results of the analysis on the original geometry 197
5.1.3 Possible flow rate increase 201
5.1.4 Solution with a metal grid as the droplet collector 204
5.1.5 Proposed inlet adaptment to test constraints 204

6. Conclusions 206
References I

1.Introduction

The Optical Particle Counter (OPC) "MicroMED" (Mongelluzzo, G. et al. 2018, 2019a, 2019b, 2019c, Scaccabarozzi, D. et al. 2018, 2019, 2020) will be part of the upcoming ESA/Roscosmos ExoMars 2022 mission and aims at the first ever direct measurement at the surface of airborne Martian dust. The instrument has been developed under the scientific leadership of the INAF – Osservatorio Astronomico di Capodimonte (INAF - OAC, Department of Planetary Science and Cosmic Physics), in co-operation with Politecnico di Milano, Spanish Instituto Nacional de Tecnica Aerospacial (INTA) and Russian Space Research Institute (IKI), and was co-founded by Regione Campania (FESR 2014-2020), Agenzia Spaziale Italiana (ASI, contract's grant number: 2016/41/H.0), and by the Spanish Ministry of Defense (contract's grant number: RTI2018-099825-B-C31). MicroMED will provide a significant contribution to the characterization of airborne dust on Mars, a very important goal of the current Martian related research, as indicated in the MEPAG goal document, which identifies the investigations that are still needed to prepare for human exploration. Dust plays indeed a prominent role in the evolution of the Mars morphology and climate, with the latter being directly influenced by the dust seasonal and long term variable concentration (Vincente-Retortillo, A. 2018). Suspended dust can significantly affect the thermal profile of the atmosphere, absorbing and reflecting the solar radiation, also influencing cloud formation and life-cycle. Despite being much thinner than Earth's, Martian atmosphere can still sustain aeolian processes. Such processes are common and diffuse all over the planet and able to trigger the motion of sand and dust grains, as evidenced by the diffuse presence of actually active dunes and dust storms. The presence of few competing factors, the arid environment and the widespread distribution of dust sources make the dust contribution one of the crucial factors that drive the planet climate. Martian dust storms can indeed last several weeks, even covering the whole planet surface and absorbing up to 80% of the incoming solar radiation. The dust lifting processes, frequent also on Earth, can occur at various scales, going from the aforementioned planet encircling dust storms to local dust devils (Murphy et al. 2016, Harrison et al. 2016, Neakrase et al. 2016, Franzese, G. 2018). Dust grains suspended in the atmosphere not only scatter the solar thermal radiation, they also act as condensation nuclei for H_2O and CO_2, thus influencing the atmospheric thermal structure, balance and circulation (Banfield et al. 2020, Fedorova, A. 2009, Smith, D. 2001). Depending on its size distribution, dust also influences the atmospheric heating balance, interfering with the climate and wind intensity, a process that is directly related to the grain properties (e.g. size, roughness, hardness). In addition, long-term effects of dust are evident on the planet

geology in cementing bedforms, leading to the formation of features like transverse aeolian ridges (TARs) (Geissler 2014, Silvestro, S. et al. 2021) and in covering entire dune fields (dust-sized volcanic ash) (Chojnacki et al. 2020, Runyon et al. 2021), thus augmenting the probability of dust layer preservation in the Martian sedimentary records. Another important phenomenon associated with the dust clouds is electrification of the grains through mutual contact, that can generate electric fields up to several kV/m. On Mars, the triboelectricity associated with dust impacts is expected to be the main charging mechanism of the atmosphere and could lead to electric potential reaching the breakdown voltage, with the consequent formation of electrostatic discharges (Eden and Vonnegut 1973, Forward et al. 2009). These phenomena can potentially affect the atmospheric composition and the habitability of the planet, as well as interfere with scientific instrumentation working on Martian surface.

There are currently no direct measurements of the airborne Martian dust, leading to significant uncertainties in its characterization. The information currently available about dust grain properties, such as size and composition, have been estimated only through indirect measurements (Drossart 1991, Pollack, J. 1995, Tomasko, M. 1999). Given the prominent role of dust in the understanding of the Martian climate, the study of the characteristics and dynamics of airborne dust, as well as the analysis of the atmosphere and weather through the study of the Martian surface environment is one of the main goals of the ESA/Roscosmos ExoMars program. The payload of the ExoMars 2022 mission includes an entire Dust Complex Suite aimed at the study of dust. However, it is not the first ExoMars mission interested in the characterization of dust lifting processes, as the 2016 mission also mounted a suite of sensors, named DREAMS, aimed at the investigation of Martian weather. DREAMS (Esposito, F. et al. 2016; Bettanini, C. et al. 2014, 2018), also led by the department of Planetary Science and Cosmic Physics at the Osservatorio Astronomico di Capodimonte, was installed onboard the *Schiaparelli* lander. DREAMS was an integrated package of 6 scientific sensors aimed at the characterization of fundamental aspects of the Martian climate and boundary layer dynamics at ground level.

Regarding the currently ongoing ExoMars 2022 mission, the Dust Complex Suite (DCS) has been installed onboard the *Kazachok* Surface Platform (Vago, J. et al. 2015). It is exclusively dedicated to analyze dust characteristics and dynamics.

The MicroMED OPC is one of the sensor of the DCS. The instrument uses the principle of light scattering, for the detection and measurement of dust grain size. MicroMED samples the dust laden air in the proximity of its sampling head with the help of a pump, that generates a pressure difference, triggering the air suction. The sampled atmosphere passes through an inlet duct whose design is conceived to concentrate the flow towards a $\sim 1 \times 1 \times 0.3$ mm^3 sensing volume, contained into the instrument main box, where a laser beam is focused. Particles crossing the spot scatter light based on their size, shape and composition. Scattered light is collected by a concave mirror, which in turn focuses it on a photodiode that records the signal. The signal is then analyzed by the electronics and used to determine the grain size from the analysis of signal amplitude (i.e. pulse height analysis - PHA). An alternative method using the signal time span is also used as a secondary method, since there is correlation between the grains speed inside the instrument and their size (Franzese, G.

2021a). MicroMED was designed to operate in Martian atmosphere, i.e. with high concentration of CO_2 (95.3% on Mars), and low pressure, density and gravity (0.6-0.8%, 1.3-1.5% and 37.8% of Earth's atmosphere, respectively Zurek, R.W. 1992, Gómez-Elvira, J. 2014).

My Ph.D. work is related to different phases of the MicroMED OPC development, from design to integration, qualification and test. Main focus was on the design of the fluid dynamic sampling system of the instrument, a key feature for the correct functioning of the OPC. During the development stage, the fluid dynamic behavior inside MicroMED was modelled via a Computational Fluid Dynamic (CFD) Analysis (Mongelluzzo, G. et al. 2018, 2019a, 2019b, 2019c). The CFD modelling allowed us to identify issues in the prototype design, the "Elegant Breadboard" (BB), and subsequently correct them in the updated model, i.e. the Proto Flight Model (PFM) design.

MicroMED PFM was then assembled and tested in 2019 at the INAF-Astronomical Observatory of Capodimonte premises. Tests have been performed using a Martian simulation chamber that simulates the Martian environment in terms of atmospheric composition, temperature, pressure and dust content (Cozzolino, F. 2020). The instrument was also tested in two separate test campaigns at the Aarhus Wind Tunnel Simulator (AWTS II) at the University of Aarhus, Denmark (Holstein-Rathlou, C. 2014), where it is also possible to simulate different wind speeds. These tests allowed us to validate the fluid dynamic design. The third chapter of this work includes a detailed discussion of the process of development, integration, space qualification and testing of MicroMED.

A terrestrial version of MicroMED has also been developed in order to test the instrument in Earth atmosphere. Such tests would provide a better understanding of MicroMED operations through direct exposure to a real (not simulated) windy dusty environment on Earth. In order to be performed though, a re-design of the instrument was needed to adapt MicroMED's fluid dynamics to the different conditions of Earth's atmosphere, since density and pressure higher by two and three orders of magnitude, respectively, and the different composition significantly affect the fluid dynamics behavior through the instrument ducts. Other components of the instrument can work efficiently in both planetary atmospheres, thus just the re-design of the instrument fluid dynamic sampling system allowed to obtain an efficient terrestrial OPC. The fourth chapter of this work describes the development of such terrestrial version of MicroMED.

The peculiar structure of MicroMED has also allowed to adapt the instrument to completely different purposes. In the frame of the Covid-19 pandemic, indeed, the air sampling features of the instrument have been exploited and adapted to bioaerosol sampling, leading to the development of the Safeair instrument, that will also be described in fifth chapter of this work.

In summary, the present work is organized as follows:

- At the beginning of this work, an introduction to the state of the art in dust research is provided. Such insight is important in order to understand the significant role that MicroMED could play in the research sector we are focusing on. The dynamics of dust in Martian (and partly in Earth) atmosphere is described, and the phenomena in play have being eviscerated. In this part of the work, I am

mainly describing results obtained by the scientific community and which I did not have an active part in; however, I have contributed to some works on the topic like Franzese, G. et al. 2020;

- After such introduction to the world of dust, an overview of the history of dust instruments developed at the INAF – OAC is provided. The department of Cosmic Physics and Planetology has a long history of dust instruments selected to be a part of space exploration missions. The description starts with GIADA, a sensor that was conceived to measure number, mass, momentum and velocity distribution of grains expelled from the nucleus of the 67P/Churyumov-Gerasimenko comet. After GIADA, the MEDUSA sensor was developed, which was an instrument that aimed at the in situ measurement of dust grain size, size distribution, concentration, deposition, electrification, velocity, and water vapor abundance in the Martian atmosphere at ground level. MEDUSA is actually a precursor of MicroMED (the name itself, "MicroMED", stands for "Micro-MEDUSA"), larger in size and weight with respect to its successor. DREAMS was the only scientific payload onboard the Schiaparelli lander and consisted of a meteorological station comprehensive of the first electric field sensor ever sent to Mars. The suite of sensor, made of a thermometer (MarsTEM), a pressure sensor (DREAMS-P), an air humidity sensor (DREAMS-H), a 2D anemometer (MetWind), an electric field sensor (MicroARES) and a Solar Irradiance Sensor (SIS), showed that it was responding to commands and ready for acquisitions during the final phases of the Schiaparelli lander mission, which unfortunately crashed to the Martian ground. Such instruments were developed before my arrival at the INAF – OAC; this is thus an introduction section to the actual work related to my Ph.D.;
- After such overview of the previous instruments developed by the INAF – OAC and aimed at the characterization of dust in space environments, an in-depth description of the MicroMED OPC is provided. MicroMED is a complex instrument, made of a number of subsystems which are all described in detail in the final sections of Chapter 1. Its functionality is based on optical methods; in particular, MicroMED samples grains from outer atmosphere and conveys them toward a 1 mm^2 laser illuminated spot. By means of such spot, the Pulse Height Analysis method is, as already said, used, which in essence relates the intensity of the scattered light signal (which is made by dust grains crossing the laser spot) to the size of the crossing dust grains. The instrument is able, after detection, to provide a histogram describing size distribution of the sampled grains, which is an information of great impact on the studies and the research related to Martian climatology, for example because it provides input data for Martian climatic models, among various utilities. Given that the volume flow rate of the instrument can also be estimated, a measure of dust concentration in the atmosphere can also be provided. My Ph.D. work has mostly been in the framework of the MicroMED OPC design, development, integration, qualification and testing;
- Chapter 2 provides an overview of the first part of my Ph.D. work. MicroMED's Elegant Breadboard (BB) had already been realized by my arrival in Capodimonte;

however, the instrument's fluid dynamic design had to be optimized for optimal performance in the range of interest of the instrument, which is related to the dust grain size and corresponds to 0.4-20 μm in dust grain diameter. In order to do that, an in-depth CFD analysis of MicroMED's BB design has been performed. Such analysis involved hundreds of CFD simulations, providing a complete evaluation of the effect of each environmental parameter, as well as different duct lengths and layouts, on the instrument's sampling efficiency. Chapter 2 of this work provides a detailed description of the method and of the CFD model used for the simulations. Such method strongly differs from the "classical" methods used in Earth atmosphere. On Mars surface, the flow is indeed laminar for characteristic lengths such as MicroMED's, the atmosphere has extremely low density, pressure and temperature. Such conditions required an *ad hoc* model, with custom settings also in the framework of trying to describe the particle motion in such fluid. In order to evaluate the instrument's efficiency, the "sampling efficiency" parameter has been defined and it was proved to be the most influential parameter on the analysis that followed;

- As a result of such analysis, a complete re-design of the MicroMED ducts has been performed. By means of CFD, the re-design has been completed, and after the re-design, a further CFD analysis has been performed to verify the improvements obtained;
- Once the design phase was concluded, MicroMED was integrated and tested. The integration was performed at OAC premises in Capodimonte in 2019. As a result, MicroMED's Proto Flight Model (PFM) and its Flight Spare (FS) counterpart were realized. Both instruments have been tested to verify perfect functionality. Tests have been performed in different forms. Such test phase is described in Chapter 3. During this section, a detailed description of OAC facilities is provided, as well as a brief description of other facilities in which MicroMED has been tested, such as the Aarhus Wind Tunnel Simulator (AWTS II) at the University of Aarhus, Denmark, where MicroMED was and will be tested in the framework of two financed test campaigns. Such campaigns are part of the Europlanet project and I am their principal investigator;
- Chapter 3 of this work also provides an insight on how MicroMED SW has to be set in order to perform tests. A section about dust concentration in the chamber is present. The determination of dust concentration inside the Martian chamber where MicroMED is tested, as well as inside the instrument itself, is very important in order to determinate the instrument's efficiency. The methods developed for such determination are provided in the section. Such methods are based both on measurements in the chamber, by means of custom systems like the Concentration Measurement System (CMS, which I designed), and by post processing analysis, by means of a code able to relate the indirect measurement performed in the chamber with the value of volume flow rate, form which dust concentration can be determined. Such methods are innovative since there are

currently no flowmeters nor volume flow rate measurement methods for such low pressure environment;

- Tests in terrestrial deserts have also been performed, during various field campaigns in the Tafilalt region in the Moroccan Sahara Desert, that aimed at advancing in the study of the dust lifting mechanisms and the structure, rise and evolution of dusty phenomena on Earth. It is indeed expected, starting from some observational evidences on Mars, that dust dynamics could be similar in the two planetary environments, albeit scaled by some factors. Hence, it is important to deeply characterize these phenomena on the Earth in order to compare and understand data that will be acquired on Mars. As part of my Ph.D. work, I have personally been a part of one of those campaigns, in July 2019;
- Tests on MicroMED have not only been focused on performances. Space qualification tests were also needed, and MicroMED has been subject to Vibrational and Thermal Vacuum qualification campaign. My role in such part was to contribute to the design of tests and to the development of the official documentation;
- Before being delivered to ESA for the integration on the Surface Platform, MicroMED was calibrated by means of tests with both polydisperse and monodisperse samples, as well as a combination of spherical and aspherical grains, so that its response to dust grains is correctly characterized. A long and detailed procedure of calibration has been performed and described in the final section of Chapter 3;
- MicroMED was always tested and characterized in Martian simulated environments both at INAF – OAC premises and at the Aarhus Wind Tunnel Facility in Denmark. In order to verify the performances of the instrument in a natural dusty environment, and also test on the field the sequences designed to operate the instrument on Mars, our INAF - OAC group has also been working at the development of a terrestrial version of MicroMED. The instrument consists of an adaptation of the Martian instrument for Earth usage. In order to realize such adaptation, a CFD analysis of MicroMED's PFM behavior in Earth conditions has been performed, with the intent of understanding criticalities and adapt its design to Earth atmosphere. The result was the design of an original terrestrial instrument to be used in desert test campaigns;
- In the framework of the Sars-CoV-2 pandemic, INAF has launched an initiative that aimed at adapting already existing technologies to the battle against the spread of the Coronavirus outbreak. In this contest, MicroMED has been adapted as an aerosol sampler. The Safeair ® instrument has been invented, and it provides a single instrument able to sample, analyze and detect the presence of pathogens in the atmosphere (the instrument can also be adapted to other viruses/pathogens). Safeair is currently ongoing an international patent procedure, and I am personally owner of 2% of the intellectual property of the invention (Patent n° 102020000018409 filed on 29th July 2020);

- At the conclusion of this work, a brief synthesis of the results obtained is provided as well as a list of all reference documents utilized during the discussion of the topics faced.

1.1 The role of dust in Martian climatology

Martian atmosphere contains a significant load of suspended dust. Dust is always present in the atmosphere, with its amount varying with the seasons and with the eventual occurrence of local and global dust storms. Airborne dust significantly contributes to the dynamic and thermodynamic evolution of the atmosphere (Zurek, R. W. et al., 1992), including large scale circulation processes, on diurnal, seasonal and annual time-scales (Smith, M. D., 2009). It plays a key role in determining the current Martian climate and probably influenced climatic conditions and surface evolution in the past. Dust particles, indeed, absorb and scatter solar and thermal radiation and act as condensation nuclei for H_2O and CO_2. In this way, dust strongly influences the atmospheric thermal structure, balance and circulation (James, P. B. et al 1994; Jakosky, B. M. and Haberle, R. M., 1992; Kahn, R.A. et al., 1992; Ryan, J.A. and Henry, R. M., 1979; Forget, F. et al., 2006; Martin, T. Z. and Kieffer, H. H., 1979; Martin, T. Z., 1981; Jakosky. B. M. and Martin, T. Z., 1987).

Even in moderately dusty situations, the influence of dust on Martian thermal structure is critical. During regional or global dust storms, more than 80% of the incoming sunlight does not reach the planet's surface. As a result, there is an intense atmospheric heating. Airborne dust is therefore a crucial climate component on Mars, which affects atmospheric circulations at all scales.

Among the main dust parameters influencing the atmosphere heating are the size distribution and abundance. For this reason, as we will see, these parameters are the main focus of the measurements performed by the MicroMED OPC.

Winds and windblown dust are the most important surface modifying agents on Mars (among currently active processes). They are responsible for erosion, redistribution of dust on the surface and weathering. Wind mobilized particles on Mars range in size from less than 1 μm, for suspended dust, to possibly 1 cm in diameter. The mechanisms for dust entrainment into the atmosphere, as well as the resulting feedback on atmospheric circulation, are still not completely understood, as the data available so far do not allow us to identify the efficiency of proposed processes (Montabone, L. et al., 2005; Newman, C. E. et al., 2002a and 2002b; Kok, J. F., 2010). The unpredictability of the global dust storms on Mars is one of the most evident consequences of this lack of understanding.

The current knowledge about the Martian dust has been mainly gained by remote sensing measurements of the atmospheric optical depth (τ). This is a measurement of atmospheric transparency corresponding to the vertical path from surface (or a specific altitude) to outer space. The clearest evidence of dust is the color of the Martian sky, which changes from yellowish-brown at high opacity ($\tau \sim 1$) to bluish-black or black if dust free ($\tau \sim 0$) (Bell III, J. F. et al., 2006). Nevertheless, remote measurements can be biased by haze, fog and suspended water ice grains (Pollack, J. B. et al., 1977; Colburn, D. et al., 1989; Leovy, C.

et al., 1972; Anderson, E. M. and Leovy, C., 1978; Jaquin, F. et al., 1986; Kahn, R. A., 1990). Data collected in previous missions allow some estimations of the dust particles' effective radius (r_{eff} = 0.50-2.75 μm) and effective variance (ν_{eff} = 0.2-0.5). The estimated size distributions (Figure 1.1) have a maximum possible diameter under 20 μm, with peak concentration around d_p = 1.2 -1.4 μm and lower concentration for particles well under 1 μm, which suggested that the dispersion of particles in the atmosphere is both ruled by gravitational settling and by turbulence induced by winds (Conrath, B. J., 1975; Toon, O. B., et al., 1977). Based on these considerations, the OPC MicroMED was developed to detect dust grains in the 0.4-20 μm diameter range.

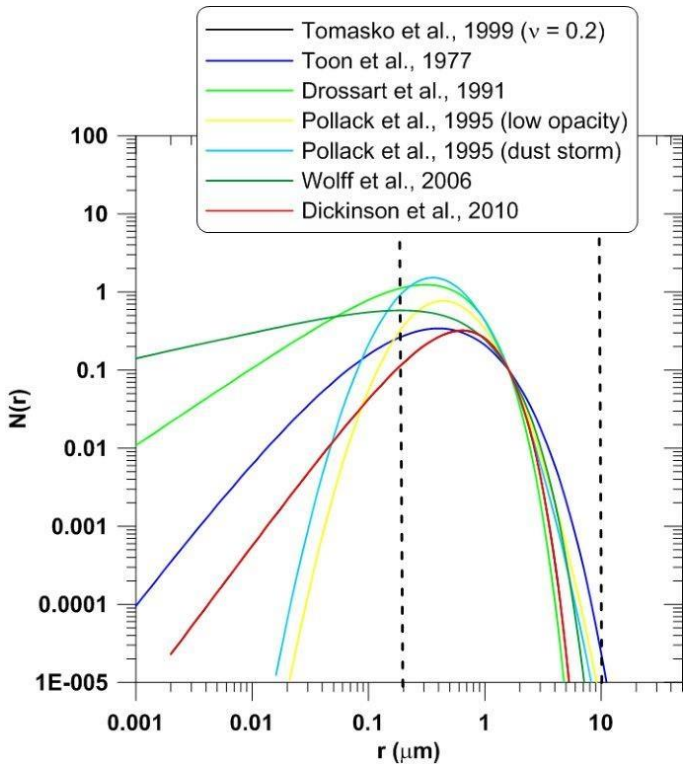

Figure 1.1 Particle size distributions (N(r)) as a function of particle radius (r) as derived by remote measurements. The curves were scaled to have N = 0.1 for r = 1.6 μm. The dashed lines in figure indicate MicroMED measurement range.

However, it has to be underlined that the particle size distributions obtained by remote measurements are based on some simplifying hypotheses about the shape of distribution, optical properties and morphology of the particles. The light scattering for non-spherical particles, which should be the most expected on Mars, is in fact quite complex to be modelled. Moreover, in polydisperse samples, the number of variables to be considered for modelling the asphericity is very high, making it quite difficult to obtain results from remote measurements. On the contrary, an estimation of size distribution coming from directly measured *in situ* data acquisition without having to assume distribution functions has not been made yet on the Martian ground. Such measurements should overcome the aforementioned limitations related to remote measurements.

Atmospheric and surface dust is globally distributed with a similar mineralogical composition over the entire planet (Pollack, J. B. et al., 1977, 1979), as a result of the so-called "dust cycle" (Figure 1.2).

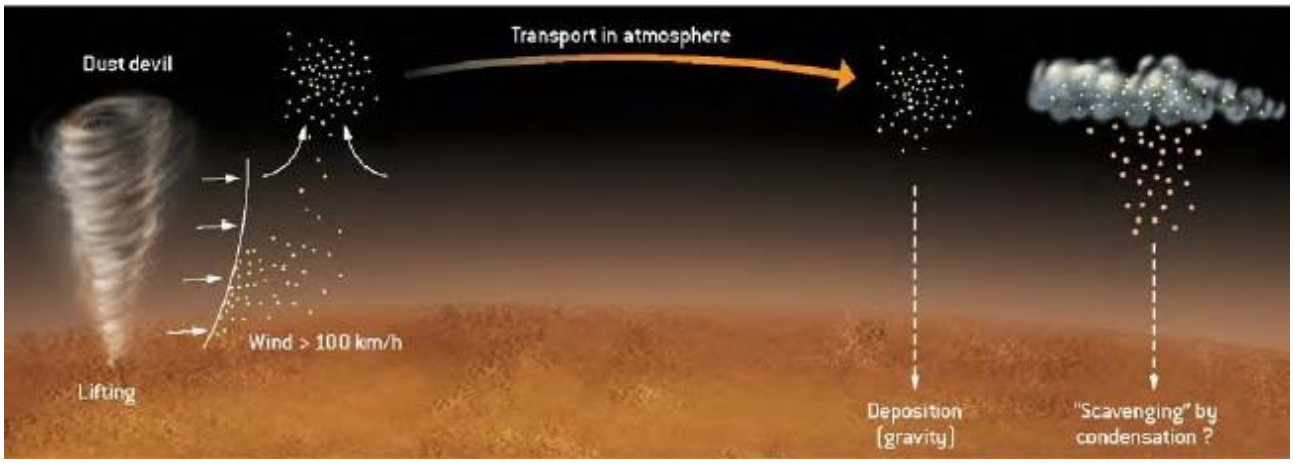

Figure 1.2 Dust cycle in the Martian atmosphere (Forget, F., et al., 2006).

The dust cycle is characterized by the phases of lifting, transport in the atmosphere, deposition and eventual scavenging by clouds and precipitation. Winds cause grains to lift off from surface. The smaller grains go into long-term ($d_p \leq 20$ μm) or short-term ($20 < d_p < 70$ μm) suspension in the atmosphere, while larger ones ($70 < d_p < 500$ μm) are lifted just over the surface, were they can bounce multiple times mobilizing other grains in a chain process (*saltation*). Grains larger than ~ 500 μm can roll or slide along the surface, driven by impacts of *saltating* particles and wind drag forces. This mode of transport is known as creep (Bagnold 1941).

Saltation is the process that triggers dust lifting also on Earth. When the wind exceeds a threshold value, soil particles with size ~100 μm are the first to be mobilized (Greeley, R. and Iversen, J. D., 1987; Iversen, J. D. and White, B. R. 1982). They move over the soil in ballistic trajectories, where they hit and mobilize other particles. Dust grains (< 60 μm in size) are very tightly bound to the soil due to strong inter-particle forces and need very strong winds to be directly mobilized. They are generally brought into suspension through the impact of sand particles in saltation, which transfer sufficient momentum to break the inter-particle forces. During impacts among sand grains, sand and soil, and sand and dust, particles exchange electric charges and become charged. This causes the formation of strong atmospheric electric fields that can influence the motion of saltating particles, impacting on the overall dust lifting process (Farrell, W. M. et al., 2004; Kok, J. F. and Renno, N. O., 2009; Esposito et al., 2016). Electrical potential of few hundreds Volts in an atmosphere with CO_2 at low pressure (6-8 mbar on average on Martian surface, Gómez-Elvira, J. 2014) can produce discharges. The Paschen breakdown voltage is close to 100 V and the electric field can be ~ 200 kV/m (Haberle and Greeley 1991). Due to low humidity, the dry Martian environment maintains charge separation.

Martian saltation process has been widely studied (e.g. Sagan, C. and Bagnold, R. A., 1975; White, B. R. et al., 1976, Greeley, R., 2002; Kok J. F., 2010) due to the observations of the

very extended dune fields on the surface of Mars (generated as on the Earth by saltating sand grains), and is now considered an important mechanism actually acting on Mars after the observation of re-cent movements of Martian dunes and some MER observations (Kok, J F., 2012; Bridges, N. T. et al., 2012; Silvestro, S. et al., 2010, 2011; Geissler, A. S. et al., 2010), although other plausible dust emission mechanisms have been suggested (Sullivan, R. R. et al., 2008; Wurm, G. et al., 2008). Surface volatile outgassing, dust storms and dust devils, and planetary baroclinic waves are also responsible of injection and transport of particles in the atmosphere. Average saltation trajectories are supposedly about 1 m long and 10-20 cm high (White, B. R., 1979).

The daily and seasonal variation of dust abundance close to the Martian surface is also very uncertain. Moroz, V. I. et al. 1993 quoted it as n (number of particles) = 1 - 2 cm^{-3} near the Mars surface. This number varies between 1 and 0.2 cm^{-3} in the range of altitude 15 - 25 km. Above the altitude of about 25 km the dust number density declines sharply. The mass density of the Martian atmosphere in standard conditions has been quoted as 1.8E-7 kg/m^3 (Metzger et al., 1999). During a dust devil, instead, the mass concentration rises to 7E-5 kg/m^3 (Metzger, S., 1999).

The Martian climate and the dust cycle are influenced by lifting events like dust storms and dust devils. They redistribute dust lifted by winds on a local or a global scale (e.g., from the southern to northern hemisphere, where dust can be partly incorporated in the polar caps).

Dust storms arise when a gust front blows loose sand and dust from a dry surface. Particles are transported by saltation and suspension causing soil erosion from one place and deposition in another. These particles and those up to tens of microns that precipitate faster, fall over most of the planet, and contribute to a dust layer that covers all surface, if not removed later by wind. Aeolian processes and windblown particles over many years determine large accumulation of dust producing bright albedo areas (~ 0.27), vast dune fields, eroded hills, drifts of fine grains, and influencing formation and structure of cratered uplands and smooth terrain in the polar regions.

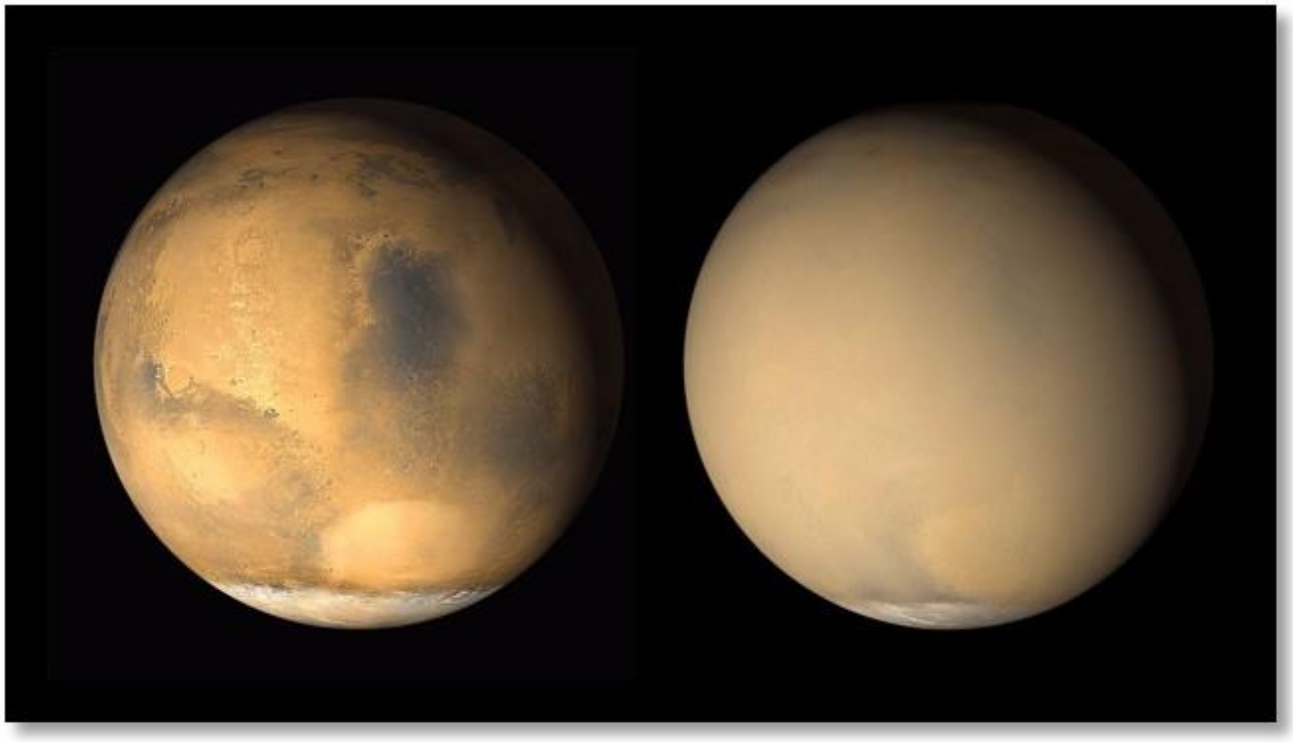

Figure 1.3 Mars before (left) and during (right) a global dust storm (Image courtesy of the Mars Orbiter Camera onboard NASA's Mars Global Surveyor orbiter).

Deposits of windblown particles may be important reservoirs for volatiles and may influence climate changes via variation of regional albedo. Dust storms can be thousands of meters wide and tens of kilometers high, tracing innumerable dark graffiti on the surface (Thomas, P. and Gierasch, P. J., 1985; Biener, K. K. et al., 2002). Local dust storms at southern hemisphere can grow into exceptional events (planet-wide dust storms), which cover the entire planet of dust, like a veil for many months (Figure 1.3). The last observed planet-encircling dust storm was observed in summer 2019.

Other than dust storms, Mars soil is interested by other significant dust phenomena, named "dust devils". Dust devils are thermally driven atmospheric vortices filled with loose sand and dust. The particles are raised from the surface by the low-pressure core within the dust devil (Sinclair, P. C., 1969; Greeley, R., 2003; Ferri, F. et al., 2003; Balme, M. and Hagermann, A., 2006). The masses of air sucked towards the dust devil axis of rotation are strongly accelerated, resulting in violent transverse winds. In combination with the vertical aspiration at the center of the dust devil, these winds succeed in lifting large quantities of dust.

Dust devils strongly contribute to Martian weather by dust entrainment, which influences atmospheric temperature, and lead to surface changes by removing thin layers of dust, causing albedo changes (Malin, M. C., and Edgett, K. S., 2001). HRSC on board Mars Express demonstrated the great influence of the Hadley circulation ascending branch for the increase in dust devil activity, especially during southern summer at latitude of 50°-60°S (Stanzel, C. et al., 2008).

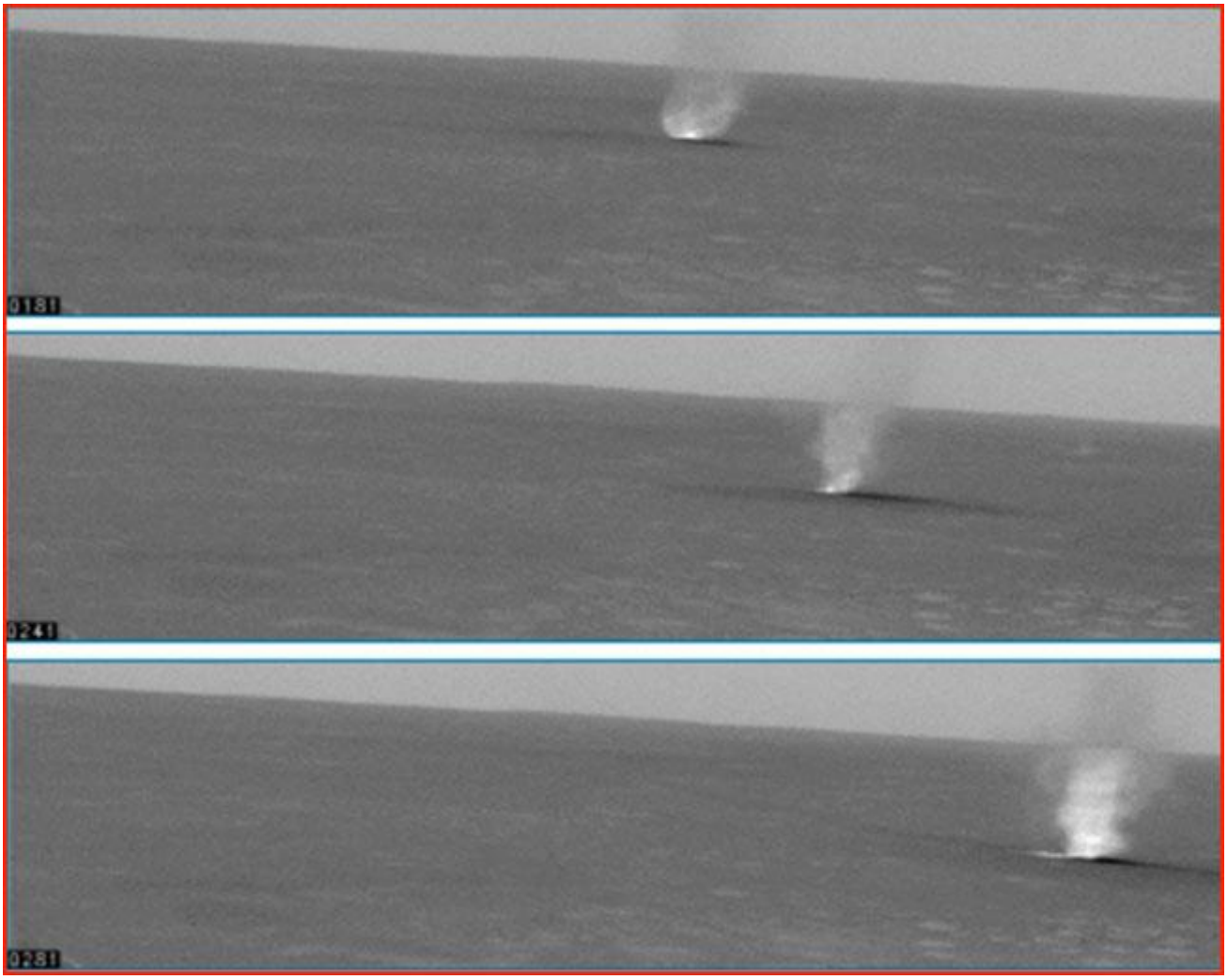

Figure 1.4 A dust devil as seen by the NASA's Spirit Rover

Dust devils (Figure 1.4) were first seen by VIS/Viking Orbiter and Camera/Viking Lander (Thomas, P. and Gierasch, P. J., 1985; Ryan, J. A. and Lucich, R. D., 1983; Ringrose, T. J. et al., 2003) and several occurrences were observed by Mars Pathfinder (Metzger, S. et al., 1999; Ferri, F., 2003), MER-A and MER-B (Greeley, R. et al., 2006), Mars Express (Stanzel, C. et al. 2008), Mars Global Surveyor (Cantor, B. A. et al., 2006), showing height up to 5000 m, diameter up to 1700 m and dust flux up to 5E-4 kg/m^2/s.

Dust devils are also frequent in the terrestrial deserts, but on Mars, they are widespread over the surface and observable in all seasons (Edgett, K. S. and Malin, M. C., 2000; Malin, M. C. and Edgett, K. S., 2001; Greeley, R. et al., 2004; Cantor, B. A. et al., 2006; Stanzel, C. et al., 2008; Reiss, D., 2018). They are more efficient in dust lifting than standard non-rotating boundary layer winds thanks also to the so called Δp-effect due to their low pressure core (Greeley, R. et al., 2003; Neakrase, L. D. et al., 2016; Bila, T. et al., 2019). Despite being studied for more than 150 years (Baddeley, M. D., 1860; Bagnold, R. A., 1941; Ives, R. L., 1947; Grant, C. C., 1949), we are still not able to fully understand and model the properties of these convective vortexes. Dust devils remain an active topic of research in particular on Mars, where they give a substantial contribution to the planetary dust budget (~50%) (Kahre, M.

A. et al., 2006; Whelley, P. L. & Greeley, R., 2008; Guzewich, S. D. et al., 2015). They actually represent the principal source of the Martian haze out of the dust storm seasons (Neubauer, F. M. 1966; Thomas, P. and Gierasch, P. J., 1985; Murphy, J. R. et Nelly., S., 2002; Fisher, J. A. et al., 2005). The vortex rotatory motion is superimposed to a forward translation, mostly leaded by the drag of the environmental wind. Hence, as a first approximation, the dust devils forward motion is representative of the local wind regime (Balme, M. et al., 2012, Franzese et al. 2021a).

Dust devils and dust storms are very common in autumn and winter as confirmed by the high dust opacity. With respect to dusty activities, the Martian year can be marked in two periods:

- Clear season: during northern spring and summer, with only few dust storms and low content of suspended dust in the atmosphere;
- Dust season: during northern autumn and winter with global and/or regional dust storms occurrence, which mostly grow up from the southern hemisphere (southern spring, i.e., Mars at perihelion) and can last several days.

In fact, when Mars is closer to perihelion (northern autumn and winter), dust, which in the former period was locally distributed in various regions, is then carried from the southern (where dust storms originate) to the northern hemisphere. Here, part of the dust is incorporated into the Polar Cap. When storms are absent, dust transportation is driven by baroclinic planetary waves. These are synoptic-scale disturbances of ~ 102-103 km, which grow at mid-latitudes due to baroclinic instability, arising from the existence of meridional temperature gradients in quasi-geostrophic equilibrium.

Dust spectra acquired by remote sensing measurements show silicon dioxide (SiO_2) structures and ferric oxide (Fe_2O_3) and aluminium oxide (Al_2O_3) traces for the dust grain composition. Possible terrestrial analogues are basalts, clay minerals composed in part of poorly crystalline ferric mineral, such as maghemite with a volume percentage of about 1.2% of magnesite, nontronite and palagonite (Toon et al., 1977; Bell III et al., 2006; Korablev et al. 1993). Moreover, dust grains covered by icy layers may also been found.

The simultaneous observation of sand saltation and dust emission by the Dust Suite Impact Sensors and MicroMED will provide significant advancement in the understanding of the nature of dust lifting processes on Mars. The role of Electric Field in accounting for a major dust lifting mechanism will also be clarified by correlating dust and sand fluxes measurements with acquisitions from the Dust Suite Electric Field Sensor.

Generally, in planetary exploration, *in situ* detection and monitoring of suspended particles, typical of planetary atmosphere, has not been performed directly. MicroMED aims at becoming the first ever instrument to perform such measurement. The technique chosen has never been used in space, and will provide direct and local measurements of dust properties. For the first time it will be possible to characterize primary airborne dust (i.e. the recently lifted dust) directly close to its emission source. The size distribution will be built

starting from single grain detections, and not assumed ad hoc, and measurements will be performed in the atmospheric layer close to the surface.

A detailed description of the methodology used as well as of the mechanical and geometric characteristics of MicroMED will be provided in the following sections.

1.2 The ExoMars programme, the Dust Complex Suite, and the scientific payload developed by INAF-OAC: GIADA, MEDUSA, DREAMS and MicroMED

The previous paragraphs highlighted the importance of characterizing Martian dust in order to improve our understanding of both past and present Martian climate. The ExoMars 2022 mission will allow important dust characterization, through the combination of several sensors and, in particular, through the suite of instrument "Dust Complex Suite", aimed at such purpose in all of his aspects (size distribution, electrical properties, etc.). A description of the ExoMars programme, as well an introduction to the Dust Complex Suite and to the history of instrument and sensors developed by INAF – OAC aimed at the characterization of dust in several Solar System environments, is reported hereafter.

1.2.1 The ExoMars Programme

ExoMars (Exobiology on Mars) is a program of the European Space Agency (ESA) in collaboration with the Russian Federal Space Agency (Roscosmos). The scientific goals of the project are: to search for evidences of extinct or extant life on Mars, characterize the water/geochemical environment as a function of depth in the shallow subsurface, investigate Martian atmospheric trace gases and their sources, perform context imaging of the landing site, long-term climate monitoring, and atmospheric investigations. The program foresees two separate missions. The first mission was launched on 14th March 2016 and included the Trace Gas Orbiter (TGO) and the Schiaparelli Entry Descent and Landing Demonstrator Module. The TGO is currently in orbit around the planet and it aims at mapping the sources of various atmospheric trace gases, characterizing their spatial and temporal variation. In particular, the TGO monitors the methane, in order to study the biological or geological origin of the gas. The TGO was also meant to help the navigation of ExoMars Rover.

The scientific payload of the Schiaparelli Lander included the DREAMS (Dust Characterization, Risk Assessment, and Environment Analyzer on the Martian Surface) meteorological station, developed under the scientific leadership of the Osservatorio Astronomico di Capodimonte (INAF – OACN), that aimed at a complete characterization of

the Martian boundary layer. A brief description of the meteorological station is provided in the upcoming paragraphs.

One of the aims of the Schiaparelli lander was to test the Entry, Descent and Landing (EDL) of a payload on the surface of Mars, in preparation of the ExoMars 2022 mission, that is set to bring a Lander (the *Kazachok* Surface Platform, see Vago, J. et al. 2015) and a Rover. The rover aims to investigate the Martian subsurface to search for signs of organic material of biogenic origin, in particular from the planet early stages. The Martian atmosphere is currently not able to shield the surface from the ultraviolet radiation, plus Mars has not an active magnetosphere, therefore the biological traces could only be found in the underground because of the exposition of the planet surface to the ionizing radiation. The rover is equipped with solar panels and, through its stereo camera (PanCam), it will be able to autonomously navigate Martian surface. It is expected to be able to travel up to 100 m per sol, in order to scan various sites in search of organic material. The sites for such research will be chosen by means of a ground penetrating radar (WISDOM), a water searcher instrument (Adron) and a close up camera (CLUPI). The rover is also able to automatically extract sample up to 2 meters deep with its drill, characterizing the borehole with an infrared spectrometer (ISEM) and establishing the mineralogy by means of the Ma_MISS spectrometer, accommodated inside the drill tip. The collected samples will be delivered to the instruments positioned inside the rover and crushed in powder in order to perform an infrared analysis (by means of the MicrOmega instrument) as well as analysis by means of a raman spectrometer (RLS) and by the organic molecule analyzer (MOMA). The study of the sub surface composition, coupled with the analysis of the trace gases performed by the TGO, will also allow to retrieve the past climatic condition of the planet.

The surface platform, instead, will characterize the atmospheric environment of the landing site, acquiring data during an entire Martian year. Overall, its main scientific goals are:

- the study of the vertical structure of the atmosphere, from the orbit to the surface;
- the determination of the present climatic conditions;
- the analysis of the aeolian processes, both for clear and dusty environment;
- the proof of the existence of an atmospheric electric field;
- the first direct measurement at the surface of atmospheric dust concentration;
- to provide ground data to validate the observations made by the orbiters;
- the study of the amount of atmospheric humidity and its daily and seasonal variation;
- the study of the internal structure of the planet, its rotation and orientation, using X-band radio measurement between the surface platform and the Earth;
- the investigation of the amount of volatiles exchanged between the atmosphere and the surface, in order to study the possible presence of subsurface water;
- the monitoring and characterization of the radiation environment, including the ultraviolet one.

Among the other instruments, the platform will carry also a METEO package, equipped with a temperature, pressure, humidity and wind speed and direction sensor. It will study the vertical atmospheric profile starting from the descending, monitoring the global circulation and the cycles of carbon dioxide and water vapor.

In addition, the lander also hosts the Dust Complex, a suite of instruments able to monitor the activity and electric proprieties of lifted dust and saltation. It is a suite of 4 sensors, namely:

- an impact sensor, for the detection of the saltating sand grains and the measurement of their electric charge;
- a mast including two electric field electrodes for the study of the atmospheric E-field, the electromagnetic activity sensor (EMA) for the observation of the possible electromagnetic discharges and a second impact sensor;
- a conductivity sensor (CS) for the measurement of the electric conductivity of the atmosphere;
- an optical particle counter (MicroMED) able to monitor the airborne dust concentration and size distribution.

The synergy between the meteorological package and the Dust Complex will allow to fully characterize the aeolian processes and the environmental conditions.

MicroMED has hence a pivotal role in the success of the Dust Complex, and it is only the most recent instrument conceived and developed by the department of Cosmic Physics and Planetology at the Astronomical Observatory of Capodimonte. The following paragraphs will introduce the reader to the history of such instruments, finally culminating in MicroMED.

1.2.2 GIADA

GIADA (Grain Impact Analyzer and Dust Accumulator, Esposito, F. et al., 2002; Colangeli, L. et al., 2007; Rotundi, E. et al., 2015; Della Corte, V. et al., 2016) on board the Rosetta probe is an instrument that was conceived to measure flux, number, mass, momentum and velocity distribution of grains expelled from the nucleus of the 67P/Churyumov-Gerasimenko comet. GIADA was constituted by three sensors: the module Grain Detection System (GDS), the Impact Sensor Plate (IS), and the microbalance system (MBS). The GDS performed in situ optical detection of the incoming dust grains without modifying their dynamical properties, and the measurement of the particle scattering cross section, which contains information on dimension, optical properties and shape. GDS looked for particles with size more than 10 μm, while smaller particles are detected by a the MBS cumulative mass deposition system. IS measured the momentum of each sampled dust grain. The coupling between GDS and IS allowed to measure the grains speed in the normal direction with respect to the IS sensing plane and their mass. Each grain entering the instrument crosses a light curtain generated by an illumination-collimator system, and is detected by two series of receivers (i.e., 4 photodetectors, each one equipped with a Winston

cone to concentrate the radiation), which, coupled with the IS signals, allow to retrieve the time of flight across the curtain to derive grains velocity. Since the detected signals are related to the geometric cross-section and the scattering efficiency of the grains, data about particle size, composition and aggregation status can be estimated through an accurate calibration. The optical detection guarantees that the dynamical properties of the grains were not be altered during detection. GIADA has been the first dust measurement instrument developed by the INAF – OAC department of Cosmic Physics, which I am currently a part of, and that developed MEDUSA, DREAMS, and MicroMED, the latter being the focus of the bulk of my Ph.D. work.

1.2.3 MEDUSA

MEDUSA (Esposito, F. et al., 2011; Colangeli, L. et al., 2009) is the acronym for Martian Environment Dust Systematic Analyzer. It is an instrument for in situ measurement of dust grain size, size distribution, concentration, deposition, electrification and velocity, and water vapour abundance in the Martian atmosphere at ground level.

The MEDUSA instrument was also designed by our department at INAF - Astronomical Observatory of Capodimonte, and its development was funded by European Space Agency (ESA) and Agenzia Spaziale Italiana (ASI) in different project phases. MEDUSA also envisaged contributions by international partners: the Dust Deposition and Electrification Stage (DDES) subsystem was developed by Innoware and Aarhus University, Denmark, while the Main Electronics was developed by Instituto de Astrofísica de Andalucía, Granada, Spain. MEDUSA inherited the knowhow and experience acquired during the development of the GIADA instrument. The MEDUSA concept was developed within the ESA ExoMars Programme. It was initially conceived to be accommodated in the Pasteur Payload (PPL) on the ExoMars Rover, and, then, relocated in the Humboldt Payload (HPL) on the ExoMars lander, which were scheduled for launch in 2016. In 2009, the MEDUSA instrument successfully passed the ESA Preliminary Design Review (PDR) with Technology Readiness Level (TRL) 5.3. Shortly after that, the ExoMars program was completely reviewed and the lander with its Humboldt payload was cancelled.

The scientific objectives of MEDUSA were part of the more general goals of the ExoMars Programme. The information obtainable by MEDUSA over different time spans (days, seasons, years) was indeed important for more general scientific objectives:

- Exobiology on Mars:
  - by determining the present climatic conditions at Mars surface;
  - by searching for water;
  - by determining the physical parameters impacting on presence of life on Mars;
  - by deriving information about past history of Mars climate;
  - by providing ground-truth for validation of data coming from orbiter observations.

- Operations on Mars:
  - by evaluating hazardous conditions due to the Martian environment;

- by placing constraints on operative conditions at Mars;
- by supporting the definition of future human exploration of Mars.

The scientific objectives can be accomplished with different kinds of measurements performed by the subsystems of the MEDUSA suite. The physical quantities to be measured by the MEDUSA subsystems are:

- Atmospheric dust grains size and dust size distribution:

The dust particle size is the equivalent diameter measured in the range of 0.4-20 μm via light scattering analysis, and in the range of 0.05-0.4 μm via accumulation on a microbalance. The dust size distribution is the fractional occurrence of the particles with respect to their size and is obtained by counting the grains analyzed in different size bins;

- Atmospheric dust particle number density:

The atmospheric dust particle number density is the number of particles per unit of fluid volume. It is derived from the previous measurement since the volume sampled by the system is known;

- Atmospheric water vapour abundance:

The atmospheric water vapour abundance is the mass or volume fraction of water in the atmospheric fluid. MEDUSA is able to measure the water vapour partial pressure by the detection of water condensation on the surface of a thermally controlled device, i.e., a microbalance. The relative humidity can be also estimated using the values of the atmospheric pressure and temperature, which are measured by other sensors, e.g., AEP (Advanced Environmental Package) in HPL. The measurement has sensitivity better than 10 ppm;

- Dust deposition/removal rate:

The dust deposition/removal rate is the dust accumulation/removal with respect to time. It is measured by the detection of scattered light from dust accumulating on a transparent surface. It has a sensitivity better than 0.1%/sol;

- Electrification of suspended dust particles:

The electrification of suspended dust particles is the amount of the net electrical charge stored in the particles. It is measurable in the range $\pm 10^3$-10^6 electrons/grain by applying electric fields to a dust accumulation surface;

- Dust velocity (horizontal component and direction):

By measuring light scattered by suspended grains, velocity and, therefore, wind speed/direction can be quantified. Dust velocity is measured in a horizontal plane with a sensitivity of less than 20%.

MEDUSA was selected to be part of an early version of the ExoMars programme. However, the ExoMars programme was significantly modified and the INAF – OAC Cosmic Physics team moved on, developing other instruments like DREAMS and MicroMED.

1.2.4 The DREAMS Experiment

DREAMS (Esposito, F. et al. 2018; Bettanini, C, et al. 2014, 2018) was the only scientific payload accommodated onboard the Schiaparelli lander. It consisted of a meteorological station comprehensive of the first electric field sensor ever sent to Mars.

The purpose of the experiment was the characterization of the Martian atmospheric boundary layer mainly in a dusty scenario, providing in particular the first investigation of the atmospheric electric properties, through the combination of meteorological and electric measurements. Such data could have also helped to study the hazards for instruments operating on the surface as well as for eventual human explorers of the planet, quantifying the dusty scenario and the magnitude of the possible electrical discharges. The meteorological station consisted of the following sensors: a thermometer (MarsTEM), a pressure sensor (DREAMS-P), an air humidity sensor (DREAMS-H), a 2D anemometer (MetWind), an electric field sensor (MicroARES) and a Solar Irradiance Sensor (SIS). Data were collected by an autonomous Central Electronics Unit (CEU) and all the systems were powered by an internal battery.

DREAMS was developed through the cooperation of six European Countries (Italy, France, Spain, Netherlands, Finland, United Kingdom). The project was developed under the scientific leadership of INAF – OACN.

The ExoMars 2016 mission reached the proximity of Mars on October 19th, 2016. However, Schiaparelli experienced a failure during the EDL phase and crashed to the ground, preventing the scientific retrieval expected by DREAMS. DREAMS was supposed to begin its operations after the touchdown, and few seconds before crashing it switched on for the sequence of operations scheduled after landing, proving to be healthy and ready to start measurements.

1.2.5 MicroMED

Atmospheric dust heavily influences the thermal structure and dynamics of the atmosphere, affecting the circulation at all the scales. This is especially true in the Martian case, where the stronger dust storms can lead to an absorption of over 80% of the solar radiation. Moreover, the surface dust and sand flux and their granulometry represent key input parameters for the Mars climate models like the one developed by Forget et al. (Mars Climate database v5.3). However, the exact mechanisms of raising and settling of dust as its temporal and geographical variability are still not well understood, in particular due to the lack of proper data. Indeed, the estimation of the suspended dust concentration and size distribution is indirectly inferred from the opacity obtained using land or orbit images. The indirect evaluation of these quantities needs several a-priori assumptions and a lot of the information related to near surface layers cannot be extracted.

MicroMED (Figure 1.5) has been developed to fill this lack of information, directly monitoring, for the first time ever, the lifted dust concentration and size distribution, as well as its variability in time. Also MicroMED has been developed under the scientific leadership of INAF – OACN. The instrument is an updated and miniaturized version of the sensor MEDUSA.

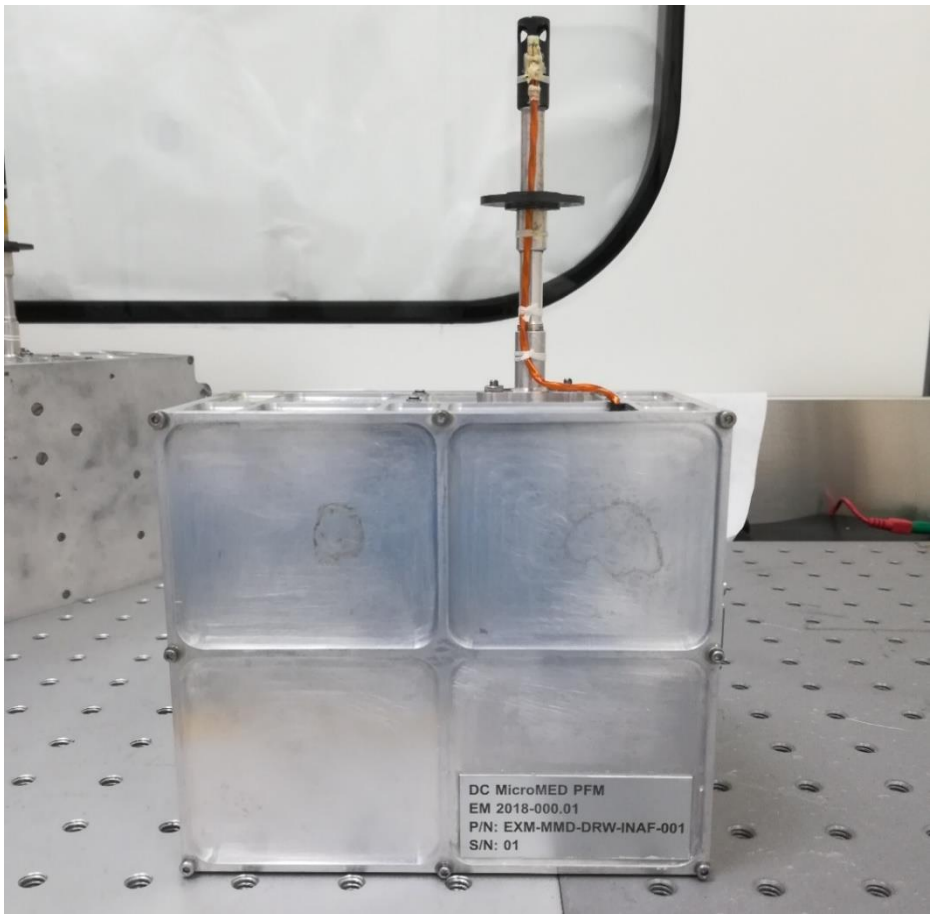

Figure 1.5 The MicroMED OPC.

The following sections will provide a detailed description of MicroMED's structure, functioning and subsystems.

1.2.5.1 MicroMED structure

MicroMED processes the light scattered from single dust particles sampled in the Martian atmosphere to measure their size and abundance. A proper fluid-dynamic system, including a pump and a sampling head, allows the sampling of Martian atmosphere with the embedded dust. The captured dust grains are detected by an Optical System and then ejected into the atmosphere. The Optical System's output signal is then amplified and processed by the electronics of the instrument.

MicroMED's architecture is mostly based on the fluid dynamic system, the optical system and the laser assembly.

The **Fluid dynamic system** is aimed at the sampling of fluid with embedded grains from Martian atmosphere. It is made of a sampling head, an inlet duct and a pump. The pump generates the suction of fluid by generating a pressure difference between the inlet and outlet sections of the instrument. MicroMED's sampling head is a cylinder with 4 circular holes equally distributed on the lateral surface of the tube nearby the cover, allowing the suction of fluid. The inlet duct is a tube in aluminium alloy, with its upper end exposed to the external environment. Its design is conceived to convey the flow toward the Optical Head (which is a box containing the Optical System and the Laser Assembly) and concentrate the flux of grains in the sensing volume of the instrument. Another tube, the outlet duct, which is aligned with the inlet tube (they share the same longitudinal axis), collects the fluid from MicroMED's Optical Head and carries it toward the pump, then ejecting it outside MicroMED and into the atmosphere.

The **Optical System (OS)** is the sensitive part of the instrument. It is where dust particles entering the instrument are detected since they cross an illuminated region (sensing volume) generated by a laser source. The laser diode is external to the OS and connected via an optical fiber. The laser light coming from the fiber is then collimated through a lens system and focused onto the sensing volume. Grains crossing the sampling volume scatter the received light. Scattered light is collected by a mirror that focuses it on the photodiode detector. A light trap captures the laser light in a way that minimizes stray-light inside the instrument. By means of a process called Pulse Height Analysis (PHA), it is possible to relate the intensity of the scattered light signal (orders of the millivolt) with the grain size, and its duration with the grain speed (since the dimensions of the sensing volume are known). A possible approach relating the duration of the signal also to the grain size (by means of the law relating grain size and their velocity) is currently under development (See Franzese et al., 2021b).

The **Laser Assembly** consists of the laser diode, the lens system that feeds the optical fiber and the optical fiber itself.

All the functions of the instrument are controlled by a **Central Electronics Board** (CEB) integrated inside MicroMED. The instrument detects each dust grain entering into the sensing region, giving as output a waveform for each grain to be processed by the CEB. The ADC of the CEB allows to sample each waveform. As baseline, the CEB stops the acquisition when the maximum number of grains that can be memorized in a single acquisition (run) are detected. This number can strongly vary depending on the number of samples detected for each signal, meaning that if more detailed waveforms are desired, a lesser number of events can be stored in the memory and viceversa. Overall, the maximum number of events that can

be stored during a run can vary from 200 to more than 5000 depending on the acquisition method.

Figure 1.6 shows an overall view of the instrument subsystems. The work described in this Ph.D. thesis is mostly focused on the fluid dynamic system, that will thus be described in deeper detail with respect to the other subsystems.

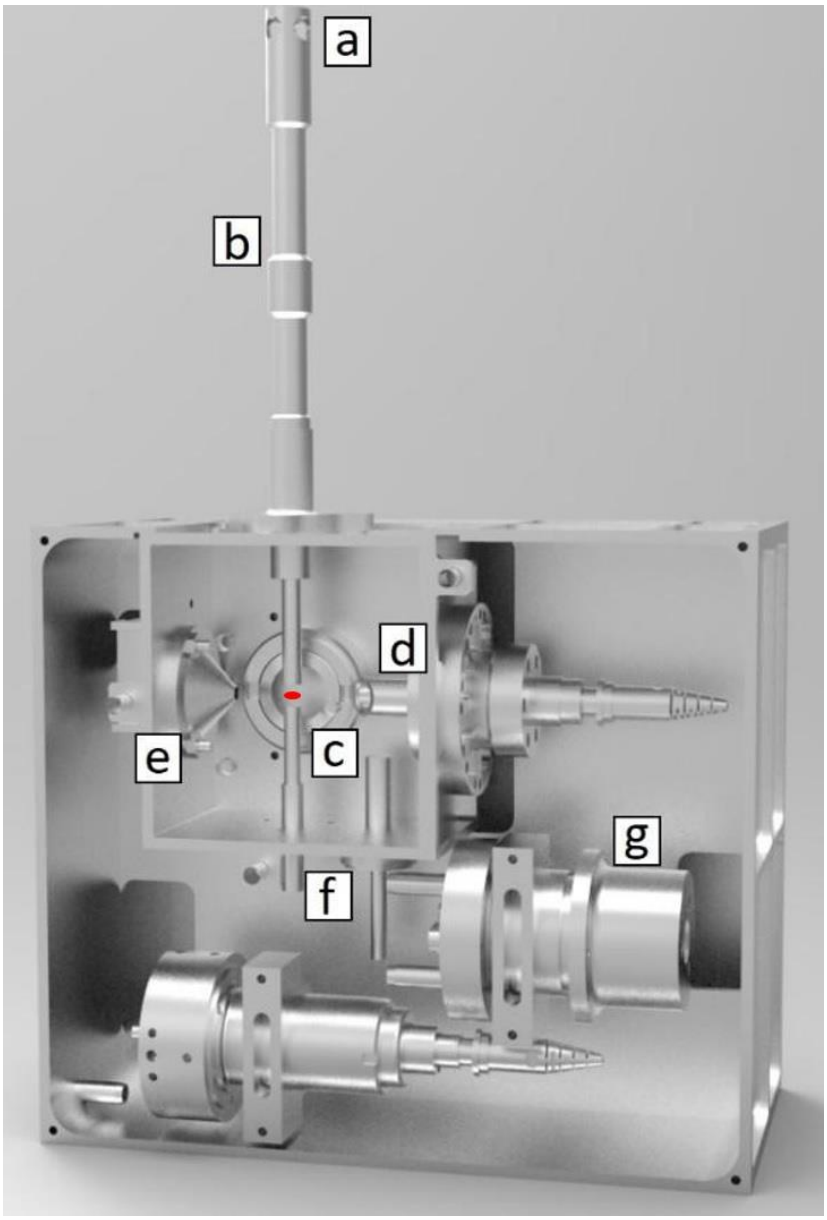

Figure 1.6 MicroMED inside view. MicroMED is made by the following subcomponents: (a) sampling head, (b) inlet duct, (c) sensing spot, (d) laser emission system, (e) light trap (f) outlet duct, (g) pump. The red dot in figure indicates the position of the sensing spot, where the laser is focused.

1.2.5.2 Fluid dynamic design

MicroMED's fluid dynamic design is shown in Figure 1.7.

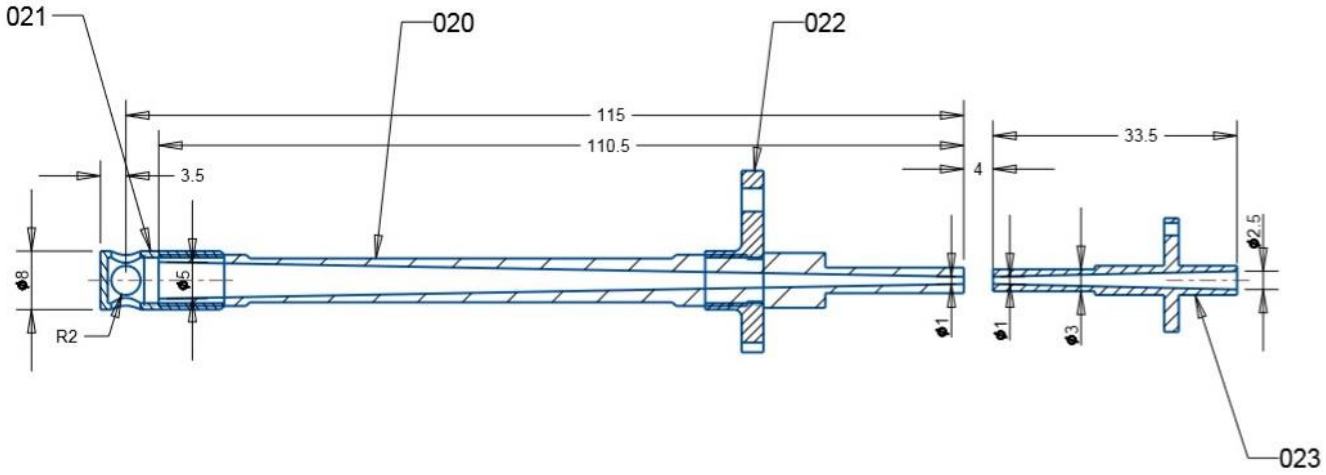

Figure 1.7 MicroMED fluid dynamic design (section). All dimensions are in mm.

The instrument will be in vertical position (with the head on the top). It is equipped with a sampling head, exposed to the flow, which has to be protected from the outside environment prior and during the landing. Four inlet holes are located on the sampling head, allowing the suction of fluid inside the instrument. An inlet duct conveys the fluid toward the sampling section. The inlet duct is 118.5 mm in length (sampling head included), with a conical section going from 4 mm of internal diameter in proximity to the sampling head to 1 mm just before the sampling section. The extremely small final diameter of the inlet duct is needed to concentrate the flow of grains in the 1 x 1 x 0.3 mm^3 sensing spot.

The sampling section is a 4 mm long gap between the inlet and outlet ducts. Here optics scan the 1 mm^2 front area sampling spot that is produced by a collimated laser beam.

The outlet duct gathers fluid and particles from the sampling section, expelling them from the instrument. It has conical section going from 1 mm of internal diameter to 2.5 mm, allowing a comfortable connection to the pump. The outlet duct is 32.5 mm in length and moves the flow toward the pump inlet.

The pump is located after the outlet duct, generating a pressure difference with respect to the inlet section of the instrument, causing suction of the fluid from outside. The driving force is then the force due to this pressure difference.

Figure 1.8 and Figure 1.9 show how the instrument works. When the pump is activated, a pressure difference is generated between the inlet and the outlet of MicroMED. Fluid is sucked inside the instrument through the four inlet holes and it is then accelerated toward the sampling section. Once the 4 mm gap at the end of the inlet duct is reached, the flow

experiences a sudden expansion, meaning a sudden deceleration of the flow. Fluid, containing suspended dust particles, is scanned and then expelled via the outlet duct. It is important to underline that the flow shows potential compressibility effects. Such effects could be due to the sudden temperature variation the fluid experiences when it enters the instrument, given that MicroMED is positioned under a thermal cover that limits its temperature range to the 253-313 K interval, while Martian atmosphere is subject to extreme temperature variations both in the day-night cycle and for the variation of the seasons.

The instrument should work at a pump condition that generates an inlet-outlet pressure difference of 200-300 Pa, that is about 30-50% of the atmospheric pressure value.

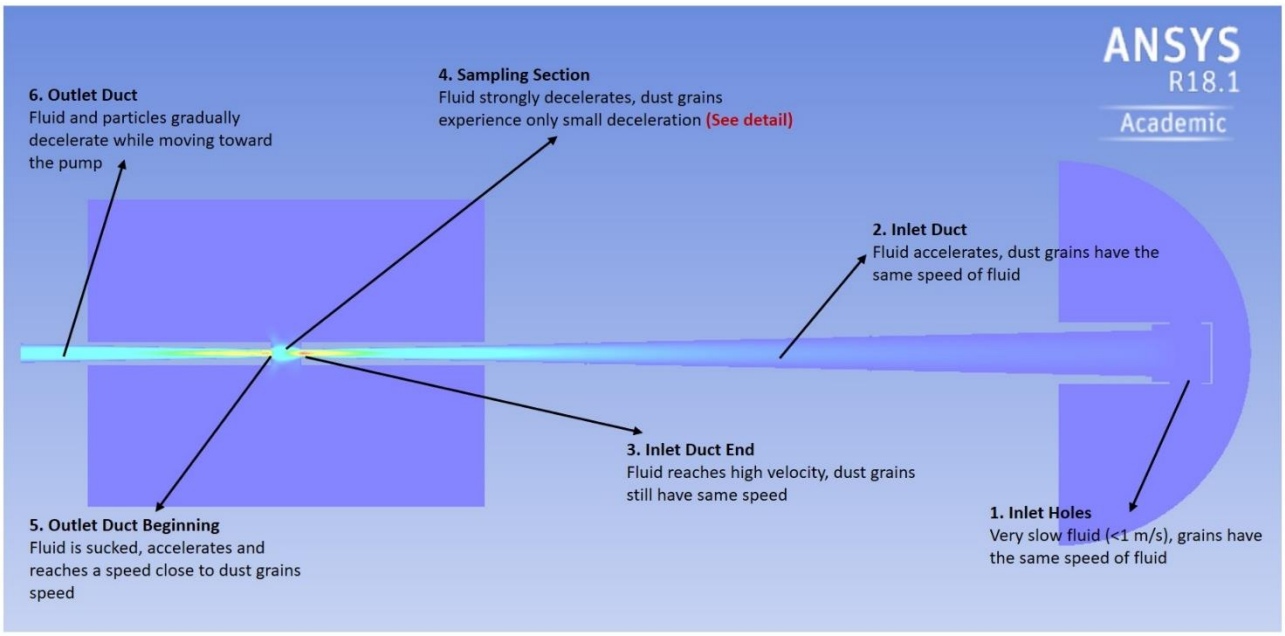

Figure 1.8 Flow evolution through MicroMED.

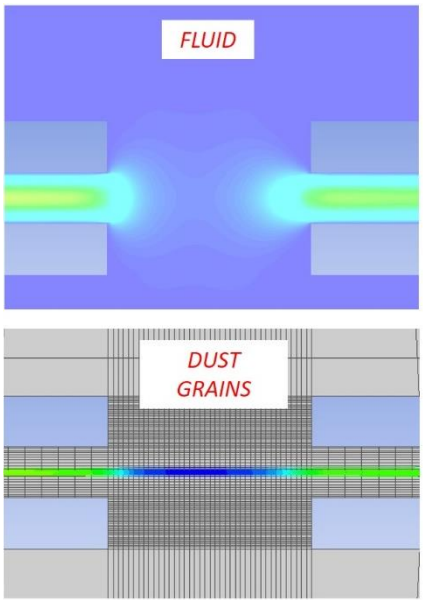

- Fluid experiences a strong deceleration because of the sudden expansion.
- Dust grains have only small decelerations as they are not strongly influenced by the expansion. This also allows them to stay around the center of the sampling plane.

Figure 1.9 Detail of the behavior inside MicroMED sampling plane.

The duct design is conceived to concentrate dust grains in the 1 mm^2 front area of the illuminated sampling spot. Grains cross the sampling spot if they meet the following behavior:

- Dust grains are immediately deflected by the pressure force generated by the pump and moved toward the inlet duct, crossing the inner rings of the duct section and avoiding contact with the walls. This is an important aspect, since the walls mean surface roughness should be about the same order of magnitude of the dust grains diameter (direct measurement during MicroMED's integration in 2019 determined that an average roughness of 23 μm is expected for all ducts), meaning particles hitting the walls will probably get stuck. If they do, they cannot be detected by the instrument;
- Dust grains reaching the sampling section are not influenced by the flow expansion and keep moving along the inner part of the duct section. By doing so, they cross the sampling spot, situated in the middle of the sampling plane. If the flow expansion happening in the sampling section deflects dust grains from their trajectory, particles might cross the sampling plane outside the illuminated spot, meaning such particles are undetected.

Laminar flow condition is desired, as turbulent flow causes larger deflections of the particles trajectories and introduces an error due to the possibility of detecting some particles more than once. The design has also to guarantee a small fraction of coincidence f (e.g. < 0.05) in order to have a single particle counter and a large number of particles detected in a short time. Size distribution and volume density of dust grains must not be altered during the

sampling and measurement process. In addition, the optics must not be obstructed by the ducts walls, mirrors do not have to be shadowed and the laser beam doesn't have to be intercepted and reflected by the instrument walls in any way (to avoid the generation of optical noise: straylight).

The following paragraphs describe how every part of the instrument was conceived in order to satisfy all the reported technical requirements. The overall fluid dynamic critical design parameters are:

- Geometrical profile of the sampling head;
- Diameter of the outflow section of the inlet duct;
- Geometrical profile of the inlet duct;
- Distance between the outflow section of the inlet duct and the sampling volume centroid;
- Diameter of the outlet duct;
- Geometrical profile of the outlet duct;
- Distance between the inflow section of the outlet duct and the sampling volume centroid;
- Pump volumetric flow rate.

Variations of these parameters allowed to simulate different configurations and find the most effective one.

1.2.5.2.1 Sampling Head

MicroMED's sampling head is a cylinder with four, 4 mm diameter symmetric holes positioned 90 degrees away one from the other, conceived to be minimally invasive. Being exposed to the outside environment, the sampling head has to be closed on top and inlet holes have to be not too big in order to avoid obstruction of conducts. The shape of the sampling head was meant to keep the flow laminar as turbulence is thought to worsen the instrument efficiency (aerosol motion would become unpredictable). The hole dimension was fixed to 4 mm in diameter, keeping a good suction ability while avoiding obstruction of the ducts. Tests for bigger holes were indeed performed (5 mm in diameter), showing bigger volumetric flow rates and bigger dust samples available but limited suction ability by the instrument. Wider holes would cause a reduction of the Δp between the atmosphere and the inside of the sampling head, therefore the pressure force acting on particles would diminish, a critical issue for the functioning of the instrument especially in windy conditions (windy conditions means faster grains are approaching MicroMED's sampling head, therefore more energy is needed to deflect grains toward the inside of the instrument). Moreover, the

possibility that bigger grains could obstruct the ducts would increase. Smaller holes, instead, would cause particles dispersion and reduce the sample of aerosol inhaled.

As for the sampling head inner duct, previous works showed the optimum diameter in order to concentrate aerosol toward the sensing region is 1-2 mm, a requirement met throughout the duct that brings the fluid from the four inlet holes to the inlet duct. Figure 1.10 shows the sampling head of MicroMED.

Figure 1.10 MicroMED's sampling head. Differently to the inlet duct which is made of aluminium alloy, MicroMED's sampling head is made of a polyimide-based plastic named Vespel.

1.2.5.2.2 Inlet duct

The inlet duct is an aluminium conduct of simple shape, able to keep the flow laminar throughout its path along the duct. A mean surface roughness of about 23 μm was achieved. This value is good enough to keep the flow laminar and improve the grain chances of being reflected by the walls after a hit. Inlet shape was conceived in order to optimize the instrument suction ability. Current configuration gives very good results in no wind conditions and allows better performances in windy environments with respect to the

breadboard version of the geometry. Research articles have been written on the topic (Mongelluzzo, G. et al. 2018, 2019a, 2019b, 2019c), showing that MicroMED, with this design, has even outperformed expectations in both still and windy atmosphere. A detailed description of the design phase will be provided in the later sections of this work.

Different configurations were developed. The first version of MicroMED prototype had a shorter inlet duct, that was then elongated to fulfill accommodation requirements of the landing platform. The thermal cover over the instrument was indeed set to 10 cm thick after the design process began, therefore a variation to the design was needed. The duct diameter was reduced from the original 6 mm to 4 mm, in order to improve the suction ability. Current configuration also allows to minimize collisions on walls for bigger dust grains (diameter > 15 μm), dramatically improving the behavior of the instrument with respect to the breadboard geometry. This has been obtained without losing suction ability.

The inlet duct is now completely conical, differently to what happened for the breadboard version. As already stated, the duct's internal diameter gradually diminishes from 4 mm to 1 mm and it is 118.5 mm long. The conical shape allows to drive the entire flow toward the sampling volume, with the particles concentrated in a 1 mm diameter jet. Reaching the 4 mm long gap, the flow expands and such expansion may cause deflection of some particles, but most of the suspended dust grains keeps their trajectory close to the sampling volume centroid, allowing detection.

1.2.5.2.3 Sensing region

The sensing region is the segment of the instrument where the actual measurements are made. Concerning the fluid dynamic aspects of this section, the length of 4 mm of this gap between inlet and outlet ducts was chosen to optimize the evolution of the particles flow through the instrument, allowing the detection of almost all of the particles reaching the sampling section (assuming ideal behavior by the Optical System). Such distance also guarantees that aluminium surfaces don't interfere nor shadow the detecting laser light in any way. The sampling volume centroid is halfway through the gap. It is followed by the outlet duct which gathers fluid and particles from the sampling section expelling them from the instrument.

1.2.5.2.4 Outlet duct

The outlet duct begins at the end of the sampling section, expelling the fluid from the instrument and allowing it to reach the pump that is generating the pressure difference. It is made of a conical tube whose diameter gradually increases from 1 mm to 2.5 mm allowing a perfect connection with the pump. Such connection is guaranteed by means of a silicon tube

linking MicroMED's outlet and the pump's inlet. The possibility of chamfering the inlet hole of the outlet duct was considered, but analysis showed such chamfering would have caused an expansion of the flow, worsening the instrument efficiency. The outlet duct design evolved from its breadboard version who was made of two cylindrical ducts, allowing, among the advantages, more gradual fluid speed variations and reduced risks of flow separation.

1.2.5.2.5 Pump

The pump is situated in the outlet section of MicroMED. Its goal is to generate a pressure difference between the inlet and the outlet sections of the instrument, causing the suction of a sufficient amount of fluid in order to have an efficient test. As for previous sections, only fluid dynamic aspects of the pump will be discussed. Fluid dynamic behaviour of the instrument was simulated considering different values of the inlet-outlet Δp in the 100-300 Pa range. CFD simulations preview MicroMED pump volumetric flow rate at the inlet to be between 1 and 2.5 l/min in operating conditions, in which the pump will generate a pressure difference of 200 Pa, a value lower than the one considered for the breadboard version (300 Pa). This value was chosen as a compromise: small dust particles tend to be deflected by the expansion of the flow inside the sampling volume since their inertia is not high enough to keep them along their original trajectory, so the pressure force generated has to be strong enough to reduce these particles tendency to deflect. On the other hand, big particles tend to hit the walls inside the inlet duct because their inertia is high and big pressure forces acting on the particles increase the probability of impacts. The compromise between these two aspects was found for the aforementioned inlet-outlet Δp value of 200 Pa.

In the PFM, the pump is connected with the instrument by means of a U-tube because of the instrument geometry constraints, reducing the pump ability to generate suction. Tests were performed with this configuration in order to account for the effect of such tube on performances. The pump is a custom model developed by Politecnico di Milano, Polo di Lecco (MetroSpaceLab premises), that are responsible for the mechanical design of MicroMED.

1.2.5.3 Optical design

The optical design is made of two optical subsystems:

- Laser feeding optics;
- Optics for the generation of the MicroMED sensing volume.

The laser feeding optics design is tailored for laser RLT830-150GS, working at 830 nm of wavelength. The optical design has been done taking into account the following parameters:

- Fibre core 50 μm (image plane);
- Fibre NA 0.22;
- Laser wavelength 830 nm;
- Conceptual mechanical mounting: laser and fibre alignment versus lenses;
- Laser case dimensions;
- Laser characteristics. In particular, from laser tests, the emitted Gaussian beam with x-divergence 40° and y-divergence 25°.

The diverging laser light coming from the photodiode is led into the fibre core by means of a system of two aspherical lenses, made of Fused Silica glasses. The distance between the fiber and the first lens is 1.3 mm.

Thermal and pressure analyses showed that opto-mechanical design is not sensitive to thermal and pressure variations.

The focusing system on sample volume is optimized to concentrate the laser beam radiation, coming from the exit surface of the optic fiber in the center of the sample volume. This system has 2 lenses. The first lens is a bi-spherical convex lens, while the second is bi-cylindrical convex lens. The material used for each lens is Fused Silica glass, and each curvature radius and thickness is optimized to concentrate the beam light, coming from the fiber, in the center of the sample volume with a blade shape. The constraint of the system is that the minimum optical density inside the volume is 0.4 MW/m^2. For optical density computation, a conservative approach has been considered, assuming that the minimum fiber output power required is 155·0.88 mW. The overall actual sampling volume is 1.3 x 1 x 0.360 mm^3.

The optical system is conceived to focus the beam in the center of the sampling volume, along the propagation beam axis, assumed as optical axis, in the plane containing the beam and the particle directions. In the plane, along the optical axis, perpendicular to the previous one, the system creates a collimated beam. More than the 88% of the rays emitted by the fiber are collected by the detector.

Energy distribution plots have also been evaluated during the design phase. On the central row a distribution with a flat plateau is obtained, and on the central column a Gaussian distribution is shown respectively.

The optical design of MicroMED will not be described further here given that it was not an integral part of this Ph.D. work.

1.2.5.4 Thermo-Mechanical design

MicroMED consists of seven mechanical groups as listed below (See Figure 1.11):

- Group 000: Optical bench, shielding box, optical head and electronics supports;
- Group 100: Pump;
- Group 200: Fiber-volume opto-mechanical system;
- Group 300: Laser-fiber opto-mechanical system;
- Group 010: Detector assembly;
- Group 020: Inlet and outlet group;
- Group 040: Light trap and reference detector.

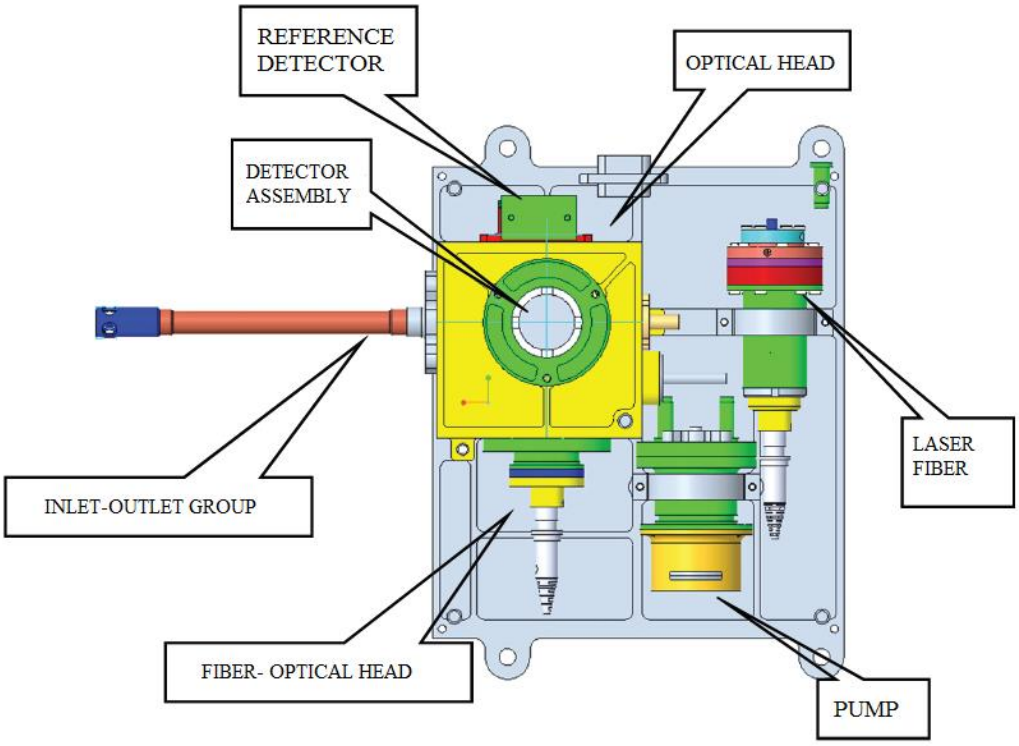

Figure 1.11 Overall review of MicroMED's design groups.

MicroMED's thermos-mechanical design was based on the following requirements:

Thermal design requirements

- Non-operative temperature range from -40°C to +50°C;
- Operative temperature range from -20 °C to 40 °C;
- Max pump power 5 W;
- Laser power 0.4 W;
- Electronics 1.17 W.

Mechanical design requirements

- First mode of vibration higher than 150 Hz;
- Mass budget with 20% contingency 500 g;
- Resistance vs. quasi-static loading 100g acceleration;
- Envelope volume 148x200x70 mm^3.

The design of the MicroMED components was developed through finite element analysis carried-out in the following three conditions:

- Modal analyses: evaluation of the modes of vibration of the instrument assemblies for the determination of the lower natural frequencies;
- Quasi-static analyses: determination of the VM stress under a quasi-static loading of 100g along three principal axes;
- Thermo-elastic analyses: evaluation of the VM stresses due to the expected thermal environment.

A detailed description of the thermo-mechanical design and assigned materials for each of the MicroMED instrument's groups is provided in various published works (Scaccabarozzi, D. et al. 2018, 2019, 2020). Figure 1.12 shows an example of modal analysis. The analysis was performed for each subsystem; however, the figure is relative to the analysis of the pumping system (Group 100).

The modal analysis and quasi-static loading analysis of each group has been performed, individuating the natural frequencies of the modes of vibration, that are in accordance with the design requirements for all subsystems.

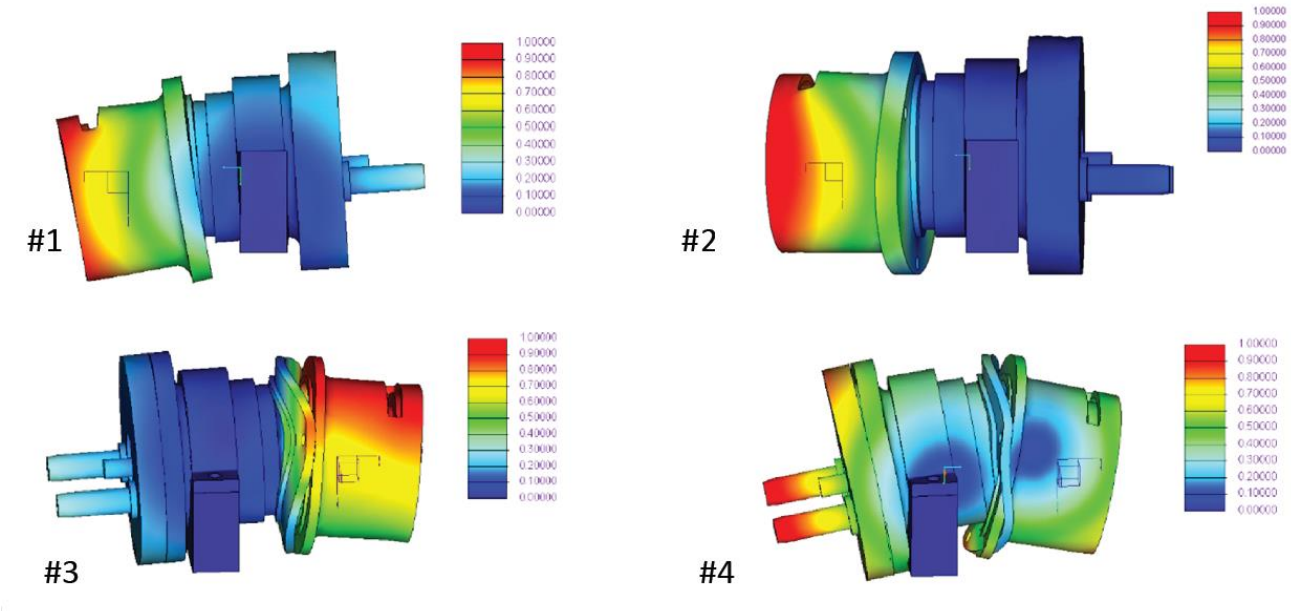

Figure 1.12 Modal analysis of the pumping system.

All structural components are in aluminium alloy Al7075-T6.

1.2.5.5 Electronics design: MicroMED's Central Electronics Board (CEB)

The CEB unit is responsible for commanding MicroMED's payload through different operational modes, and conducting communications with Earth through Impact Sensor computer. Payloads for space operation, and more specifically for planetary exploration, are limited by strict budgets of mass, volume and power. Also the allowed data budget is reduced, due to the limited download-to-Earth capability at mission level. This requires on-board pre-processing and certain level of autonomy in different decision-making processes during real-time operation, in order to maximize the scientific return. Moreover, the complexity of MicroMED, with a Martian dust pumping system, a laser-based high-speed acquisition science, and more than 20 housekeeping sensors, demands for high computing and control capabilities, while assuring the high reliable standards required by space-type missions. All these requirements drove MicroMED CEB's design, which combines a strong research in the advance use of Commercial of the Shelf (COTS) alternatives (Jiménez, J. et al. 2011, Alvarez, M. et al. 2015, Arruego, I. et al. 2015b, Martín-Ortega, A. et al. 2017), a cohesive hardware-software co-design to rise up the overall performance, and a large heritage developing control and processing systems for space applications (Rodriguez, S. et al. 2005, Martin-Ortega, A. et al. 2008, Arruego, I. et al. 2015a, Martín-Ortega, A. et al. 2019).

Figure 1.13 depicts 3D-model of CEB's electronics architecture, displaying the mayor functional modules.

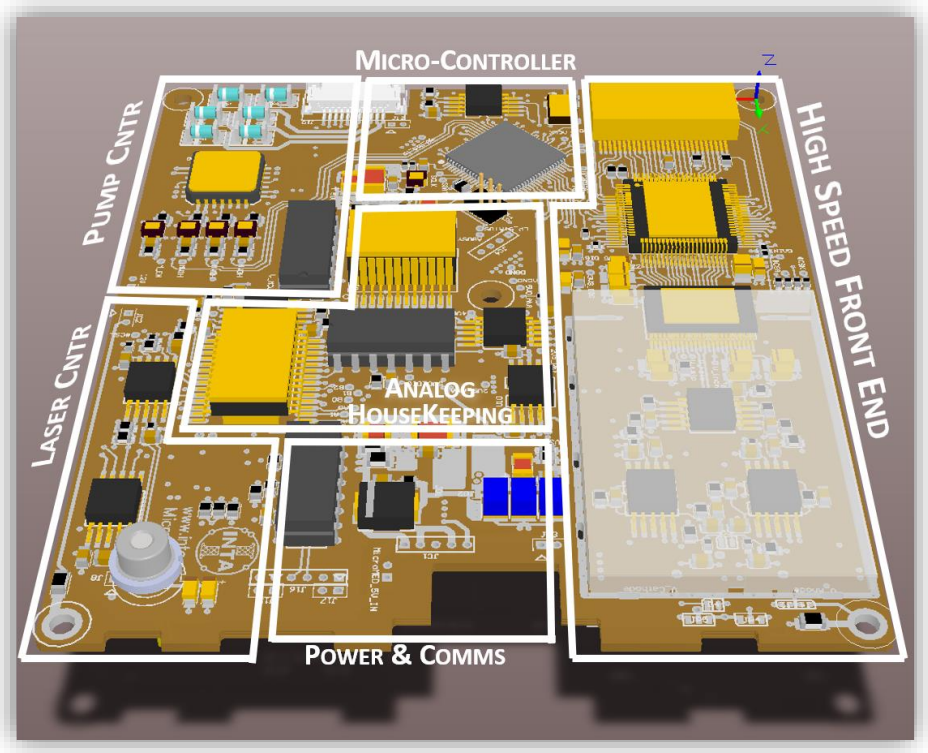

Figure 1.13 MicroMED CEB's Electronics Architecture.

The CEB is able to operate in different modes and to account for a number of different activities:

- Analog Housekeeping: These housekeeping signals are periodically check to maintain the health status of MicroMED and to avoid damaging the different sensors and actuators. Moreover, data gathered by this module as temperatures, differential pressure or laser current is used at Earth, to generate different high-level scientific products;
- Pump and Laser Controllers: Pump control is driven by means of 3 pairs of Pulse Wide Modulated (PWM) signals and controlled in closed loop with Input Capture peripheral (Zhang, W. et al. 2007) for each hall sensor coming from the motor. A dedicated spike filtering circuit with low bandwidth is used for acquiring pump power consumption, which is controlled by application software to avoid overcurrent situations while operating MicroMED. An extra level of intelligence has been developed, to detect and correct stuck situations, either provoked by possible high energy particles over hall sensors, or by obstruction of the rotating blades of the pump. A complex Proportional, Integrative and Derivative (PID) controller has been optimized for dynamically control the pump rotation on different pressure and wind speed scenarios, minimizing the speed error ratio to levels below 1% (less than 30 rpm at 3000 rpm nominal speed);
- Pump Start-Up Control: Laser control is based in a configurable current fail-safe closed loop circuit derived by a Rad-Hard Digital to Analogue Converter (DAC).

Laser is powered by a slow 2-seconds ramp-up, thermally controlled to avoid damaging and over-stressing the laser device. Current controlled closed loop is completely hardware, while an additional software fail safe routine is used to double check possible overcurrent situations;

- High-Speed Front-End Electronics: This module is divided in 3 stages comprising, analogue processing (1), digitalization (2) and digital processing (3). Specific low noise power filtering and routing has been designed to maximize the Signal to Noise Ratio (NSR) of the whole Front-End Electronics (FEE). Two specific copper-gold EMI shields have been manufactured and installed on top and bottom parts of the FEE, in order to minimize radiated noise from CEB and other external sources;
- Power and Communications: Power interface with Impact Sensor Computer is divided in two secondary power supplies of +5.0V and +12.0V. The first one is the main power supply of MicroMED payload, being used for all the components abovementioned except from the pump controller, which is driven by the +12.0V line. This +5.0V main line is internally filtered and divided in several power supplies needed by the analogue acquisition, and the cores of the micro-controller and FPGA;
- On Mars Operations: MicroMED has been designed to execute three different operational modes during its lifetime on Mars surface. Science operation is conducted through the nominal mode, while other two calibration modes are foreseen to allow in-situ calibration during the whole mission. These two calibration modes shall be executed every 30-days to allow calibration formulas to adapt to ageing and radiation effects on electronics and materials. Thus, maintaining performance and prolonging the instrument's utile life;
- Science Mode: This mode is the one to be executed nominally several times per Sol (Martian day) during the mission. MicroMED operates for small executions (from 10 to 360 s) depending of the different parameters uploaded from Earth through the Context Table. Context Table is a set of parameters (that will be described in Section 3.2.2.3), that must be sent for each execution of MicroMED, defining a context to maximize the science return at each operational situation. Nominal operation is divided in 4 mayor steps comprising Configuration and Real-Time update, Health Check and Science Preparation, Science mode and Data Transmission;
- Optical & Pump Calibration Modes: Optical and Pump sub-systems are susceptible to experience small changes during launch, cruise to Mars, landing and surface operation. In order to be able to adapt the calibration formulas to those changes, specific calibration modes have been developed.

1.2.5.6 MicroMED's accommodation on the ExoMars Lander

MicroMED is accommodated as shown in Figure 1.14. An analysis was performed to individuate eventual criticalities in the installment, and no issues are foreseen for the expected temperature environment. All the instrument components can indeed withstand operational temperatures between -40 and +60 °C, and storage between -60°C and +60 °C. The non-operational temperature range of all components can be extended also below -60°C in case the final platform configuration would lead to a wider temperature range. Design and testing have been performed to warrant compliance with the expected temperature environment.

Figure 1.15 shows a picture of MicroMED integrated on the Surface Platform.

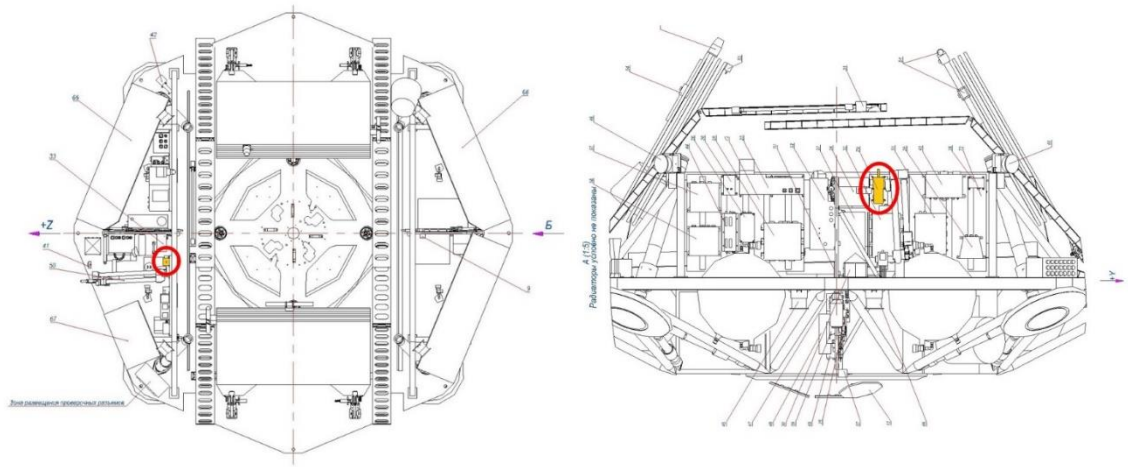

Figure 1.14 MicroMED accommodation on the Kazachok Surface Platform (MicroMED is highlighted in yellow and circled in red, drawings are courtesy of IKI).

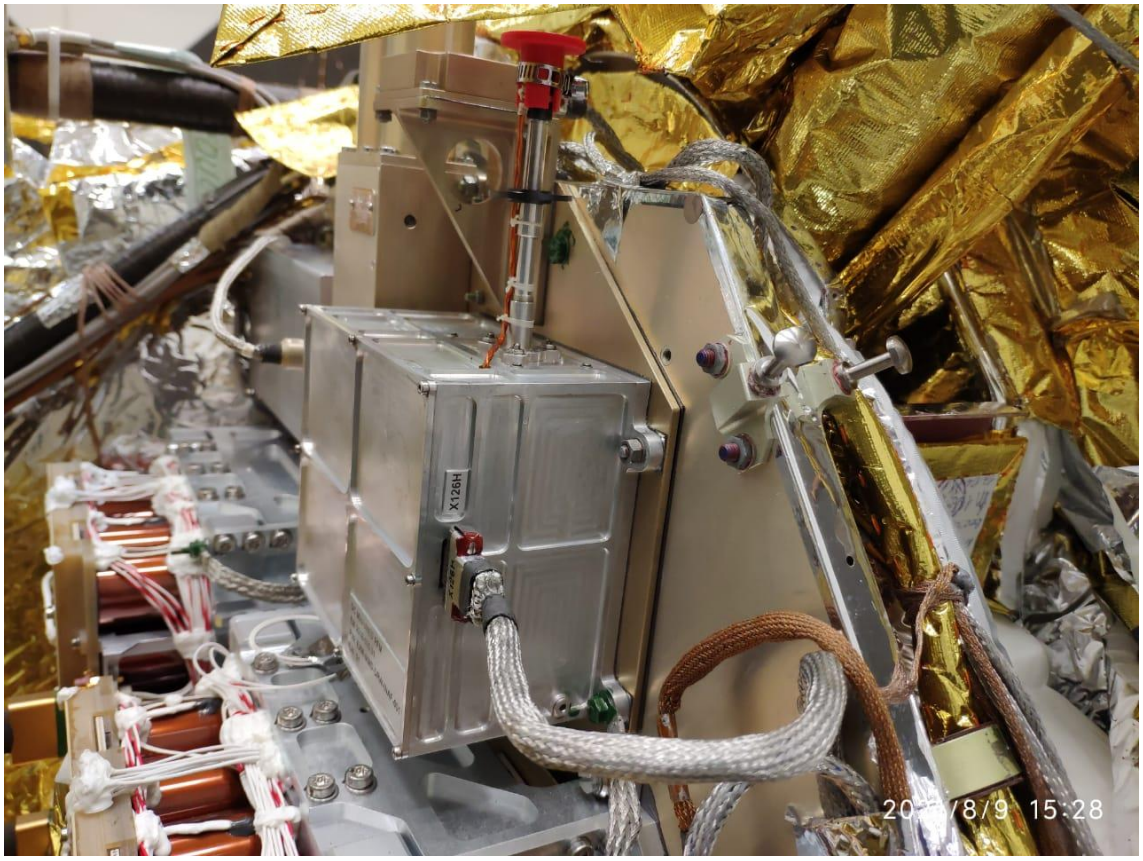

Figure 1.15 MicroMED installed on the Kazachok Surface Platform.

2.The fluid dynamic design of MicroMED

At the beginning of my Ph.D. work at the Astronomical Observatory of Capodimonte, MicroMED's Elegant Breadboard (BB) version (Figure 2.16) had already been designed, integrated and tested at the Capodimonte premises. The process of MicroMED's BB design and development is well described in Ventura, S., 2011 and Cozzolino, F. 2015.

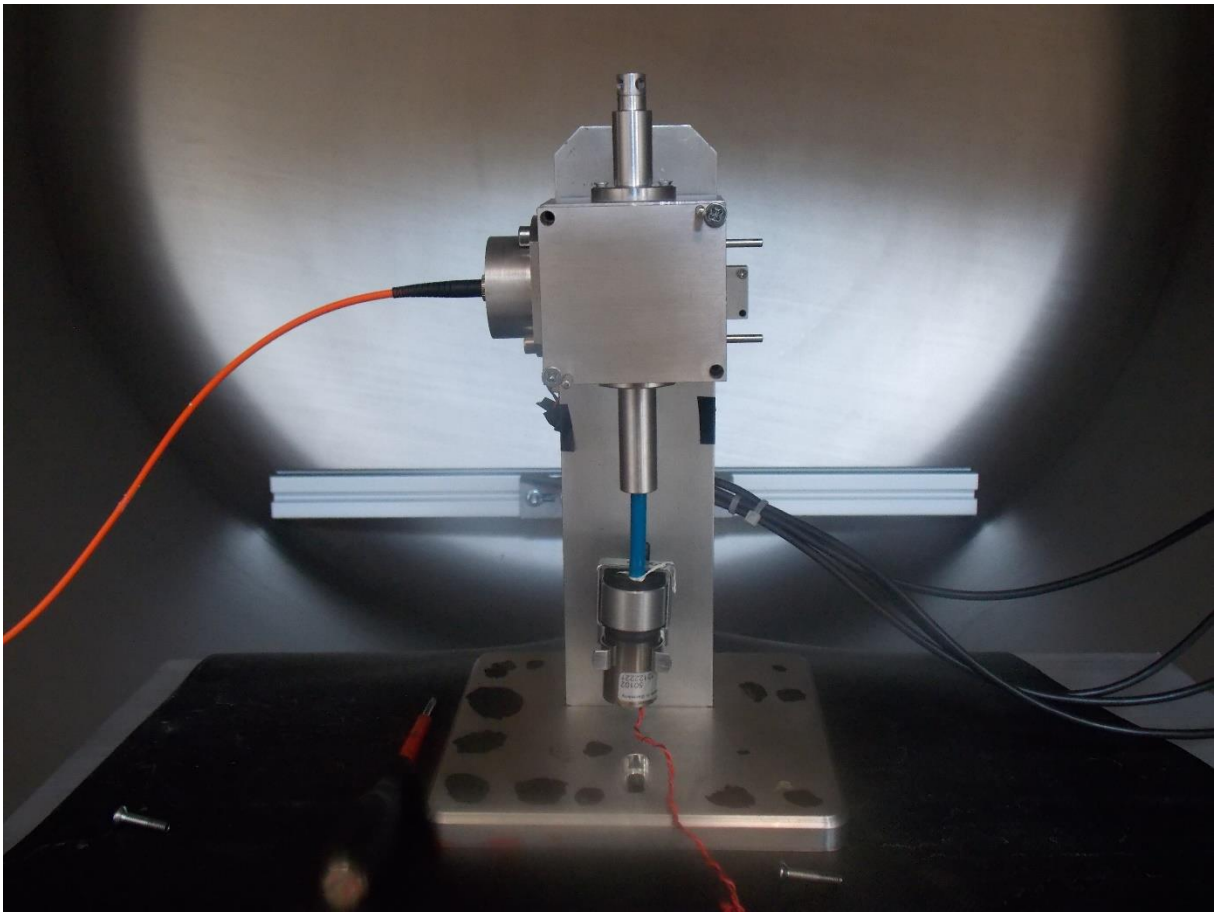

Figure 2.16 MicroMED's Elegant Breadboard.

During the development of the mission, geometry constraints on the lander changed, so that the fluid dynamic design had to be redone. Moreover, during tests, it appeared that MicroMED's BB could have issues in the detection of grains in the upper measurement range (the instrument aims at detecting dust in the 0.4-20 μm diameter range, and grains over 10 μm in diameter could be detected with less accuracy by MicroMED).

The first task of my Ph.D. work was then to perform an in-depth CFD analysis of MicroMED's BB design in various environmental conditions (atmospheric pressure and temperature, instrument temperature, that could differ from the atmospheric one, pump operating conditions among other parameters). The analysis goal was to point out the dependency of MicroMED's ability to gather grains and concentrate them in its sensing spot. This ability depends on environmental parameters as well as on the grain size. The final purpose was to develop an updated design for the Proto Flight Model (PFM) of MicroMED that optimized the fluid dynamics of all dust grains in the instrument's measurement range.

The following sections will describe the methods of such analysis, the results obtained, the adjustments that had to be made and the process that led to the development of MicroMED's PFM fluid dynamic design.

2.1 CFD analysis of MicroMED's Elegant Breadboard

MicroMED's Elegant Breadboard version (Ventura, S., 2011 and Cozzolino, F. 2015) has been designed and integrated at the INAF – OAC premises in Capodimonte in 2014. The instrument layout is the same described in Section 1.2.5, even though geometric parameters could vary. Its feasibility was already verified in previous works (Scaccabarozzi, D. et al., 2018), and its design, as already stated, was conceived to optimize the detection of suspended dust grains in the 0.4-20 μm diameter range.

Computational Fluid Dynamics (CFD) allowed to simulate the different environmental conditions the instrument might be exposed to, deriving information about how the instrument behavior changes while varying operating and environmental conditions. To facilitate the analysis, the "sampling efficiency" parameter was defined as the ratio of dust grains that are correctly detected by MicroMED to the total number of grains that are sampled by MicroMED. In the CFD post processing phase, it is indeed possible to track dust grains that flow through the instrument, determining their trajectory. It can thus be determined whether dust grain trajectories cross the plane containing the laser focus (called "sensing plane") inside the 1 mm^2 laser illuminated spot. Hence, it is possible to determine the percentage of dust grains crossing the spot for each simulated grain size. By means of this parameter, the quality of the fluid dynamic design of MicroMED was evaluated, since the sampling efficiency parameter is a measure of the instrument's ability to concentrate dust grains in the sensible region of the instrument, allowing a correct detection of such grains.

Moreover, since a measurement of concentration is one of the goals of the instrument, information on the volumetric flow rate have to be obtained from CFD runs in order to relate the number of detected particles to the volume of fluid sampled by MicroMED during a run.

The following sections will describe the CFD method used for the analysis, as well as the main results and outcomes of the analysis.

2.1.1 CFD model

The CFD code "Fluent" ® by Ansys, in its version v18.1, was utilized for the analysis. As well known, CFD methods are based on the conservation equations of mass, momentum and energy for the flow which are valid only if the continuum hypothesis is valid. To verify that, the Knudsen number (Kn) for MicroMED was calculated (Kn is the ratio of the gas mean free path to the instrument characteristic length) and it was verified that $Kn < 0.1$ (the regime is considered continuum if $Kn < 0.1$, while in transitional regime if $0.1 < Kn < 50$). For our

applications, the maximum Kn was indeed 0.007, allowing the use of conventional Navier-Stokes based solvers like Ansys Fluent ®.

The analysis showed the regime can be considered laminar, allowing the use of laminar model for simulations. The Reynolds number for the present application is indeed always under 1000 given both the extremely low density of Mars atmosphere (1.6-1.8E-2 kg/m^3, Gomez-Elvira J. et al., 2014) and the small characteristic dimensions of MicroMED (order of magnitude of the millimeter, please refer to Section 1.2.5.2 for the details).

The model will be described is terms of environmental conditions to be considered, and in terms of the settings chosen for the model. A description of the method used to simulate the discrete phase (the dust grains embedded in the fluid) is also provided.

2.1.1.1 Environmental conditions

CFD runs were performed simulating the different environmental conditions the instrument might face during the execution of the operations on Mars surface. The goal was to understand the evolution of key fluid dynamic parameters (sampling efficiency and volumetric flow rate above all) while variating environmental conditions. Thus, in our simulations, atmospheric pressure, atmospheric temperature and instrument temperature values were set in agreement with those predicted for the ExoMars 2022 landing site (Oxia Planum) by the Mars Climate Database (MCD) v5.3 and from instrument thermal analysis. Overall, atmospheric pressure varies seasonally on Mars (Zurek et al., 1992; Gomez-Elvira J. et al., 2014). Three different values (6, 7 and 8 mbar or 600, 700 and 800 Pa) of atmospheric pressure were simulated in accordance with the range of values measured by the Curiosity Rover during its mission (Gomez-Elvira J. et al., 2014). Daily variations were also taken into account during the simulation campaign. The highest variation according to the aforementioned climatic model was 38 Pa and this was the value considered during the analysis. Five different atmospheric temperature values (190, 230, 250, 270 and 280 K) were assumed for the runs. Since MicroMED will be under a thermal cover while on the lander, its temperature will be limited to the 253-313 K range. Therefore, in first place "cold instrument" (T_i=253 K) and "hot instrument" (T_i=313 K) scenarios were simulated, considering the two extreme values of the interval. A further enhancement of the analysis was provided as runs were performed for 6 additional values of instrument temperature in the 258-303 K range (258, 263, 273, 283, 293, 303 K). The presence of the thermal cover will reasonably create temperature gradients between the outside and the inside of MicroMED; this aspect has been taken into account during the analysis. Eight different pump operating conditions were considered, related to an inlet-outlet pressure difference between 250 and 500 Pa (with a 50 Pa spacing). This pressure difference is the way in which the presence of the pump has been simulated during runs. To this purpose, "pressure inlet" and "pressure outlet" boundary conditions have been used for runs, as we will show in the later sections. Simulations used CO_2 as gas since it constitutes 95.3% of Martian atmosphere, but runs with air were also executed in order to complete the validation of the model by means of a direct comparison

with tests also in air (CO_2 tests have also been performed at our premises and have been used for such validation). Table 2.1 synthesizes the input parameters used for the simulations.

Parameter	Min value	Max value	Nr. of values
p_a	600 Pa	800 Pa	3
T_a	190 K	280 K	5
T_i	253 K	313 K	8
Δp	250 Pa	500 Pa	8

Table 2.1 Input parameters for CFD runs on MicroMED's Breadboard. The input parameters considered are: atmospheric pressure (pa), atmospheric temperature (Ta), instrument temperature (Ti), pressure difference induced by the pump between MicroMED's inlet and outlet sections (Δp)

2.1.1.2 CFD runs setup

2.1.1.2.1 Fluid modelling

Previous works about MicroMED already demonstrated how Fluent was a proper solver for the study of such instrument. As already stated, Knudsen number never rises over 0.007, making the continuum hypothesis for the flow valid, therefore allowing a Navier-Stokes based solver like Fluent to be used (Ventura, S., 2011).

Original simulation of the flow considered the gas as incompressible and ideal. However, further analysis showed how, despite Mach number being almost always under 0.3, the gas shows some compressibility effects. This is due to the fact the instrument generated a pressure difference in the order of hundreds of Pascal, that would be a negligible difference in Earth conditions, but it means a strong percentage decrease for Martian conditions, where atmospheric pressure ranges from 600 to 800 Pa.

Figure 2.17 shows the CFD computational domain considered. The instrument is basically described as a box (accurately representing MicroMED's optical head) with inlet and outlet conducts linked to the box itself. The outlet section of the domain is representative of the inlet section of the pump, while the inlet section of the instrument is represented by a detailed description of MicroMED's sampling head geometry. Around the sampling head, a fluid hemisphere 25 mm in diameter has been designed in order to simulate in a more realistic way the floating of low speed dust grains around MicroMED's sampling head. The presence of the pump has been simulated by means of the pressure difference that it is able to generate. Such difference can be related to the pump operating conditions as a curve relating Δp and pump rotating speed has been developed by means of laboratory tests. In order to describe such pressure difference, "pressure inlet" and "pressure outlet" boundary

conditions were imposed in the computational domain. The pressure inlet condition was imposed outside the instrument, on the hemispherical surface surrounding the instrument's head (green surface in Figure 2.17). This choice allowed to improve the model, as it previously imposed a null velocity for particles on the holes' surface, a condition that is not representative of the physical reality. The current condition allows to have small velocities for particles in proximity of the inlet holes, a better description of the real behavior of the dust grains. Grains are still supposed to be injected through this hemisphere with an initial velocity of 0, which again is not realistic. However, some runs were performed to understand whether a different velocity profile for grains entering through the hemisphere influenced the results. Tests showed that the initial velocity of dust grains has little to no effects on the results of the runs in this case. The advantage is that the release of grains happens far from the instrument's holes. Brownian forces were not included in the model because their effect is negligible in the grain diameter range considered, especially for the upper range of the instrument.

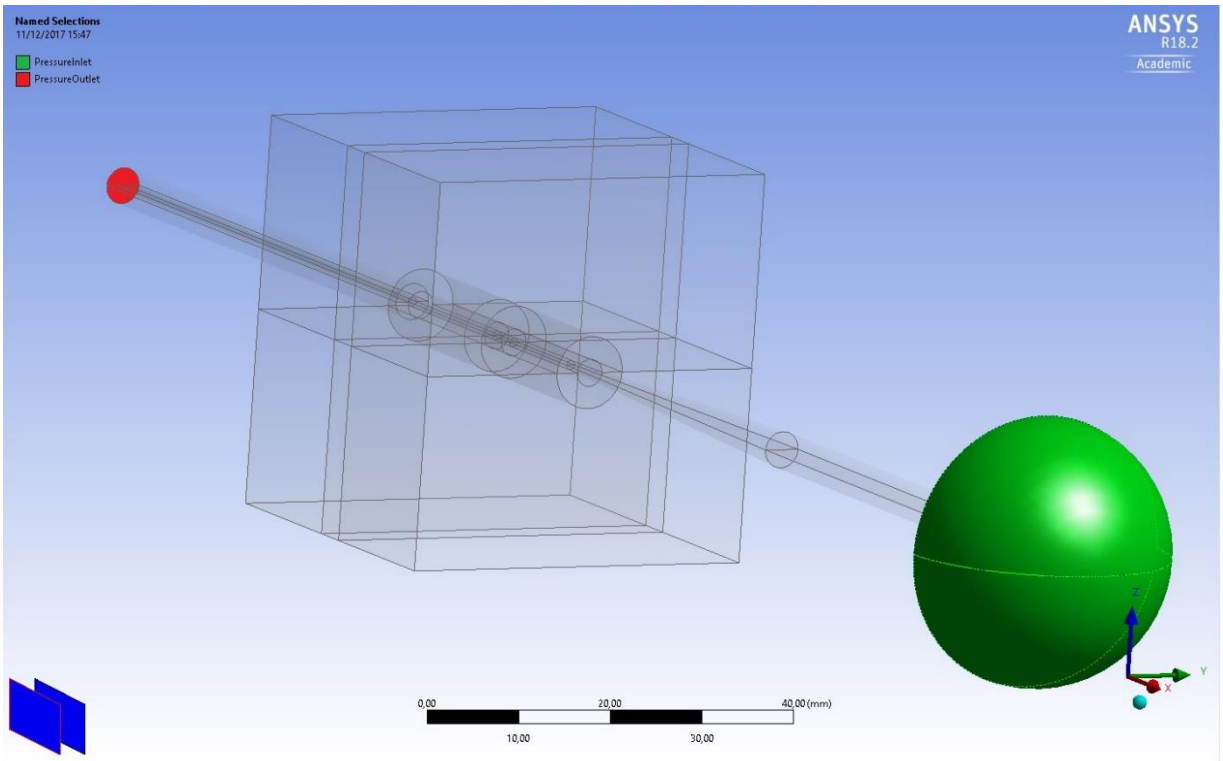

Figure 2.17 CFD computational domain (perspective view). In the figure, Pressure Inlet (green) and Pressure Outlet (red) BC application surfaces can be individuated.

At the walls, a no-slip condition with low pressure correction was set. All of these parameters allow to simulate no wind conditions for the instrument. Evaluations of

MicroMED behavior in presence of wind were also made and will be shown later in this section.

Modelling the fluid also means setting conductivity, viscosity and specific heat conditions at different temperatures, following a law that was set to be piecewise-linear. Runs in air used the default conductivity, viscosity and specific heat conditions for air as set by Fluent.

2.1.1.2.2 Discrete Phase modelling

CFD simulations included a discrete phase model in order to track dust grains in the gas to study their behavior. The only forces acting on the particles were assumed to be the gravitational force and aerodynamic drag force. Gravitational force was calculated using the classic $F_g=mg$ equation, with gravitational acceleration equal to 3.71 m/s in Martian conditions and particle mass being evaluated by particle diameter, assuming the particle as spherical and of constant density (Martian dust density was set at 2730 kg/m^3 – Greeley, R. et al., 1980).

Drag force was calculated using the following equation:

$$F_d = \frac{\mu}{\rho_p d_p^2}\frac{18 C_d Re_p}{24}\left(u - u_p\right) \quad [1]$$

In which μ is the dynamic viscosity of the fluid, ρ_p is the particle density, d_p is the particle diameter, Re_p is the Reynolds number calculated using the particle diameter as reference length and using particle velocity, u is the fluid velocity, u_p is the particle velocity. C_d is the drag coefficient, calculated by mean of the equation:

$$C_d = \frac{\left(\alpha_1 + \frac{\alpha_2}{Re} + \frac{\alpha_3}{Re^2}\right)}{C_c} \quad [2]$$

Such formula includes three parameters (α_1, α_2, α_3) whose values change based on the Reynolds number value, as the code (reported next) will show. It also includes the Cunningham correction factor, evaluated using the equation:

$$C_c = 1 + Kn_p\left(1.257 + 0.4e^{-\frac{1.1}{Kn_p}}\right) \quad [3]$$

Such correction factor (Cunningham, E., 1910) adapts the drag coefficient value by evaluating the Knudsen number with respect to the particle radius and correcting it accordingly. The high Knudsen number obtained for grains in the measurement range of the instrument (Kn_P ranges from 0.67 to 33.45) highlighted the need for such correction factor.

The drag force equation was implemented in Fluent by means of a User Defined Function (UDF) that was written in C language. Figure 2.18 reports a flow chart of the code implemented, able to deduce the correct drag law for each grain in the CFD simulation. Loading the code file plus a library H-file allows to introduce into the solver any user defined law desired.

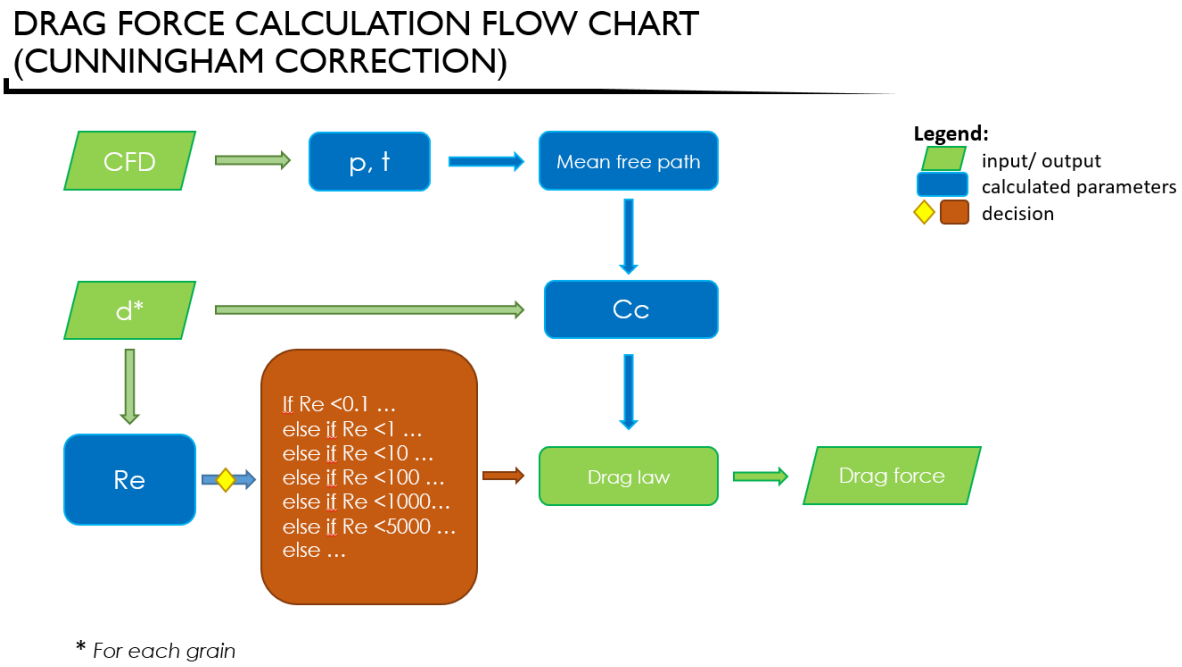

Figure 2.18 Flow chart of the user defined function describing the particles drag law. d is grain diameter, p and T are ambient pressure and temperature coming from the CFD calculation, Cc is the correction factor to be introduced into the grain drag law, Re is Reynolds number.

It has to be underlined that the code accounts for only part of the drag force equation, as viscosity, particle density and diameter, fluid and particle velocities are not included in the code since Fluent ® calculates such values during the simulations.

Regarding for the injections, as many as 16 different particle sizes were considered, always in the 0.4-20 μm diameter range. Dust grains concentration data were estimated for the 16 different sizes in accordance with the expected size distribution curve coming from previous spectroscopic observations (See Figure 1.1 in Section 1.1). Such values were

considered realistic; however, tests were made, showing different values of concentration do not influence the sampling efficiency results. Table 2.2 shows the flow rate values considered for size distributions.

Diameter [μm]	Flow rate [kg/s]	Diameter [μm]	Flow rate [kg/s]
0.4	2.28E-14	5.0	2.07E-12
0.6	1.36E-13	10.0	4.95E-13
0.8	3.79E-13	15.0	1.43E-13
1.0	7.1E-13	16.0	1.3739E-13
1.2	1.13E-12	17.0	1.3547E-13
1.6	1.79E-12	18.0	1.3038E-13
2.0	2.52E-12	19.0	1.1445E-13
4.0	3.31E-12	20.0	8.02E-14

Table 2.2 Flow rate values for the 16 particle sizes simulated.

2.1.1.2.3 Mesh modelling

In order to have consistency in results and efficiency in the execution of the runs, reducing computational time and increasing precision of the results, the quality of the mesh is probably the most important aspect. A three-dimensional CAD design of the instrument was generated by means of the *Ansys Design Modeler* software, then different meshing files were generated and used for runs. A 500,000 elements mesh is able to guarantee good precision keeping computational time in check (1,000,000 element mesh gave comparable results - 1% difference - with longer computational times), and a 494,000 element symmetric mesh was used for carbon dioxide runs. The mesh was indeed relative to half the body, as the XY plane is a symmetry plane for the instrument. For air runs, a different mesh of 503,000 elements was used, considering the whole body.

Figure 2.19 and Figure 2.20 show the two meshes.

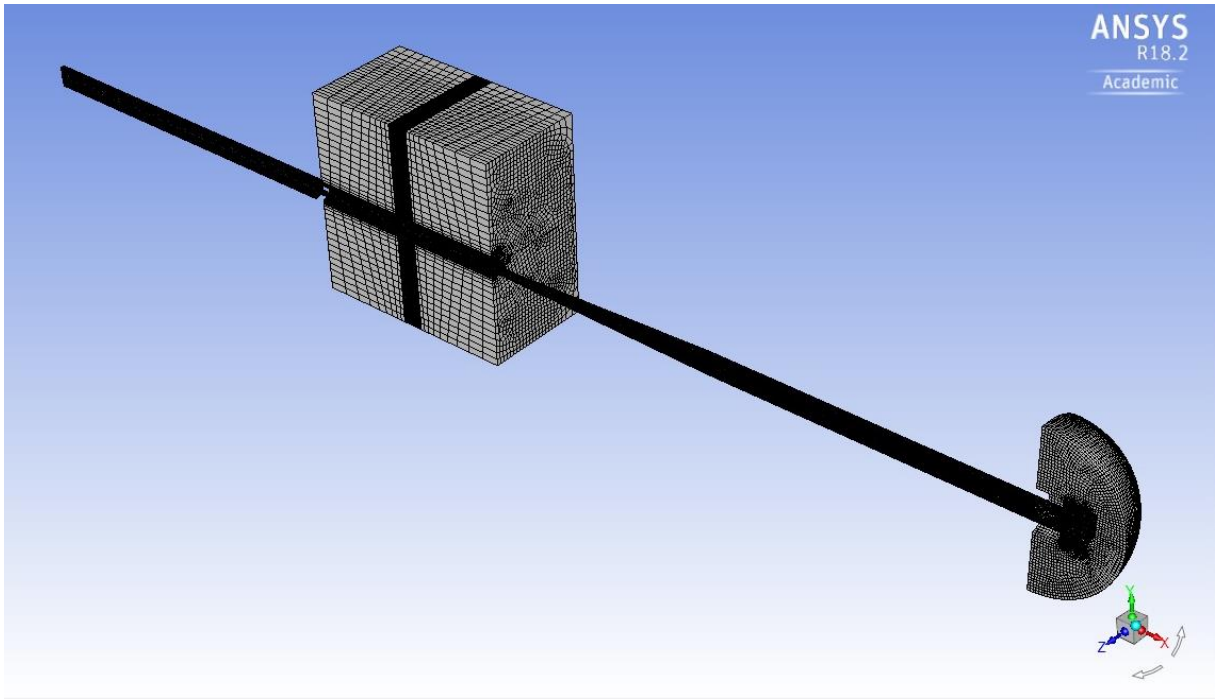

Figure 2.19 View of the symmetric mesh used for carbon dioxide runs.

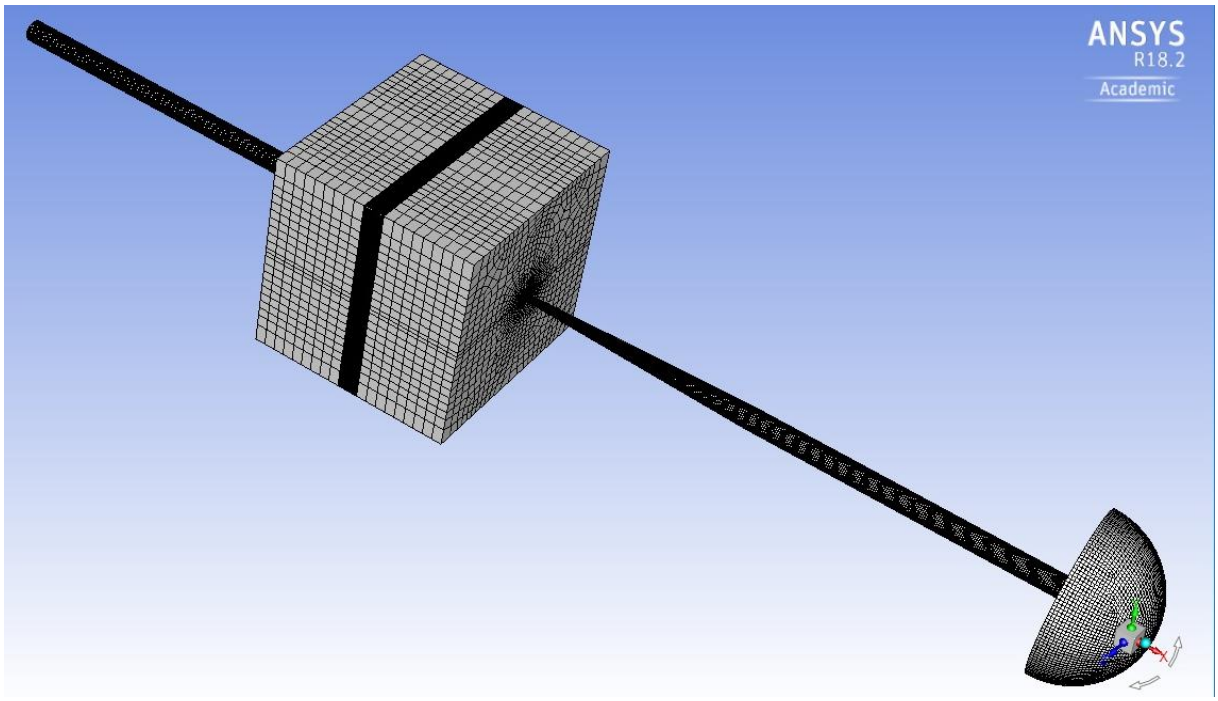

Figure 2.20 View of the symmetric mesh used for carbon dioxide runs.

2.1.1.3 Fluent run setup

The present paragraph shows which settings and models were chosen for Fluent runs. Images will also be used to help the comprehension and allow to easily reproduce the runs. Figure 2.21-Figure 2.27 show the settings used for runs.

2.1.1.3.1 General settings

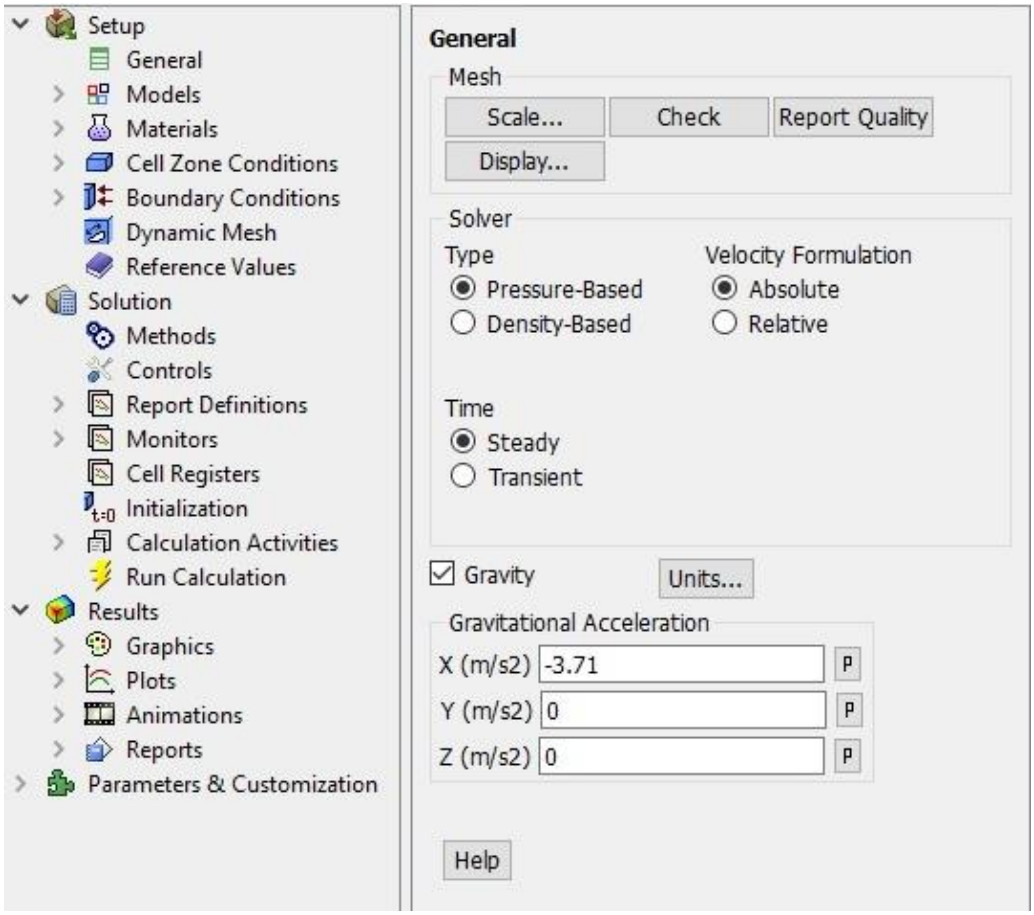

Figure 2.21 General settings

- **Solver:** Pressure-based
- **Time:** Steady
- **Velocity formulation:** Absolute
- **Gravity:** on (Gravity value relative to Mars, equal to -3.71 m/s^2)

2.1.1.3.2 Models

- **Energy equation**: on
- **Viscous:** laminar ("low-pressure, boundary slip")
- **Discrete Phase:** on

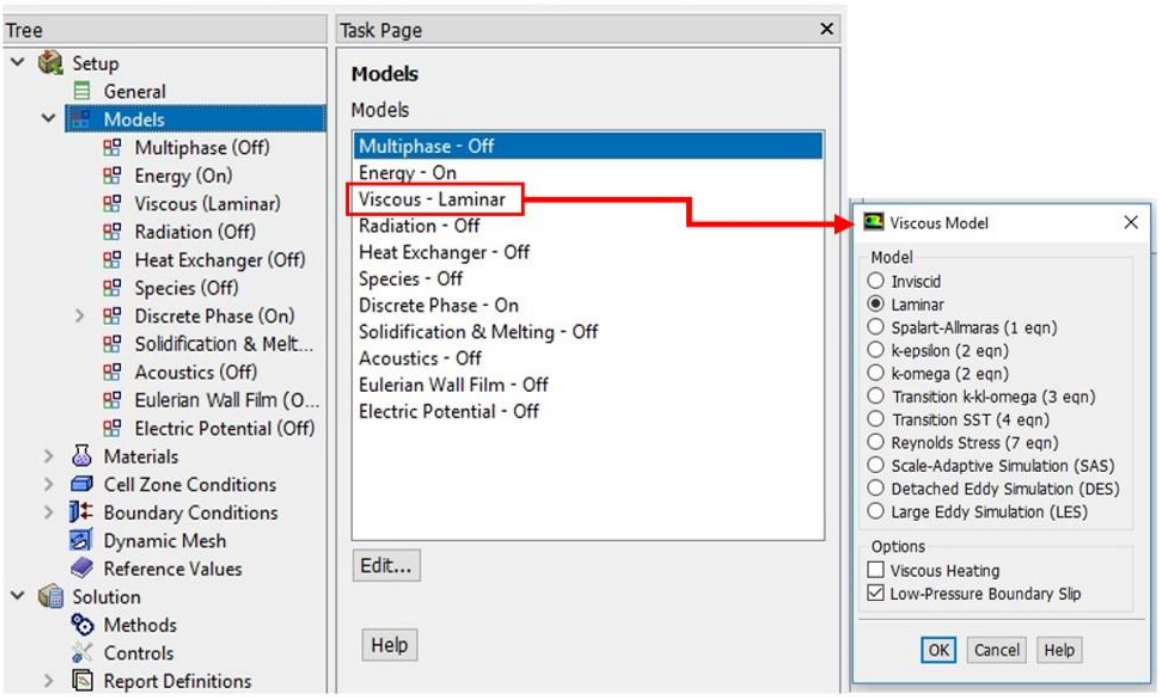

Figure 2.22 Model settings

2.1.1.3.3 Discrete Phase model

As already stated, 16 different injections were created in the Discrete Phase section. Figure 2.23 shows an example of injection setting, allowing to see how parameters were set. These are the settings needed for the injections:

- **Injection type:** surface
- **Release from surface:** pressure inlet
- **Particle type:** Inert
- **Material:** martian dust (already present in the files)
- **Diameter:** depending on the injection
- **Temperature:** 150 (a default value of 150 K was set, according to previous works as this value does not influence the results)
- **Velocity magnitude:** 0 (this value is not realistic; however, this value does not influence the results for non-wind runs)
- **Total flow rate:** depending on the injection and according to Table 2.2

Inject using face normal direction: on

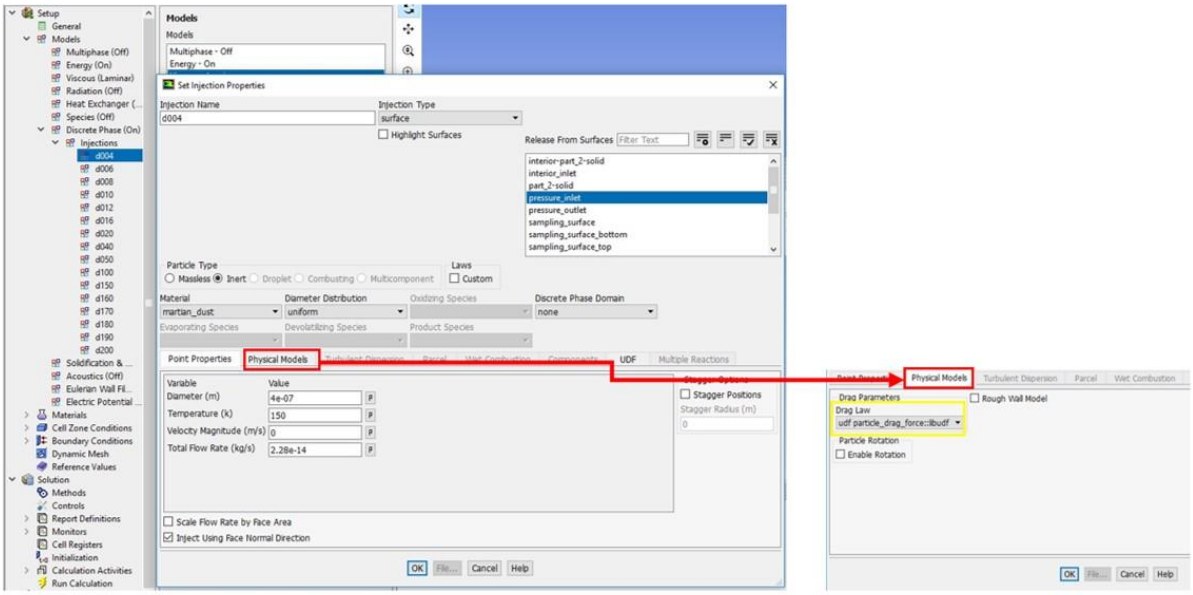

Figure 2.23 Discrete phase settings

Then, in the *Physical Model* tab, the user defined drag law reported earlier in this section has to be loaded (yellow box in Figure 2.23).

Dust grains in MicroMED's measurement range have a strongly variable Stokes number, meaning that there could be a different behavior between large (15-20 μm) and

small (0.4-1 μm) dust grains, with small dust grains more likely to follow the fluid streamlines along their entire path through the instrument. Stk has been calculated by means of the formula:

$$Stk = \frac{t_0 U_0}{d_c} \quad [4]$$

Where t_0 is the relaxation time, U_0 is the characteristic velocity of the fluid far from the obstacle the grain is approaching, d_c is the characteristic diameter of the obstacle approached by the dust grain. The relaxation time is related to the grain diameter, density and material by means of the formula:

$$t_0 = \frac{\rho_d d_d^2}{18\mu_g} \quad [5]$$

Where ρ_d is the particle density, d_d is their diameter while μ_g is the gas kinematic viscosity.

2.1.1.3.4 Materials settings

Materials have to be set for fluid, solid and inert particles. Solid material is aluminium, that is part of the Fluent ® material database. Default values were chosen.

As for fluid and inert particles, custom values were set. Figure 2.24 shows settings for these two materials. Carbon dioxide was set as the fluid material, adding the following specifics:

- **Gas density:** ideal gas
- **Gas specific heat:** piecewise-linear (according to data in Table 2.3)
- **Gas thermal conductivity:** piecewise-linear (according to data in Table 2.3)
- **Gas viscosity:** Sutherland

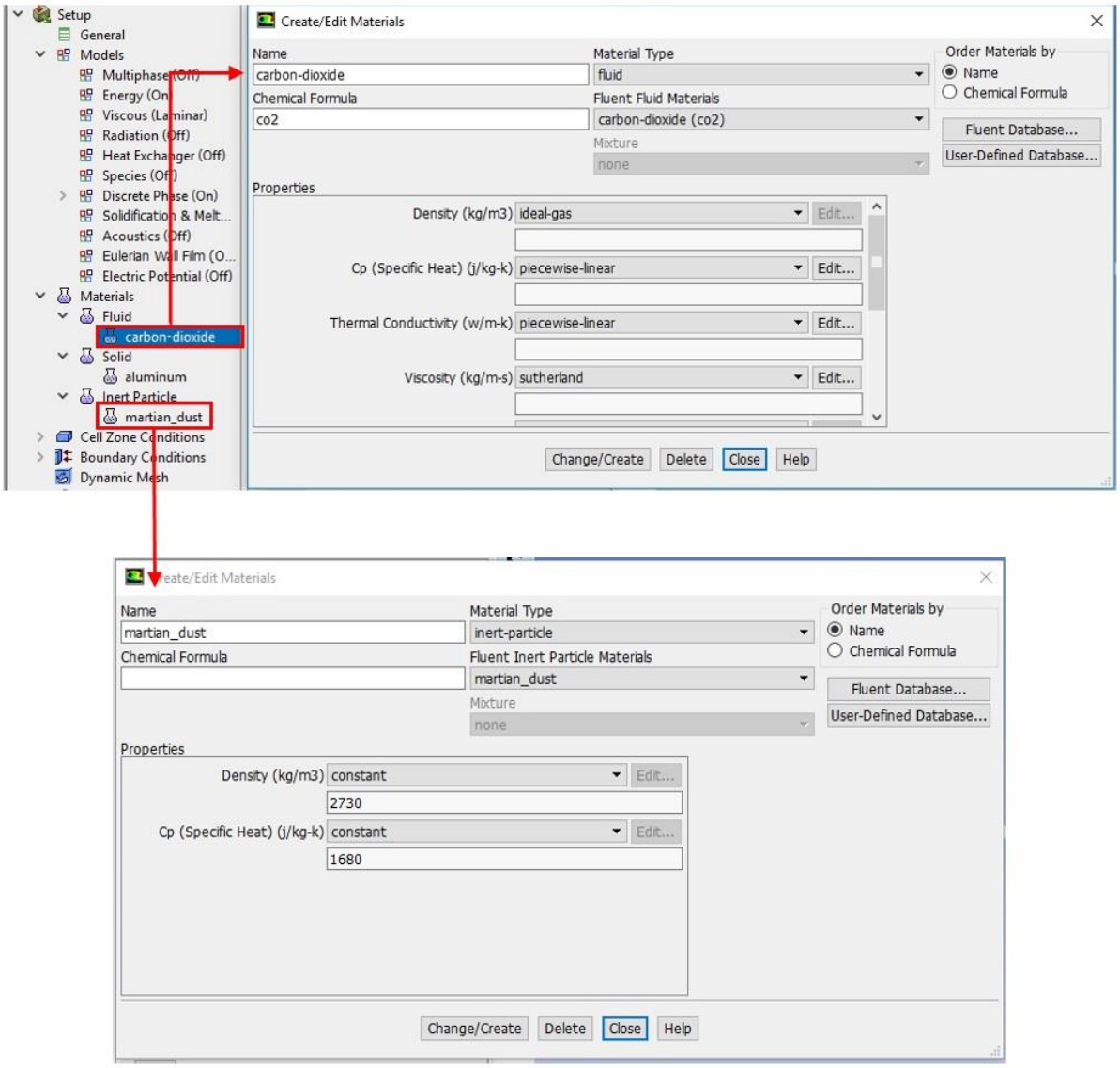

Figure 2.24 Materials settings.

For the other parameters, default values were chosen. Specific heat and thermal conductivity values were set following values shown in Table 2.3. Such values refer to a 600 Pa atmospheric pressure and have been calculated in previous works, written by the team at INAF – OAC (Internal reports). However, the ideal gas hypothesis allows to use such values for similar pressures (runs were always run in the 600-800 Pa pressure range).

Temperature [K]	**C_p [J/Kg·K]**	**μ [Pa·s]**	**λ [W/m K]**
217	754.45	1.09E-05	0.0106
227	765.73	1.14E-05	0.0113

237	777.04	1.19E-05	0.0120
247	788.31	1.24E-05	0.0127
257	799.50	1.29E-05	0.0134
267	810.57	1.34E-05	0.0142
277	821.48	1.39E-05	0.0149
287	832.22	1.44E-05	0.0157
297	842.76	1.49E-05	0.0165
307	853.10	1.54E-05	0.0173

Table 2.3 Specific heat (C_p), viscosity (μ) and thermal conductivity (λ) data for carbon dioxide.

Dust grains material was called "Martian dust"; constant density of 2730 kg/m^3 and constant specific heat of 1680 J/Kg·K were set.

2.1.1.3.5 Boundary conditions setting

Once the mesh is loaded, named selections come into play, as *pressure-inlet*, *pressure-outlet*, *wall-part-2-solid*, *interior-part-2-solid*, *wall-cold* and *symmetry* zones appear (they were defined with *Ansys DesignModeler*), whose names already tell which kind of boundary condition is needed. Figure 2.25 shows settings chosen for such boundary conditions.

The *wall-cold* region was created since it is a region of the instrument walls that differs in temperature with respect to the rest of MicroMED since it is not under the thermal cover. It refers to the part of the inlet and of the sampling head that comes out of the thermal cover. The presence of such region in the boundary conditions allowed more flexibility in the simulation of different temperature cases.

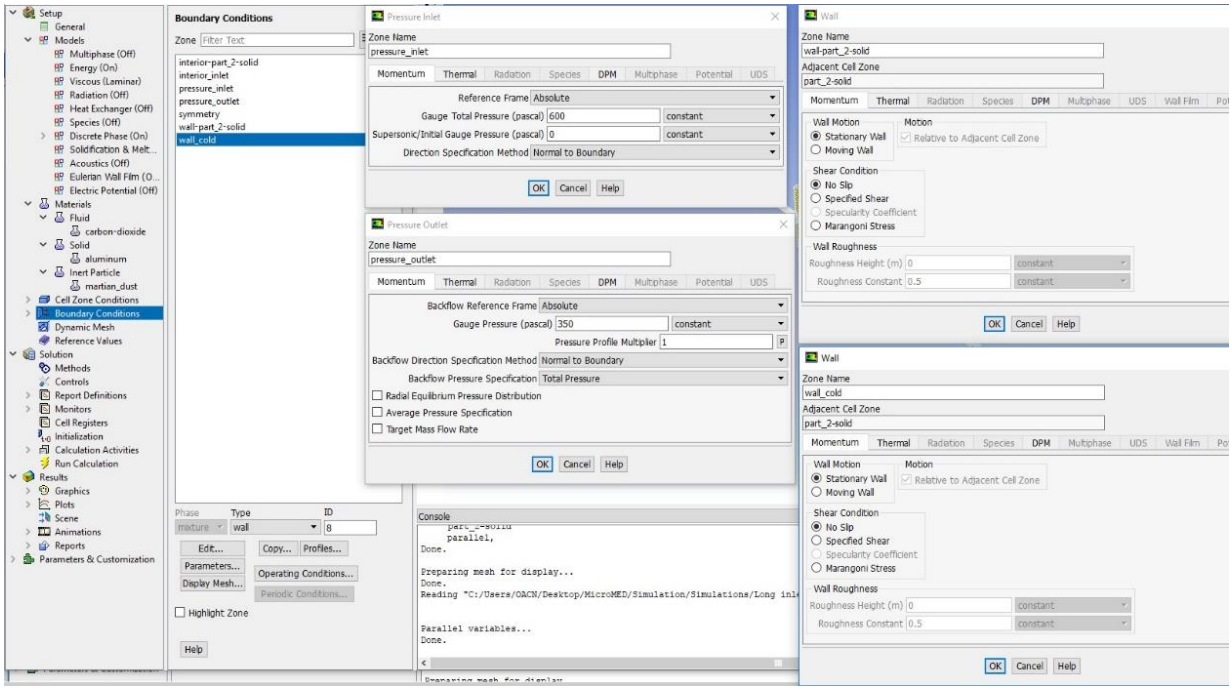

Figure 2.25 Boundary conditions settings.

As for the boundary condition settings, the following conditions were imposed, with data changing from case to case:

Pressure inlet:

- **Momentum:** Atmospheric pressure
- **Thermal:** Atmospheric temperature
- **DPM:** escape

Pressure outlet:

- **Momentum:** pressure at the outlet (set according to the case)
- **Thermal:** Instrument temperature
- **DPM:** escape

Wall-cold:

- **Wall Motion:** Stationary wall
- **Shear Condition:** No slip
- **Thermal:** Atmospheric temperature
- **DPM:** trap

Wall-part-2-solid:

- **Wall Motion:** Stationary wall
- **Shear Condition:** No slip

- **Thermal:** Instrument temperature
- **DPM:** trap

The "trap" condition on the walls was chosen in accordance with the aforementioned assumption that dust grains remain stuck on the walls once they hit them. As said before, a more detailed study of this assumption is currently under development, trying to shed light on an aspect that is not easy to simulate such as the eventual reflection of grains of walls. The difficulties come not only from the reflection law, which is not easy to determine also because of the unpredictable characteristics of the inner wall surface, but also because electrostatic and effects might come into play. CFD runs currently do not consider electrostatic forces, which may cause a momentary adhesion of grains on the walls, before a release due to the particle electrical discharge (MicroMED walls are connected to the electrical ground).

2.1.1.3.6 Solution Methods

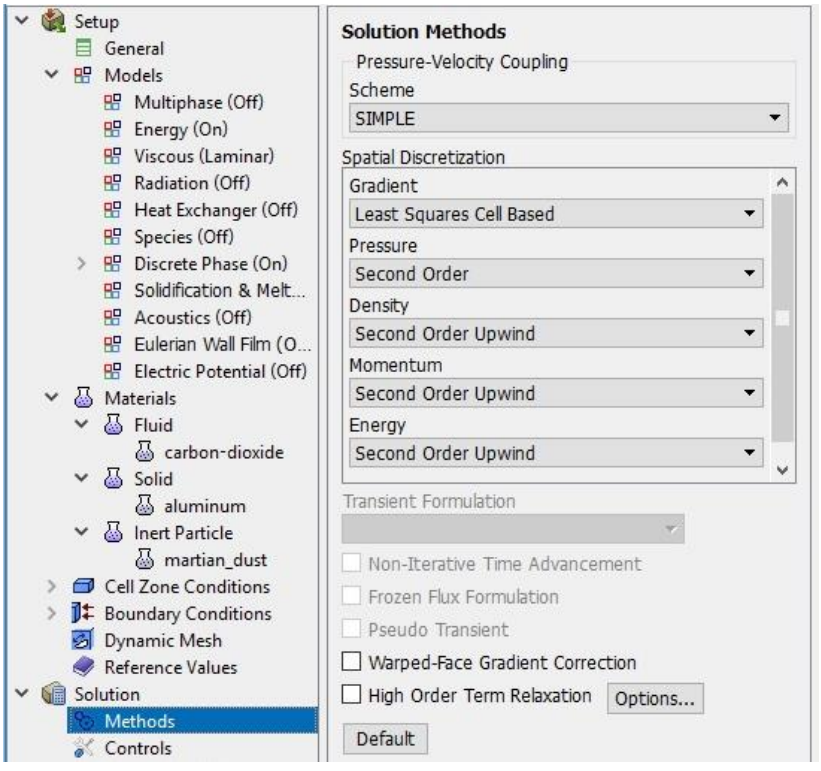

Figure 2.26 Solution methods.

- **Scheme:** SIMPLE
- **Pressure:** Second Order
- **Density, Momentum and Energy:** Second Order Upwind

2.1.1.3.7 Run initialization

Since runs consider movement of the fluid through conducts, atmospheric conditions were set as the initialization values for the runs.

2.1.1.3.8 Run execution

Runs always converge to the default residual level of 1E-05. Convergence is obtained on a number of iterations that is variable from 300 to 2200, depending on the values given to parameters.

2.1.1.3.9 Sampling efficiency evaluation

Dust grains flowing through MicroMED can be detected by the optical system of the instrument only if they pass through the 1 mm^2 diameter spot where the laser light is focused. CFD Simulations allow to track dust grains while they move inside MicroMED to understand whether their behavior matches the desired conditions for correct measuring. Fluent allows to export the particle tracking data into a DPM file by mean of the *Sample* option (the option can be found in the *Reports* → *Discrete Phase* section, see Figure 2.27). For each particle crossing a chosen plane, Fluent can provide position (three coordinates x, y and z), velocity (u, v and w components), diameter, mass flow, mass, frequency and time. As Figure 2.27 shows, surfaces of interest are *interior inlet* representing the front area of the four holes at the inlet of the instrument and *sampling surface*, representing the plane containing the 1 mm diameter sampling spot. Tracking is obviously needed for all injections sizes.

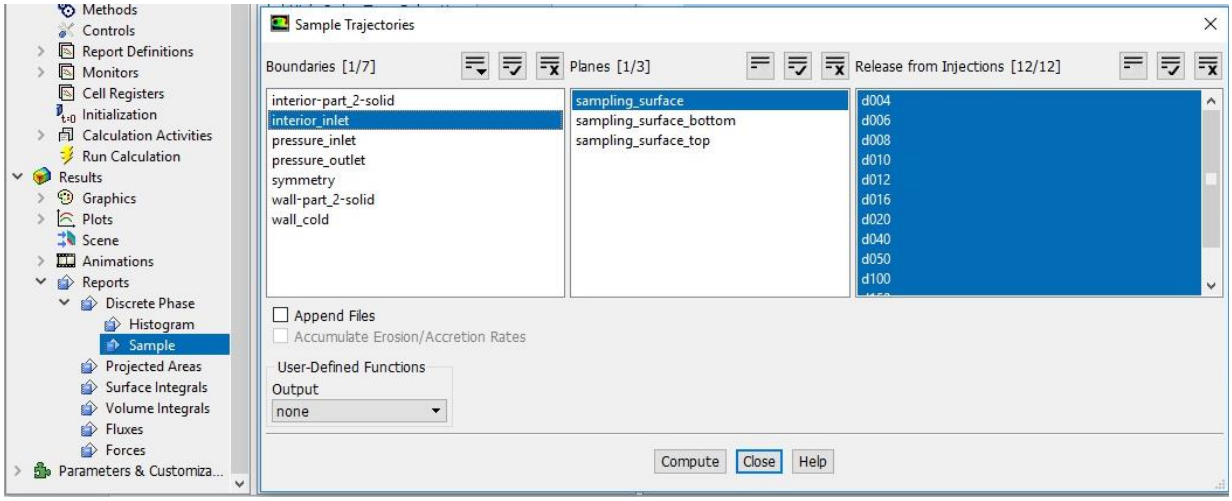

Figure 2.27 Discrete phase tracking option.

In order to evaluate the sampling efficiency, only position, velocity and diameter are needed. Given the x, y and z component of position, the actual position of every particle in the selected plane (the x-coordinate is fixed in the plane) can be derived by:

$$Position \ \ in \ \ plane = \sqrt{y^2 + z^2} \qquad [6]$$

While particle velocity can be calculated using:

$$Velocity = \sqrt{u^2 + v^2 + w^2} \qquad [7]$$

The sampling volume is centered around the sampling plane origin (y = 0, z = 0 are the coordinates for the center), meaning the position equation also identifies the distance of the particle crossing point from the center of the sampling spot. If such distance is bigger than half a millimetre (5E-4 m or 0.0005 m) the particle can't be detected. If this distance has a value under 0.0005 m, it is detected by the instrument (assuming ideal functioning of the optical detector). This allows to create comparative files, confronting the number of particles of a specific diameter crossing the inlet to the number of particles of the same size that are efficiently detected by the optics.

Excel files containing the DPM files information, as well as the calculation of the sampling efficiencies for every particle diameter, were generated. Figure 2.28 shows how such Excel files were set up. The red box highlights the table that allows to calculate the

sampling efficiency, as particles of every dimension considered are counted at the inlet and in the sampling surface and the ratio is calculated.

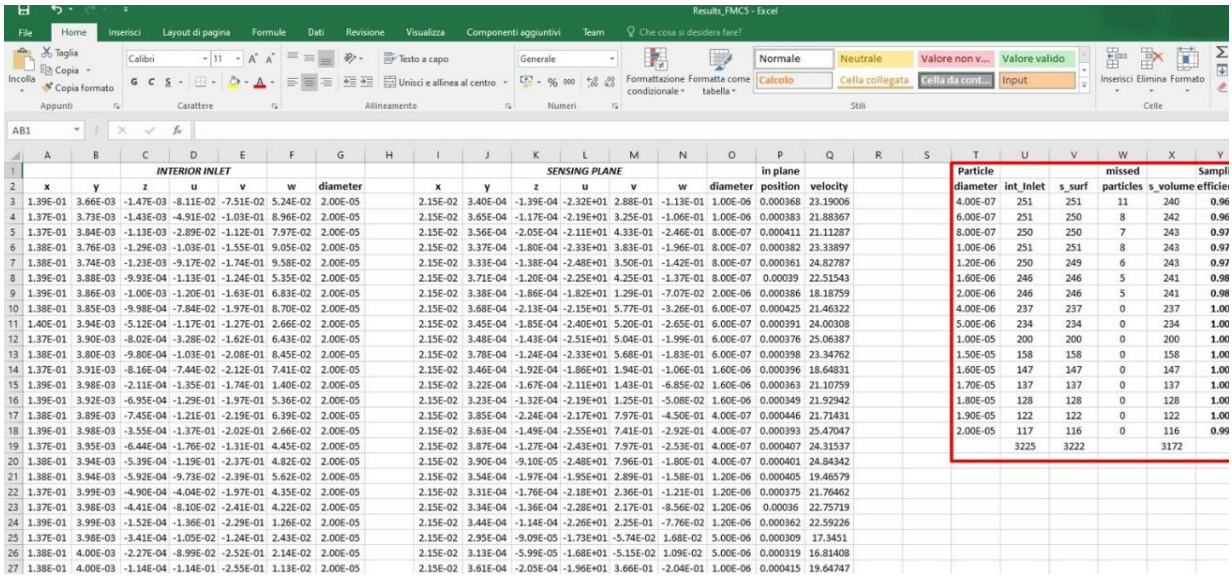

	A	B	C	D	E	F	G	H	I	J	K	L	M	N	O	P	Q	R	S	T	U	V	W	X	Y
1	INTERIOR INLET								SENSING PLANE							in plane				Particle			missed		Sampl
2	x	y	z	u	v	w	diameter		x	y	z	u	v	w	diameter	position	velocity			diameter	int_Inlet	s_surf	particles	s_volume	efficie
3	1.39E-01	3.66E-03	-1.47E-03	-8.11E-02	-7.51E-02	5.24E-02	2.00E-05		2.15E-02	3.40E-04	-1.39E-04	-2.32E+01	2.88E-01	-1.13E-01	1.00E-06	0.000368	23.19006			4.00E-07	251	251	11	240	0.96
4	1.37E-01	3.73E-03	-1.43E-03	-4.91E-02	-1.03E-01	8.96E-02	2.00E-05		2.15E-02	3.65E-04	-1.17E-04	-2.19E+01	3.25E-01	-1.06E-01	1.00E-06	0.000383	21.88367			6.00E-07	251	250	8	242	0.96
5	1.37E-01	3.84E-03	-1.13E-03	-2.89E-02	-1.12E-01	7.97E-02	2.00E-05		2.15E-02	3.56E-04	-2.05E-04	-2.11E+01	4.33E-01	-2.46E-01	8.00E-07	0.000411	21.11287			8.00E-07	250	250	7	243	0.97
6	1.38E-01	3.76E-03	-1.29E-03	-1.03E-01	-1.55E-01	9.05E-02	2.00E-05		2.15E-02	3.37E-04	-1.80E-04	-2.33E+01	3.83E-01	-1.96E-01	8.00E-07	0.000382	23.33897			1.00E-06	251	251	8	243	0.97
7	1.38E-01	3.74E-03	-1.23E-03	-9.17E-02	-1.74E-01	9.58E-02	2.00E-05		2.15E-02	3.33E-04	-1.38E-04	-2.48E+01	3.50E-01	-1.42E-01	8.00E-07	0.000361	24.82787			1.20E-06	250	249	6	243	0.97
8	1.39E-01	3.88E-03	-9.93E-04	-1.13E-01	-1.24E-01	5.35E-02	2.00E-05		2.15E-02	3.71E-04	-1.20E-04	-2.25E+01	4.25E-01	-1.37E-01	8.00E-07	0.00039	22.51543			1.60E-06	246	246	5	241	0.98
9	1.39E-01	3.86E-03	-1.00E-03	-1.20E-01	-1.63E-01	6.83E-02	2.00E-05		2.15E-02	3.38E-04	-1.86E-04	-1.82E+01	1.29E-01	-7.07E-02	2.00E-06	0.000386	18.18759			2.00E-06	246	246	5	241	0.98
10	1.38E-01	3.85E-03	-9.98E-04	-7.84E-02	-1.97E-01	8.70E-02	2.00E-05		2.15E-02	3.68E-04	-2.13E-04	-2.15E+01	5.77E-01	-3.26E-01	6.00E-07	0.000425	21.46322			4.00E-06	237	237	0	237	1.00
11	1.40E-01	3.94E-03	-5.12E-04	-1.17E-01	-1.27E-01	2.66E-02	2.00E-05		2.15E-02	3.45E-04	-1.85E-04	-2.40E+01	5.20E-01	-2.65E-01	6.00E-07	0.000391	24.00308			5.00E-06	234	234	0	234	1.00
12	1.37E-01	3.90E-03	-8.02E-04	-3.28E-02	-1.62E-01	6.43E-02	2.00E-05		2.15E-02	3.48E-04	-1.43E-04	-2.51E+01	5.04E-01	-1.99E-01	6.00E-07	0.000376	25.06387			1.00E-05	200	200	0	200	1.00
13	1.38E-01	3.80E-03	-9.80E-04	-1.03E-01	-2.08E-01	8.45E-02	2.00E-05		2.15E-02	3.78E-04	-1.24E-04	-2.33E+01	5.68E-01	-1.83E-01	6.00E-07	0.000398	23.34762			1.50E-05	158	158	0	158	1.00
14	1.37E-01	3.91E-03	-8.16E-04	-7.44E-02	-2.12E-01	7.41E-02	2.00E-05		2.15E-02	3.46E-04	-1.92E-04	-1.86E+01	1.94E-01	-1.06E-01	1.60E-06	0.000396	18.64831			1.60E-05	147	147	0	147	1.00
15	1.39E-01	3.98E-03	-2.11E-04	-1.35E-01	-1.74E-01	1.40E-02	2.00E-05		2.15E-02	3.22E-04	-1.67E-04	-2.11E+01	1.43E-01	-6.85E-02	1.60E-06	0.000363	21.10759			1.70E-05	137	137	0	137	1.00
16	1.39E-01	3.92E-03	-6.95E-04	-1.29E-01	-1.97E-01	5.36E-02	2.00E-05		2.15E-02	3.23E-04	-1.32E-04	-2.19E+01	1.25E-01	-5.08E-02	1.60E-06	0.000349	21.92942			1.80E-05	128	128	0	128	1.00
17	1.38E-01	3.89E-03	-7.45E-04	-1.21E-01	-2.19E-01	6.39E-02	2.00E-05		2.15E-02	3.85E-04	-2.24E-04	-2.17E+01	7.97E-01	-4.50E-01	4.00E-07	0.000446	21.71431			1.90E-05	122	122	0	122	1.00
18	1.39E-01	3.98E-03	-3.55E-04	-1.37E-01	-2.02E-01	2.66E-02	2.00E-05		2.15E-02	3.63E-04	-1.49E-04	-2.55E+01	7.41E-01	-2.92E-01	4.00E-07	0.000393	25.47047			2.00E-05	117	116	0	116	0.99
19	1.37E-01	3.95E-03	-6.44E-04	-1.76E-02	-1.31E-01	4.45E-02	2.00E-05		2.15E-02	3.87E-04	-1.27E-04	-2.43E+01	7.97E-01	-2.53E-01	4.00E-07	0.000407	24.31537				3225	3222		3172	
20	1.38E-01	3.94E-03	-5.39E-04	-1.19E-01	-2.37E-01	4.82E-02	2.00E-05		2.15E-02	3.90E-04	-9.10E-05	-2.48E+01	7.96E-01	-1.80E-01	4.00E-07	0.000401	24.84342								
21	1.38E-01	3.94E-03	-5.92E-04	-9.73E-02	-2.39E-01	5.62E-02	2.00E-05		2.15E-02	3.54E-04	-1.97E-04	-1.95E+01	2.89E-01	-1.58E-01	1.20E-06	0.000405	19.46579								
22	1.37E-01	3.99E-03	-4.90E-04	-4.04E-02	-1.97E-01	4.35E-02	2.00E-05		2.15E-02	3.31E-04	-1.76E-04	-2.18E+01	2.36E-01	-1.21E-01	1.20E-06	0.000375	21.76462								
23	1.37E-01	3.98E-03	-4.41E-04	-8.10E-02	-2.41E-01	4.22E-02	2.00E-05		2.15E-02	3.34E-04	-1.36E-04	-2.28E+01	2.17E-01	-8.56E-02	1.20E-06	0.00036	22.75719								
24	1.39E-01	3.99E-03	-1.52E-04	-1.36E-01	-2.29E-01	1.26E-02	2.00E-05		2.15E-02	3.44E-04	-1.14E-04	-2.26E+01	2.25E-01	-7.76E-02	1.20E-06	0.000362	22.59226								
25	1.37E-01	3.98E-03	-3.41E-04	-1.05E-02	-1.24E-01	2.43E-02	2.00E-05		2.15E-02	2.95E-04	-9.09E-05	-1.73E+01	-5.74E-02	1.68E-02	5.00E-06	0.000309	17.3451								
26	1.38E-01	4.00E-03	-2.27E-04	-8.99E-02	-2.52E-01	2.14E-02	2.00E-05		2.15E-02	3.13E-04	-5.99E-05	-1.68E+01	-5.15E-02	1.09E-02	5.00E-06	0.000319	16.81408								
27	1.38E-01	4.00E-03	-1.14E-04	-1.14E-01	-2.55E-01	1.13E-02	2.00E-05		2.15E-02	3.61E-04	-2.05E-04	-1.96E+01	3.66E-01	-2.04E-01	1.00E-06	0.000415	19.64747								

Figure 2.28 Example of an Excel file containing particle tracking.

2.1.2 Validation of the model

In order to evaluate the quality of the model, CFD simulations were compared with tests performed on MicroMED's BB in the Martian Simulation Chamber located at the INAF - Astronomical Observatory of Capodimonte in Naples, Italy (Cozzolino, F. et al., 2020). The chamber allows to reproduce Martian conditions in terms of ambient pressure, instrument temperature and atmospheric composition. Instrument temperature can be accurately varied within MicroMED's operative temperature range thanks to a custom system called *Autonomous Thermal Simulator* (Russo, G. et al., 2020).

As a verification of the model, the average values of dust grain speed in the sensing spot (a key fluid dynamic parameter), as measured by the MicroMED instrument, were used for comparison with the simulated dust grain speed. A simulation set using air as gas was performed at ambient conditions, given that some preliminary tests were performed in laboratory conditions. Tests used different monodispersed grains samples of SiO_2 (with three different diameters of 1, 4 and 10 μm) and the comparison shows there is a good match between CFD and experimental results (See Table 2.4). Overall, 2 runs with monodispersed 2 μm grains, 5 with monodispersed 4 μm grains and 4 with 10 μm monodispersed ones have been considered in the described validation. Please consider that each run has a maximum number of grains acquired of 750, providing a significant statistical sample to the evaluation. Values obtained from CFD are well within 3 σ from test results for the 10 μm grains (for which there is a smaller sample though, so a less reliable statistic) while, for 1 and 4 μm ones, there are 2% and 8% differences on the average value, respectively. The model has then been

considered affordable. Once the model has been validated, the sensitivity analysis described in the upcoming sections has been performed only relying on the CFD simulations and, from such results, assumptions have been derived that have been used for the interpretation of MicroMED's results. However, tests performed on the instrument have then confirmed the affordability of such results. Figure 2.29 and Figure 2.31 report velocity histograms for the three aforementioned dust grains size derived from tests.

Size [μm]	CFD	Tests
1	21.0±0.1	21.5±0.1
4	20.4±0.1	22.1±0.2
10	16.0±0.3	16.5±0.7

Table 2.4 Comparison between average values of dust grains speed [m/s] in the sensing region obtained by CFD simulations and by laboratory tests. During tests, grain speed can be directly derived from the length of the signals (the time needed by the grain to cross the entire spot) and the length of the spot itself, by means of the relation: grain speed = length of the spot / time needed to cross the spot.

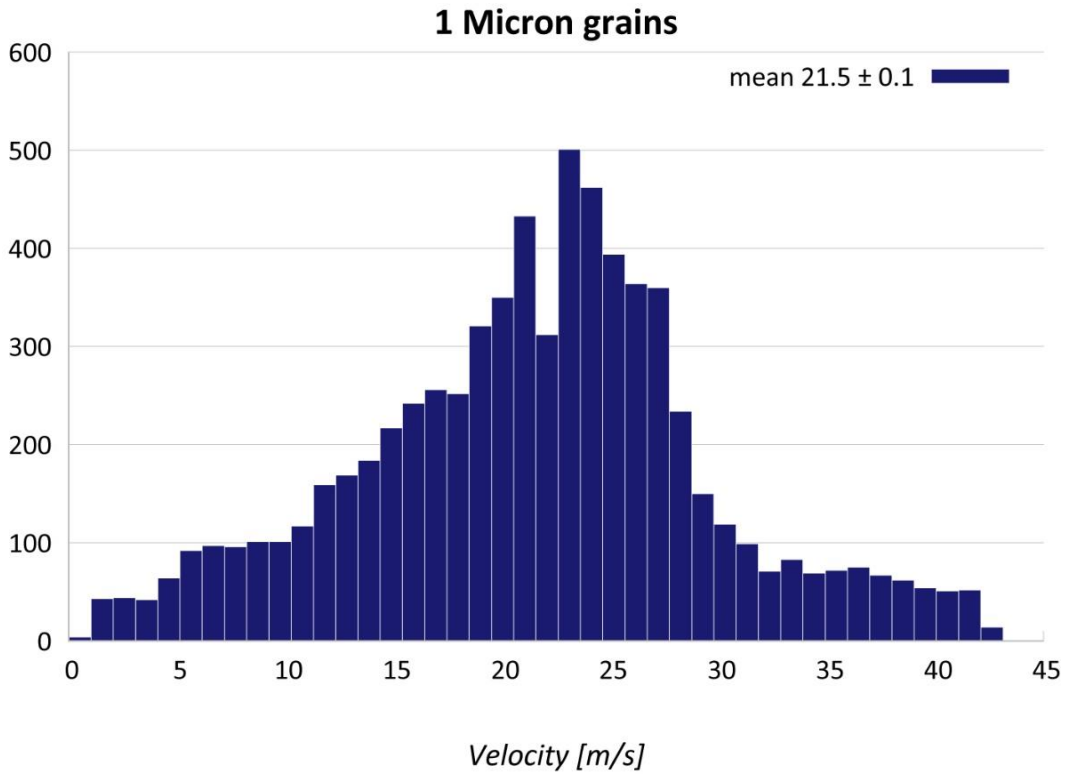

Figure 2.29 Velocity histogram derived from tests for 1 μm monodispersed particles.

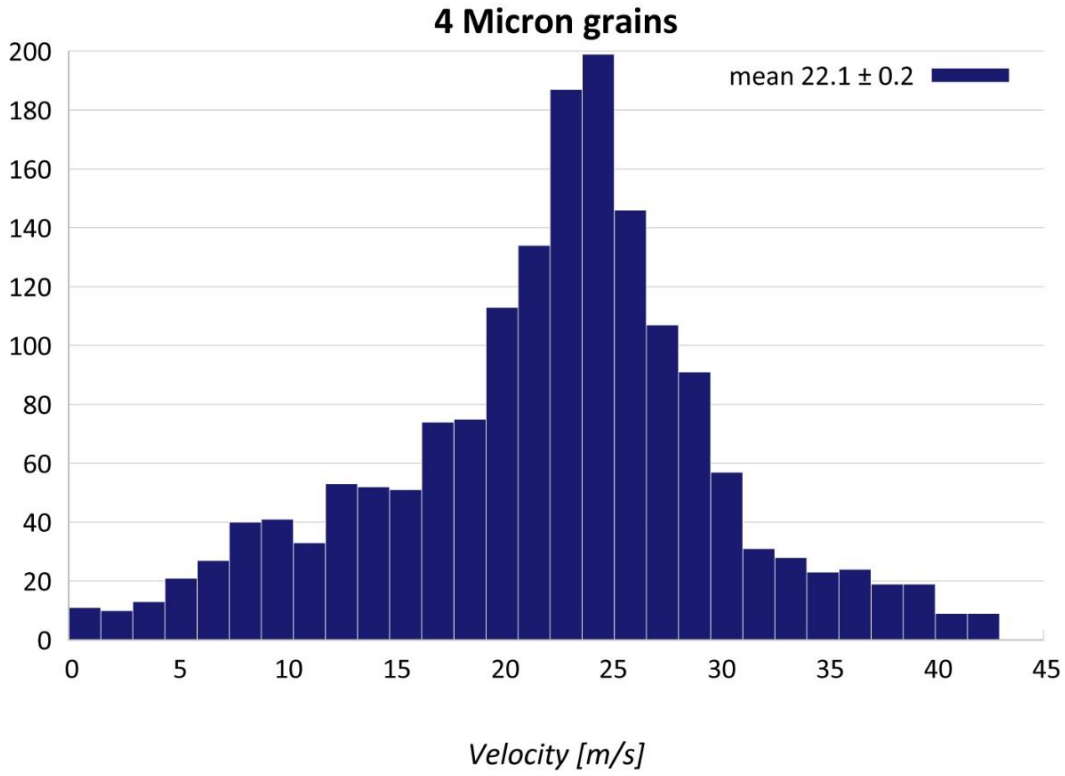

Figure 2.30 Velocity histogram derived from tests for 4 μm monodispersed particles. The Y-axis of the plots indicates number of signals.

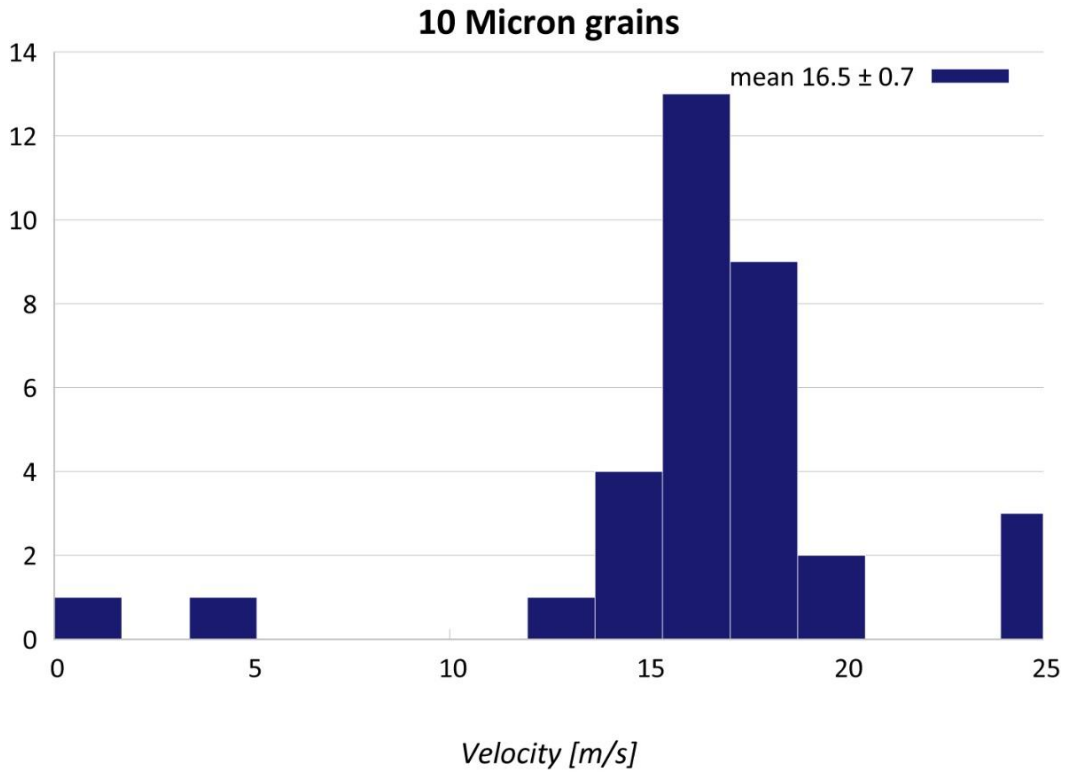

Figure 2.31 Velocity histogram derived from tests for 10 μm monodispersed particles. The Y-axis of the plots indicates number of signals.

2.1.3 Results and discussion

2.1.3.1 Sampling Efficiency

Results show different behaviors for small (0.4-1 μm in diameter), intermediate (1-15 μm) and large (15-20 μm) particles. Grains of intermediate dimensions are always well detected as sampling efficiency values range from 95% to 99.5%. On the other hand, the instrument ability to detect smaller and bigger grains changes with environmental parameters, so the instrument is able to optimize the efficiency of the instrument for the entire 0.4-20 μm diameter range only in the optimum operating conditions described hereafter. The following paragraphs will indeed describe the effect of the main environmental parameters on the instrument's sampling efficiency and discuss the derived optimum condition.

2.1.3.2 Influence of instrument temperature on sampling efficiency

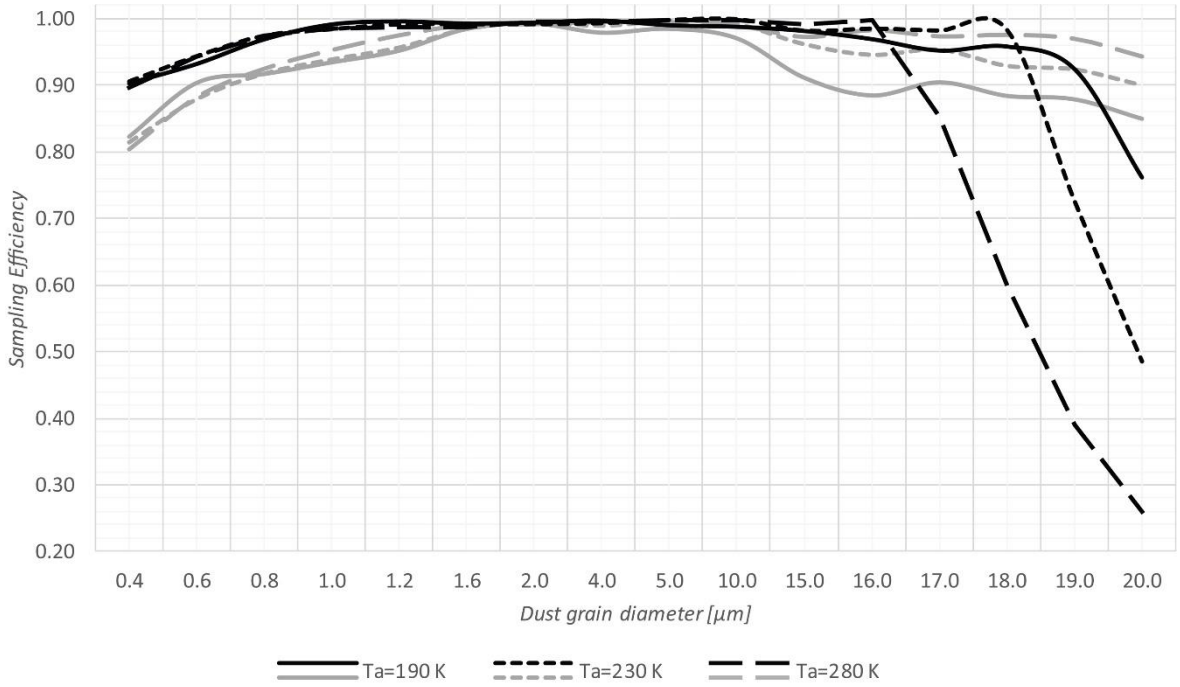

Figure 2.32 Effect of instrument temperature on the instrument sampling efficiency. Plots are relative to pa=700 Pa, Δp=300 Pa. BLACK: Ti=253 K, GREY: Ti=313 K.

Instrument temperature is the most influential parameter. As we can see in Figure 2.32, very different results are obtained for "cold instrument" runs (having T_i=253 K) and "hot instrument" runs (having T_i=313 K). Detection of small grains is more accurate for "cold" instrument (efficiency improvements up to 8%) and for low pump rotating speed (generating an inlet-outlet pressure difference of 250 Pa, the minimum value considered in the analysis). When pump rpm speed increases, hot and cold runs show similar results for small grains. On the other hand, the detection of big dust grains (15-20 μm) might be more problematic

since high pump speeds (needed for better sucking ability) increase the chances of hits on the walls. Consequently, some of those particles might become undetectable. When the instrument is cold this chance heavily increases, probably because fluid inside the instrument is denser thus it offers more resistance to the deflection of grains inside the instrument's head, enhancing the chances of impact. This efficiency drop is critical and it was one of the main focuses of the present study. An improvement to the instrument design was developed based on these results in order to avoid such behavior without altering other key features of the instrument. For instance, the ability to have a high volumetric flow rate must be maintained (it might be reduced by changing of inlet and/or outlet geometry, worsening the instrument ability to sample grains) and other fluid dynamic properties also have to be retained (different geometry may reduce the fluid speed inside the instrument, so deflection of dust grains outside the sampling spot might happen with higher probability).

The detailed analysis of the new fluid dynamic design is provided in Section 2.2.

2.1.3.2.1 Influence of atmospheric pressure on sampling efficiency

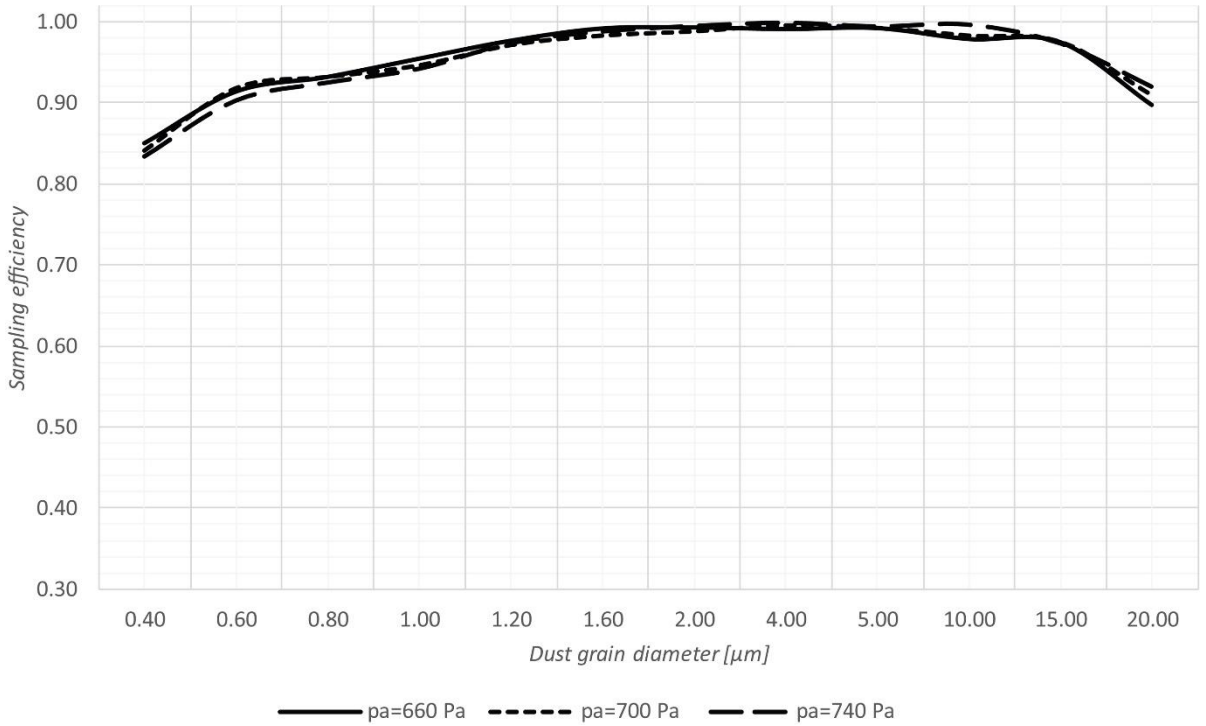

Figure 2.33 Influence of daily pressure variations of the instrument sampling efficiency (Ta=230 K, Ti=253 K).

As already stated, Mars' atmospheric pressure follows seasonal behavior. According to the MCD Model (Mars Climate Database v5.3), daily variations are small compared to the absolute value of ambient pressure and simulations show they have little influence on sampling efficiency (See Figure 2.33). Therefore, the seasonal value of pressure is the only variable. However, its value can be considered constant during the single run giving the short duration of the measurement session (whose duration is variable but is no longer than 120

seconds). Consequently, it was not considered necessary to install an absolute pressure sensor on MicroMED, an assumption confirmed by the fact that even seasonal atmospheric pressure values have small effects on the instrument ability to suck and detect particles (See Figure 2.34). This probably happens because the changes in the atmosphere physical parameters (viscosity and density) are not relevant to the point of changing the shape of the fluid stream. On the other hand, a differential pressure sensor is needed in order to achieve the proper functioning of MicroMED, since the pressure difference between the atmosphere and the outlet section of the instrument allows to evaluate and control the volumetric flow rate and understand the actual operating conditions of the pump.

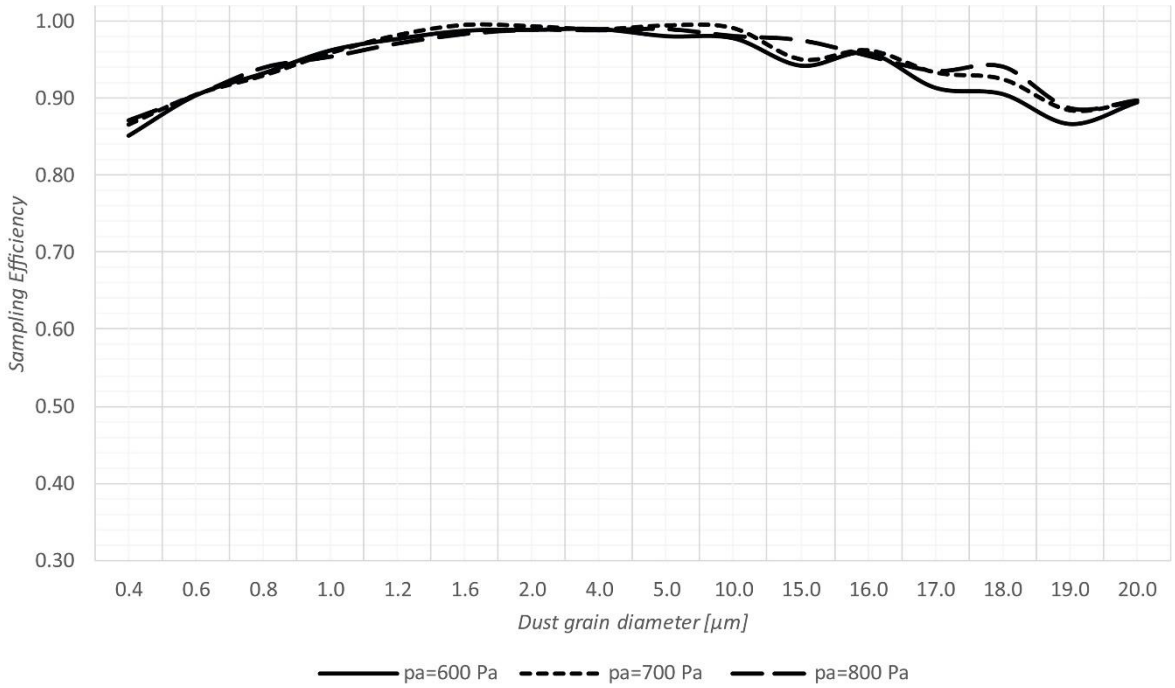

Figure 2.34 Influence of seasonal atmospheric pressure on sampling efficiency (Ta=190 K, Ti=253 K).

2.1.3.2.2 Influence of atmospheric temperature on sampling efficiency

Ambient temperature has a small effect on sampling efficiency. The fluid indeed reaches thermal equilibrium with the instrument rapidly. As already known, the instrument's temperature is imposed by its position under the spacecraft thermal cover. This condition induces a small influence of ambient temperature on grains' dynamics and on sampling efficiency (always smaller than 7%, see Figure 2.35).

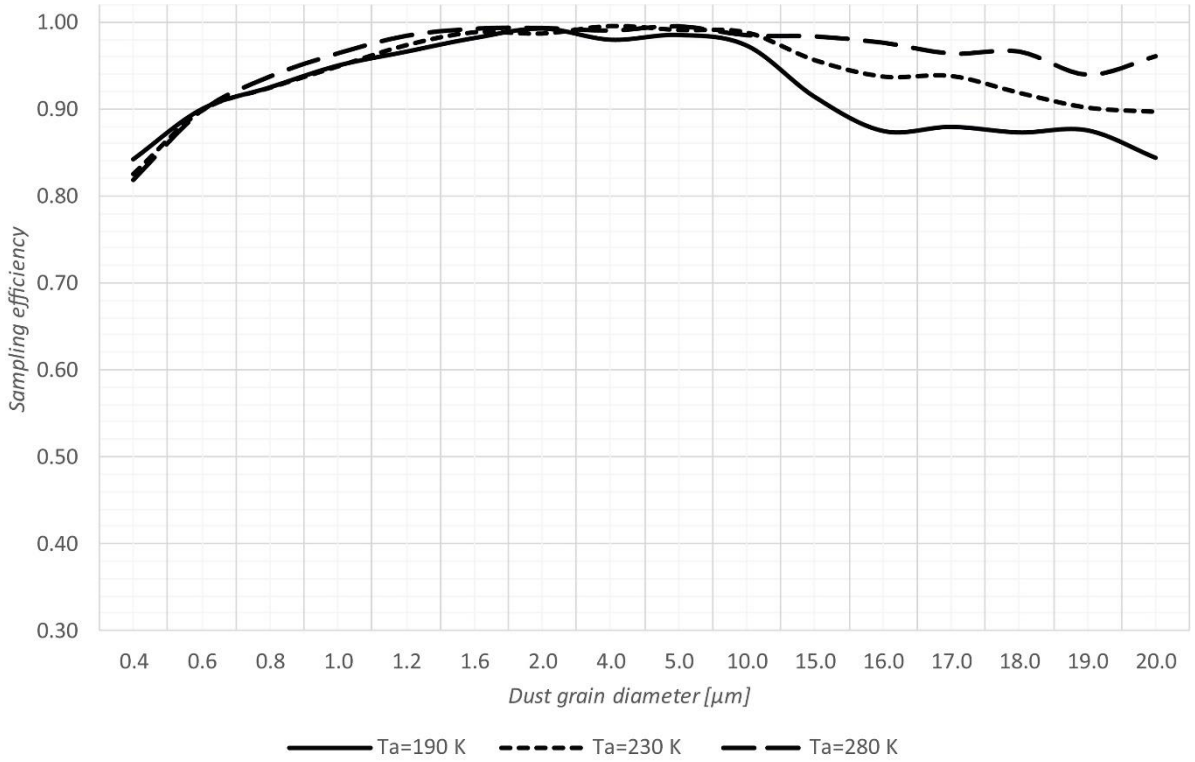

Figure 2.35 Influence of atmospheric temperature on sampling efficiency (pa=600 Pa, Ti=313 K).

2.1.3.3 Effect of density

Mars atmosphere density is very low compared to Earth's. The order of magnitude of such density is 1E-2 kg/m^3, but ambient pressure and temperature play a huge role in its variations, that can be relevant. Mars atmospheric density was estimated using the following equation, that can be found on NASA's website (https://www.grc.nasa.gov/www/k-12/airplane/atmosmrm.html), relating atmospheric density to pressure and temperature:

$$\rho = \frac{p}{[0.1921 \cdot (T+273.1)]} \quad [8]$$

Where p is in kPa and T is in Celsius degrees. Such equation was implemented in an Excel worksheet allowing to obtain the evolution of density for different ambient temperatures and pressures. Table 2.5 shows such relation; atmospheric density increases with an ambient pressure increase and an ambient temperature decrease. At an ambient temperature equal to 230 K, for instance, atmosphere density is respectively equal to 1.36E-2 kg/m^3, 1.58E-2 kg/m^3, 1.81E-2 kg/m^3 for atmospheric pressure values of 600, 700 and 800 Pa, respectively. This shows a clear increase with pressure, in accordance with the linear proportionality law described by the equation. For an atmospheric pressure value of 600 Pa, changing ambient temperatures from 190 K to 230 K and then 280 K would make the density value decrease from 1.64E-2 kg/m^3 to 1.36E-2 kg/m^3, then 1.12E-2 kg/m^3, showing the inverse proportionality between ambient density and temperature.

Density can thus assume very different values among different runs. This aspect influences the sampling efficiency, especially for bigger particles, for two reasons:

- Volumetric flow rate changes with density;
- A less dense fluid has smaller impact on the particles trajectories, meaning the particles trajectory deflection is smoother because particles move in a condition that is somehow closer to vacuum condition.

pa [Pa]	Ta [K]	ϱ [kg/m³]	pa [Pa]	Ta [K]	ϱ [kg/m³]
560	230	1.27E-02	700	270	1.35E-02
600	190	1.64E-02	700	280	1.30E-02
600	230	1.36E-02	740	230	1.67E-02
600	250	1.25E-02	760	230	1.72E-02
600	270	1.16E-02	800	190	2.19E-02
600	280	1.12E-02	800	230	1.81E-02
640	230	1.45E-02	800	250	1.67E-02
660	230	1.49E-02	800	270	1.54E-02
700	190	1.92E-02	800	280	1.49E-02
700	230	1.58E-02	840	230	1.90E-02
700	250	1.46E-02			

Table 2.5 Density variation with atmospheric temperature and pressure.

The flow is more rarefied, therefore its ability to drag grains with it along the duct is diminished. Such behavior influences the sampling efficiency of particles bigger than 15 μm: higher atmosphere temperatures would mean less dense atmosphere, smoother deflection of the particles trajectories, meaning more grains hit the wall and get stuck, worsening the sampling efficiency. Same behavior is met for variations of atmospheric pressure that imply reductions of density.

2.1.3.4 Effect of gravity

Gravity has been analyzed as a possible influencing parameter on MicroMED performances. For this purpose, a series of CFD runs have been made, keeping all parameters constant except gravity (twin cases for g = 9.81 m/s² – Earth – and g = 3.71 m/s² – Mars – have been simulated). Results showed that gravity has little effect on sampling efficiency (< 3% in all cases and ~ 0% in most cases) and even smaller effect on grain velocity (maximum difference of ~ 0.3 m/s). For this reason, gravity has not been considered as an influential parameter. Its effect could be perceived during tests, but such effect are going to be limited to the environment, especially to the deposition of grains (In the dust injection phases described in Section 3.2.1.4, for example), rather than on MicroMED's behavior.

2.1.3.5 Compressibility of the flow

Dust grains velocity was an important design parameter, given that its value in the sampling section of the instrument has to be low enough for the electronics to be able to detect the grains. In MicroMED's sampling section, dust grains speed never exceeds 46 m/s, which is an acceptable value for the correct functioning of the instrument. In the sampling section, fluid speed is significantly lower than dust grains speed. This is due to the expansion the fluid experiences once it exits the inlet duct, slowing its velocity. However, the influence of this expansion on dust grains motion is small. Despite their trajectory may be slightly affected, most of the grains keep indeed the same velocity reached in the final section of the inlet duct. After the gap, fluid speed strongly increases. Despite Mach number is almost always under 0.1 and under 0.3 for most cases, there is a possible compressibility effect, favored by the extremely low pressure and density of Mars atmosphere. Moreover, instrument temperature is in most cases very different from the atmosphere's one. Therefore, the sampled fluid experiences a sudden temperature increase reducing its density. Given these aspects, the original assumption of uncompressible flow was abandoned, and flow field was considered compressible.

2.1.3.6 Particle tracking

During CFD simulations, dust grains are tracked while flowing through the instrument. A detailed description of the methods used for particle tracking is provided in Section 2.1.1.2. The position in which dust grains cross the sensing spot is an important aspect in the analysis not only from a sampling efficiency standpoint, but also from a post processing point of view, as laser light is more powerful in the inner section of the sampling spot, so grains that cross the spot close to the center allow an easier detection even for smaller particles (that have small scattering intensity, meaning weaker signal). Therefore, the exact position where the grains cross the sampling volume is a key aspect and is thus treated as a design parameter. This information can be used to describe the quality of the Breadboard fluid dynamics and helped in the development of the updated design. Figure 2.36 and Figure 2.37 show positional histograms for two particle dimensions in the sampling range (2 and 10 μm in diameter, respectively). Small particles can be deflected outside the illuminated spot (whose border is highlighted by a vertical line in Figure 2.36) but their distribution is peaked inside the sampling spot. The same behavior is obtained for the 10 μm particles, meaning that the fluid dynamic design is able to make dust grains converge to the sampling spot for such grain dimensions. In both cases, velocity histograms are peaked around the highest value of velocity suggesting that most of the dust grains flow through the duct while being in the inner rings of the conduct where fluid speed is higher (Figure 2.38 and Figure 2.39). Bigger

grains are detected with smaller efficiency not because they do not converge (they never exceed a distance of 300 μm from the center of the sampling spot, hence well inside the limit) but because they tend to hit the inlet walls, getting stuck.

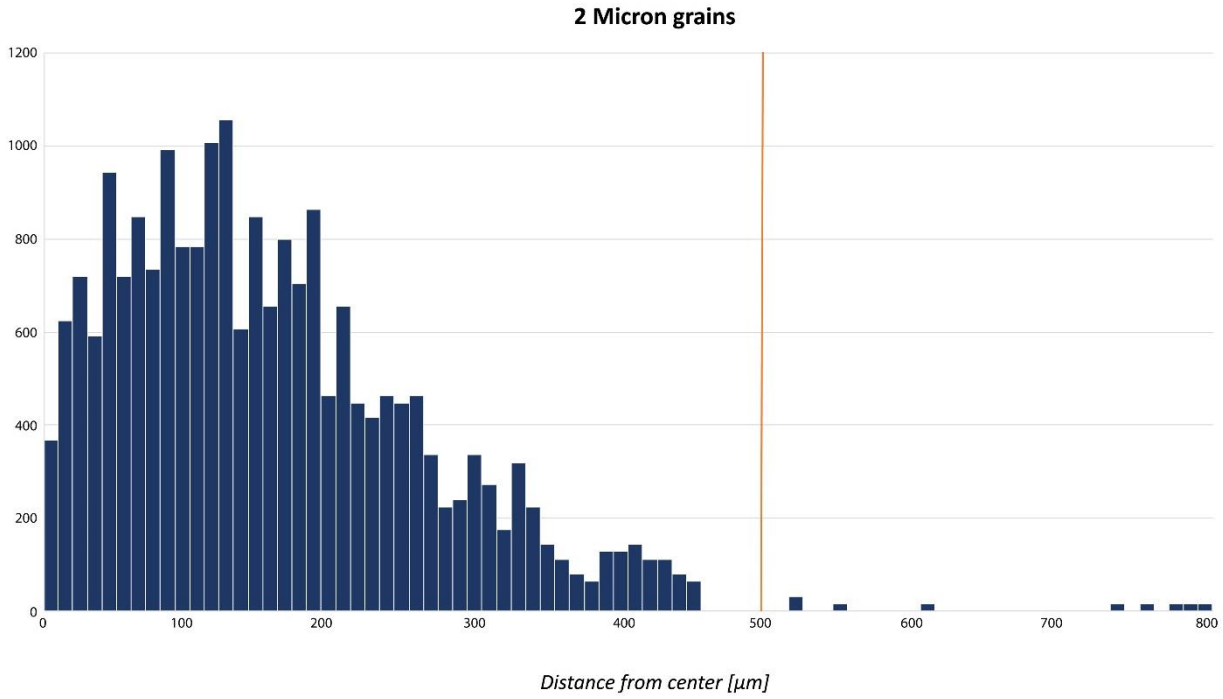

Figure 2.36 Example of position histogram for 2 μm grains (the vertical line represents the sampling spot border).

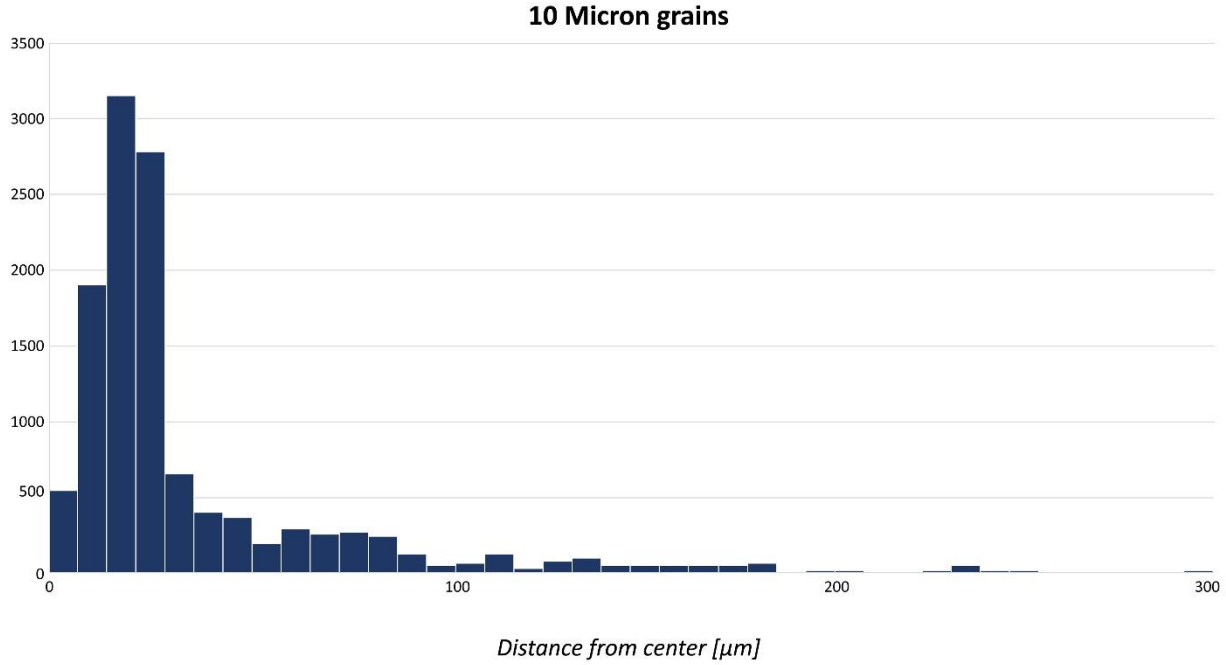

Figure 2.37 Example of position histogram for 10 μm grains.

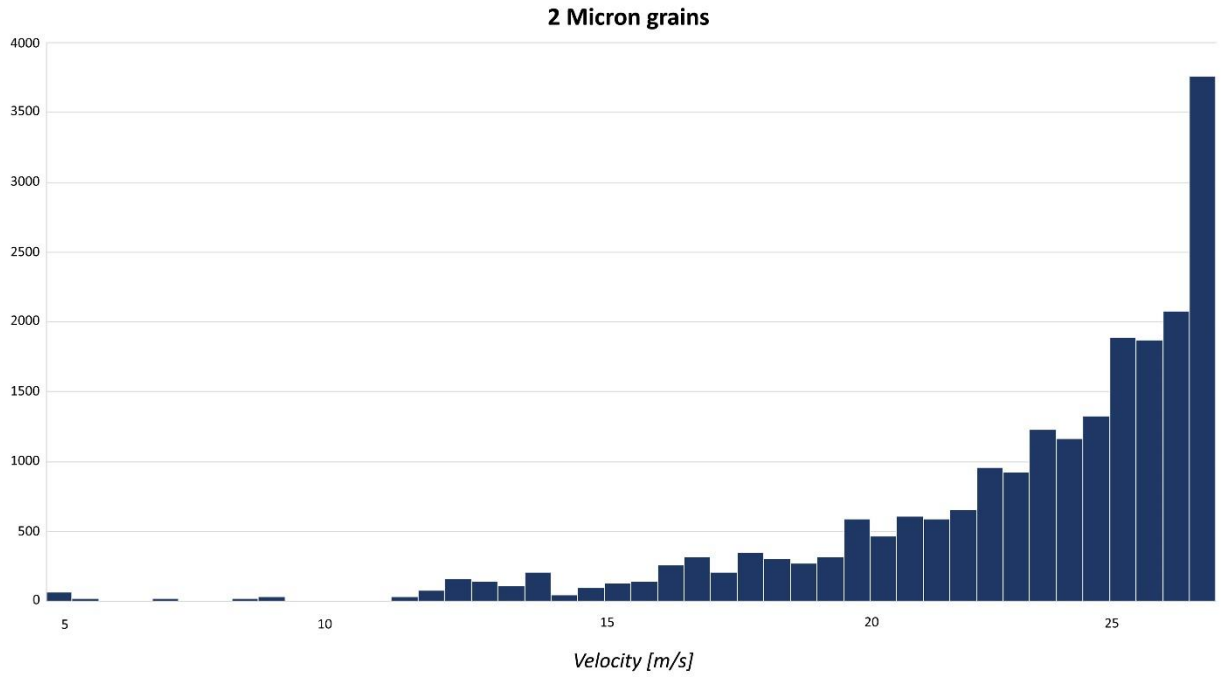

Figure 2.38 Example of velocity histogram for 2 μm grains.

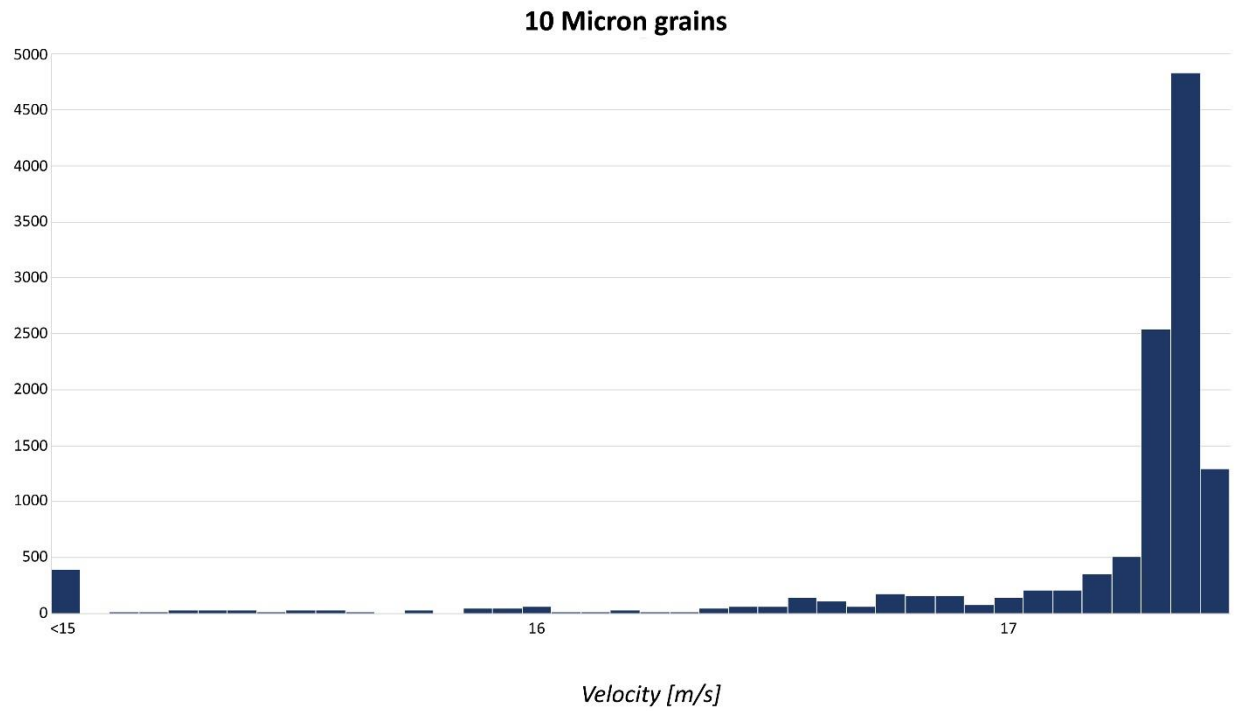

Figure 2.39 Example of velocity histogram for 10 μm grains.

2.1.3.7 Optimum operating conditions

Our simulations show that the optimum operating conditions can be obtained with a 300 Pa pressure difference between MicroMED's inlet and outlet. This condition provides good sampling efficiency when the instrument is cold, avoiding drops in the sampling efficiency of large (15-20 μm diameter) dust grains, without altering the instrument ability to detect smaller ones. A Δp = 300 Pa indeed guarantees sampling efficiency values over 85% (most times over 90%) for every dust grain diameter in the 0.4-20 μm range when the instrument is hot, representing a good testing condition regardless of the values assumed by environmental parameters.

2.1.3.8 Volumetric Flow Rate

Volumetric flow rate measurement at the inlet section is also needed to obtain the dust grain concentration value in Mars atmosphere, through the ratio between the number of detected dust grains and the volume of fluid sampled. Variations of atmospheric pressure, atmospheric temperature, instrument temperature all have effects on volumetric flow rate.

As in the case of sampling efficiency, the most influential parameter is instrument temperature. Volumetric flow rate values vary up to 30% between "cold" and "hot" instrument runs (See Figure 2.40). It is also possible to see a gradual increase of volumetric flow rate along the instrument related to the compressibility of the flow.

Ambient temperature also has an influence but only at the inlet section (variations up to 10%), since the fluid, once inside the instrument, is only influenced by instrument temperature because thermal equilibrium is reached (See Figure 2.41).

Volumetric flow rate experiences 3-8% variations due to daily pressure. Percentage wise, seasonal pressure has a bigger influence but only the flow rate value at the outlet section is affected, with average volumetric flow rate variations of about 7-8% with peaks up to 16% (Figure 2.42).

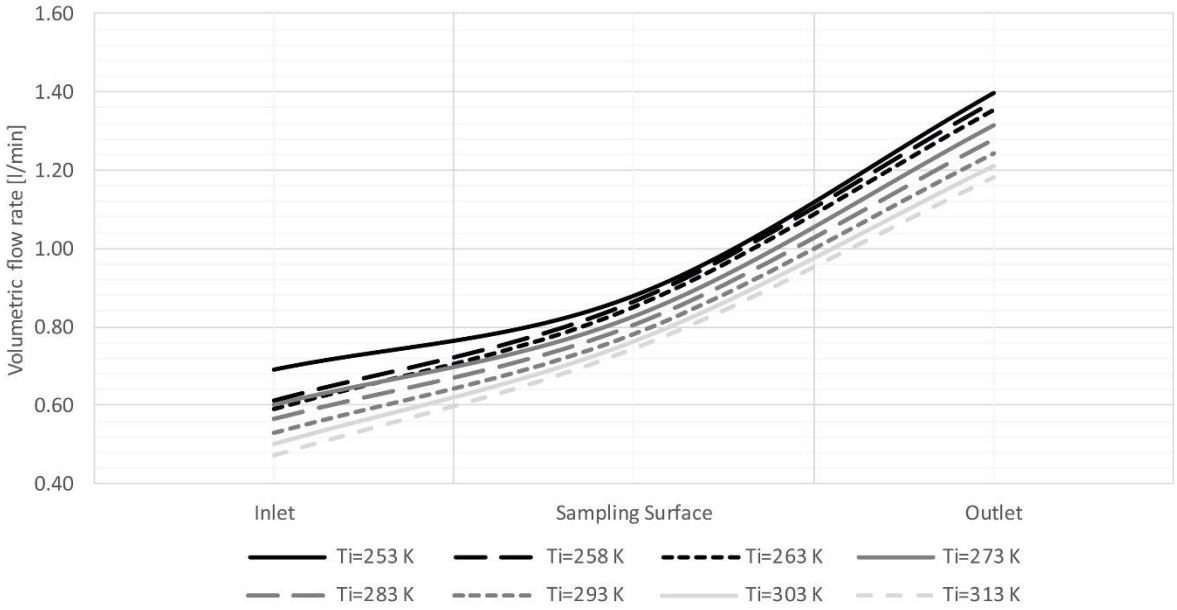

Figure 2.40 Influence of instrument temperature on the instrument volumetric flow rate (Pa=600 Pa, Ta=250 K).

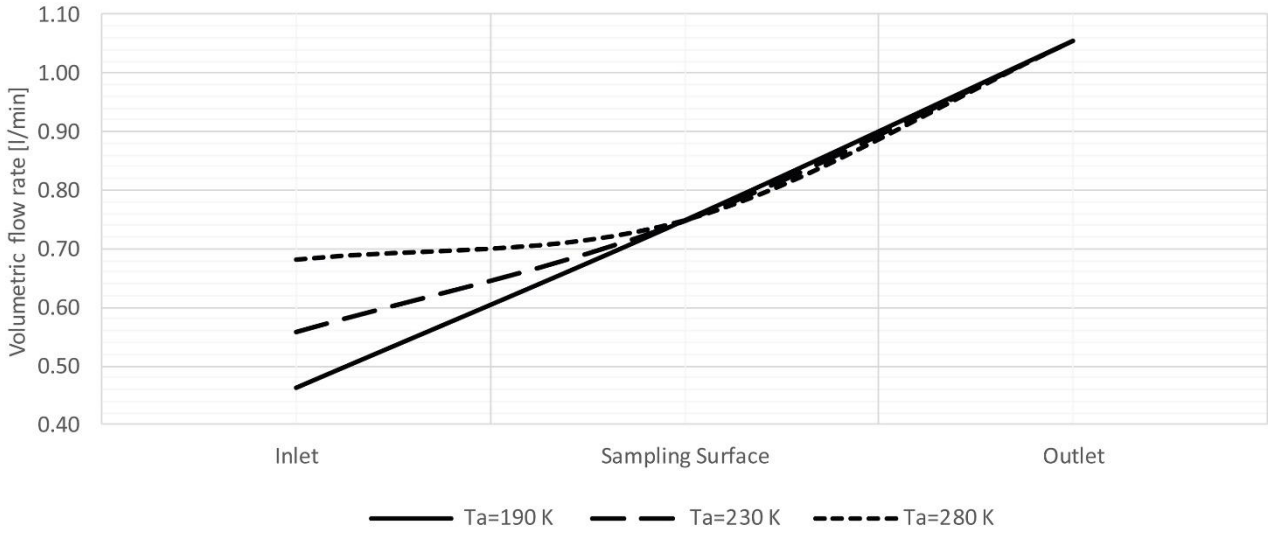

Figure 2.41 Influence of atmospheric temperature on the instrument volumetric flow rate (Pa=600 Pa, Ti=253 K).

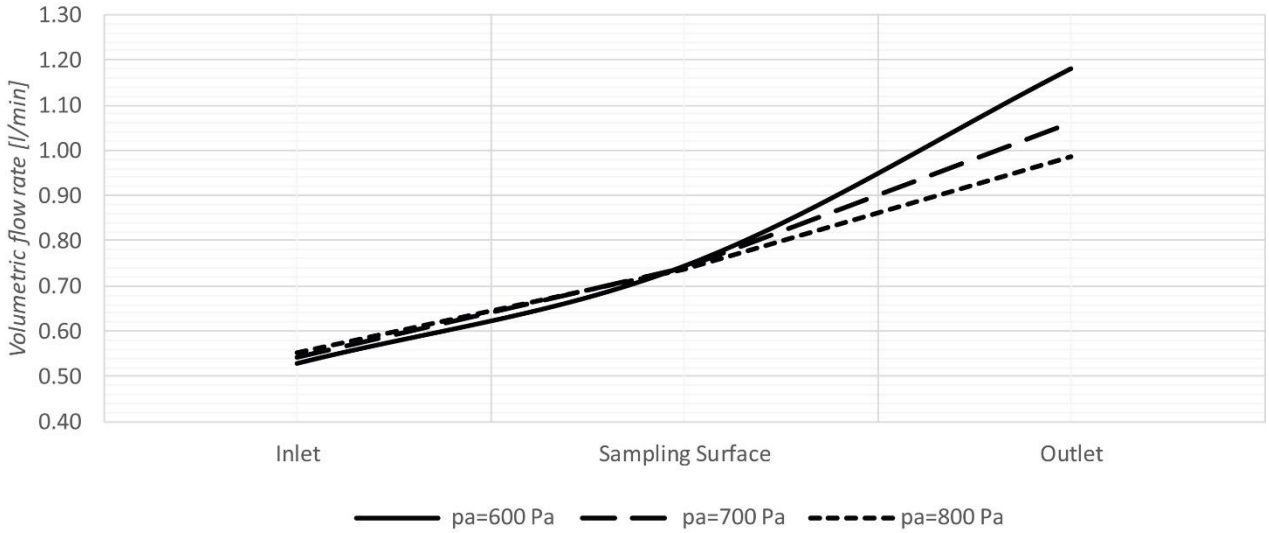

Figure 2.42 Influence of atmospheric pressure on the instrument volumetric flow rate (Ta=280 K, Ti=313 K).

2.1.3.9 Behavior in windy conditions

MicroMED's BB behavior in presence of wind was studied by means of CFD simulations and results have been compared with data obtained from tests performed in Capodimonte and at the Planetary Environment Facilities (AWTSII) at Aarhus University in Aarhus, Denmark (Holstein-Rathlou, C. et al., 2014), which is described in Section 3.2.5.1. The instrument showed good performances for wind speed up to 7 m/s. For each wind speed the instrument could detect dust grains under a threshold value that gets smaller with the increase of wind velocity. The analysis shows CFD simulations strongly underestimate the instrument ability to detect particles in windy environments. Figure 2.43 shows that, according to CFD, the instrument should not be able to detect large dust grains even when wind speed is only 2 m/s, in contrast to what experienced during tests at AWTSII in Aarhus. This could be partly due to the fact that Fluent considers the particles as spherical. Unsteady effects due to non-uniformity of the particles shape are not considered and the grains are simulated as more steady than they really are. However, an underestimation of performances by the CFD simulations was verified also for tests with spherical particles. CFD results can thus be considered as conservative; an improvement of the model that simulate the effect of non-sphericity of dust grains is still currently under analysis.

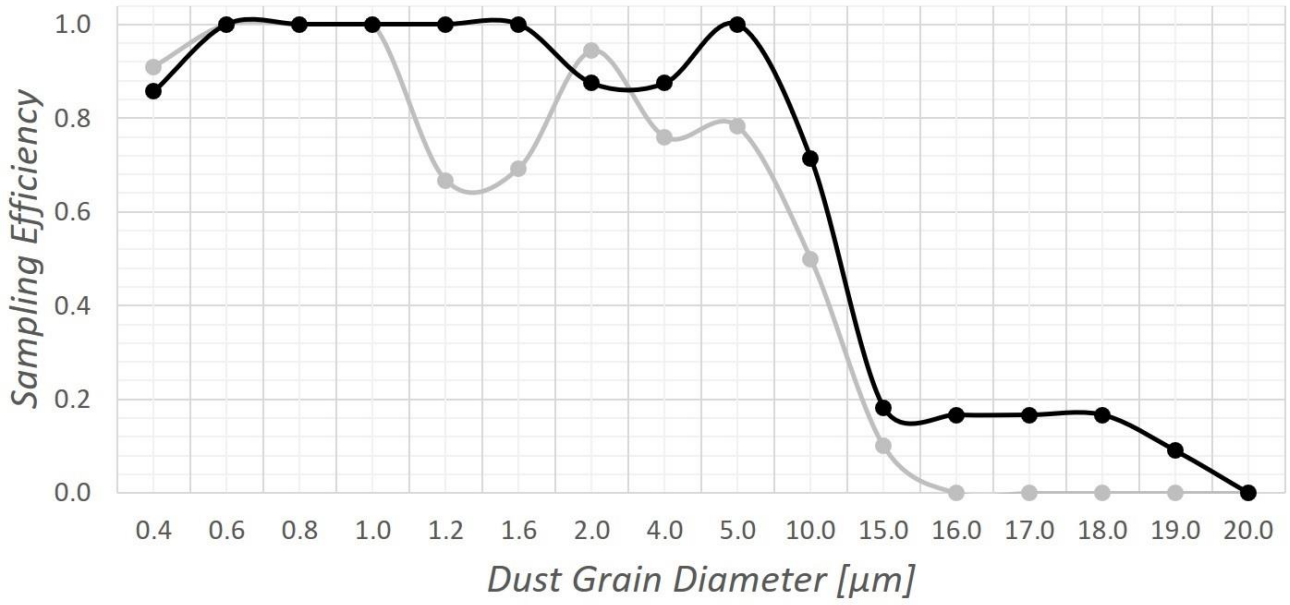

Figure 2.43 Comparison between the behavior in windy environment (V=2 m/s) of the Elegant Breadboard (GREY) and the newly updated version (BLACK) of MicroMED (pa=600 Pa, Ta=280 K, Ti=253 K).

2.1.3.10 Brief summary of the results obtained from MicroMED's BB CFD analysis

We know MicroMED is conceived to measure both abundance and size distribution of dust grains embedded in Martian atmosphere. In order to optimize the efficiency of the instrument, a CFD analysis of the instrument's BB version was performed and its theoretical results have been discussed, focusing on the achievable sampling efficiency and the required volumetric flow rate.

In this first part of the analysis, we can notice that instrument temperature is the most influential parameter on sampling efficiency. Its effect is different depending on particles size. Dust grains of small dimensions (diameter < 1 μm) are better detected when instrument temperature is low, while the detection of larger grains (diameter > 15 μm) is more efficient for high instrument temperatures. Grains of intermediate dimensions (diameter between 1 and 15 μm) are always well detected. The instrument ability to detect large dust grains may experience a drop when the instrument is cold, a condition that highlighted the need for a geometry upgrade. An updated geometry has in fact been designed and its analysis will be reported in detail in the following sections.

Ambient pressure values (both seasonal and daily values) have small effect on the instrument sampling efficiency. Therefore, an absolute pressure sensor was not deemed necessary on MicroMED. The only pressure sensor present in the instrument is a differential pressure sensor needed to evaluate the pressure difference generated by the pump (which triggers the suction of fluid) because it allows us to evaluate the actual operating conditions during tests.

Also ambient temperature has limited influence on MicroMED's efficiency as the fluid rapidly thermalizes with the instrument, highlighting the dominant role instrument temperature has on its functioning.

Compressibility of the flow that was supposed before the runs was verified.

Particles tracking showed the instrument design works efficiently, conveying dust grains toward the inner section of the sampling spot where laser light is more intense, improving the instrument chances to detect diffracted light.

The optimum operating conditions was found to be the one related to a Δp generated by the pump of 300 Pa with respect to Martian atmospheric pressure. This condition optimizes the instrument sampling efficiency for the entire sampling range.

Volumetric flow rate is mainly influenced by instrument temperature, similarly to what was found for sampling efficiency. Pressure and ambient temperature have smaller effects.

The developed CFD model underestimates the instrument ability to detect dust grains in windy conditions, probably because the model only simulates spherical particles. An improvement of the model considering non-sphericity of grains is under development.

2.1.4 Undesired phenomena individuated during the analysis

The described CFD analysis showed a couple of criticalities in the Elegant Breadboard design, causing a reduction of the sampling efficiency for both large and small dust grains, with different extents and causes. These phenomena are described hereafter.

2.1.4.1 Collisions on the inlet walls

Given the particular geometry of the Elegant Breadboard's inlet head, fluid streams coming from opposite holes of the sampling head tend to cross (See Figure 2.44). The sharpness of the bending depends on the dust grains inertia: the lower the inertia, the sharper the deflection. This is an important aspect as large dust grains are a lot more likely to hit the duct walls. Given the assumption that the walls' mean surface roughness is of the same order of magnitude of the particles diameter, this may cause adhesion of the particles to the walls, preventing their detection. The Elegant Breadboard's duct shape promoted such phenomenon. The Flight Model design was thus modified to avoid the crossing of the trajectories and to linearize the fluid streamlines during the suction, also helping the laminarity of the flow which is a design parameter (since it improves the instrument efficiency). A description of the updated design will be provided in Section 2.2 and is actually already been introduced in Section 1.2.5.

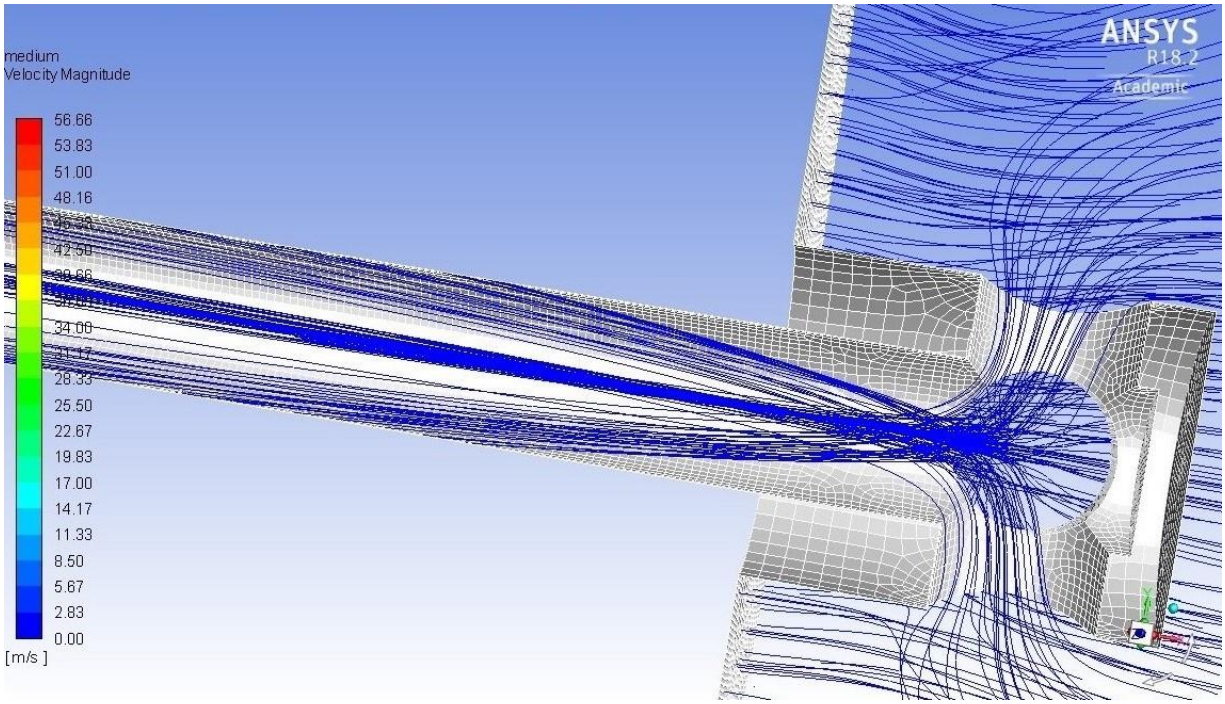

Figure 2.44 Particles trajectories inside the Elegant Breadboard's inlet head and duct.

2.1.4.2 Deflection of dust grains' trajectories

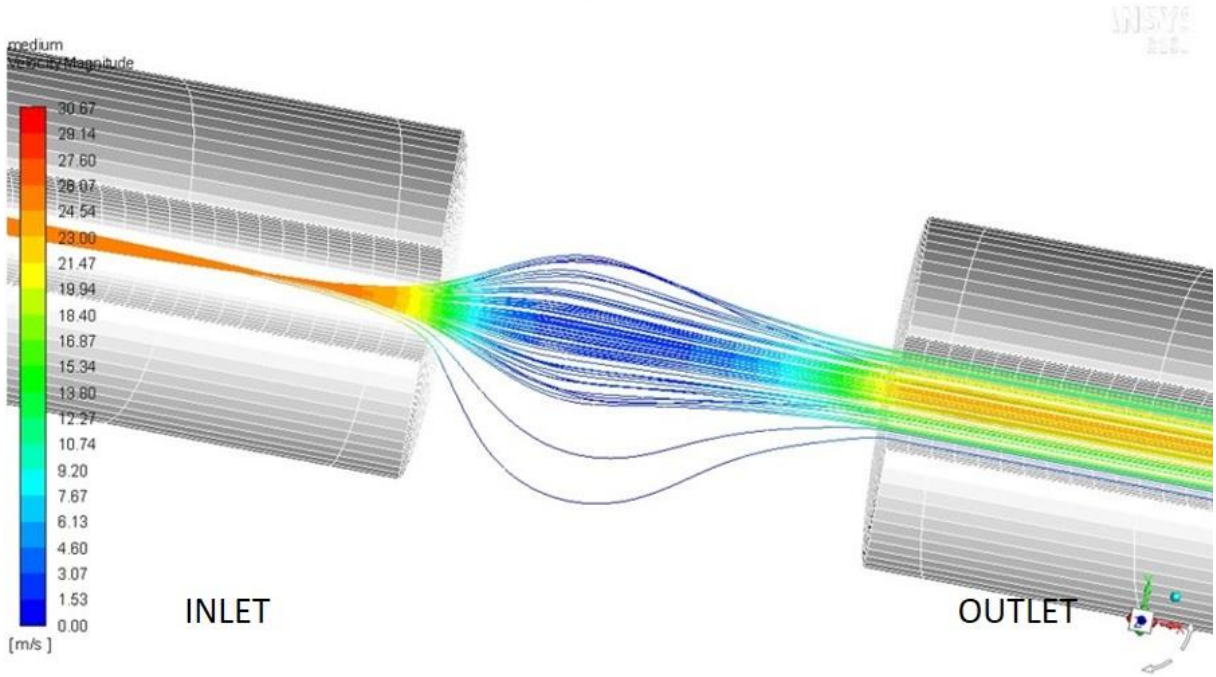

Figure 2.45 Dust grains behavior inside the sensing section of MicroMED's Elegant Breadboard.

Inside MicroMED's optical head and at the end of the inlet duct, a 4 mm gap is present, needed for the optical scan of the flow. The final section of the inlet duct has a 1 mm internal diameter. When the fluid reaches such gap, it expands, possibly deflecting the particles trajectories. There is indeed the chance that some of the dust grains follow the streamlines and cross the sensing plane outside the 1 mm^2 laser illuminated spot, preventing their detection. This behavior is especially possible for small dust grains given their low Stokes number. Such phenomenon could alter the efficiency of MicroMED's Elegant Breadboard depending on the environmental conditions. Therefore, the geometry update was aimed at having good performances in every possible operating condition. Figure 2.45 shows the possible undesired behavior of particles. Please notice that the velocity range considered in Figure 2.43 and Figure 2.44 is quite different because the figures are focused on evidencing the phenomena described, they thus refer to different test cases. Varying the parameters in play, a vast range of instrument behaviors (hence of fluid speed) can be obtained.

The following section will show the updated design that was developed for MicroMED's Flight Model as well as an in-depth analysis of the results of the CFD analysis performed on such design.

2.2CFD analysis of MicroMED's Flight Model design

MicroMED's Elegant Breadboard version has been analyzed by means of an in-depth CFD analysis in order to individuate the environmental parameters that mostly affect the performances of the instrument and with the purpose of individuating eventual undesired physical phenomena that should be corrected. Some phenomena have been individuated (See Section 2.1.4) that are thought to be detrimental to the sampling efficiency of MicroMED. This section will describe the process of optimization of the design of MicroMED's fluid dynamic system, aimed at improving MicroMED's sampling ability (especially for large grains, that were the toughest to be detected with MicroMED's BB) and at the correction of such phenomena.

2.2.1 Geometry variations

The CFD analysis performed on MicroMED's BB highlighted a couple of undesired phenomena that are thought to be an issue for an efficient sampling of grains in the entire measurement range. Such phenomena, described in Section 2.1.4, have been efficiently corrected by adopting some geometry variations to the sampling head as well as the inlet and outlet ducts.

Figure 2.46 provides an overview of the variations adopted for the sampling head and the inlet duct. The walls of the sampling head are now thinner, reducing the length of the small conducts that convey the flow toward the main duct of the inlet. Such reduction is responsible for a smoother deflection of grains, which is positive since the BB geometry caused a deflection of dust grains that was basically of ~ 90° toward the inside of the instrument once they enter the sampling head. The inlet duct, which has the same length (118.5 mm, see Section 1.2.5) due to integration constraints on the surface platform (the length of the inlet duct has to allow the sampling head to exit the thermal cover while the rest of MicroMED is under it), has now a simpler shape: it is a simple cone with 4 mm internal diameter at the base of the sampling head and a 1 mm internal diameter at its end, inside the instrument. For MicroMED's BB, the duct had a more complex geometry which was a combination of two cylindrical sections interspersed by a conical section.

MicroMED's outlet was also adapted; it was made shorter due to geometric constraints during the design phase of MicroMED's Flight Model. Such shortening of the duct is also beneficial for the performances since the pump is now closer to the sampling head, allowing a stronger pressure force on the sampled grains. MicroMED's outlet (Figure 2.47) is now 32.5 mm long, compared with 88.5 mm for the BB version, and it has a simply conical shape, with a 1 mm internal diameter at the beginning of the outlet duct, thus close to the sensing spot,

and a 2.5 mm internal diameter at its end, where a silicon U-tube connects the outlet duct to the pump. MicroMED's BB had an outlet duct which was the combination of two cylindrical sections of 1 and 4 mm of internal diameter, respectively.

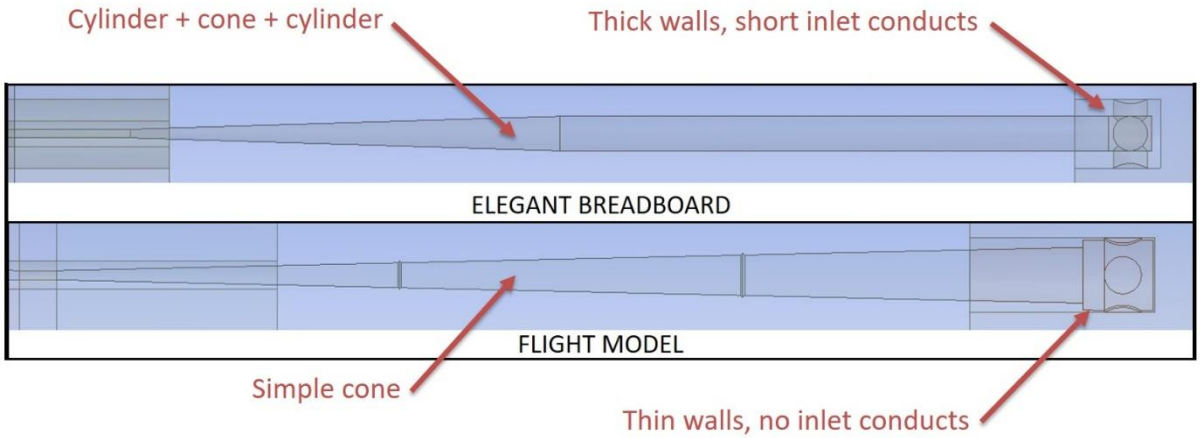

Figure 2.46 Geometry variations of MicroMED's sampling head and inlet duct (drawings not to scale).

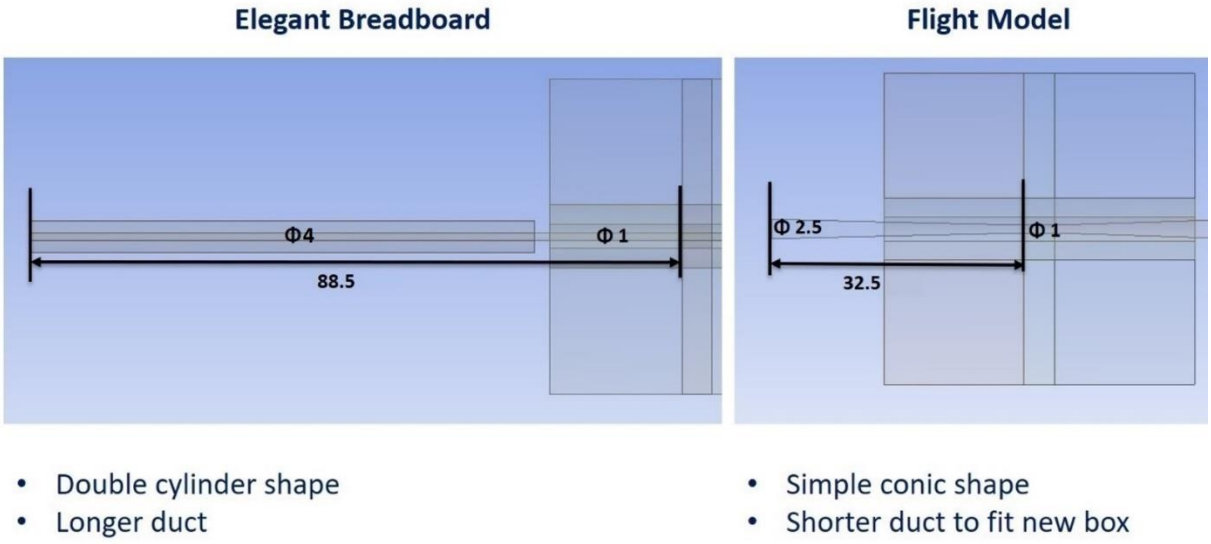

Figure 2.47 Geometry variations of MicroMED's outlet duct (dimensions in mm).

2.2.2 CFD model

The CFD model used and the principles that led to its development are the same described in Section 2.1.1. Geometry files have obviously been updated for this new phase of the analysis, but the model, as well as the range of each environmental parameter considered, were unvaried. Please refer to Section 2.1.1 for all the details.

2.2.3 Results

Results are here reported as a comparison with the Elegant Breadboard's status, showing the improvements obtained. The effect of environmental parameters on MicroMED's efficiency was previously analyzed (Section 2.1) for the Elegant Breadboard. Present analysis shows similar effects for the Flight Model. Instrument temperature is the most influential parameter both on sampling efficiency and in the evaluation of the volumetric flow rate, which is needed in order to determine dust concentration in the sample of gas sampled. The analysis performed on the Elegant Breadboard showed other parameters can influence MicroMED's behavior. Moreover, the optimum conditions for tests had to be deduced since good efficiency was not guaranteed in any environmental conditions. The Flight Model design provides improvements of the efficiency for every size and basically guarantees good efficiency for every possible condition. The analysis performed on the Flight Model also shows how optimum results can be obtained with a Δp generated by the pump in the 200-300 Pa range. The Elegant Breadboard needed at least 300 Pa Δp in order to work, so the current design allows more flexibility in the choice of the operating conditions and a reduction of the power consumption of the instrument. The following sections describe the results obtained for such updated design.

2.2.3.1 Sampling efficiency of large dust grains

As shown in Figure 2.48 and Figure 2.49, CFD runs predict a significant improvement of the instrument ability to detect large (15-20 μm diameter) dust grains. When the instrument is "hot" (T_i= 313 K, see Section 2.1.1.1) MicroMED's BB was already sufficiently efficient for such dust sizes, however the updated design provides improvements as big as 10-14%. When the instrument is "cold" (T_i= 253 K, see again Section 2.1.1.1) the improvement is clear. The impacts of dust grains on the walls completely disappear, so that 100% of the large dust grains can be correctly detected by MicroMED's optical system compared to roughly 30% obtained with the Elegant Breadboard design (Figure 2.48).

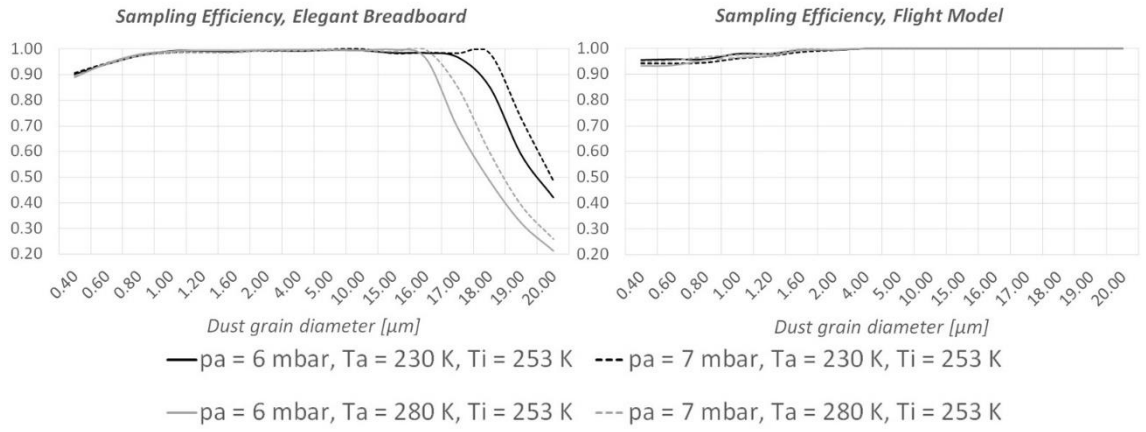

Figure 2.48 Comparison between the sampling efficiencies of MicroMED's Elegant Breadboard and Flight Model for "cold instrument conditions" (Ti = 253 K).

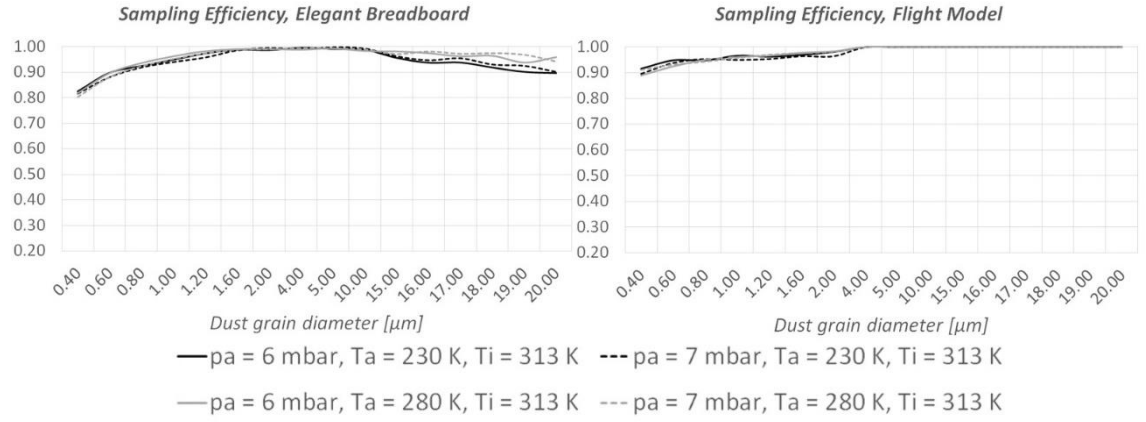

Figure 2.49 Comparison between the sampling efficiencies of MicroMED's Elegant Breadboard and Flight Model for "hot instrument conditions" (Ti = 313 K).

The instrument ability to detect large dust grains was confirmed by tests performed at the INAF - Astronomical Observatory of Capodimonte Laboratory (Cozzolino, F. et al., 2020). In such laboratory, as will be shown in greater detail in Section 3.2.1, a Martian Chamber and a Clean Room are installed, allowing to reproduce Martian conditions in terms of pressure and atmospheric composition, to reduce the amount of atmospheric dust that could alter the measurements and to keep the instrument sterile in accordance to the Planetary Protection constraints. Moreover, the ATS (Autonomous Thermal Simulator, Russo, G. et al., 2020) system installed in the Capodimonte laboratory allowed to perform tests at different instrument temperatures, simulating the possible different conditions foreseen at the lander level during the mission. During such tests, the instrument appeared to show a good ability to detect even large dust grains, the toughest to be detected, as Figure 2.50 shows. The test showed in Figure 2.50 was made injecting in the Martian chamber monodispersed SiO_2 19.7 μm spherical calibrated particles (For test setup, see Section 3.2).

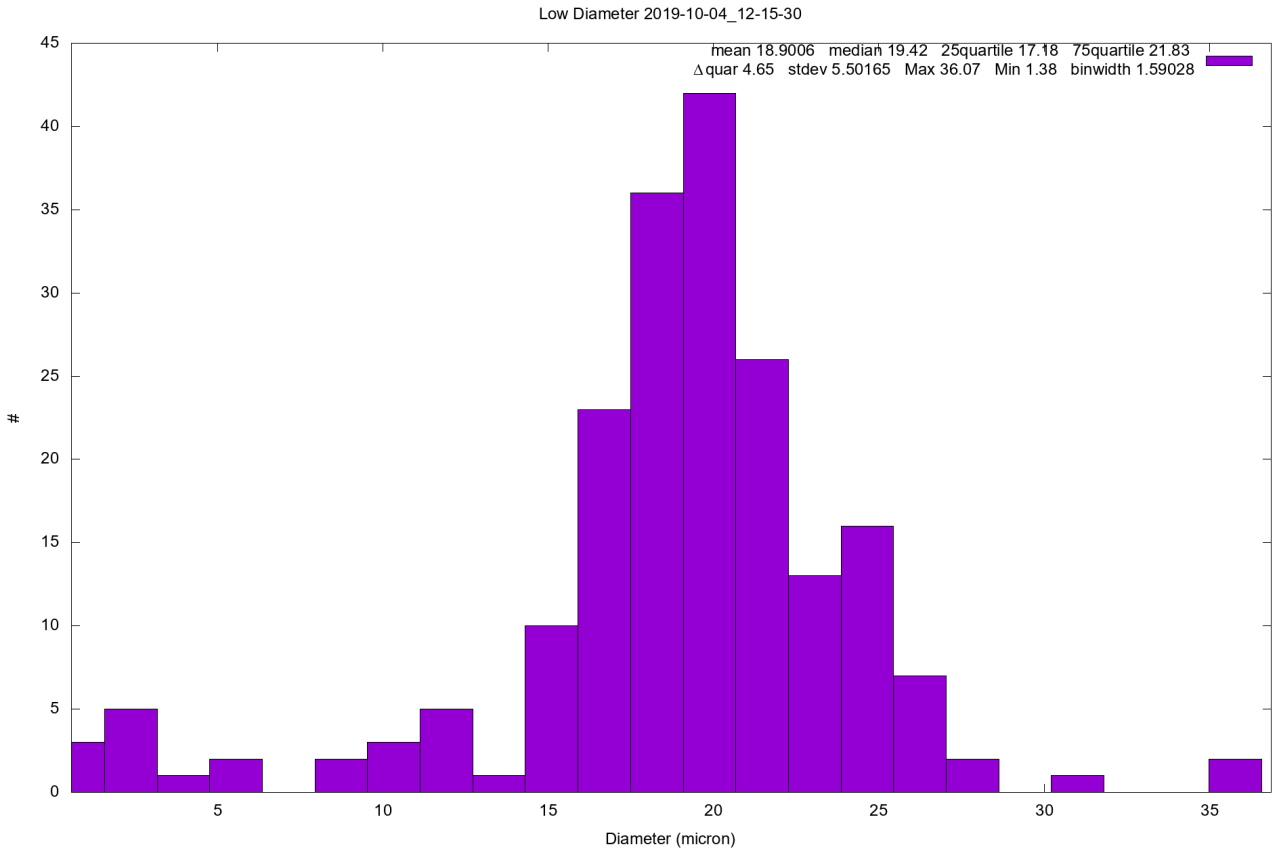

Figure 2.50 Example of test performed at the Capodimonte laboratory injecting 19.7 μm calibrated SiO_2 particles.

2.2.3.2 Dust grains position in the sensing plane and evaluation of dust grain size distribution

Particle trajectories along MicroMED were analyzed in order to understand not only if they cross the laser illuminated spot, but also how far from the center of the spot they do. As already stated, given that laser light is more uniform and intense at the center of the laser spot, errors in the determination of the dust grain size are smaller when particles cross the spot close to the center and grains are easier to be correctly detected. For this reason, position histograms were derived from CFD simulations, determining the quality of the fluid dynamic design. The Elegant Breadboard already guaranteed good results in such aspect and the geometry variations adopted for the new design could potentially make the particles more "spread" through the sensing plane. Indeed, in some cases the streamlines deflection is smoother for the new design, therefore dust grains are more distributed inside the sampling spot rather than more concentrated. The comparison was made for two different working conditions, given that the optimum operating condition for the Elegant Breadboard version is related to an inlet-outlet pressure difference of 300 Pa while the Flight Model already works efficiently at 200 Pa, which was the operating condition considered. Results show that the new design does not alter the chances of a grain to cross the sampling spot in the proximity of the center (roughly 91% of all dust grains inhaled are within 400 μm and

86% are within 350 μm from the center of the spot, numbers pretty close the ones obtained for the Breadboard design, see Figure 2.51). There are some cases where the efficiency for small dust grains could slightly decrease (by less than 3%) because of the dynamics previously described, but the geometry variation provides a definite improvement of the overall percentage of particles that are now detectable. For large dust grains (See Figure 2.48) there is a definite improvement (sampling efficiency 70% higher in some cases as already stated). Moreover, the new design provides efficiency over 89% for all the small grains (diameter < 1 μm) for every possible environmental condition, differently to the Elegant Breadboard that had cases of efficiency dropping below 80%.

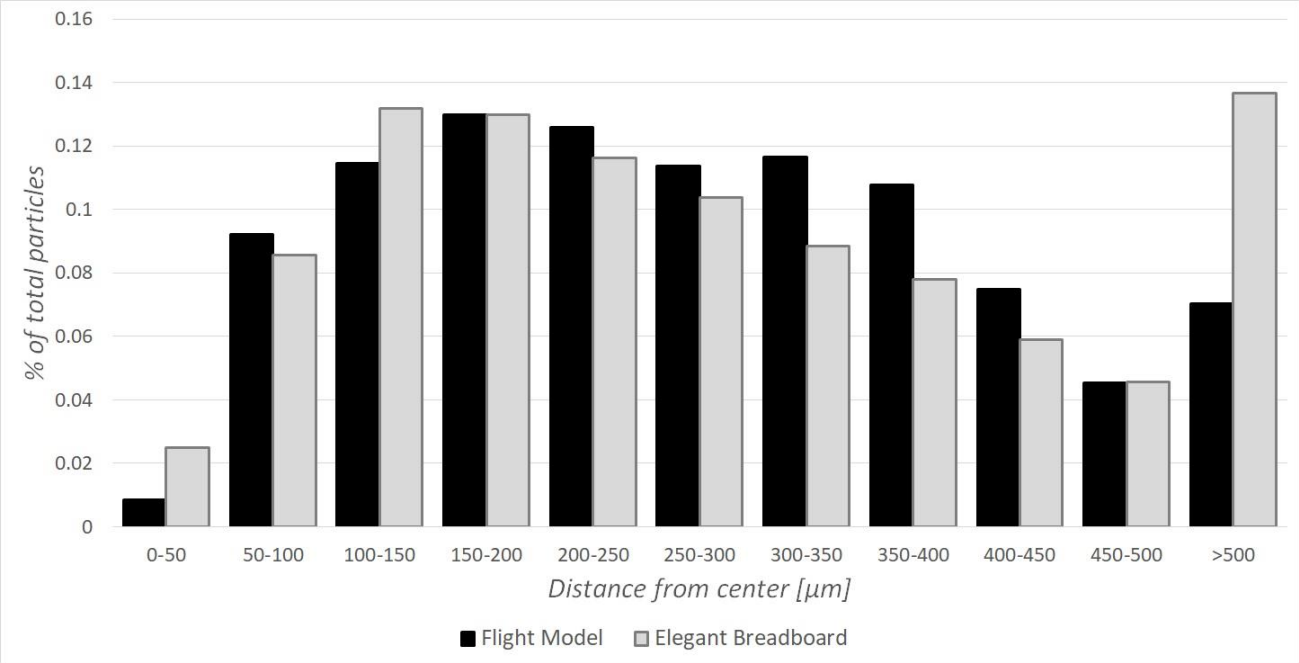

Figure 2.51 Example of position histogram comparing the distance of crossing particles from the center of the laser spot for both the Elegant Breadboard (GREY) and the Flight Model (BLACK) design.

The new design also gave tangible improvements in terms of the instrument's ability to reproduce the input dust grain concentration. Figure 2.52 shows the Flight Model is able to describe the size distribution of the particles inhaled with much better accuracy with respect to the previous design.

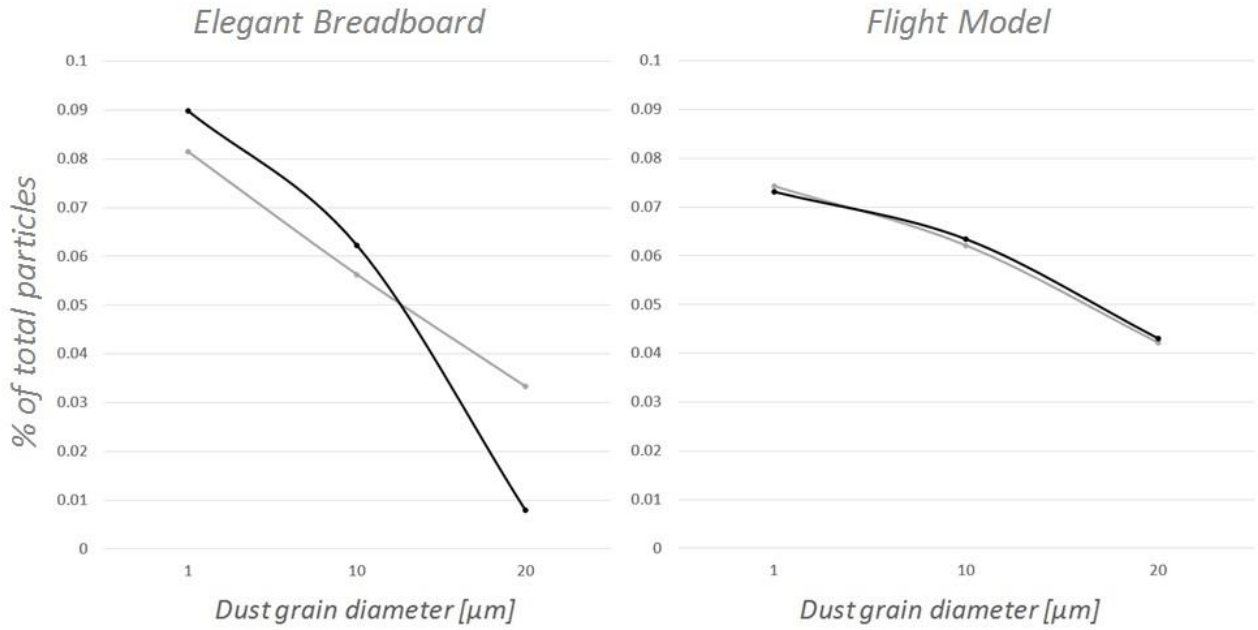

Figure 2.52 Comparison between the Elegant Breadboard's and the Flight Model's ability to correctly deduce size distribution (GREY: real distribution, BLACK: measured distribution).

2.2.3.3 Results in presence of wind

A CFD analysis to predict MicroMED's behavior in windy environments was also performed, given that sustained wind is present in most occurrences on Mars. A CFD model was developed to simulate windy conditions, changing boundary conditions from the traditional CFD model described in Section 2.1.1.2 in order to generate a wind (of set speed) that passes over MicroMED's sampling head. Dust grains could only be simulated as spherical, which is expected to make simulated particles more stable than real particles, so the results obtained could underestimate the instrument ability to detect real particles while in presence of wind (More stable dust grains are less probable to be deflected inside MicroMED). Indeed, while CFD analysis of the Elegant Breadboard stated that MicroMED could be unable to detect dust grains starting from a wind speed of 2 m/s, a test campaign performed at AWTS II facility at Aarhus University in Aarhus, Denmark (Holstein-Rathlou, C. et al., 2014) showed that small dust grains are well detected, while the detection of large dust grains is related to a threshold value. For every size, there is a threshold value of wind speed after which MicroMED is unable to detect grains of such size: the larger the size of dust grains, the smaller the speed threshold value. Preliminary results of such test campaign seem to show that the instrument was able to see dust grains for wind speeds up to ~ 7 m/s. Such results have already been discussed in Section 2.1.3.9. A detailed description of the results obtained at the AWTS II facility is instead provided in Section 3.2.5.1.

Results of CFD simulations on the Flight Model's geometry, compared with those on the Elegant Breadboard, showed clear improvements in the ability to detect small dust grains and a moderate improvement in the ability to detect larger grains. Figure 2.53 shows a

comparison between the two analyzed geometries, highlighting the better overall efficiency obtained. According to CFD analysis, though, efficiency is still low. However, tests at the AWTS were also performed on MicroMED's Flight Model and preliminary results show the improvement was probably bigger than what predicted by the CFD. It was found that MicroMED's updated design not only improves the instrument's efficiency in the detection of large dust grains but it also provides good efficiency. As Figure 2.54 shows, MicroMED was able to detect 20 μm diameter particles even at the highest possible wind speed for the facility (15 m/s), which confirms that the CFD model is conservative and that MicroMED's Flight Model better detects dust grains also in presence of wind. Since the analysis of the measured signals is still ongoing, the figure reports data in terms of signal intensity (as measured by the instrument's detector) and not in size. However, the run relative to such figure was performed injecting only 20.07 μm calibrated spherical particles with a wind speed of 15 m/s. The figure was still reported to show hundreds of samples can be obtained in such tests. Such results confirm that the CFD model should be improved to predict MicroMED's behavior in windy conditions with better accuracy. Moreover, the Flight Model's ability to work properly with lower pump rpm speeds could help as it could be possible to increase the pump speed if necessary. The analysis of data obtained in such test campaign (plenty of tests were performed with 10 different monodispersed spherical sizes and with JSC-1 non-spherical Martian simulant, as well as tests with other broad distribution samples), however, are still preliminary, therefore they are only mentioned in this work.

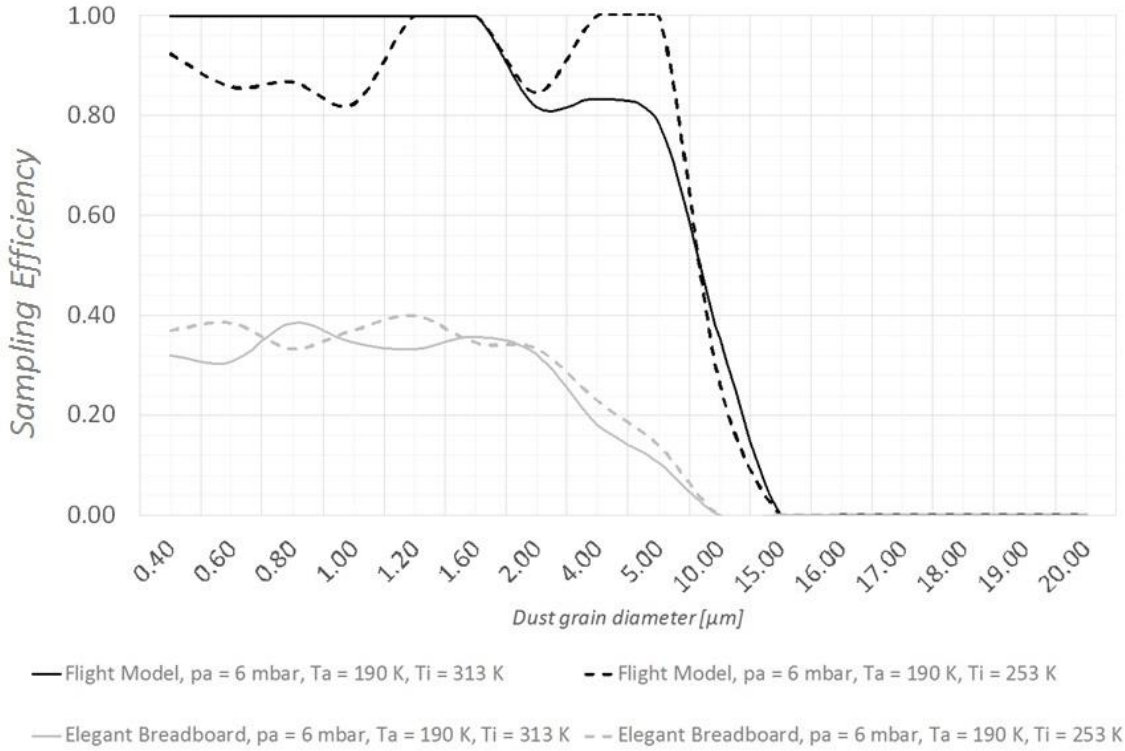

Figure 2.53 Comparison between Flight Model and Elegant Breadboard in terms of sampling efficiency, wind speed 2 m/s.

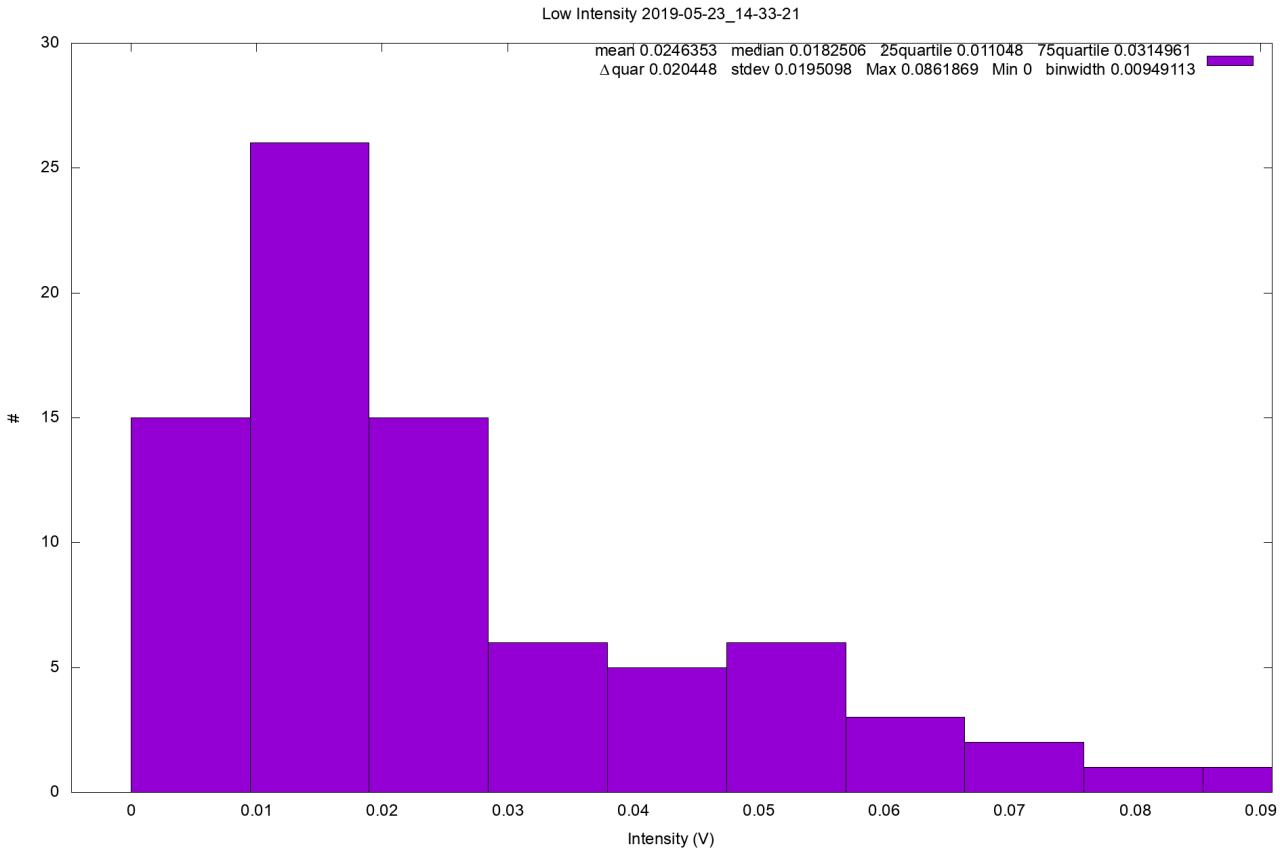

Figure 2.54 Example of test performed at AWTS in Aarhus, Denmark. The plot is reported in terms of signal intensity as the analysis is not ready, however tests were performed with 20.07 μm particles only.

2.2.3.4 Brief summary of the results obtained from MicroMED's FM CFD analysis

MicroMED's Flight Model design was designed as a result of a CFD simulation campaign aimed at the improvement of the instrument ability to detect dust grains, especially large ones (15-20 μm in diameter), in every possible environmental condition the instrument could face during the ExoMars 2022 mission. This is important since the actual operating conditions of the instrument while on Mars vary with time. The analysis shows that the updated fluid dynamic design improves the detection efficiency of dust grains. The key result is a huge improvement in the ability to suck and detect large dust grains, avoiding hits on the walls and obtaining more accurate results in the measurement of size distribution curves for the samples. Optimum operating conditions can be obtained for an extended range of Δp generated by the pump, which allows more flexibility in the choice of operating conditions in relation to the environment. The analysis results were confirmed by tests performed at the Astronomical Observatory's Laboratory in Naples, Italy, where abundant samples of large dust grains were detected by the instrument. The analysis was also extended to windy operating conditions. The model showed to be extremely conservative in predicting the outcome of tests. However, CFD results predicted an efficiency improvement which was confirmed by tests performed at the AWTS II facility in Aarhus, Denmark. Indeed, tests

showed that MicroMED's Flight Model is able to detect significant amounts of large dust grains even at high wind speed (speeds until 15 m/s were tested), confirming that an improvement was obtained, as predicted by the CFD model.

3.Integration, test and qualification phases of the MicroMED OPC

After the completion of the design phase, MicroMED's Proto Flight Model (PFM) and Flight Spare (FS) were integrated. The integration had to follow a detailed procedure and it had to be compliant with the constraints related to the European standards for space activities, set by the European Cooperation for Space Standardization (ECSS). The following section will describe the procedure adopted for integration, as well as the consequent phase of tests performed to verify MicroMED's functionality and performance. Tests comprehended both functional tests, aimed at verifying the functionality of MicroMED's subsystems, and performance tests, whose purpose was instead to verify the quality of MicroMED's scientific retrieval.

After such verification, MicroMED was then space qualified by means of Vibrational and Thermal Vacuum test procedures. Finally, the instrument was calibrated using both monodisperse and polydisperse samples of dust grains, providing a calibration curve needed for the correct interpretation of MicroMED signals.

This section will also provide detailed information about the integration, test and qualification procedures, the documentation produced to cover the activities and to satisfy the requirements of the European standards. As a part of my Ph.D. work, I had an extended role in all of these phases.

3.1MicroMED's Flight Model integration

MicroMED's Flight Model version has been integrated in 2019, after the conclusion of the design phase).

MicroMED's assembly starts from the integration of its subassemblies, whose list is provided hereafter:

- Group 000: Optical bench, shielding box, optical head and electronics supports;
- Group 100: Pumping system;
- Group 210: Fiber-volume optomechanical system
- Group 300: Laser-fiber optomechanical system
- Group 010: Detector assembly;
- Group 020: Inlet and outlet group
- Group 040: Light trap and reference detector;

Every mechanical part was washed and sterilized before integration, in accordance with planetary protection constraints, which are ruled by the ECSS. Standard washing procedure for mechanical parts foresees cleaning with isopropyl alcohol, but some elements have been sterilized by means of a dry heat procedure in an oven. After such procedure, the components have been always handled with clean tools and with hands protected by nitrile sterile gloves. All the assembly procedure was carried out in a class 100(ISO 5) clean room, while the tests have been conducted in class 10000 (ISO 7).

During this first phase, calibrated tightening torques have been used. Subsystems have been assembled and all screws have been fixed with Nusil CV-1144-0 before mechanical testing. Group 300, which includes the laser and the lenses that convey the emitted light toward the optical fiber (See Section 1.2.5), and Group 210, which receives light from the optical fiber and conveys it toward the sensing region of the instrument, have been assembled and optically aligned, in order to optimize the output optical power. After alignment, the groups have been integrated on the Optical Head, the main box of the instrument.

Successive phases include the integration of the Optical Bench and of the electronics.

Figure 3.55 (a-c) shows some details of the successive phases of the integration as well as the completed instrument.

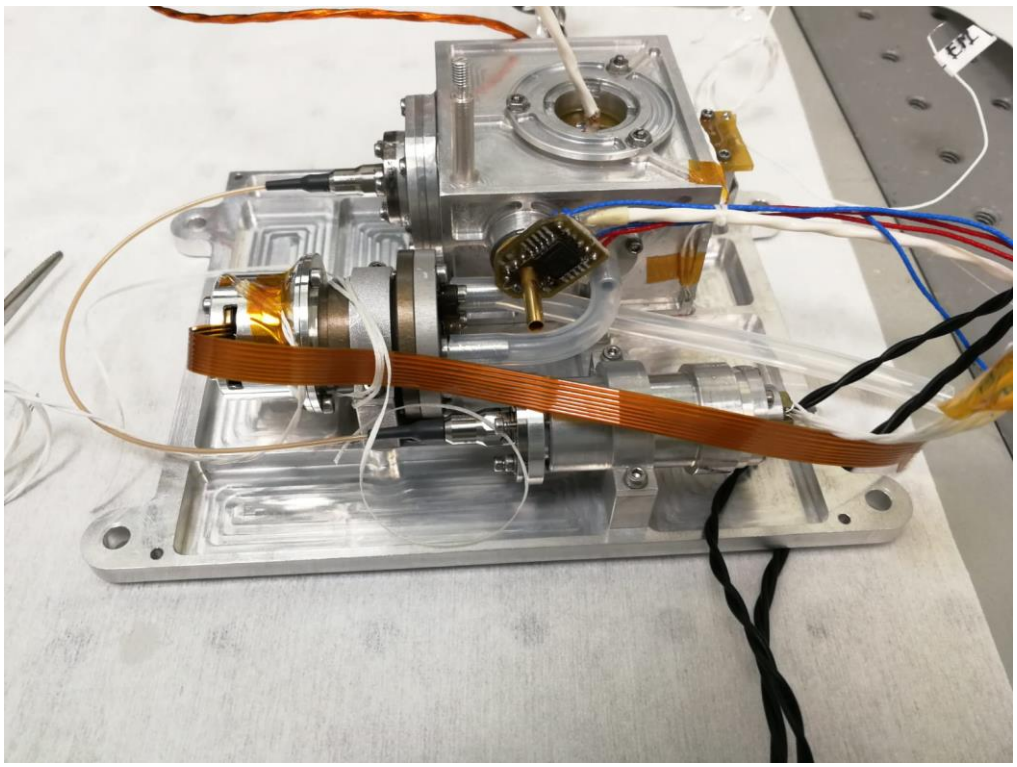

(a)

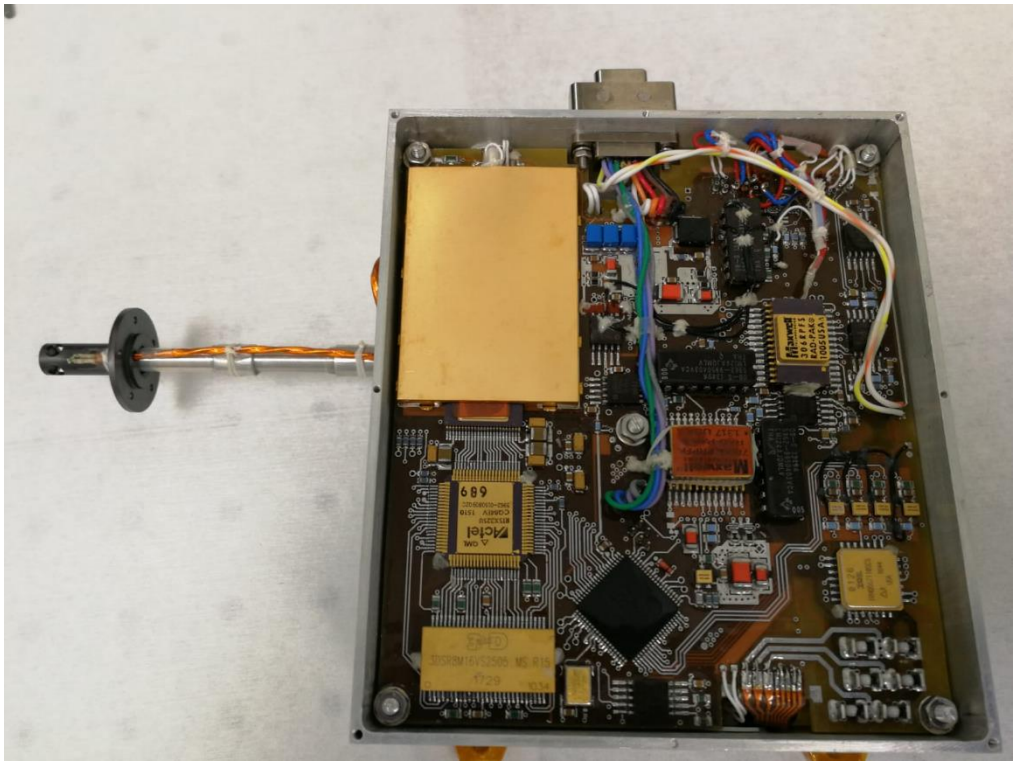

(b)

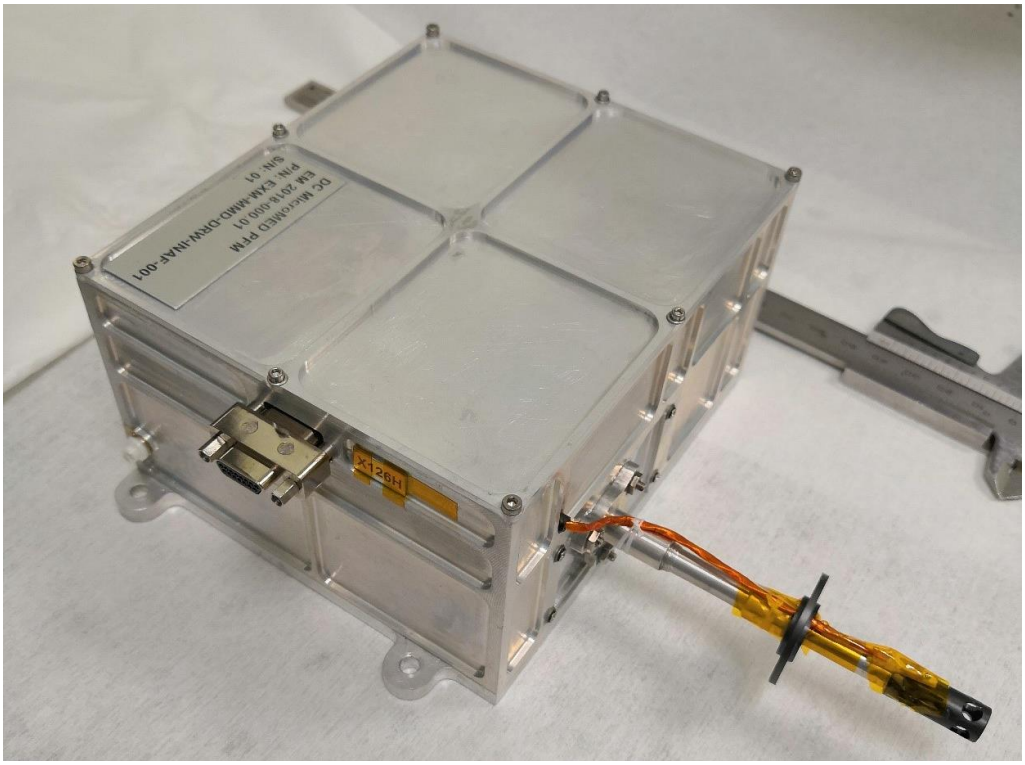

(c)

Figure 3.55 MicroMED after integration of the subassemblies (a), after integration of the electronics (b), after the completion of the integration phase.

3.2 Functional and performance tests on MicroMED

After integration, an intensive campaign of functional and performance tests has been performed on MicroMED to verify both the correct functionality of the instrument and the quality of its performances. The following section will provide an overview of the facility in which tests have been performed, the methodology used for tests and the main results, that verified that MicroMED is well able to perform at the required level of performance.

3.2.1 INAF – OAC premises

At the INAF – Osservatorio Astronomico di Capodimonte (OAC) premises in Capodimonte, Naples, Italy, a Martian Chamber has been installed, able to reproduce Martian conditions in terms of atmospheric pressure, composition, instrument temperature and dust presence (Cozzolino, F. et al., 2020). Such chamber (Figure 3.56) contains a custom dust injection system that is able to provide a localized dust distribution with no aggregations for a correct calibration of the instrument. Such chamber is contained into a Clean Room that allowed testing in sterile conditions, conformingly with the Planetary Protection constraints.

The tests performed aim at simulating the data acquisition of MicroMED under Martian conditions. An atmosphere 95% of CO_2 (number of moles) has been prepared inside the chamber. In order to create this condition, the chamber, which before the tests is filled with air at atmospheric pressure, has been brought to a pressure of 1 mbar with the aid of a vacuum pump and then filled with CO_2 until a pressure ~ 6-7 mbar was reached.

This pressure range is indeed the near surface condition expected during operations on Mars. The temperature condition will be set and controlled using a custom system named Autonomous Thermal Simulator or ATS (Russo, G. et al., 2020) and has been changed in accordance with the requirements of each specific test.

Figure 3.56 Martian Chamber at the INAF – OAC premises in Capodimonte.

3.2.1.1 Equipment needed for the tests and preparation of the samples

Tests at OACN premises required a number of tools and instrumentation devices for their correct execution. A key aspect of the test has been the preparation of the sample. Calibrated SiO_2 grains, produced by Microparticles ®, have been used. Grains have been weighed by means of a microbalance and hosted inside glass test tubes. In such tubes, they have been sterilized inside an oven at 190°C for at least eight minutes, in accordance with the imposed sterilization procedures.

After the sterilization, the samples have been sometimes put in solution with ethanol and hosted inside sterilized polypropylene test tubes. This procedure is aimed at avoiding the formation of aggregates of dust. Ethanol indeed helps avoiding the formation of such aggregates and, once the solution is sprayed into the chamber, the extremely low pressure of the Martian chamber would cause an immediate evaporation of the ethanol, leaving the single dust grains in suspension into the chamber and separated one from the other. Before the test, however, a pulsing vortex mixer has been used to break the aggregates already present in the samples and avoid their further formation. It has to be underlined that the formation of aggregates has to be avoided since it would result into an alteration of the test result, as grains would appear not as single grains (of calibrated diameter) but as a larger grain.

3.2.1.2 Vacuum System

The Martian simulation chamber is a vacuum chamber (See Figure 3.56), based on a cylindrical stainless-steel vessel, 1300 mm in diameter and 2296 mm in length made by Trinos Vacuum ®. An A100L Pfeiffer Vacuum ® pump has been used to pressurize the chamber. The pump (Figure 3.57 (b)) with its chiller system (Figure 3.57 (c)) is placed outside the clean room, powered at 230 V. The hydraulic connection pump-chamber is regulated by a manual valve gate (Figure 3.57 (a)); the gate is opened to pressurize the chamber before the tests and to expel the CO_2 atmosphere after the measurement, through a discharge pipe connected to the pump itself.

After the CO_2 expulsion, a second valve that connects the chamber to the clean room is opened for the depressurization of the chamber. Ambient pressure inside the chamber is measured using a Pfeiffer Vacuum ® capacitance gauge installed on one of the chamber flanges, and displayed on a monitor.

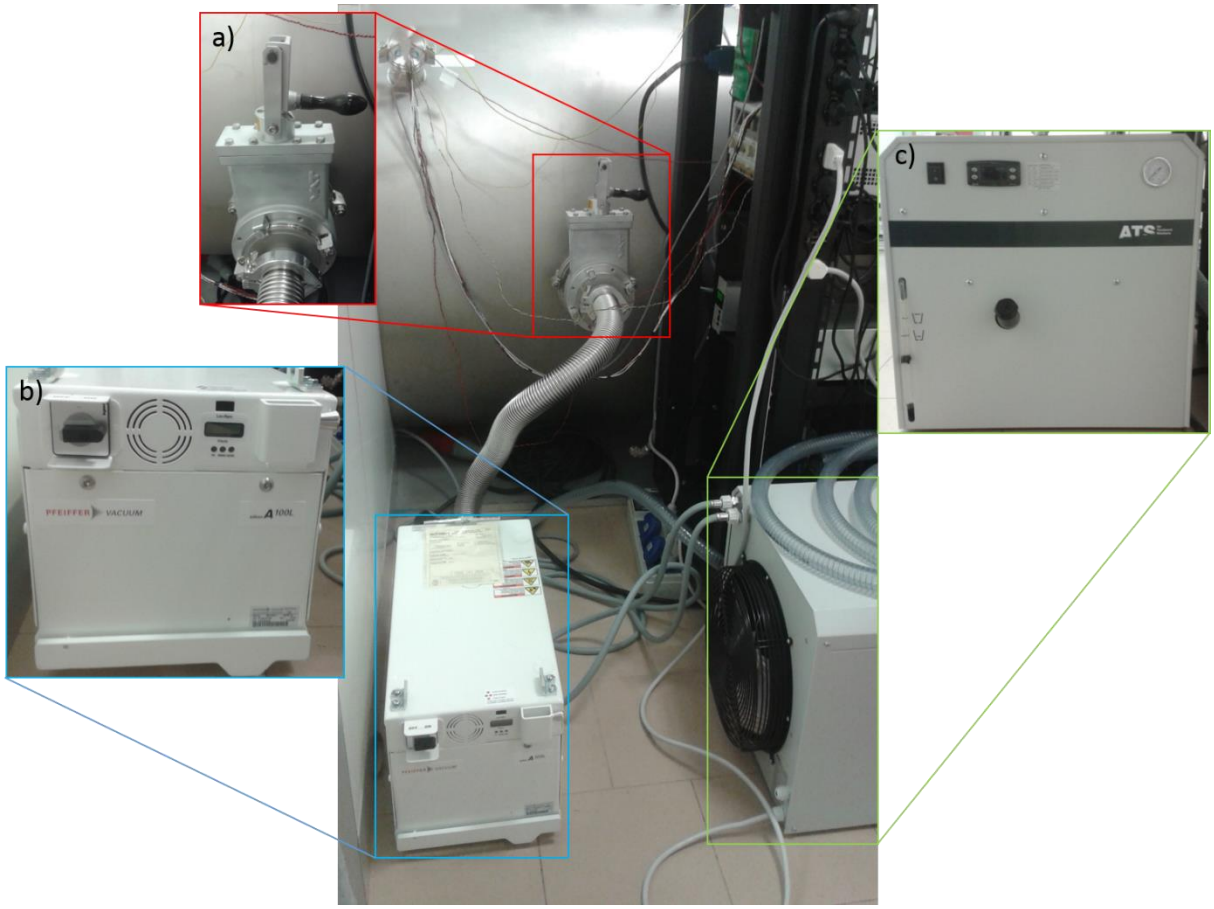

Figure 3.57 Side view of the vacuum chamber. From this angle it is possible to see the gate valve used for depressurization (a), the vacuum pump (b) and its chiller system (c).

3.2.1.3 Thermal environment management

MicroMED has been hosted inside a custom thermal chamber to check its acquisition performances at different temperature. The thermal chamber system has been developed by

the Trans-Tech ®, in accordance with the specific requirement of MicroMED in terms of size and shape, electronic connections and range of operation.

The system consists of:

- A controller with the electronics;
- A chiller system placed outside of the vacuum chamber;
- A thermal box (Figure 3.58) placed inside.

The internal and the external components are connected by cables and hydraulic pipes passing through a flange of the chamber. The whole system can be set and monitored using a specific software on a computer.

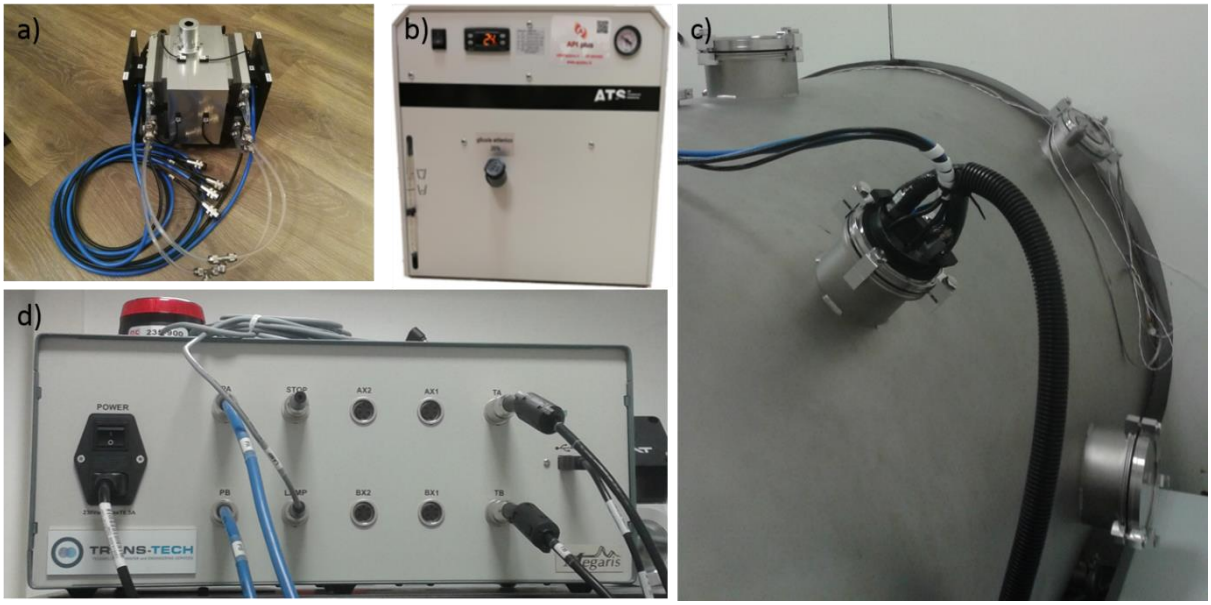

Figure 3.58 The Autonomous Thermal Simulator system, used for MicroMED's thermal regulation: a) Thermal box; b) Chiller system; c) Flange on the vacuum chamber side for the cables passage; d) Control box.

3.2.1.4 Dust Injection system

An injection system has been realized, capable of injecting a flow of thousands of separated grains inside the chamber. The injection system has been developed and improved through several intermediate steps, before obtaining the desired performance. The following section will describe the dry, wet and updated dry injection systems. Before the start of my Ph.D. work the original dry injection system was used; however, during my Ph.D. work I have actively contributed to the conception, the development and the characterization of the two following injection methods. It has to be underlined that the realization of an injection system under terrestrial gravity is actually tough, since the stronger gravity should fasten the deposition of grains, reducing their availability to MicroMED. However, tests have shown that such injection systems are able to provide MicroMED a good amount of grains.

3.2.1.4.1 Dry Injection System

The first version of the injection system was made up of a holder containing dry particles, connected to the chamber through a gate valve. When the valve was opened, the pressure difference between the holder (ambient pressure) and the chamber (1 mbar) triggered the aspiration of the particles into the chamber. Tests with this type of injection indicated a couple of issues:

- The flux of particles is focused in a very restricted area inside the chamber, so it was not possible to reproduce a uniform distribution inside the chamber itself;
- The formation of groups of aggregated particles, that as well known represents a critical issue for the calibration of MicroMED.

In order to verify the reliability of the system, several tests have been performed. To monitor the distribution of grains inside the chamber, several aluminium stubs have been deployed on its base as shown in Figure 3.59. Each stub was covered with an adhesive carbon disc on which the injected particles could sediment. All carbon discs were then analyzed with a Zeiss ® Scanning Electronic Microscope (SEM). Some of the observed samples with the respective aggregates are shown in Figure 3.60 (a, single aggregate and b, multiple aggregates).

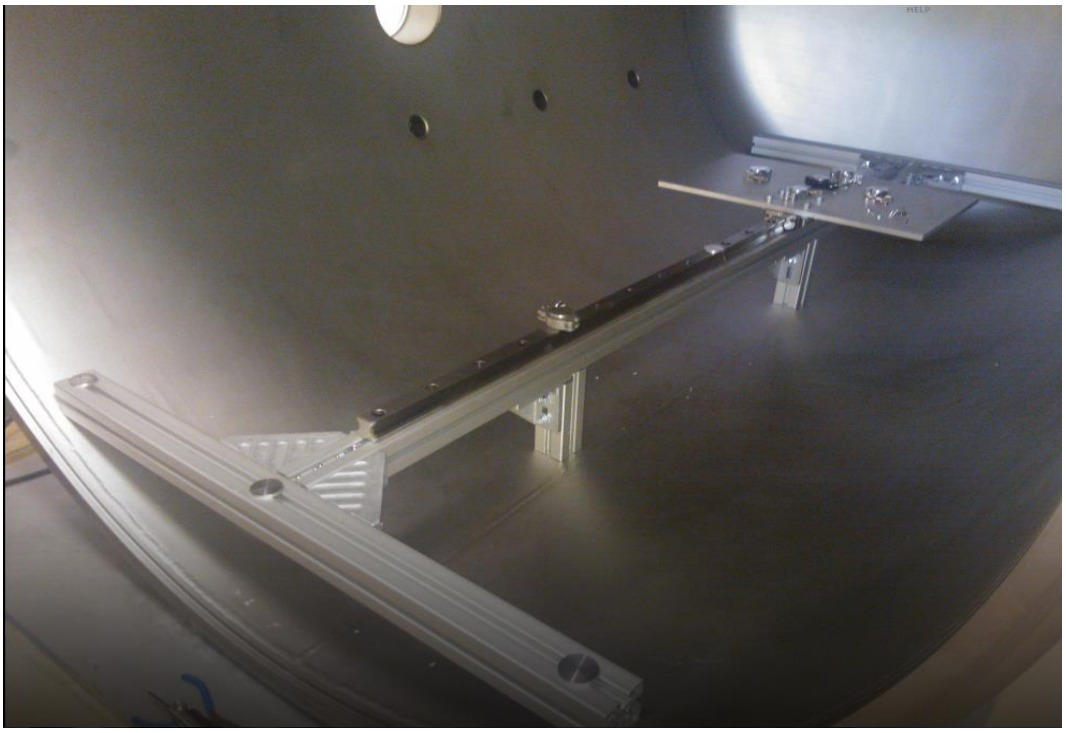

Figure 3.59 Experimental setup made of aluminum stubs provided with carbon discs for the verification of the particles distribution inside the Martian chamber.

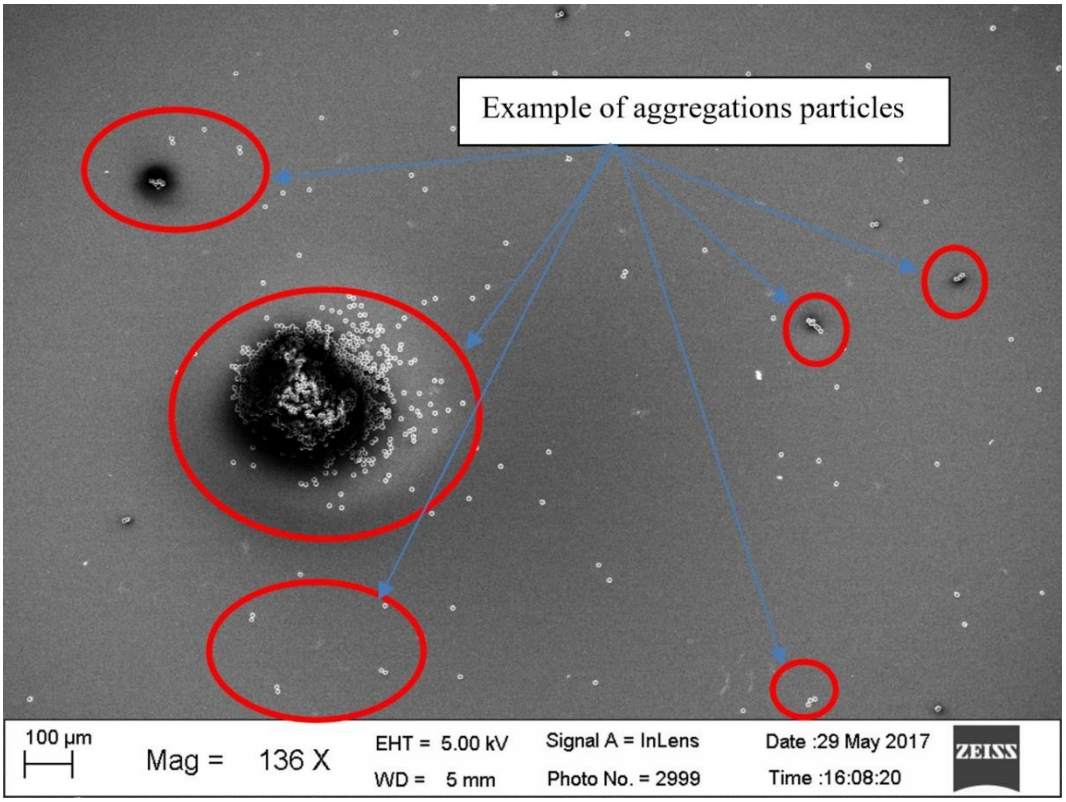

Figure 3.60 Evidence of particles aggregation in the chamber after injection of dry particles. Details of SEM. Parameters: Mag = Magnification, WD = Work Distance, EHT = Power Supply of Gun, Scale Bar = 100 µm.

3.2.1.4.2 Wet Injection System

In order to solve the problem of the particle aggregates presented in the Dry Injection System, a different injection system has been developed, using grains embedded in solution with ethanol. The sample is prepared in a glass test tube, removing the internal residues with compressed air. A microbalance is used to weight the amount of grains needed for the sample, then such grains are put into the glass tube, placed inside an oven at ~ 200 °C for at least eight minutes to sterilize the sample and finally mixed with ethanol inside the glass test tube in order to transfer its contents to the sterilized test tube, where this injectable solution is preserved until the execution of the test. Before the tests, the solution is put into an ultrasonic bath (Transsonic ®) for 30 minutes to prevent the formation of aggregates and the deposition of the grains in the lower portion of the test tube.

The system is shown in Figure 3.61 and it is constituted by a dispenser (Grimm Aerosol Dispensers mod 7811, see Figure 3.62, a second vacuum cylindrical chamber (called "pre-chamber"), considerably smaller than the Martian vacuum chamber, and a gate valve. The first version of aerosol generator used in this system is shown in Figure 3.10. It nebulizes a solution of water and particles to be injected into the pre-chamber. The nebulization process

consists in the reduction of a liquid in very small parts (droplets), which is obtained, for example, by colliding the liquid with a jet of air at high speed, or forcing the liquid to pass through a very narrow orifice. Before the nebulization, the solution is placed in an ultrasonic chamber in order to well separate the embedded grains. The Nebulizer flow rate is adjustable. The maximum flow rate is 7 l/min and can be obtained in atmospheric pressure conditions (1 atm).

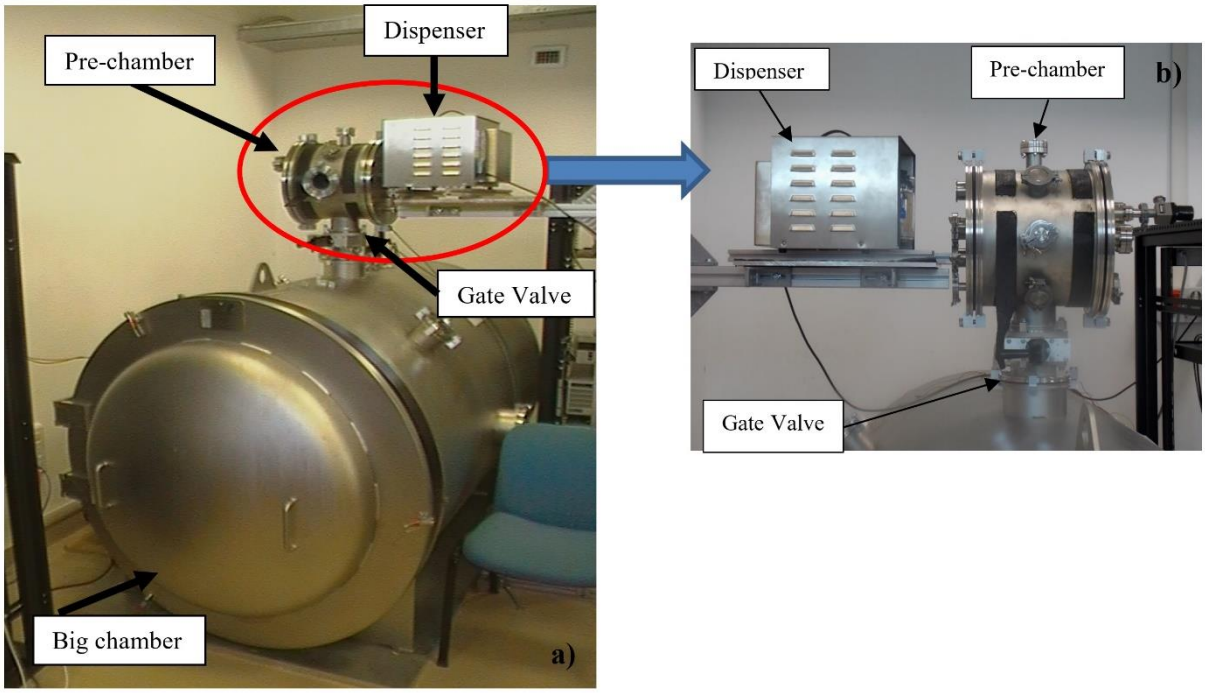

Figure 3.61 Martian Simulation chamber. a) The complete system; b) "Wet" injection system.

As for the pre-chamber, its dimensions are 30 cm in diameter and 25 cm in height. The injection system is connected to the top of the first chamber (Figure 3.61 (a)). Between the second and the first chamber there is a gate valve (Figure 3.61 (b)) which is operated by hand. The pre-chamber is needed with the original wet injection system, the one using the particle generator (Figure 3.62).

Such nebulization system has then been upgraded; the particle generator has been eliminated and the nebulizer has been placed inside the chamber and in proximity of MicroMED (Figure 3.63). The upgrade was needed because the original wet injection system, that makes use of the dispenser, has a limitation in terms of environmental conditions, as it can only work at a pressure of 1 atm. This means that when the gate valve between the pre-chamber and the simulation chamber is opened, the strong pressure difference causes the particles to acquire a very high speed, hence to bounce on the chamber basement and walls before being sampled by MicroMED. This causes a large dispersion and loss of particles. To improve this aspect, the particle injection system has been simplified in order to control the

input velocity of the particles in the simulation chamber. As shown in Figure 3.63 and as already mentioned, the Grimm ® dispenser was removed and the nebulizer was placed inside the Martian chamber and in proximity of MicroMED's sampling head. Such nebulizer is filled with the solution of ethanol and dust grains and it is directly connected with a CO_2 tank, so that, once the tank is opened, the flow of CO_2 inside the nebulizer generates bubbles and causes the expulsion of droplets of the solution in the chamber. As already underlined, ethanol immediately evaporates once it is introduced in the low pressure environment (~ 6 mbar) of the Martian chamber, so dust grains are dried and remain in suspension in the area surrounding the nebulizer, which includes MicroMED. Several measurements have been performed by injecting only ethanol to understand if the droplets that are generated could somehow be sampled by MicroMED, altering the measurement. Test results have showed that MicroMED does not reveal the presence of ethanol inside the instrument.

This configuration allows to control the pressure gap between the two chambers, as well as the particle velocity and has proved to be efficient in providing MicroMED a realistic and uniform distribution of grains around the instrument.

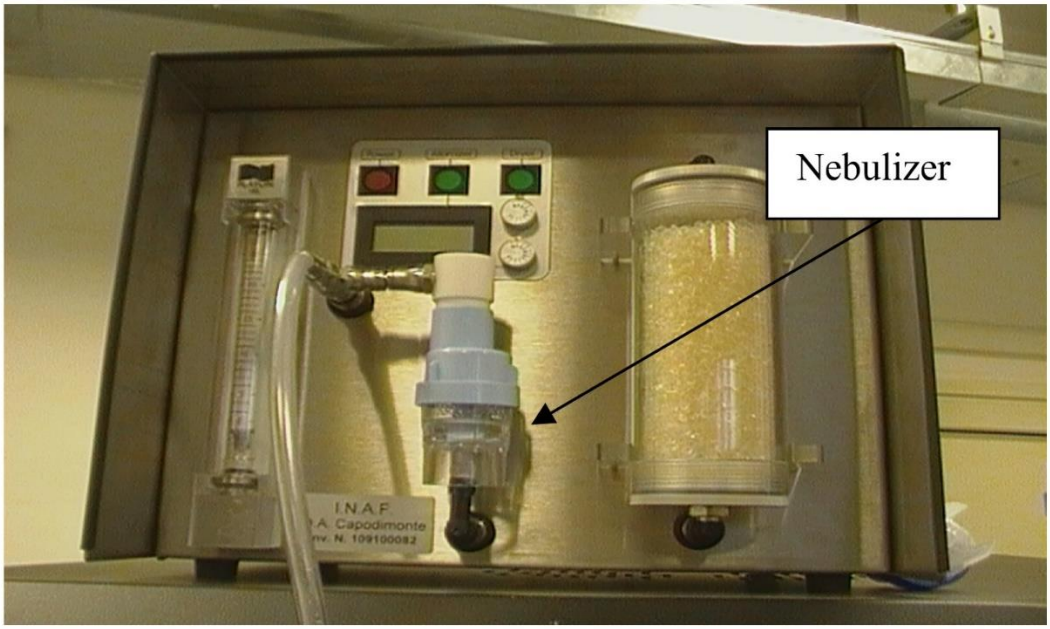

Figure 3.62 Particle Generator Model 7811.

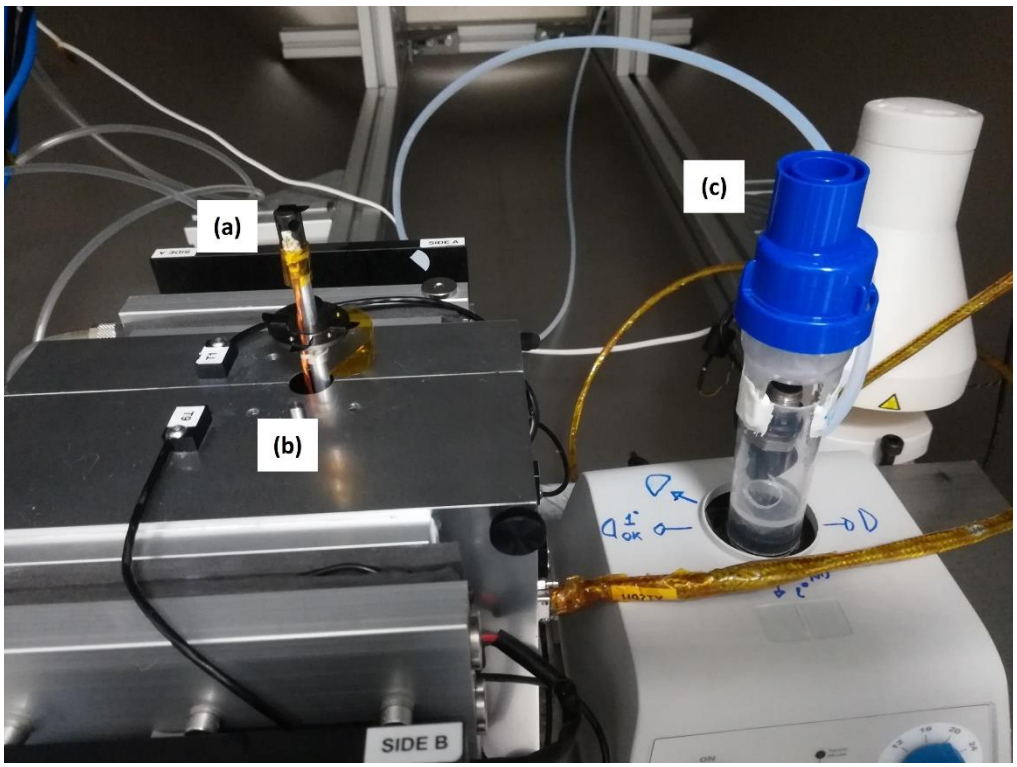

Figure 3.63 Upgraded nebulization system placed in proximity of MicroMED. The nebulizer (c) is close to MicroMED's sampling head (a). MicroMED is contained in the ATS's thermal box (b).

With the upgraded version (Figure 3.63), the injection is performed by opening a gate valve on the outside of the Martian chamber, connecting the nebulizer with the CO_2 tank. The flux of CO_2 is actually split through a T junction and delivered to two different flanges of the vacuum chamber. The pipe that connects the canister to the nebulizer passes through a flange, with a valve able to regulate the flux, and it is used to nebulize the sample. A second flange delivers the gas inside the vacuum chamber to reproduce Martian atmospheric conditions.

3.2.1.4.3 Upgraded dry injection system

The upgraded wet injection system described above can also be used with dry particles. The presence of nebulizer allows to avoid the formation of aggregates in co-operation with a pulsing vortex mixer, installed underneath the nebulizer. Just before injection, the pulsing vortex mixer is switched off to avoid interference with the injection process. Such system has been able to provide large samples of grains in the surroundings of MicroMED and has therefore been used for most of the tests whose results are reported in the later sections of this work.

3.2.1.5 Verification of the experimental dust injection systems by means of particle spatial distribution measurement inside the Martian simulation chamber

Once the Simulator Chamber was implemented, a series of measurements were carried out to verify the functionality of the injection system and the spatial distribution of the particles in the simulation chamber. The verification described hereafter is relative to the first wet injection system, but the same verification has been performed with good results for the upgraded injection systems.

Aluminum stubs have been positioned as mentioned above (Figure 3.59). The injection system generates an aerosol of particles that in the first version of the wet injection system is distributed inside the pre-chamber, in the later versions directly into the main Martian chamber. As already explained, when the gate of the pre-chamber is opened, the pressure difference between the simulation chamber (1 mbar) and pre-chamber (1 atm) causes a suction toward the simulation chamber, with consequent high speed flow. The particles bounce on the bottom of the chamber and are spread. Once the equilibrium condition of 6 mbar is reached, the bounced particles deposit for gravity on the discs positioned at the base of the chamber. At the end of the settling process the disks are analyzed with the SEM.

The disks have been numbered, each corresponding to a precise position within the chamber. In particular, the disks 3, 4, and 5 have been positioned at the gate valve which represents the entry of the particles in the simulation chamber. The disks 1, 2 and 6 have been positioned respectively at one meter from the disk 3, at 0.7 meters from disk 3 and 0.15 cm from disk 5.

The test was performed using monodispersed particles with size 0.5, 1.30, 2.8, 4.32, 6.36, 8.43, 11, 14.98 μm. The same set of particles has also been used during the calibration of MicroMED (even though they are only a part of the samples considered). From the analysis of the stubs to the SEM it is clear that injecting the particles with this system avoids the formation of the aggregates of particles that were present with the original dry injection system (Figure 3.64) The results about distribution particles inside the Martian chamber are shown in Figure 3.65, where the trend of the numerical density of the particles as a function of the position of the disks, for each used particle size, is shown.

The plots show that the “wet” injection is able to spread well the dust grains into the simulation chamber on the whole size range considered. The smaller particles tend to disperse more, distributing almost uniformly throughout the chamber, while the larger diameter particles tend to be distributed in the region corresponding to their entrance area (the area under the gate valve).

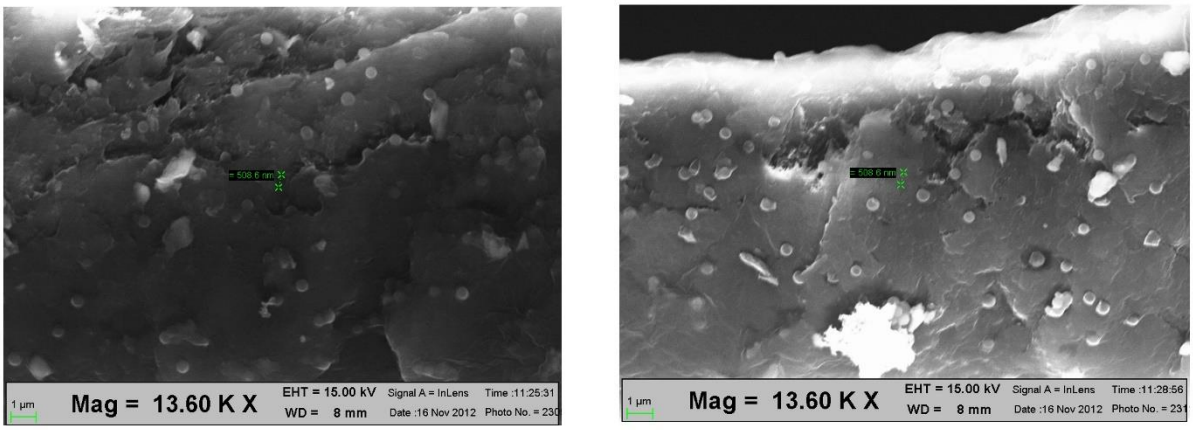

Figure 3.64 Image taken from the SEM analysis of samples taken during the verification of the dust injection setup. It can be observed that there is an overall absence of aggregates using the original Wet Injection System. The two images are relative to disk 3 (on the right) and disk 5 (on the left). The green marker shows the size of particles, which is 508.6 nm in this example image. Similar results have been obtained for the upgraded wet and for the upgraded dry injection systems.

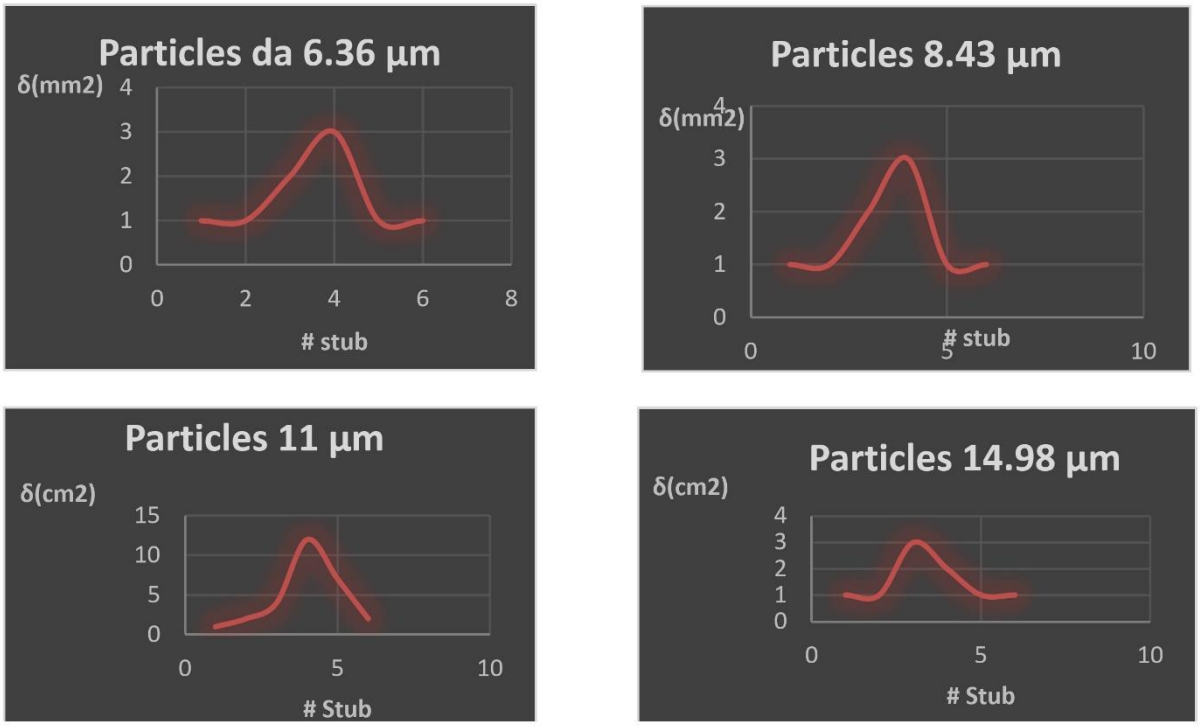

Figure 3.65 Particle distribution according to the position of the sampling discs positioned in the simulation chamber. Y-axis shows the density value, while x-axis indicates the position (i.e. the number, as indicated in the section above) of the discs.

Such tests verify that the wet injection system is an improvement with respect to the original dry system; however, the upgraded dry injection system has provided similar results and has been used diffusively during the various MicroMED's test sessions.

3.2.1.6 The Concentration Measurement System (CMS) and the methods used for the determination of dust concentration in the chamber

In order to estimate the dust grain concentration inside the Martian chamber, the Concentration Measurement System (CMS) has been developed. Such system has been installed inside the Martian chamber to provide a reference value of suspended grain concentration during the runs of data acquisition with the MicroMED sensor. The system is composed by an aluminum cone (Figure 3.66) connected on its edge to the Gardner Denver Thomas® pump. A PTFE filter is placed inside the cone and transversely to the air flux, hosted on a porous brass support. The support allows the free passage of the particles inside the MicroMED sensible range, while the filter blocks all the grains of diameter greater than 0.2 μm. As part of my Ph.D. work, one of my responsibilities was to conceive and design such system, which has been developed following an analysis aimed at providing a good practical result.

After each run of acquisition, the filter has been removed and analyzed by means of SEM, to count the number of grains collected. Figure 3.67 shows an example of image taken from such SEM scans.

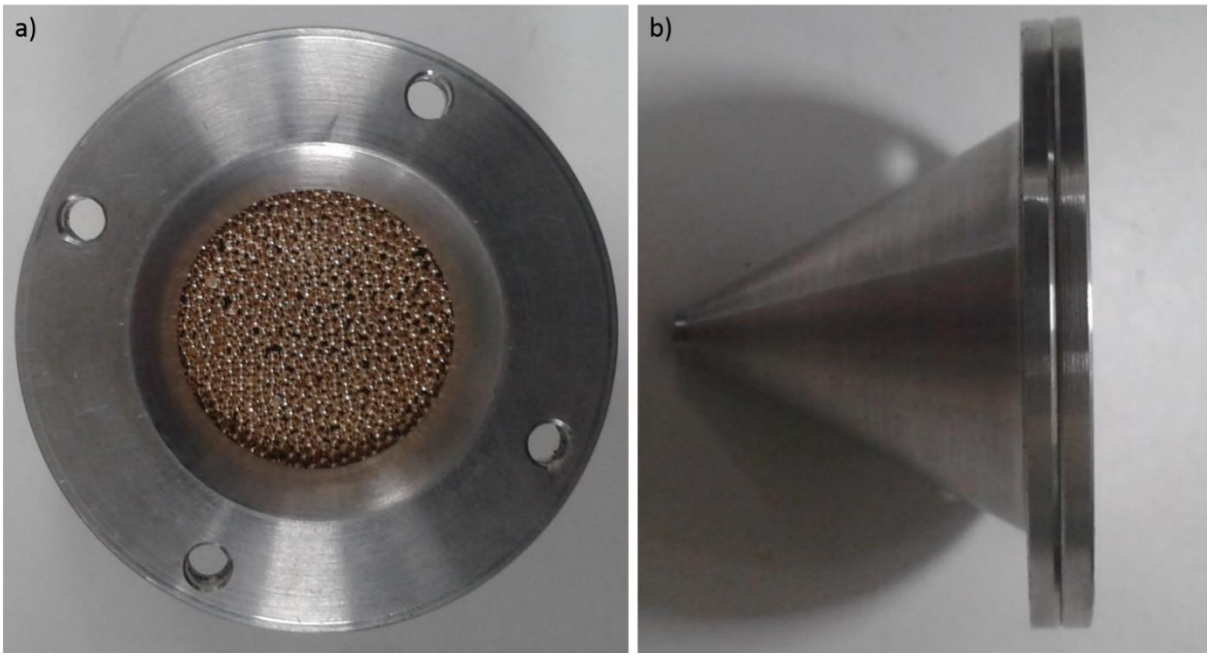

Figure 3.66 The frontal (a) and lateral (b) views of the CMS system. In a) it is possible to see the porous brass support which the PTFE filter is positioned on.

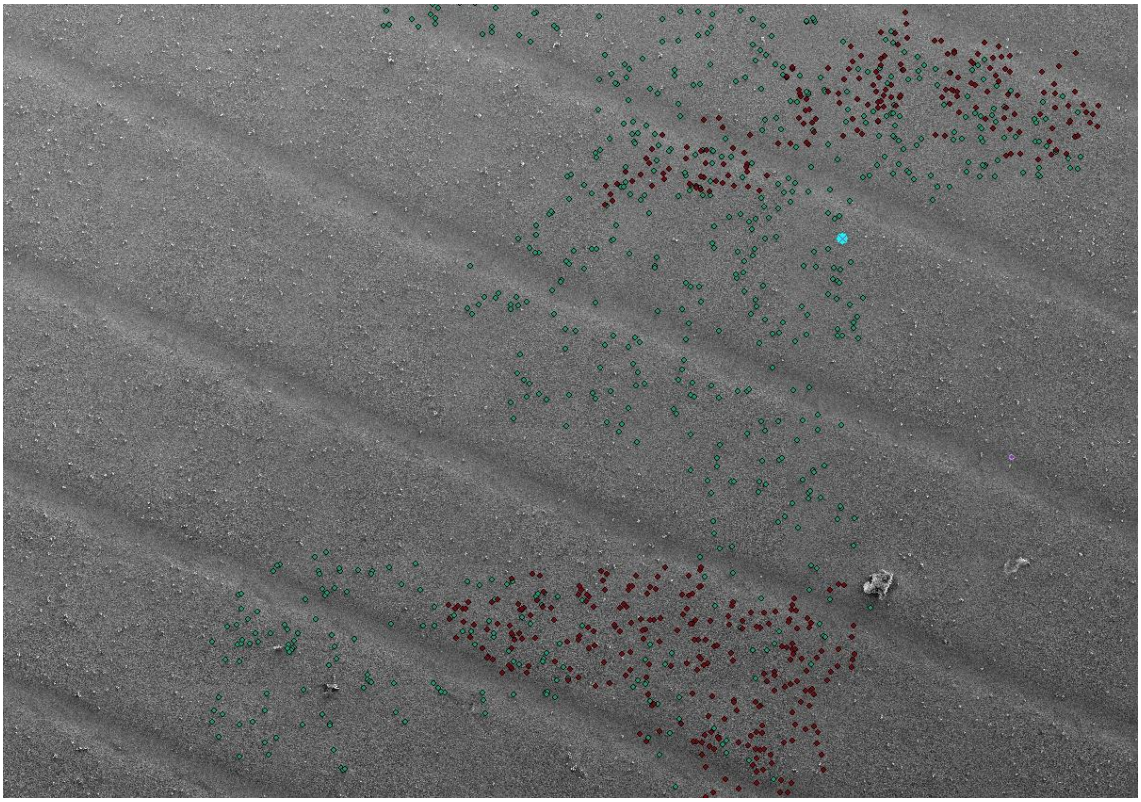

Figure 3.67 Example of image taken from the SEM analysis of the CMS samples. Colored grains are the ones already counted.

It is possible to estimate the suspended grain concentration inside the chamber through the knowledge of the volume flow rate of the system, the duration of the measurements and the number of particles collected by the filter.

It is key, for an optimal result, to position the CMS in proximity of MicroMED, in order to provide a realistic estimation of dust concentration around MicroMED's sampling head, but avoiding fluid dynamic interference with MicroMED's sampling. An example of such test setup is provided in Figure 3.68.

Figure 3.68 Experimental setup with the CMS (on the right) installed in proximity of MicroMED (on the left) and on the injection system (center, with the blue cap).

The CMS is the main system used for the determination of concentration in the chamber. Methods using either carbon stubs or silica wafers have also been used. These two methods are based on the same principle and have been used at times even though they are still under development. The basic principle is to estimate the deposition in the cylinder of fluid which is over either the stub or the wafer. Such method is currently still under development so it is not considered both in the analysis and in the following sections of this work.

3.2.2 Functional tests

In various phases of the MicroMED project, it has been necessary to verify the functionality of the instrument in a fast and efficient way. Verification of the instrument functionality after integration or during the space qualification phase is pivotal to the success of the mission. To this purpose, a number of tests called "functional tests" have been designed, and an official document has been produced to describe such tests and their results. Part of my Ph.D. work has been to contribute to the design of such tests and to write

the aforementioned related official document. This section will provide a brief insight on such procedures.

3.2.2.1 Test setup and configuration

To execute such tests, MicroMED has to be connected to its EGSE (a hardware box that enables to operate MicroMED by means of a PC software with a user-friendly interface) for power supply and command/telemetry communication inside. The Electrical Test setup is shown in Figure 3.69. The connection between the EGSE laptop and the EGSE can be of two different types, using (1) a short cable with USB RS45 connection or (2) an HW box + UDP-5 long cable with DB9 connectors.

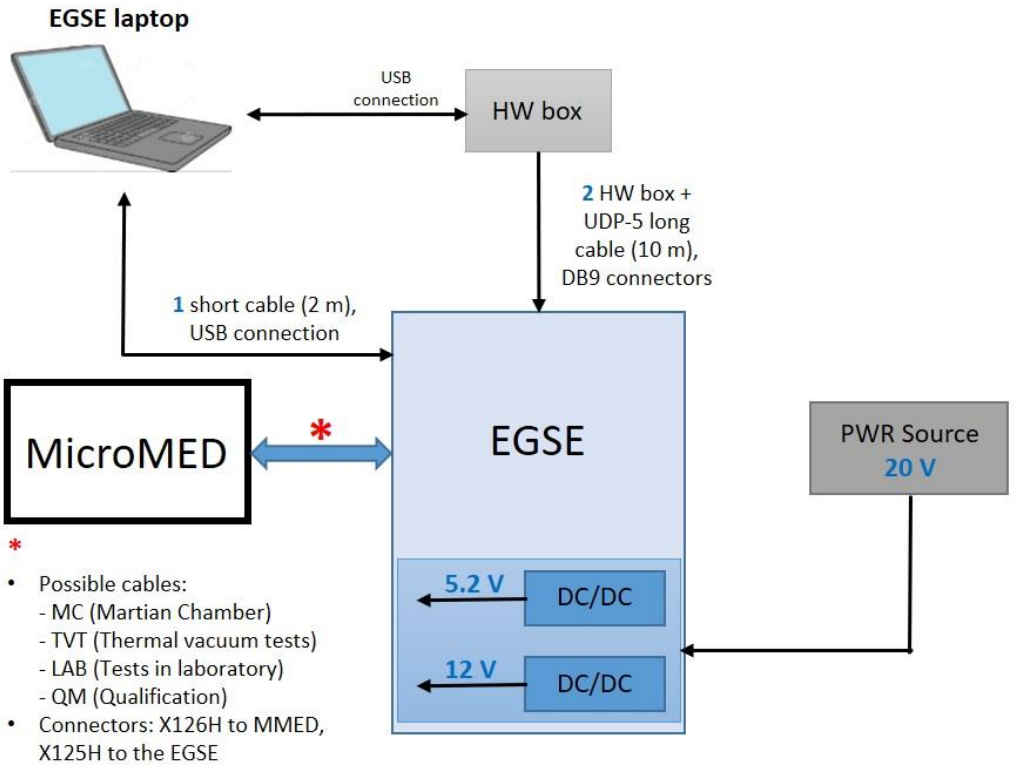

Figure 3.69 Test set-up for functional tests.

The long cable option (2) has been conceived for cases where the operator has to interact with MicroMED while being far from the instrument, for example when MicroMED is inside the Martian Chamber. In any other case, connection (1) with short cable has been used. The data and power lines will be transmitted via N°1 dedicated cable K4H-MC. Grounding of the instrument has to be guaranteed.

3.2.2.2 Functional Tests description

Functional tests have been executed using MicroMED EGSE at different steps of the Assembly Integration and Test (AIT) Flow envisaged for MicroMED Models, i.e. after each environmental test, in order to verify the instrument proper functioning.

Two levels of functional tests have been envisaged:

- Full Functional Test (FFT);
- Reduced Functional Test (RFT).

Full Functional Tests have to be performed at ambient conditions, therefore in these tests the laser can be switched on since the laser operative temperature range is (-20°C, +38°C), allowing to use nominal conditions of current (166 mA) and time of operations (120 s). For Reduced Functional Tests instead, conditions have to be checked in order to avoid the usage of laser outside of its operative range.

The pump operative range is (-35°C, +55°C), allowing usage in nominal conditions of speed (3000 rpm) for the both FFTs and RFTs. The duration of operations is 120 s for the FFTs and 60 s for RFTs.

As said before, housekeeping data are analysed and their values are compared with the Expected Values reported in the procedure tables that have been prepared and reported in the official MicroMED documentation. If values obtained meet the expectation, the test is considered successful. In essence, functional tests are designed to verify the nominal behavior of the subcomponents of MicroMED (laser, pump, pressure and temperature sensors, etc.) without the execution of tests with dust, i.e. without the acquisition and the subsequent analysis of signals coming from sampled dust grains.

3.2.2.3 Use of "Context Tables"

The user friendly interface of MicroMED's software, that can be seen in Figure 3.70, requires the upload of a so called "Context Table" (CT). Such tables provide a collection of input data that are key to the acquisition (like maximum time of execution, number of signal samples per grain acquisition etc.) and to the post processing phases of tests (maximum number of grains acquirable, % of data to be acquired in Low or High channel, since MicroMED allows tests to be performed at two levels of amplification depending on the size of the grains under analysis, etc.), as well as to the actual operating conditions of the instrument (laser power, pump rpm speed, etc.). An Example of such table is provided (Table 3.6). Input data of the context tables vary based on the typology of tests. As an example, the CT shown in Table 3.6 is relative to an Optical Functional test, a test only aimed at the verification of the optical system. For this reason, it is obviously needed to power the laser (potentially to different current values in successive tests) but it is not needed to switch the pump on, since the pump is not the unit under test in this case and in functional tests there is no dust grain acquisition, so sampling is not needed. The CT of Table 3.6 sets indeed a pump rpm speed value of 0 rpm (the pump is kept switched off throughout the duration of the test).

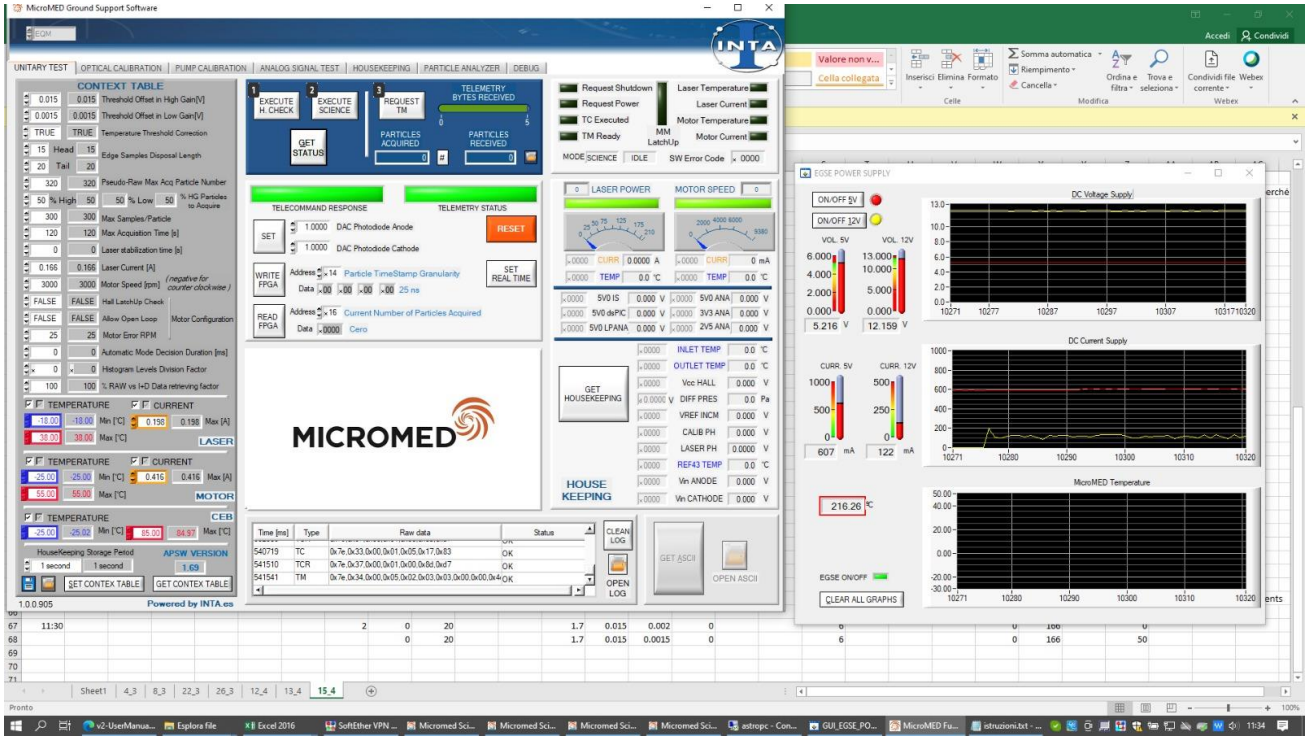

Figure 3.70 User friendly interface of MicroMED software.

BYTE ORDER	PARAMETER NAME	SCIENCE VALUE OF PARAMETER	VALUE TO SEND
0	TC ID (0x07)	SET CONTEX TABLE TC	**0x07**
1 (MSB)	OHPhotodiode_Value_Minimum_Threshold	0V	**0x00**
2 (LSB)			**0x00**
3 (MSB)	Head Samples Disposal & Tail Samples Storage	0	**0x00**
4 (LSB)			**0x00**
5 (MSB)	Contingency_Laser_Minimum_Temperature	-20ºC	**0xb9**
6 (LSB)			**0xca**
7 (MSB)	Contingency_Laser_Maximum_Temperature	+38ºC	**0xee**
8 (LSB)			**0xc1**
9 (MSB)	Contingency_Laser_Maximum_Consumption	210 mA	**0x00**
10 (LSB)			**0x07**
11 (MSB)	Contingency_Motor_Minimum_Temperature	-35ºC	**0xb9**
12 (LSB)			**0xca**

13 (MSB)	Contingency_Motor_Maximum_Temperature	+55ºC	**0xff**
14 (LSB)			**0x0c**
15 (MSB)	Contingency_Motor_Maximum_Consumption	416 mA	**0x16**
16 (LSB)			**0x66**
17 (MSB)	Contingency_MM_Minimum_Temperature	-40ºC	**0x00**
18 (LSB)			**0x89**
19 (MSB)	Contingency_MM_Maximum_Temperature	+85ºC	**0x00**
20 (LSB)			**0x70**
21 (MSB)	Photodiode value minimum threshold in Low Gain	0V	**0x00**
22 (LSB)			**0x00**
23 (MSB)	Histogram_ Acquisition_Particle_Number	0	**0x00**
24 (LSB)			**0x00**
25 (MSB)	Contingency_Check_Status	All contingencies active	**0x00**
26 (LSB)			**0x1f**
27 (MSB)	Pseudo-Raw Max_Acquisition_Particle_Number	0	**0x00**
28 (LSB)			**0x00**
29 (MSB)	Max_Acquisition_Time	120 s	**0x00**
30 (LSB)			**0x32**
31 (MSB)	Raw VS I+D Data retrieving factor	0 %	**0x00**
32 (LSB)			**0x00**
33 (MSB)	Laser_Current	166 mA	**0x07**
34 (LSB)			**0xa2**
35 (MSB)	Motor_Speed	0 rpm	**0x00**
36 (LSB)			**0x00**
37 (MSB)	Max_Samples_Per_Particle	0	**0x00**
38 (LSB)			**0x00**
39 (MSB)	Housekeeping_Storage_Period	@ 2 s	**0x00**
40 (LSB)			**0x02**
41 (MSB)	Automatic_Mode_Dectection_Duration	0 ms	**0x00**
42 (LSB)			**0x00**
43 (MSB)	Histogram Level Division Factor	0 %	**0x00**
44 (LSB)			**0x00**

45 (MSB)	High Gain Acquisition Percentage	0 %	**0x00**
46 (LSB)			**0x00**
47 (MSB)	Reserved	Reserved	**0x00**
48 (LSB)			**0x00**

Table 3.6 Example of Context Table used for MicroMED functional tests.

3.2.3 MicroMED performance tests

MicroMED has been intensely tested throughout the various phases of the project. Tests to verify MicroMED's ability to correctly sample, detect and identify dust grains of different type and shape have been performed and have produced a significant amount of data that has sharpened our knowledge of the MicroMED OPC and of the features and characteristics of our facility in Capodimonte (even though tests have also been performed elsewhere, as we will see in the later sections of this work).

This section provides an insight of the execution and results of such performance tests. Preparation of the test in terms of grounding and electrical interface is identical to the procedure already described for the functional tests in Section 3.2.2.1. A description of the facility, of our chamber and of the preparation of the test setup inside the chamber, as well as the preparation of the samples, has already been provided in Section 3.2.1. This section will provide information on the additional procedures and activities needed to correctly perform and analyze performance tests with the MicroMED OPC.

3.2.3.1 Procedure for the execution of a standard test

The standard procedure for the execution of a MicroMED performance test starts with the preparation of the dust grain sample to be injected in the Chamber. As already described in Section 3.2.1, our Martian Chamber is positioned inside a Clean Room in order to be compliant with the planetary protection requirements imposed by the ExoMars 2022 mission. For this reason, the operators in charge of such preparation have been required to wear sterile coveralls, FFP2 or FFP3 face mask (depending on the eventual risk related to the presence of PM10 or thinner airborne particles) and sterile gloves as well as provide to repeatedly sterilize every object and tool to avoid contamination.

Once properly dressed, operators have to enter into the clean room, open the Martian Chamber and fill the nebulizer shown in Figure 3.68 (c) with either the already described solution of grains and ethanol or only grains, depending on the typology of injection chosen for the test. In case of wet injection, the nebulizer is filled by means of a pipette controller and 5 ml of solution are poured inside. For dry injection, such operation is instead performed

with a spoon able to gather 1 mg of particles at once. For the wet injection, the nebulizer is positioned on a pulsing vortex mixer, able to keep the solution in constant movement, avoiding deposition of grains on the bottom of the nebulizer. Such operation is done to avoid that the solution injected into the chamber has low concentration of grains. This problem does not occur in case of dry injection, so the pulsing vortex miser is kept switched off in such cases. Once the nebulizer is filled, the CMS is installed (see Section 3.2.1.6 for a brief description of the system) to monitor dust grain concentration around MicroMED. MicroMED is positioned inside the ATS Thermal Chamber (Figure 3.58 (b)) so that its temperature can be set to the desired value for the test in the entire MicroMED operative temperature range (-20°C, +40°C). Once such operations are concluded, the Martian chamber is closed and the chamber is pressurized, bringing its internal pressure to less than 1 mbar. At this point, CO_2 is injected into the chamber to recreate Martian environment in terms of pressure (~ 6-8 mbar) and atmospheric composition (95%+ of CO_2). The entire process of pressurization of the chamber requires about 15-20 minutes. The conditions described above led to a microclimate inside the Chamber of ~ 22 °C and 32 % relative humidity.

At the end of such test preparation phase, the test is ready to be performed. MicroMED's software (SW) is opened on a laptop. MicroMED's SWs are actually two, as one is responsible for the switch on of the instrument and the verification of the current absorption of each line of MicroMED, while the other allows to perform the test, loading the CT into the instrument's electronics and downloading the results of the tests (the latter SW is called Ground Segment software - GSSW).

By means of the GSSW, whose interface is shown in Figure 3.70, after the loading of the CT an "Health Check" phase is performed, a procedure lasting about 30 seconds aimed at verifying the nominal behavior of all subsystems before launching the test. During this phase, the system measures and manages the straylight, waits for the laser stabilization and the pump operating at full capacity, measures the average noise and its standard deviation, set the final threshold to trigger the acquisitions. After such phase, the scientific test can be performed. Acquisition is launched and simultaneously injection is made inside the chamber by opening the CO_2 duct connected to the nebulizer. In case of wet injection, the pulsing vortex mixer has to be switched off just before the injection. After a maximum duration of the test that can be set to whatever value is desired, the GSSW allows to download telemetry data to be either previewed immediately or processed at a later date.

It has to be underlined that MicroMED's science test duration depends on the outcome of the test itself. The GSSW indeed sets a maximum duration for the test after which the acquisition is stopped (it is usually set at 60 or 120 seconds), but given that the amount of memory available is limited the run can be immediately stopped before such limit time value when the science data have already filled MicroMED's memory. This obviously means that MicroMED tests can have very diverse durations, which is an important clarification that will be useful in later sections of this work. As for the output data, the MicroMED team has developed a SW providing a user friendly interface (See Figure 3.71) that is able to process data in the matter of seconds after the end of tests. Such SW, called MicroMEDTelemetry, has allowed to verify results and have preliminary information on the outcome of the tests even

during the test campaign, in between runs. The in-depth analysis of the results has then obviously been performed at a later date, providing the results needed.

The following sections will provide an overview of performance tests performed after integration of MicroMED. Such tests were aimed at verifying the PFM's ability to correctly sample, detect grains and individuate their size. Results show MicroMED's PFM is able to determine grain size with good precision and it is able to sample grains even in the upper measurement range (d > 15 μm), which is a significant update over the BB geometry.

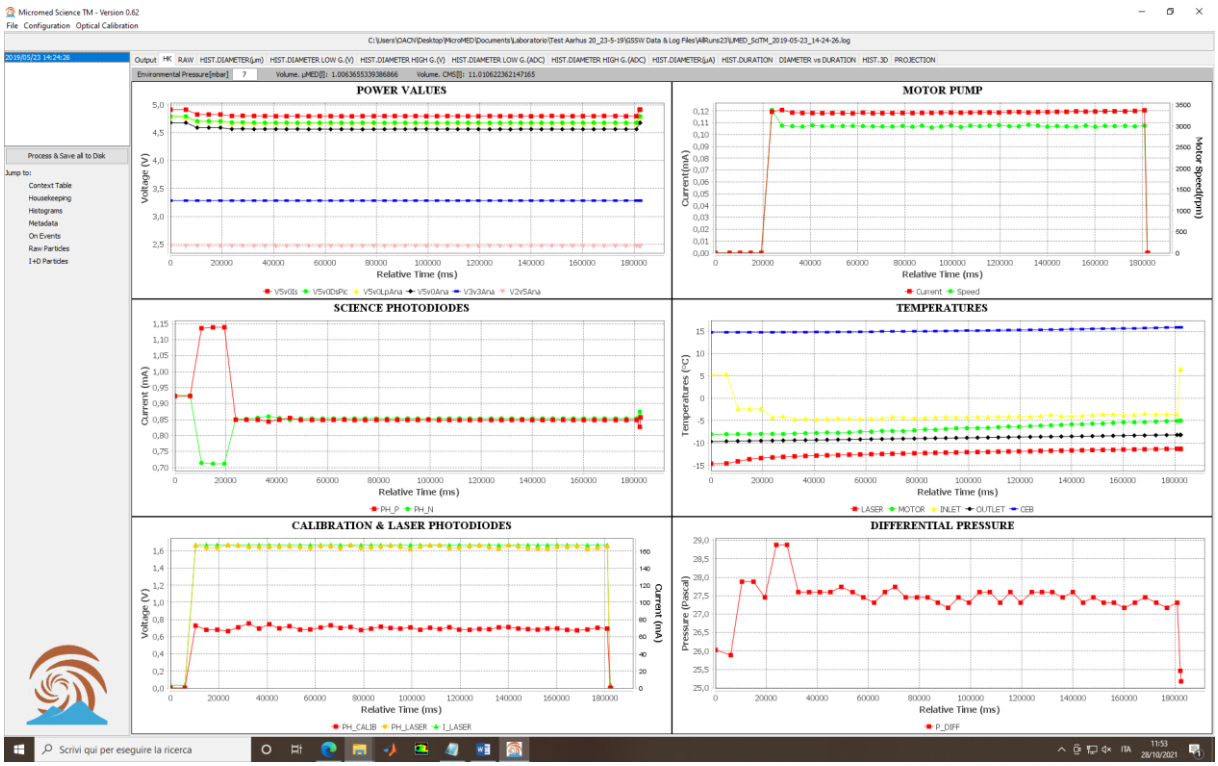

Figure 3.71 User friendly interface of the MicroMEDTelemetry SW.

3.2.3.2 Results – overview

Performance test results are mostly reported in terms of histograms, that report the size distribution of the sampled grains in each run. Given that performance tests have been performed with monodispersed calibrated dust grains produced by Microparticles ®, such histograms can be used to verify that the instrument is able to correctly detect the size of the grains. It has to be underlined that the laser illuminated spot is only ideally uniform, and that in reality its power distribution is uniform and at peak value in the inner sections of the spot while power decreases going toward the edge of the spot. This is significant as the light scattered by crossing grains is less intense when the grains cross the edges of the spot. Histograms thus verify the extent of the phenomenon and consequently the quality of the fluid dynamic design, since one of the design goals was to concentrate the flow of grains as close to the center of the spot, i.e. to the longitudinal axis of the inlet duct, as possible.

3.2.3.3 Results – small grains (d ≤ 1 μm grains)

The smallest dust grains tested in the entire test campaign on MicroMED have been 0.8 and 1 μm diameter grains. Small grains are indeed very tough to be detected since the amplitude of the scattered light signal is comparable with the electronic noise experienced by the instrument. The process has then been to gradually reduce noise sources to increase MicroMED's ability to correctly detect grains with no interference. Results are positive and show MicroMED can detect 1 μm grains with good accuracy. Figure 3.72 shows an example of the dimension histograms obtained for dust grains of 1 μm in diameter. The histogram shows a clear peak around the grain radius size of 0.5 μm, hence 1 μm in diameter.

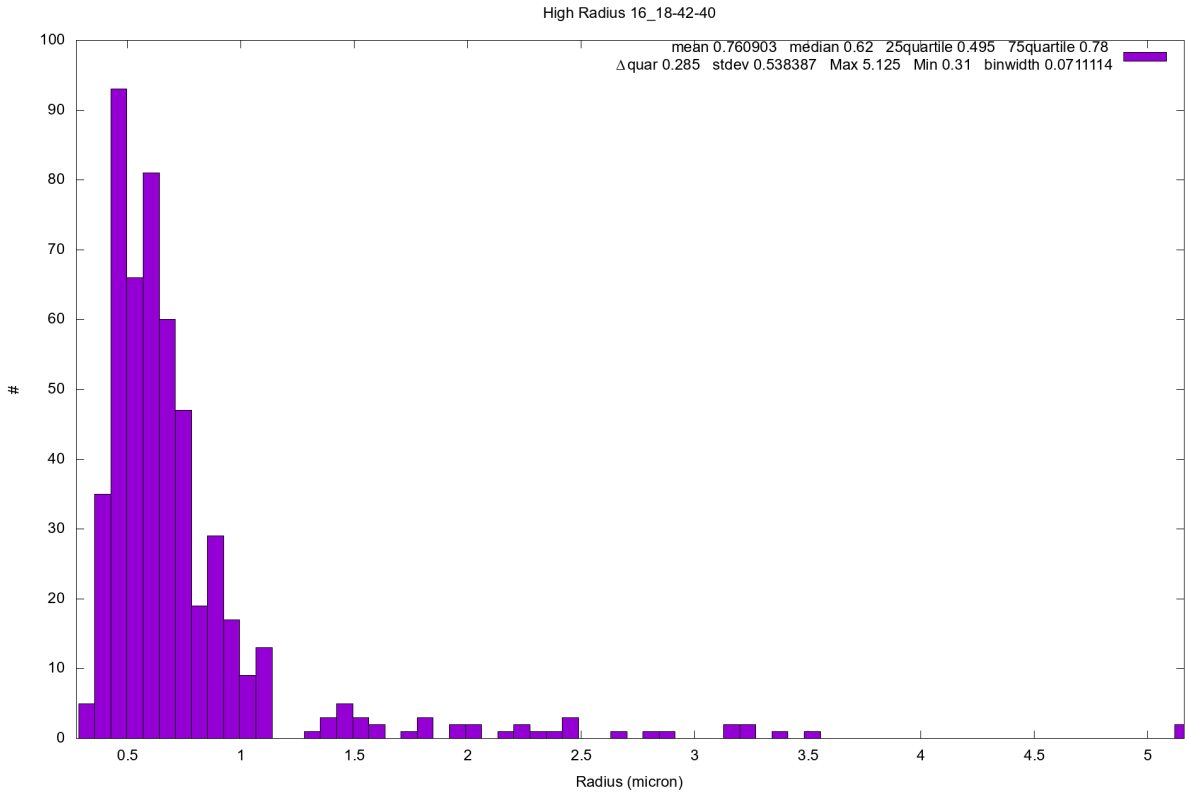

Figure 3.72 Example of dimension histogram for 1 μm diameter dust grains.

3.2.3.4 Results - intermediate (1 μm < d < 15 μm) grains

Intermediate grain sizes are all detected with good accuracy by MicroMED. Such grains are easily detectable by MicroMED with no noise issues and also easily sampled by the instrument since their inertia is not high enough to influence their sampling. Also MicroMED's BB was able to detect grains in this range of diameters with good accuracy, so

good results were expected and have been obtained. Results are reported for different sizes in the range. Figure 3.73 shows an example of the dimension histograms obtained for dust grains of 2 μm in diameter. Figure shows the histogram is peaked around the nominal value of 1 μm in radius.

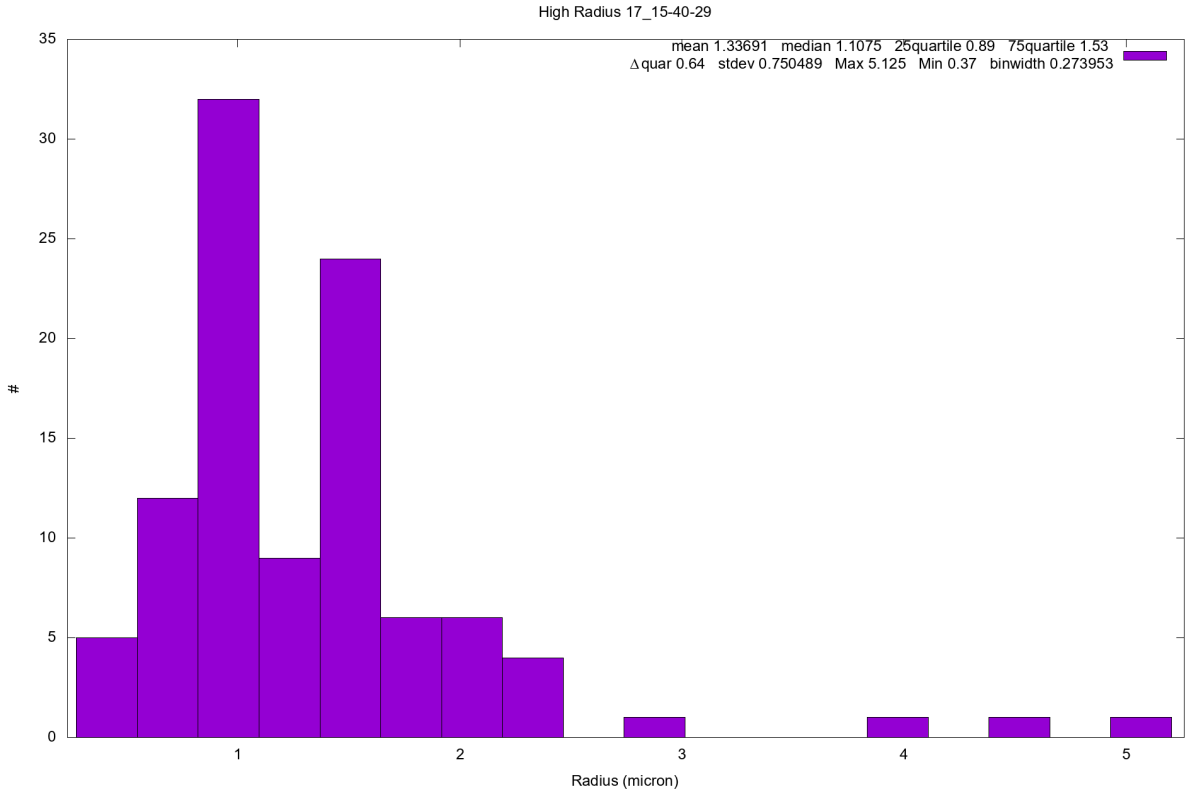

Figure 3.73 Example of dimension histogram for 2 μm diameter dust grains.

Similar results are obtained for the entire range of grains that have been identified as "intermediate". Figure 3.74-Figure 3.76 show some examples of grains in the range, more specifically they report results for grains of 4, 10 and 15 μm in diameter (2, 5 and 7.5 μm in radius). For grains larger than 10 μm, some smaller signals, possibly noise signals, have been acquired. The analysis of this lower peak in the histograms has been part of the present work and is described in the later sections.

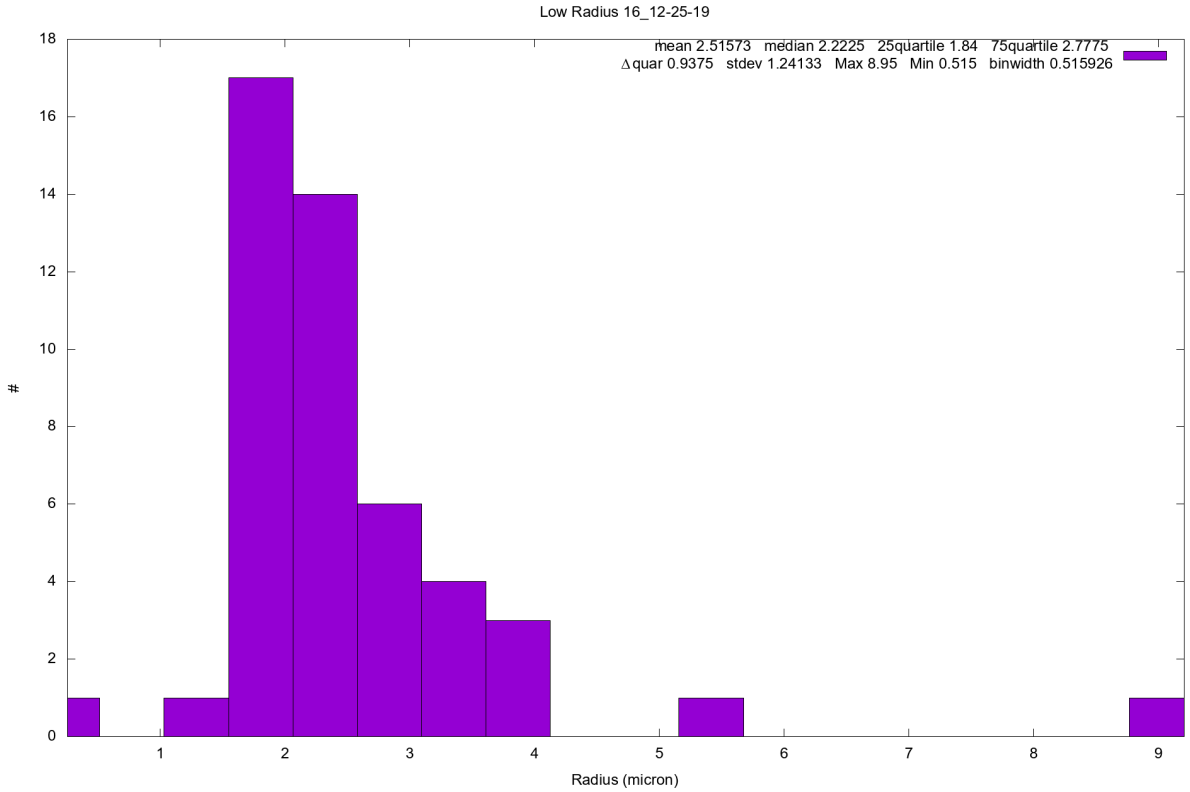

Figure 3.74 Example of dimension histogram for 4 µm diameter dust grains.

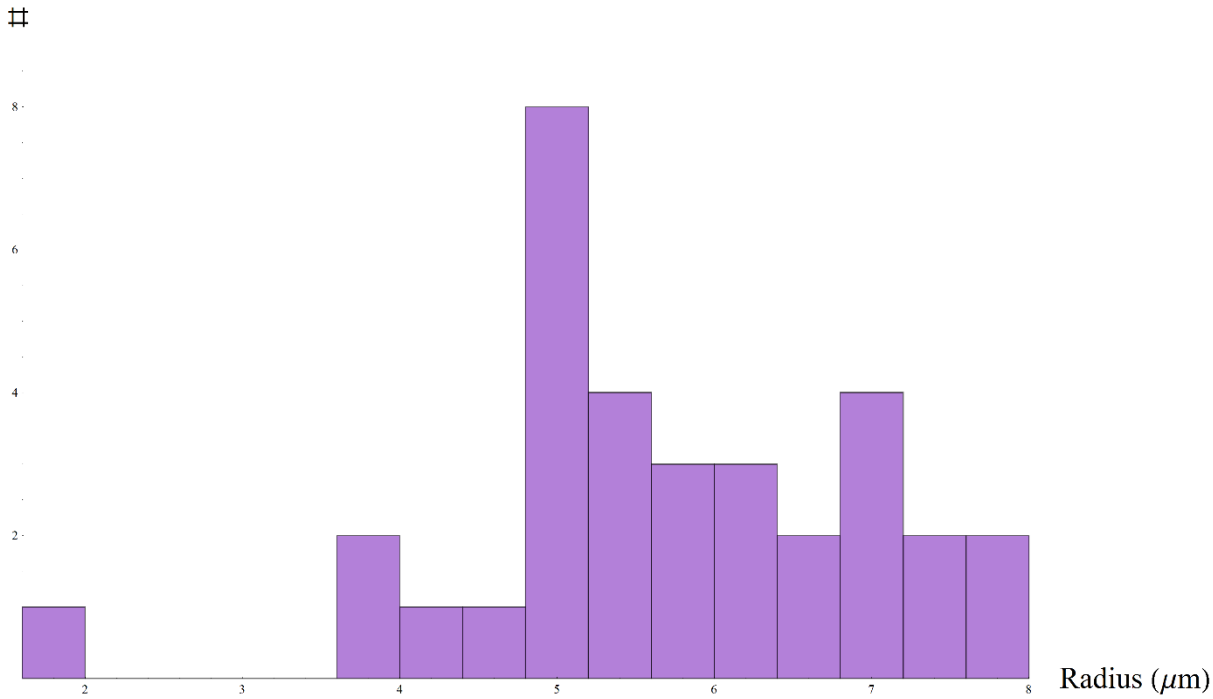

Figure 3.75 Example of dimension histogram for 10 µm diameter dust grains.

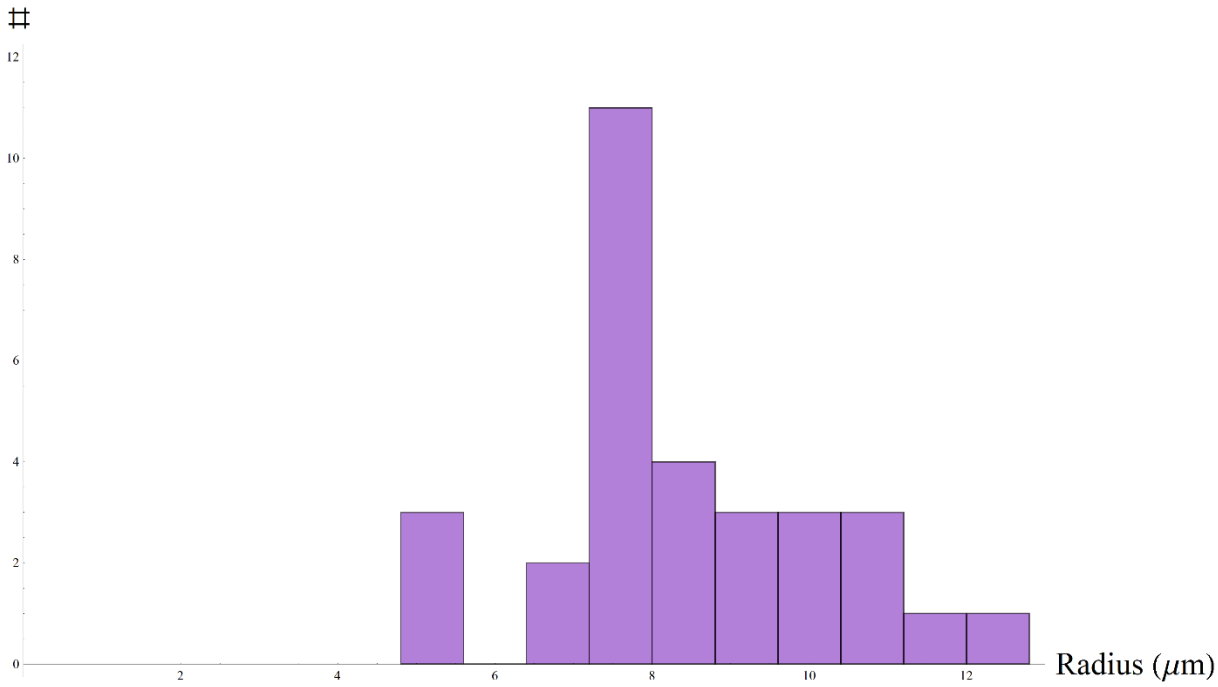

Figure 3.76 Example of dimension histogram for 15 μm diameter dust grains.

3.2.3.5 Results – large (d > 15 μm) grains

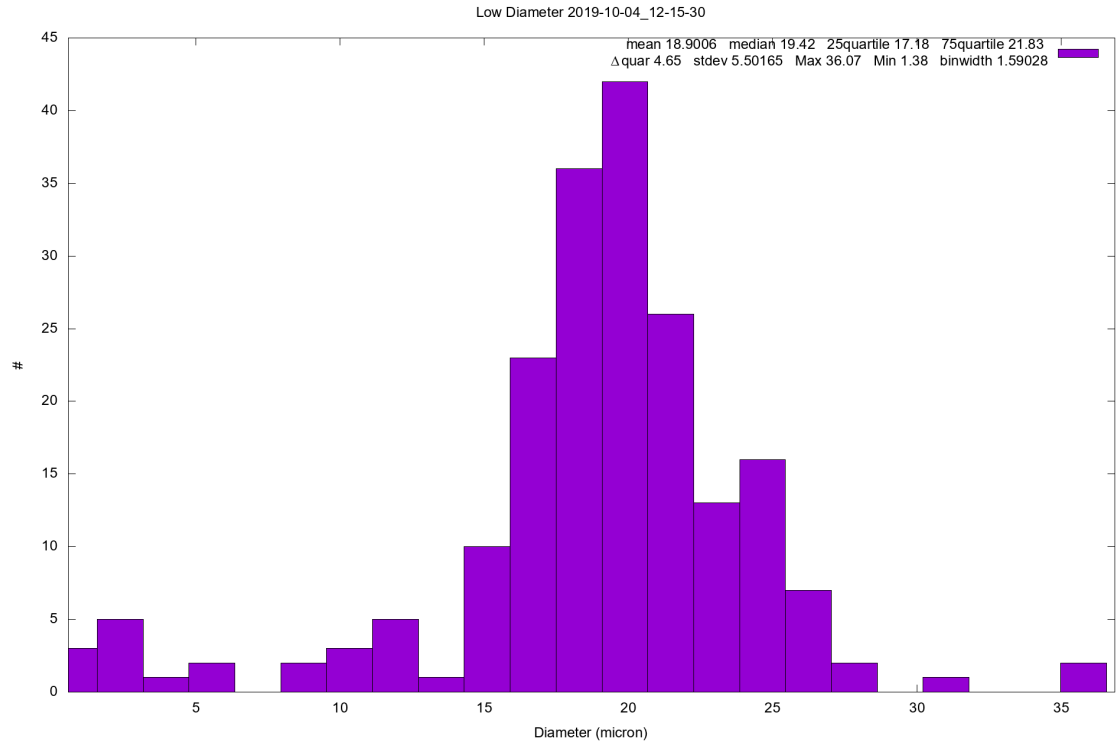

Figure 3.77 Example of dimension histogram for 20 μm diameter dust grains.

Figure 3.77 shows an example of the dimension histograms obtained for dust grains of 20 μm in diameter. Figure shows that the PFM design is able to sample and correctly detect large dust grains which is a significant update with respect to the BB geometry. MicroMED is able to detect such grains also in presence of wind, as we will see in the later sections. Tests have been successful; however, during tests with large grains, it has happened in some occasions that histograms presented a bimodal trend, with a secondary peak usually in the 4-10 μm diameter range, well below the nominal diameter of the injected large grains. The analysis of the reasons that could have led to the presence of secondary peaks in histograms has been deep and a description of such analysis is reported in Section 3.2.4.

3.2.3.6 Brief overview of the results of performance tests in stationary CO_2

Performance tests in the Martian chamber have been aimed at a number of aspects related to MicroMED's PFM correct functioning:

- The instrument ability to detect particles;
- The instrument ability to determine dust grain sizes with good accuracy;
- The instrument ability to collect big samples for a better statistical analysis;
- The software ability to collect only true signals.

The tests showed that the instrument is able to detect particles throughout the sampling range except for the lower extreme of the measurement range (under 1 μm in diameter), where noise is still a factor that needs further work.

During tests with large dust grains, some small signals (probably noise) have been acquired, reducing the actual samples detected by MicroMED. This aspect is currently under analysis as the number of small signals has to be reduced as much as possible in such tests. A complete section on such analysis is provided later in this work (See Section 3.2.4).

The results of the runs match well with the curve obtained by means of the Mie theory, meaning the instrument is working with good efficiency and accuracy.

3.2.4 Bimodal histograms

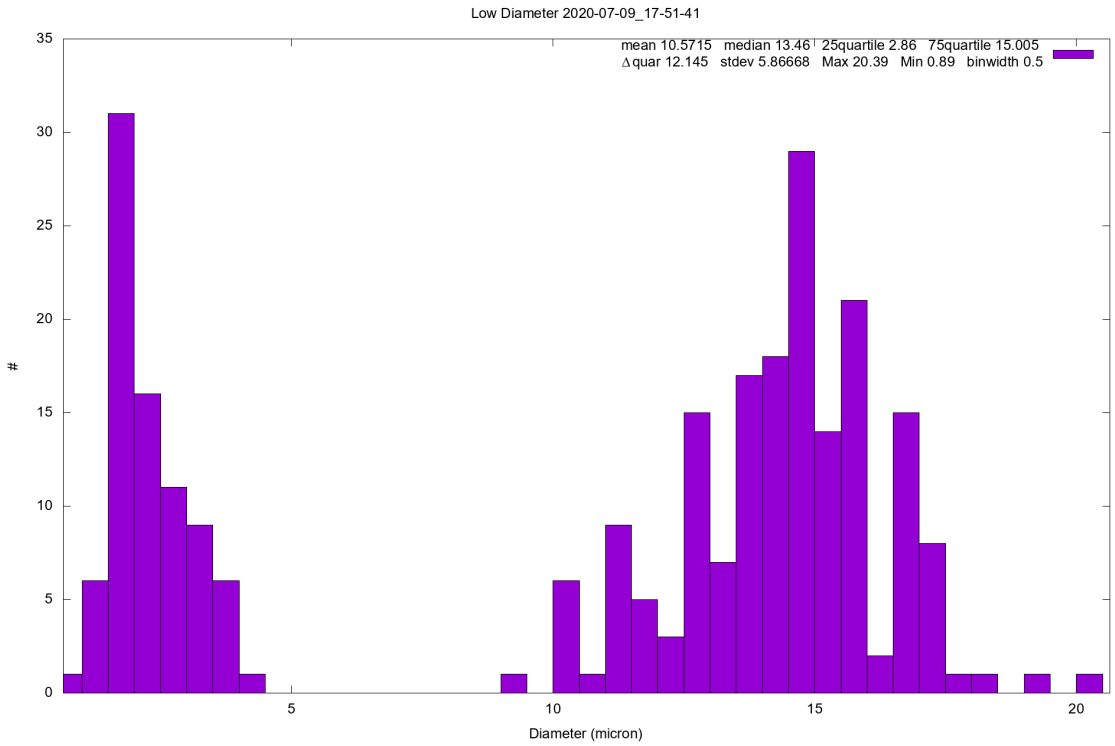

Figure 3.78 Example of bimodal histogram. It can be easily noted that there is a secondary peak relative to a dimension around 7 μm in diameter in this example.

During tests with monodispersed grains, an unexpected result has sometimes been obtained. Specifically, histograms have sometimes presented a secondary peak at a diameter value well below the expected value for tests. Figure 3.78 shows an example of this result.

This phenomenon has been individuated especially for large dust grains, and its peculiarity has demanded additional investigation since the range of diameters in which the secondary peak is found most likely excludes noise phenomena but at the same time there is no immediate explanation for it. For this reason, an in-depth analysis of the instrument behavior has been performed to try to individuate the possible cause for this phenomenon. The main hypotheses advanced by the group are the following:

- Potential noise issues (the phenomenon is not related to amplification as it has been individuated both in tests performed considering Low and High Channel, which are the two channel MicroMED can acquire into);
- Fluid dynamic issue #1: the hypothesis made during the CFD analysis of grains getting stuck on the wall is not true. Grains rebound on the walls and the chaotic movement of the rebounding grains may cause the grain to cross the spot on the borders, where light is less intense, causing a smaller scattered signal, hence a lower detected diameter;

- Fluid dynamic issue #2: MicroMED runs are often characterized by a pump induced Δp that is higher than the design value of ~ 2-3 mbar. This has both been due to the pump outperforming expectations, and to the fact that if consecutive tests are executed, ambient pressure in the chamber may rise which also means suction is more efficient. These conditions, according to the CFD analysis described in Section 2.2, should not alter the instrument behavior while they improve its sampling capability; however, a detailed series of CFD runs has been performed with the idea of confirming this assumption;
- Fluid dynamic issue #3: When grains are sampled in high quantities, i.e. in an environment rich of grains, MicroMED fills its memory in a few seconds and the run is immediately stopped. However, even if the pump is switched off the suction does not stop immediately as the pressure gradient generated by the pump does not immediately go to zero. This means some grains are still sucked, and flowing into the instrument, when the effect of the pump finishes, they are only subject to gravity and electrostatic forces. This could cause such grains to deposit on the inner walls of the duct. When the pump is switched on again for the following test, MicroMED samples such grains, that are detached from the walls or are still in suspension inside MicroMED and tend to cross the spot not following their designed track but randomly and possibly closer to the duct walls, crossing the spot close to its border and causing a smaller scatter of the laser light.

These different aspects have all been investigated; however, my role in this part of the work has been to analyse the fluid dynamic issues that could lead to the presence of the secondary peak and try to individuate a cause. The following sections describe such analysis.

3.2.4.1 Possible noise issues

The possibility of noise issues has been evaluated during the post processing of MicroMED's tests. However, the analysis has showed that MicroMED's noise, when present, is peaked at around 1.3 μm in diameter with a tail reaching 2 μm in diameter. On the opposite, the second peak of the bimodal histogram is never peaked under 4 μm in diameter, showing that they are reasonably unrelated events. In the rare cases where both phenomena happened, a multimodal distribution with three peaks has been observed (Figure 3.79). Overall noise issues have been analyzed and successfully managed by the MicroMED team, and such issues are reasonably not the cause of the bimodal histograms here described.

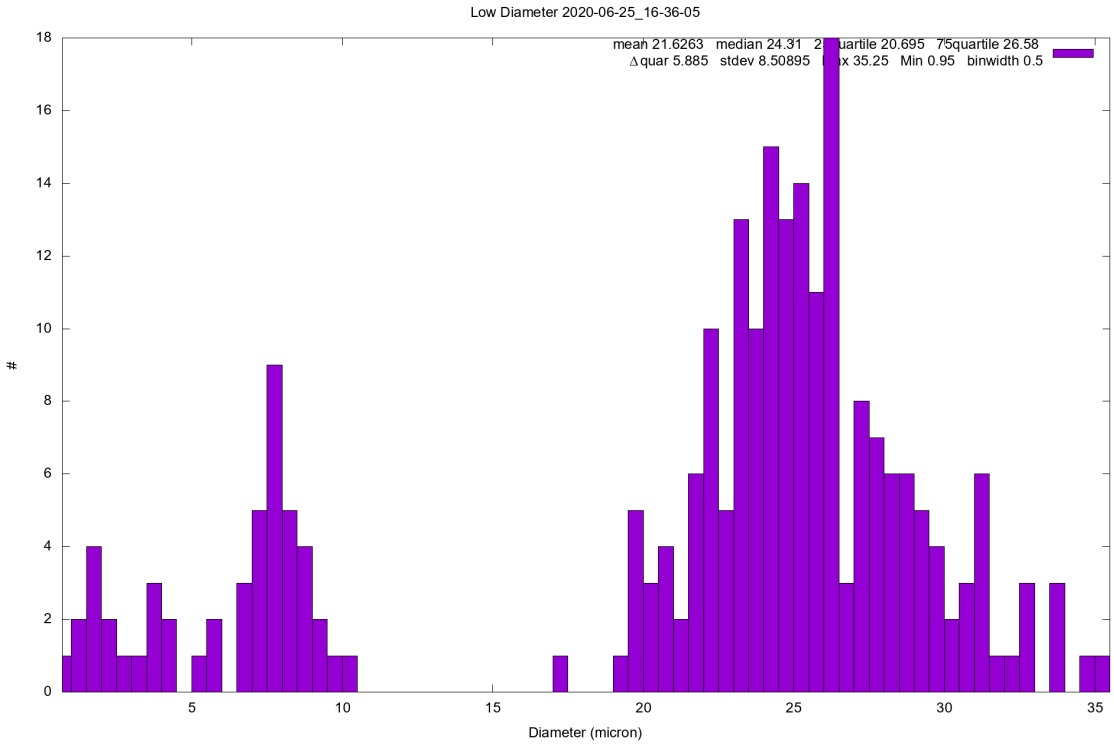

Figure 3.79 Example of multimodal histogram, occasionally obtained during tests. The peaks are, in ascending order: electronic noise, the second peak whose origin is debated here, and the actual dust grain distribution.

3.2.4.2 Fluid dynamic issue #1: rebounding of grains

The CFD analysis performed on MicroMED also provides position histograms (as already shown in Sections 2.1.3.4 and 2.2.3.2) to determine not only if, but also where dust grains cross the laser illuminated spot. A comparison between the data described by such histograms and the shape of the optical power profile inside the sensing spot has been made, with the intent of simulating the signal outcome of MicroMED. In particular, from the histograms it is possible to derive what percentage of grains cross each region of the spot, and since an estimation of the scattered light of each grain can be made depending on where it is expected to cross the spot, a distribution of the outcomes can be estimated. However, such comparison has not been able to justify double peaked histograms. Even when grains cross the extremities of the spot (the spot can be seen in Figure 3.80), the signal should still be higher. For example, for 20 μm grains, grains that cross the extremities scatter enough light to appear like 8 μm grains, while the second peak of the histogram can be noted at around 5 μm.

For this reason, to generate such a low signal, grains should cross the plane containing the laser spot very far from the spot itself. Such behavior could eventually be caused by rebounding of grains on the walls. As already pointed out, we know that in this analysis, the assumption that grains that hit the walls get stuck on them has been made. This assumption comes from experience, given that grain size is of the same order of magnitude of the wall

mean surface roughness, so they can get stuck, and grains are also subject to triboelectrification. This aspect has not been strictly considered in the CFD analysis, however it is possible that grains that reach the walls stay on the walls for some time also because they need to unload their electrical charge. Grains could then be released by the walls and get caught in the fluid stream, which would then concentrate these grains toward the longitudinal axis of the duct, close to the center. With the purpose of trying to understand whether this phenomenon could be explained by rebounding of grains, a CFD analysis has been performed, considering grains as able to bounce on the walls instead of getting caught. Results have then been compared with results obtained for the analysis with the "traditional" hypothesis of grains getting stuck on the walls to understand whether there is a significant amount of grains that cross the spot far from the center, possibly explaining the phenomenon. A potential contribution due to a misalignment between the inlet and the outlet duct has also been investigated in addition to the rebounding to possibly individuate undesired behavior by dust grains.

Results show that it should not be possible for grains to cross the spot this far from the center of the spot even when they rebound on the walls while being very close to the end of the inlet duct. Figure 3.81 shows that the distribution obtained for grains rebounding on the final section of the inlet walls cause a larger dispersion of grains, however they are still confined in a centered region of the spot. The figure refers to 15 μm grains, that during tests have produced a number of bimodal histograms. In the CFD simulation, none of those grains cross the spot farther than 320 μm from the center of the 1 mm spot (which in the figure is indicated by the 1000 μm line). In essence, it appears that reflection is not the cause for the bimodal histograms observed.

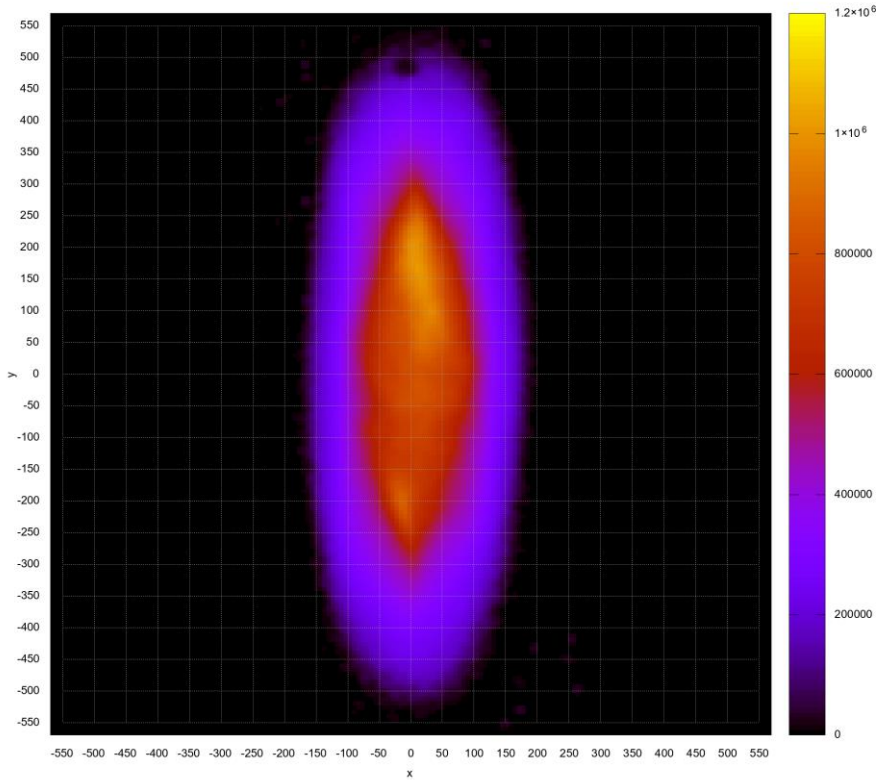

Figure 3.80 Image of the laser light spot. Dimension on the axis are in μm.

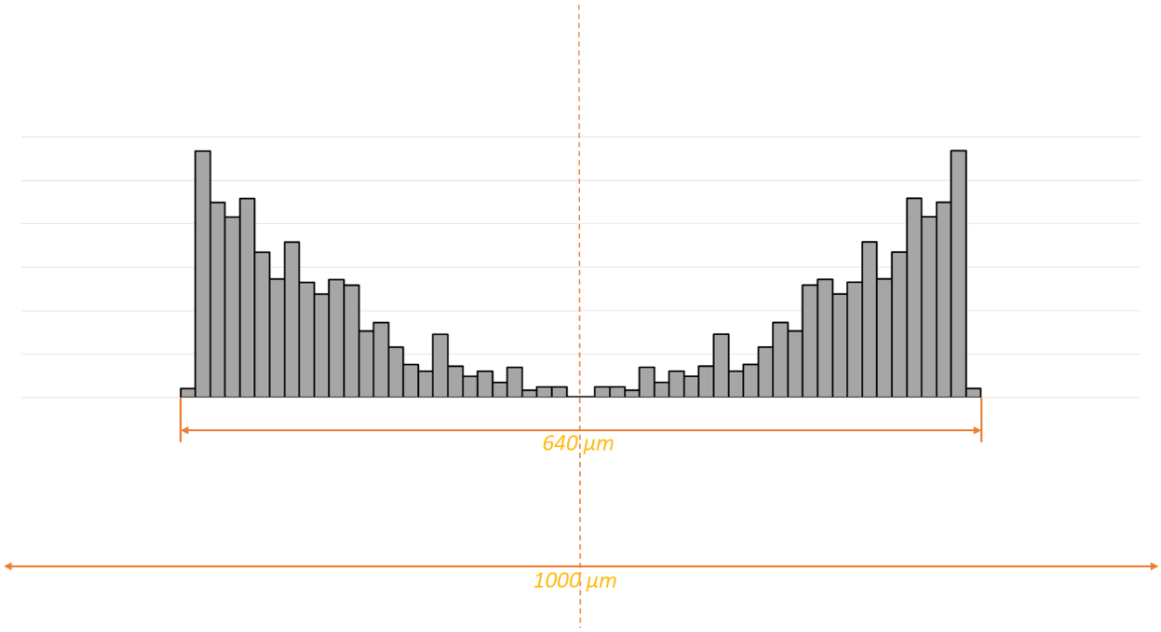

Figure 3.81 15 μm dust grain distribution in the case of grain reflections on the inlet walls. The histogram refers to the following conditions: pa = 6 mbar, Ta=Ti=295 K, Δp = 2 mbar. Reflection causes a larger distribution of grains in the spot, however grains stay well inside the spot itself even for sizes like this one that have experienced some bimodal histograms during tests.

3.2.4.3 Fluid dynamic issue #2: effect of extreme Δp on grain trajectories

The effect of increased pressure force generated by the pump on performances has been evaluated. It has indeed been evidenced that MicroMED's pump has exceeded expectation, which has led to some runs with a higher pump generated Δp with respect to the design conditions. This eventuality is also potentially triggered by an increase of the ambient pressure in the chamber following repeated tests (it has sometimes happened that tests have been executed consecutively). According to the CFD analysis performed on MicroMED's PFM (Section 2.2), the instrument's sampling efficiency is still very good (just slightly worse – 1-2% maximum – for grains under 1 μm) even for Δp up to 5 mbar. However, the analysis of such phenomenon has been deepened in the framework of trying to decipher the bimodal nature of those histograms. A further CFD analysis has been performed with this purpose, showing that, even though there is an effect on distribution, this effect is not enough to explain the bimodal nature of the histograms. Figure 3.82 shows indeed that the increase of the pump induced Δp actually causes a larger dispersion of the grains in the spot, however even for a Δp of 5 mbar (that has never been experienced in tests, the maximum values registered has been ~ 4.5 mbar) all grains are still well inside the laser illuminated spot (whose border is 500 μm from the center, grains cross the spot never farther than 350 μm from the center). The figure is relative to 15 μm grains, but similar results have been obtained for other sizes that during tests have experienced bimodal histogram cases.

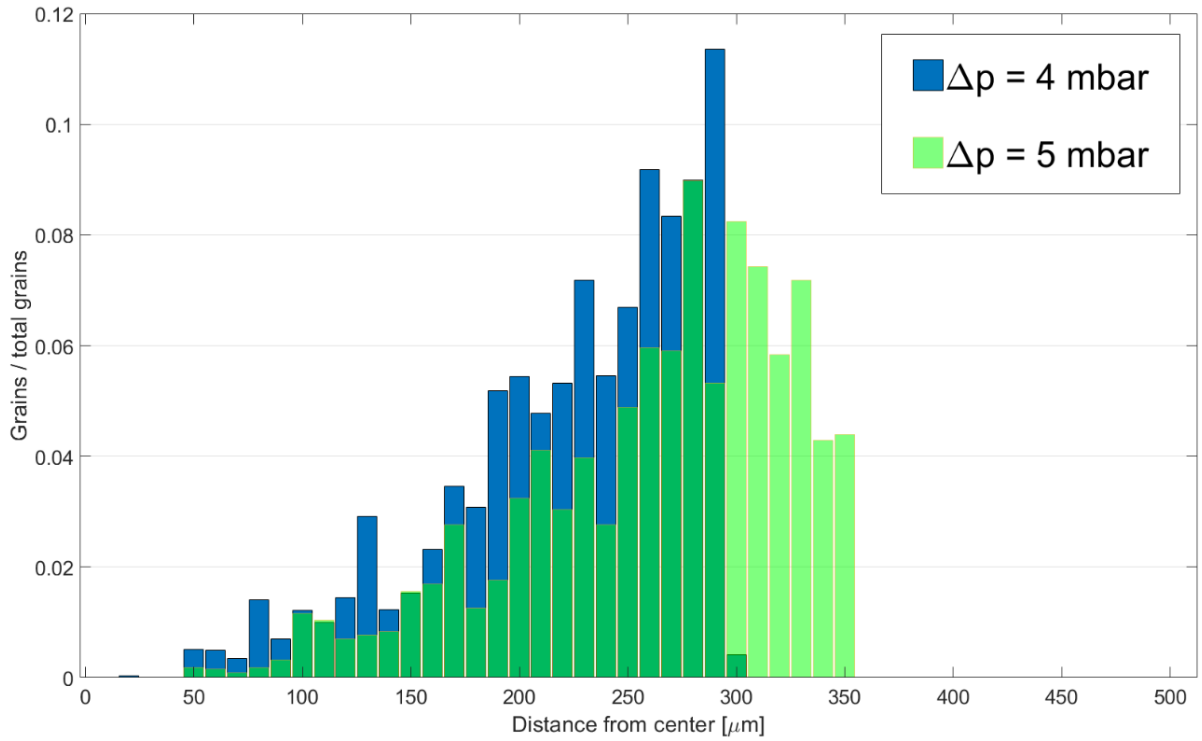

Figure 3.82 Position histograms for 15 μm dust grains in case of high pump generated Δp. The increase of the pressure force generated causes a larger dispersion of the grains; however, grains stay inside the laser illuminated spot.

3.2.4.4 Fluid dynamic issue #3: deposition of grains on the inner walls of MicroMED's inlet

A further issue investigated has been the eventual deposition of grains inside MicroMED's duct. The basic idea is that, especially for dry injection, the amount of grains available to MicroMED is very high (estimations are that up to 40 particles/cm^3 could be available, which corresponds to expected dust storm conditions). Such a large amount of grains causes a saturation of MicroMED's memory in the matter of a fraction of a second (some runs have had durations of ~ 0.2 seconds). However, given that the pump is switched on during the *Health Check* phase, a 30 second long phase preceding the science tests of MicroMED, the pump is in cruise conditions at the beginning of the science test (the transitory part happens during the Health Check). This means that, a fraction of a second later, when the acquisition is stopped because of the reached limit data storage, the pump is switched off but needs some time to be stopped (fractions of a second). There is hence a timeframe in which the pump is still generating suction even though MicroMED has concluded its acquisition, and given the large amount of grains present, dust grains are still sucked inside MicroMED. At some point the effect of the pump vanishes, but dust grains have entered MicroMED and reasonably tend to deposit, being subject to gravity and electrostatic forces. It is thus expected that such deposited grains could detach from the walls if the MicroMED's pump is switched on again very soon (few minutes - during repeated tests) before they had the chance to detach by means of gravity and/or electrostatic discharge. Since their starting point is not outside MicroMED anymore, it could happen that some grains, detaching from a portion of the walls which is close to the laser spot, do not have enough time to adjust their trajectory toward the inner rings of the duct sections and cross the spot close or after the border.

Based on this idea, a CFD investigation of the matter has been performed. Results are positive, as the dynamics evidenced by the CFD runs could explain the bimodal nature of the histograms under study. Figure 3.83 shows position histograms for grains detaching at different levels of MicroMED's inlet duct. Given that MicroMED's inlet duct is made of three sections tightened up one to the other, it has been simulated that grains may detach from such sections of the walls. In essence, CFD simulations have been performed, with the purpose of comparing them to "normal" simulations, for grains detaching from the following positions:

- Grains detach from the walls of MicroMED's sampling head;
- Grains detach from the walls of the first part of MicroMED's inlet, that is the farthest from the sensing region (here called "Wall 1");
- Grains detach from the walls of the mid part of MicroMED's inlet (here called "Wall 2");
- Grains detach from the walls of the final part of MicroMED's inlet, that is the closest to the sensing region (here called "Wall 3").

Figure 3.83 shows that the furthest the detachment occurs along the duct, the larger the position histogram is, to the point that grains cross the plane that includes the laser spot at a distance that is more than 3 times the dimension of the spot. In such region, laser light is tangibly less intense than in the spot. This aspect is significant, as it may explain the bimodal histograms. Moreover, given that, rather than a continuum of dimensions, the second peak is pretty localized at certain dimensions, it could be that grains deposit in a specific point of the ducts. Such analysis is still ongoing, so there are no definitive results; however, this phenomenon might explain the bimodal trend of the histograms under study. Table 3.7 shows mean and median distance from the center of crossing grains; it can be easily noticed that grains cross farther from the longitudinal axis of the duct when they detach closer to the spot. Results are here reported for the case of inlet-outlet misalignment. Similar results have been obtained for aligned ducts albeit less evident than for the misaligned case. For example, grains detaching from the "wall 3" segment of the inlet have a mean distance from the center of 723 μm and a median distance of 585 μm. Grains detaching from the same segment but for perfectly aligned ducts have a mean distance of 475 μm and a median distance of 471 μm. This supports the theory that the phenomenon obtained might be a combination of duct slight misalignment with detachment of grains from the walls. The misalignment, which in the CFD simulation is 100 μm, is far less significant in the integrated version of MicroMED since an alignment process has been made with positive results. Therefore, its effect on the results is interesting in theory but it should fortunately not be significant for MicroMED's PFM behavior.

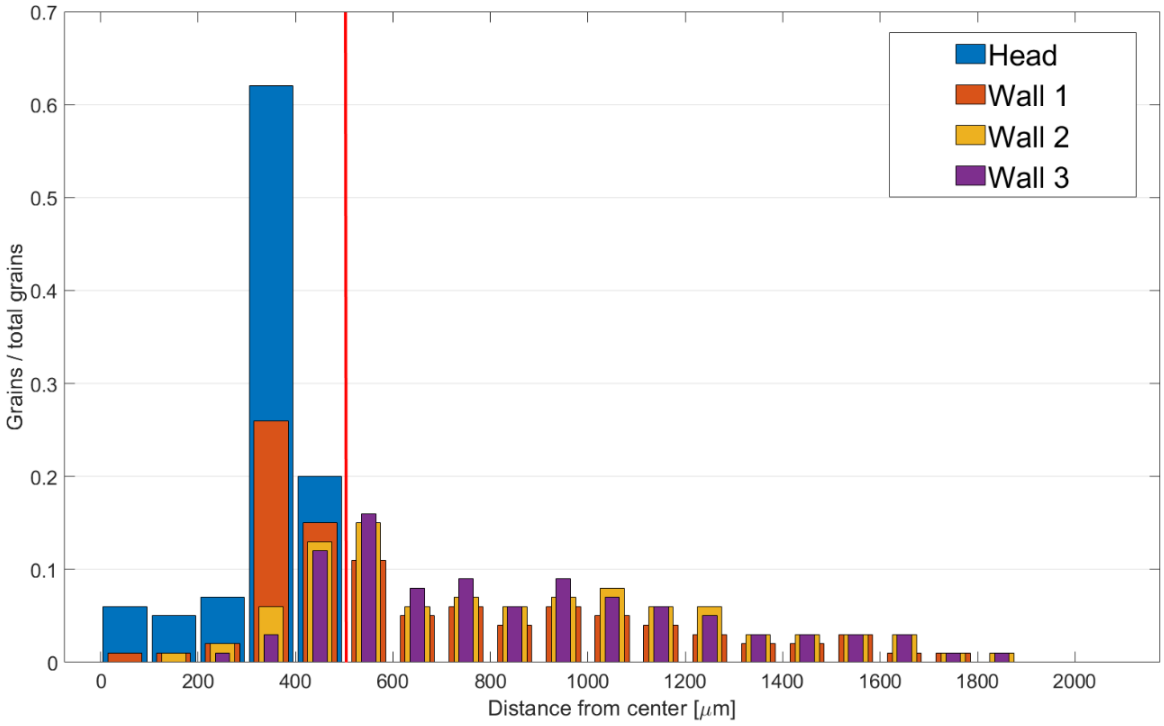

Figure 3.83 Position histograms for detachment of grains from MicroMED's inner walls at progressive distances from the sensing region of the instrument. It can be noted that grains detaching at a close distance from the sensing region can cross the spot very far from its center, well outside of the range that gives full (and calibrated) scattering of light. Distances of detachment that are progressively closer to the spot give progressively larger distributions. The figure refers to the following conditions: grain diameter 11 μm, pa = 6

mbar, Ta=Ti=295 K, Δp = 4 mbar, misalignment between the inlet and outlet ducts (this causes a further intensification of results, even though the effect is limited as Section 3.2.4.2 already said). The red line in the figure represents the border of the laser illuminated spot, showing that detached grains often cross the laser spot plane outside of the spot. Sampled grains are not reported in this figure; however, all 11 μm grains that are sampled from the outside cross the spot within 200 μm of the center according to the CFD analysis of Section 2.2.

Type of grains	Mean distance [μm]	Median distance [μm]
Detached from the head	254	325
Detached from "Wall 1"	504	401
Detached from "Wall 2"	662	538
Detached from "Wall 3"	723	585

Table 3.7 Mean and median distance from the spot for both regularly sampled and for sampled after detachment dust grains. These values are exacerbated by the misalignment between inlet and outlet.

Another aspect that leads to the deduction that this phenomenon could be the cause of the bimodal trend is that, in a series of consecutive acquisition, it has been observed that often the second mode of the histogram is not present for the first acquisition, while it is present for the following ones, and it is decreasing for further consecutive tests. In essence, the first acquisition is performed when there is huge availability of grains (i.e. immediately after injection of grains in the chamber). This means that MicroMED fills its memory with samples grains very fast; even if there were grains deposited inside, only a small number of them would be detected. This first run causes suction of grains that may deposit inside. Once the following run is performed with no additional injection of grains, the second mode appears in the histogram and a high percentage of the acquired grains belong to this second mode. This could be due to the high quantity of grains deposited inside, while the environment around MicroMED is not full of grains anymore because deposition has started for outside grains (there is usually a 2-3 minute time window between consecutive acquisitions, a time in which most of the grains in the surroundings of MicroMED deposit). As for the further acquisition, the grains deposited inside MicroMED reduce in number because the previous runs have already detached most of them, while there are less incoming grains that deposit and there are less incoming grains that are correctly detected. This means that the ratio of the number of grains that belong to the second mode to the total number of grains acquired during a run is minimum for the first test after injection, increases starting from the second test (with no active injection) and then gradually reduces because the deposited grains reduce on MicroMED's inner walls. Figure 3.84 shows an example of this possible behavior. The first points of the Figure are relative to consecutive injection cases (depicted as "11" in the figure), and this is why the second mode grows. There is always renewed availability of grains which increases the potential deposits inside. When tests are performed without active injection ("-11" in the figure) the aforementioned possible trend is observed.

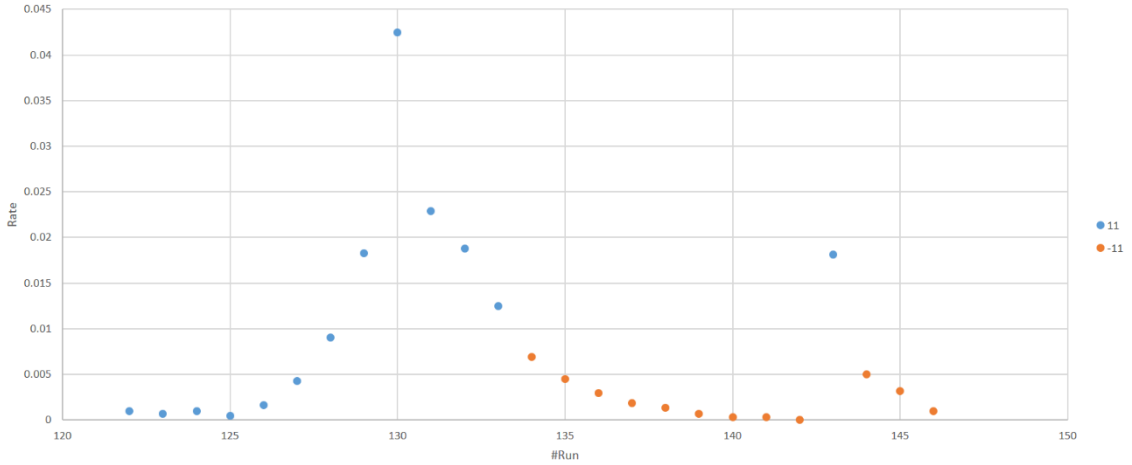

Figure 3.84 Evolution for consecutive MicroMED tests of the ratio of the number of grains belonging to the second mode to the total number of detected grains. For the first run, which has active injection of grains, the main mode is dominant. For the following runs, this ratio peaks and then gradually reduces until a new injection is performed. The figure is relative to 11 μm grains, but similar results have been obtained for other sizes.

Overall, this phenomenon is at the moment the most plausible explanation of the bimodal nature of such histograms. If this is the case, the issue will probably be not detrimental to MicroMED's efficiency on Mars for several reasons: 1) MicroMED runs are generally not consecutives but delayed by hours, 2) the phenomenon is generally most evident for large grains in the atmosphere, that are not expected to be relevant on Mars (for small grains the bimodal trend of histograms could happen but would be tough or even impossible to see because the peak would be at extremely low diameter values and masked by the instrument noise) and 3) large amounts of grains like the ones that are expected to create the issue only happen during dust storm (~ 30-40 particles/cm^3), while in normal haze conditions (~3-4 particles/cm^3) the deposition of grains should not influence the performances.

3.2.5 MicroMED performance tests in presence of wind – test campaign at the AWTS II simulator

MicroMED's performance tests in windy conditions have been partially discussed in Section 2.2.3.2. As Figure 2.54 showed, MicroMED was able to detect 20 μm diameter particles even at the highest possible wind speed for the facility (15 m/s), which confirms that the CFD model is conservative and that MicroMED's Flight Model better detects dust grains also in the presence of wind. Such preliminary analysis has then been deepened, and this section shows the further results obtained in this context. The section describes the Aarhus Wind Tunnel Simulator II, the facility located at the University of Aarhus, Denmark, where tests have been performed. Such tests have been performed in the framework of two test campaigns proposals approved and funded in the context of the Europlanet program (one

already performed, the other one to be performed in 2022) in which I was the principal investigator. After such brief description, test setup, execution and results are provided.

3.2.5.1 The AWTS II Facility

The Aarhus Wind Tunnel Simulator II (AWTS II, Holstein-Rathlou, C., 2014) is a facility located at the University of Aarhus, Denmark, where it is possible to perform tests in low pressure environment and in the presence of wind. The facility is able to reproduce extreme environmental conditions, specifically low temperature, high or low humidity, and reduced pressure. This facility is able to control wind flow, pressure, temperature, and gas composition with the purpose of allowing testing and calibration of sensors under a wide range of environmental conditions. The ATWS II is a unique prototype facility (Merrison, J.P., 2011; Rasmussen, K. et al. 2009). Low temperature wind tunnels are common in the aerospace and automobile industries; however, they have not been applied to metrology and there are not many low pressure wind tunnels in the world. Basic elements of the AWTS II is a climatic chamber housing a recirculating wind tunnel (Figure 3.85). The climatic chamber is made of a cylindrical vacuum chamber (2.1 m of inner diameter, 10 m in length) that can be depressurized up to 0.02 hPa and pressurized with gas (or air) up to 1000 hPa. A multilayer super insulation provides thermal insulation of the outer chamber from a relatively thin inner chamber wall. Although the outer chamber is made of mild steel, it has been coated with a zinc alloy in order to avoid rusting in the presence of humid air. The inner chamber wall is made of stainless steel, and other structures within the wind tunnel are made of aluminum, providing good resistance to high humidity. The facility has been constructed in three sections, one dedicated to wind generation on one end, a central section which houses the unit under test, that can be allocated on a thermal control subsystems consisting of a thermal plate, and the upwind section is designed for flow control, monitoring, and other forms of access. The wind tunnel is divided also vertically, into three sections. The midsection is actually the main wind tunnel, with the other two used for return flow (to recirculate the air/gas).

The chamber provides an adequate access to the sensors involved in the test. To this purpose, eight large access ports have been included within the test section; nine access ports are also available in other chamber sections. Figure 3.86 reports a schematic of the chamber as well as a picture to show its dimensions in relation to human operators. The facility is equipped with a suite of environmental sensors monitoring temperature, pressure and relative humidity monitoring. Of particular interest for our application is the wind speed monitoring system, which consists of a commercial FlowLite ® 2D laser Doppler anemometer (LDA) with high spatial and temporal resolution. This is interesting because the LDA uses tracer dust to monitor wind speed, and dust grains injected during our tests can work to this purpose. The presence of the LDA, which potentially allows to determine an estimation of dust concentration in the chamber, has also been used as a verification of MicroMED test results.

The wind generation subsystem consists of two (horizontal) fans mounted on a single (vertical) axle; each aluminum fan is 1.8m in diameter and driven by an electric motor. In

order to avoid exposure of the high power motor to the controlled environment of the chamber, the drive mechanism for the fan system has been mounted externally and coupled to the axle with the use of a commercially available magnetic coupling. Detailed description of the facility is provided in Holstein-Rathlou, C. et al., 2014.

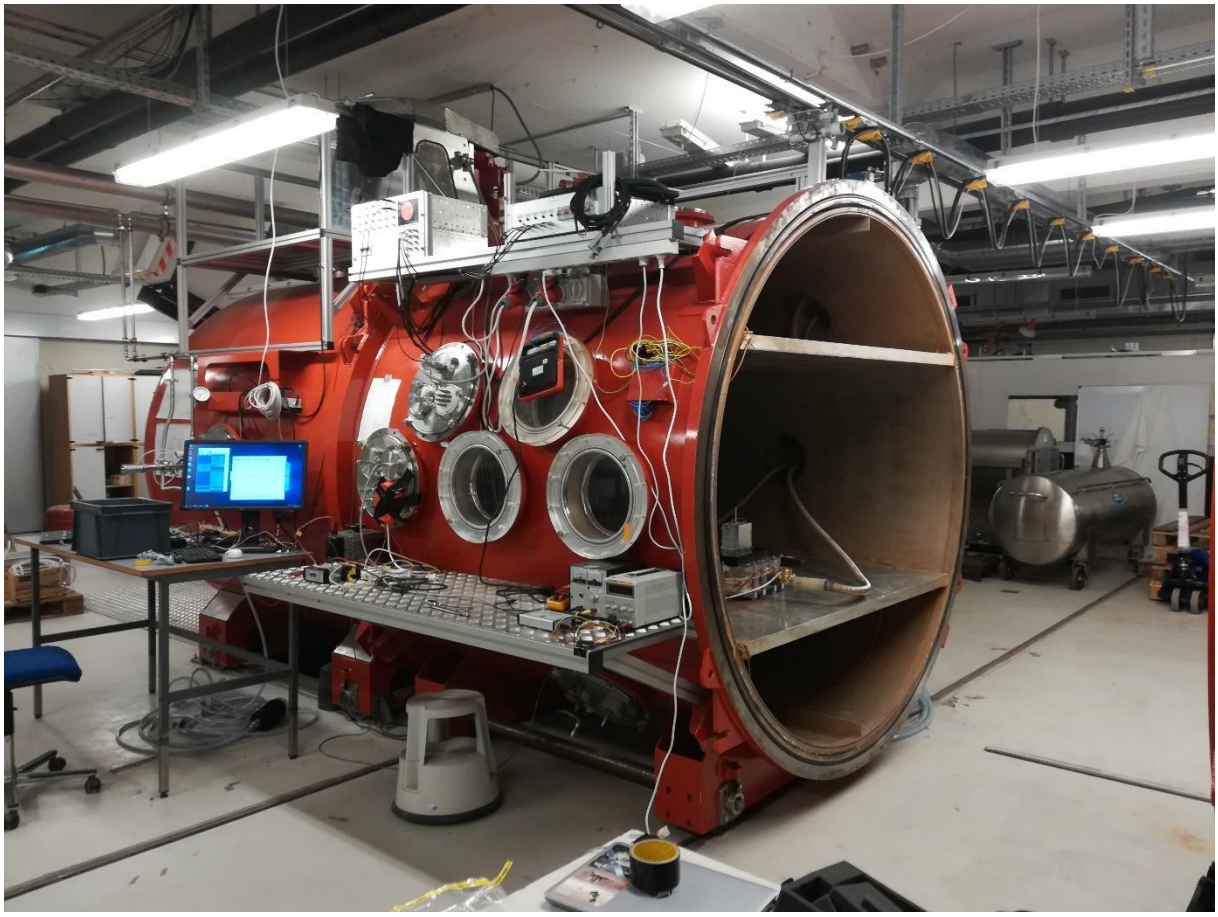

Figure 3.85 Outside view of the opened climatic chamber present at the AWTS II facility.

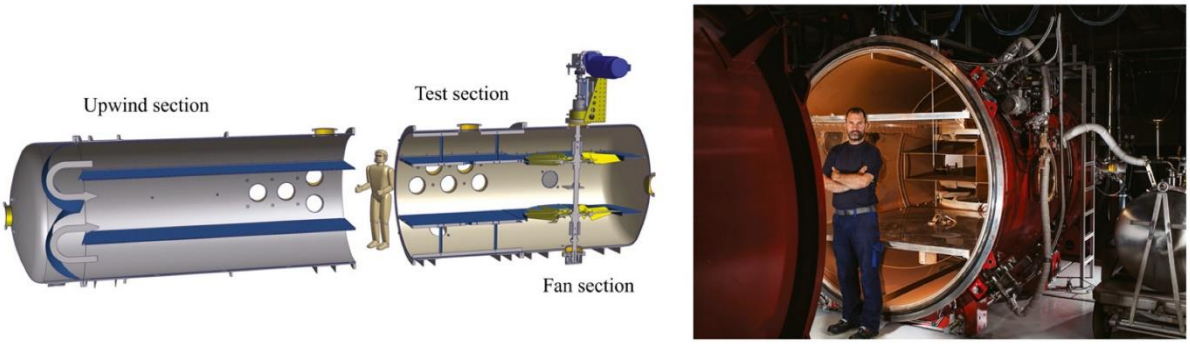

(a) *(b)*

Figure 3.86 Schematic drawing of the AWTSII wind tunnel (a) showing the upwind, test, and fan sections with a mannequin for size. Flow direction is illustrated. On the right, a picture of the wind tunnel (b), in which fans can be seen in the background, as well as the external part of the cooling system. This figure is taken from Holstein-Rathlou, C. et al., 2014.

3.2.5.2 MicroMED's installation at the AWTS II Facility

MicroMED was installed in the AWTS II Martian Chamber as shown in Figure 3.87. it was positioned in the midsection of the chamber, so that the main flow could invest the instrument, minimizing wall effects. The instrument was placed on a cold plate, providing the possibility to modify the instrument temperature in accordance with MicroMED's already known operative temperature range (-20 °C, +40 °C). Tests were performed at three main temperatures (-15°C, +22°C and +35°C), keeping a 5°C margin with respect to the operative range, to avoid stresses on MicroMED sensitive subsystems, especially its laser. The interest in changing temperatures is due to the fact that the CFD analysis of the instrument (Mongelluzzo, G. et al., 2018, 2019a, 2019b, 2019c; see also Section 2.1.3 and 2.2.3) has shown that instrument temperature could be an influential parameter on the MicroMED detecting performances. While instrument temperature was considered in the analysis, ambient temperature was not. Such parameter is not influential on performances (See Sections 2.1.3 and 2.2.3 mentioned above), moreover the presence of the thermal cover on the ExoMars lander significantly reduces the effect of daily and seasonal ambient temperature variations at the surface of Mars, which is usually a serious issue for instrumentation. For this reason, all tests have been performed at the laboratory temperature of about 15°C (The low pressure environment inside the Martian Chamber has produced a slight reduction of this temperature, however the parameter was not taken into account during the analysis). MicroMED was installed roughly 4 meters downwind and half a meter below the dust injection valve. The injection was indeed performed using a gate valve on the side of the chamber. Once the chamber fan is activated and fluid speed reaches the desired value, dust is injected orthogonally to the longitudinal axis of the chamber and dragged by the flow toward the instrument (Figure 3.87). About 1 g of dust grains was introduced into the chamber with each injection, and multiple acquisitions (up to 4) were performed with a single injection. The Laser-Doppler Anemometer (LDA) installed at the facility was used to verify that dust grains reach the proximity of MicroMED sampling head. LDA data were stored for comparison with dust concentration data obtained by MicroMED. The LDA was installed on the side of the chamber, so the laser beams could be focused close to MicroMED sampling head, passing through a window on the side of the chamber (Figure 3.88). LDA data also provided verification of the fluid velocity during tests. During this test campaign, velocity was set in the 0.5-15 m/s range. This velocity range is comparable with expected conditions on Mars. For example, the Curiosity Rover's environmental monitoring station has indicated that wind on Mars is usually present, with average values around 5 m/s and gusts that can surpass 10 m/s (Gómez-Elvira, J. et al., 2014).

Tests were performed with the same spherical calibrated monodisperse grains of SiO_2 used for performance tests, with sizes going from 11 μm to 20 μm in diameter, as well as with polydisperse samples including sizes over the upper measurement limit of the instrument. Tests with the latter sample were conceived to determine whether the instrument was able to detect such (large) grains, even if they would cause the saturation of the signal coming from MicroMED photodiode (since they partially exceed the projected instrument sampling

range). The focus on the upper size range of the instrument is due to the indication of the CFD analysis that such grains are tougher to be sampled, especially for increasing wind speed (Mongelluzzo, G. et al., 2019a). As an example, results will be shown for 11 μm dust grains, because of their intermediate dimension in the instrument measuring range. Comparable results have also been obtained for other grain sizes in the MicroMED measuring range. The results will be shown in terms of the instrument acquisition rate [Hz] and in terms of the ability of MicroMED to fill its memory with grain data, in order to determine the influence of each input parameter on the instrument ability to detect dust grains. The acquisition rate is representative of the number of grains detected each second by MicroMED. This parameter is a solid estimation of MicroMED ability to detect dust grains, even though its knowledge is not enough to determine the instrument efficiency with respect to the availability of grains around the sampling head. LDA data is currently under analysis in order to provide a quantitative efficiency estimation, however some preliminary indication can be derived from an observation of such data, as will be presented hereafter.

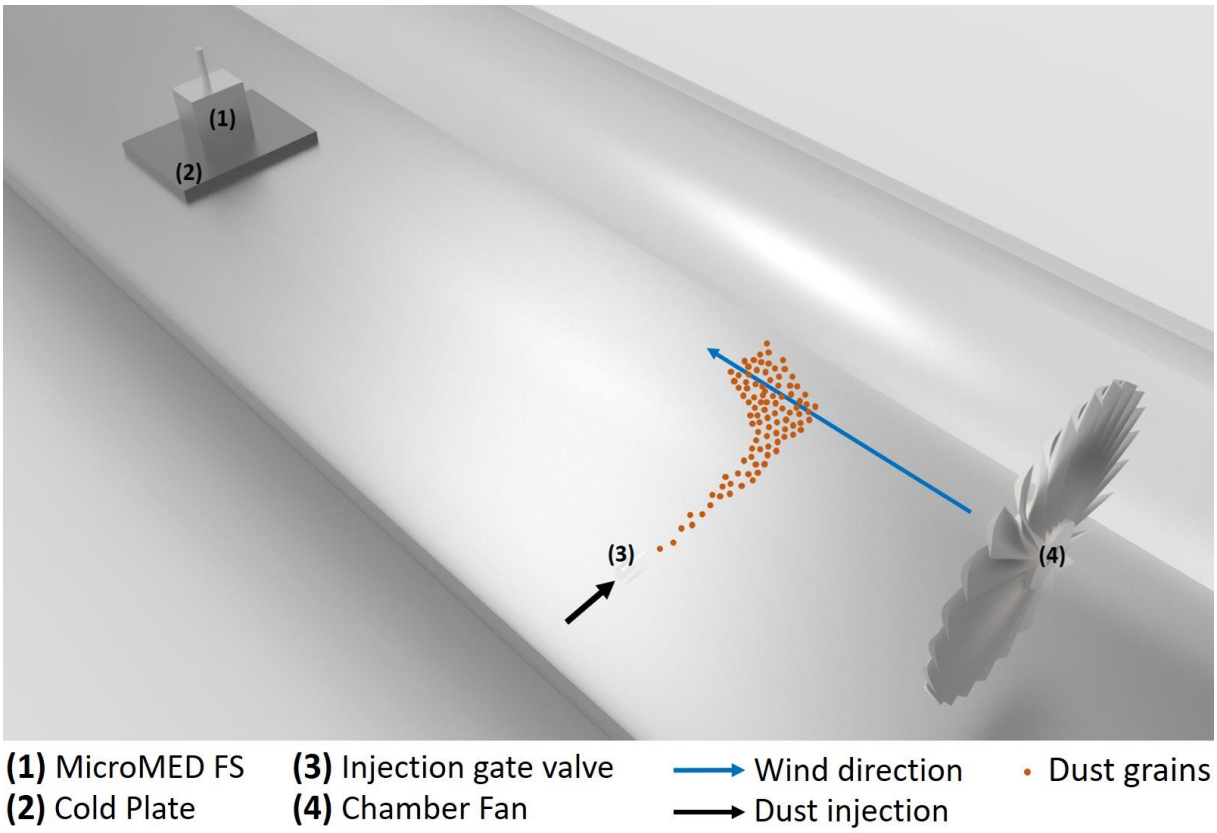

Figure 3.87 Schematic of the test setup inside the AWTS II Martian Chamber.

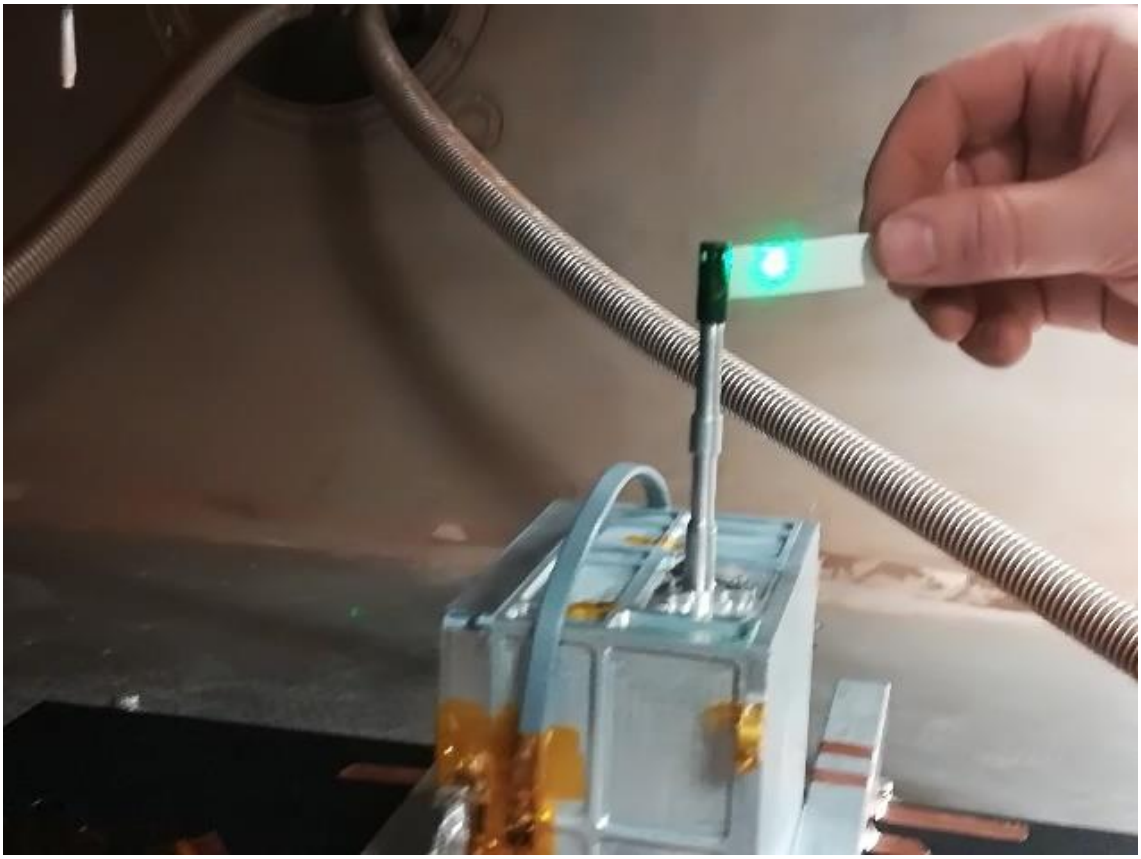

Figure 3.88 Position of the LDA focus with respect to MicroMED inlet.

3.2.5.3 Results of the test campaign

Tests involved both monodisperse and polydisperse samples of dust grains. The presented analysis focuses on results obtained from tests with monodisperse particles. In particular, for each grain size the instrument was tested with constant wind speed throughout each test, but increasing wind speeds from one test to the other. Figure 3.89 shows the evolution of MicroMED's acquisition rate with temperature. The rate/temperature correlation is well described by a linear fit *"$y = a + bx$"* in which the slope b of the curve, along with its standard deviation, is reported in the figure.

Figure 3.90 shows the number of signals acquired by MicroMED in terms of the percentage of the total memory available. It can be noted that the instrument is able to acquire grains for all the wind speeds tested. The MicroMED trend is also compared with the amount of LDA counts.

We have to take into account that each acquisition has had a different time duration, since, as already underlined, once the memory is filled the run is immediately terminated, while in case that the memory is not completely filled, the run duration is set by software to a maximum value that is usually either 60 or 120 seconds. It has then been decided to normalize results for the run duration, evaluating MicroMED's acquisition rate. This rate is presented in Figure 3.91 as a function of the wind speed. In the figure, MicroMED's

acquisition rate is compared with the LDA counts like in Figure 3.90. Here, the windy cases are plotted, hence for speeds > 4 m/s, that are the main focus of the current test campaign and that are interesting for the Martian predictions.

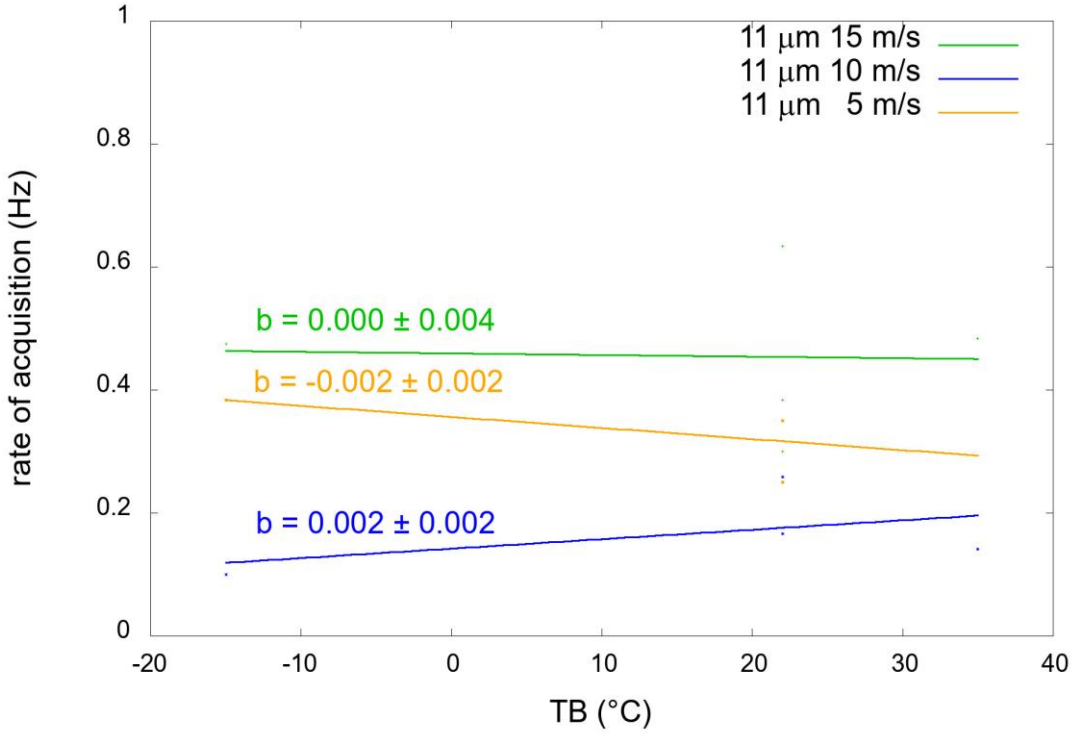

Figure 3.89 Influence of instrument temperature on MicroMED acquisition rate. A simple linear fit "y = a + bx" has been performed, with a resulting coefficient b compatible with 0 for each wind speed.

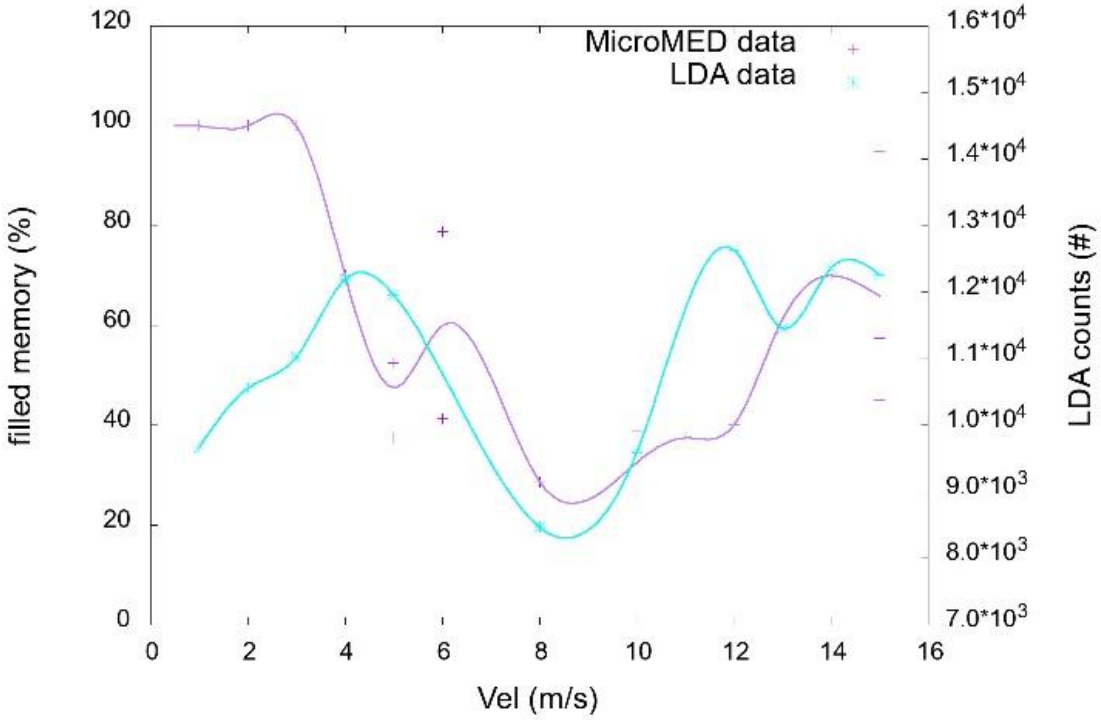

Figure 3.90 The number of signals acquired by MicroMED (purple curve) expressed as the percentage of instrument filled memory in function of the wind speed. On the second axes the number of LDA count is presented (turquoise curve). The left scale is relative to the percentage of filled memory, the one on the right is relative to the LDA counts.

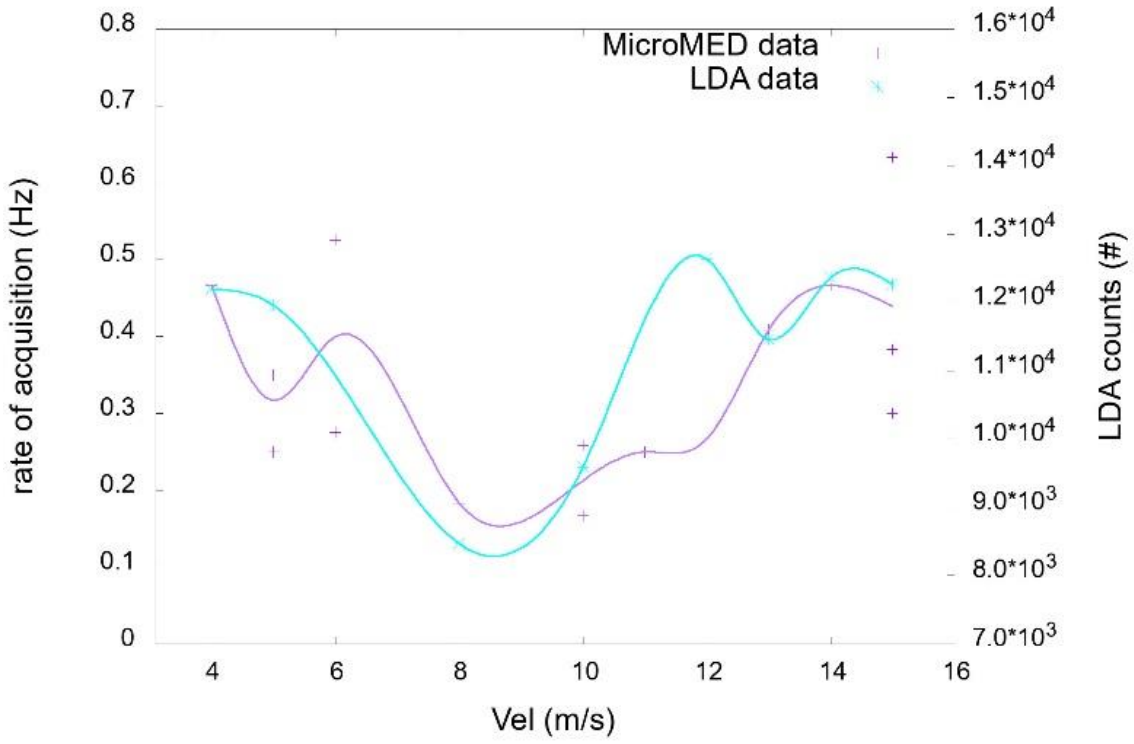

Figure 3.91 MicroMED's acquisition rate average trend compared with the number of grains detected by the LDA and its average trend for windy conditions (V > 4 m/s). The scale on the left is related to the acquisition rate trend, while the one on the right is relative to the average number of grains detected by the LDA at each wind velocity. It can be noted that MicroMED and LDA data share a similar trend for intermediate wind velocities. MicroMED's acquisition rate has overcome expectations, as a reduction with wind speed was expected, while it can be appreciated that the rate is stable.

3.2.5.4 Discussion of the results

Figure 3.90 shows the evolution of MicroMED acquisition rate with temperature. It has been observed that the influence of instrument temperature on the acquisition rate is extremely marginal. A linear fit *"y = a + bx"* is well suited to describe this relation, and the slope *b* of the curve, which is reported in the figure, is compatible with zero within the uncertainties. This is an important result as it allowed a significant simplification of the calibration procedure. The limited impact of temperature allowed indeed an easier prediction of the instrument behavior during the mission, since the instrument temperature variations are now expected to have limited impact on performances. This adds to our expectation that the change of the seasons and the day-night cycle on the planet, which can cause a significant temperature gradient on Mars surface, do not significantly alter MicroMED behavior, because of the presence of the thermal cover. This result also impacts the current analysis, as it allows to consider all runs performed in the campaign, even at different temperatures, as a common data set, helping to determine the influence of wind speed on the instrument's acquisition rate with greater accuracy, since the statistical sample available has now been increased.

The verification of MicroMED performances for different wind speed scenarios can be appreciated in Figure 3.90 and Figure 3.91. Figure 3.90 shows that MicroMED is able to detect dust grains for all the wind speeds tested. MicroMED's memory is completely filled in few seconds for wind speed under 3 m/s. This means a huge sample of grains is obtained. The inertia of the grains is indeed very low for such speeds and grains can thus be easily caught by the instrument. These data confirm the positive results obtained at the INAF – OAC premises (See Section 3.2.3 for example), where numerous low wind speeds tests have already been performed. A drop of the percentage of filled memory is visible for higher wind speeds, with a minimum value around 8 m/s. After the minimum, an increase can be appreciated for wind speeds rising up to 15 m/s. Such increase is probably due to the injection system as increased wind speeds are probably able to detach grains settled during previous tests from the chamber walls. These grains are then dragged into the main flow, increasing the number of available grains. However, for each wind speed tested, MicroMED has acquired a significant amount of grains, giving enough statistics for the study of the environmental dust distribution.

In order to account for the different duration of the runs, as a MicroMED's acquisition rate has been evaluated, and its average trend is reported in Figure 3.91 (purple curve). The figure shows a comparison between the average MicroMED's acquisition rate trend and the average trend of the LDA counts (turquoise line). This figure can be used to describe MicroMED's performances in windy (V > 4 m/s) conditions, whose verification was the main goal of the test campaign. A significant decrease of MicroMED's acquisition rate with wind velocity is expected, however it can be seen that its value is stable, which exceeds expectations (Mongelluzzo, G. et al., 2019a). The acquisition rate actually experiences a slight increase with wind velocity, which is due to the injection system (as already described) and to the set-up configuration of the experiment. The peculiar trend of Figure 3.91 will demand additional investigation. The reduction of the number of grains acquired for intermediate wind speeds can be influenced by the higher grain inertia, but it is probable that it is mostly due to the characteristics of the injection system. LDA data indeed confirm the trend detected by MicroMED. After an initial minimum, which is due to the small wind drag at low speeds, the number of grains available in the chamber reach a maximum at a speed of about 4 m/s. The LDA counts then decreases with a minimum around 8 m/s, and finally experiences an increase for higher speeds. The correspondence between MicroMED and LDA data hints at the fact that MicroMED collects grains with comparable accuracy for all wind speeds, and that the reduction of the instrument's acquisition rate and consequently of the ability to fill its memory is due to a lesser availability of grains rather than to a reduction of the efficiency. The quantitative evaluation of the MicroMED efficiency is currently still in progress. Such quantification will shed light on these aspects and verify whether, as expected, the instrument has similar efficiency throughout the wind speed range tested.

There can also be a contribution of the grain size to the results. Overall, for smaller dust grains, due to the low deposition rate (grains in the lower range of the instrument are expected to remain suspended for minutes), it was experienced that huge amounts of grains reach the proximity of MicroMED sampling head, driven by the wind speed, even for low velocities. On the other hand, large dust grains are heavier, so when wind speed is not high

enough, they tend to deposit on the chamber floor before reaching the proximity of the instrument, becoming unavailable. A CFD analysis on the topic is planned, aimed at describing the chamber fluid dynamics and quantifying the phenomena that have been detected during the test campaign.

As already stated, efficiency rates are still unavailable as an in-depth analysis of the LDA data is needed to provide an estimation of the dust grain density in the atmosphere surrounding MicroMED and compare it with the grain density detected by the instrument. Currently, only the trends of the curves for the two instruments can be compared. A detailed analysis of data is currently ongoing in order to provide a quantitative comparison of the two curves.

3.2.5.5 Brief summary of the results of the test campaign

In order to complete the instrument characterization, tests in windy conditions were needed. To this purpose, a test campaign was performed at the AWTS II facility at the Aarhus University (Denmark). MicroMED was tested in a dusty environment with winds up to 15 m/s, conditions that are similar to the ones expected on Mars. Particular emphasis was given to dust grains in the upper region of the instrument measuring range. Such grains are indeed more difficult to be collected because of their higher inertia, and the instrument ability to detect such grains had to be verified, since the preliminary CFD analysis of performance indicated potential issues in the detection of large grains.

Results show that temperature has a marginal influence on the instrument's acquisition rate, so during the analysis of the influence of wind speed, runs for all instrument temperatures were considered as a common data set. This aspect is significant as it also simplifies the ongoing MicroMED calibration procedure. On the other hand, the variation of the wind speed has a strong influence on the instrument acquisition rate. For low wind speeds ($V < 4$ m/s) the positive results obtained at the INAF – OAC premises have been confirmed. For high wind speeds ($V > 12$ m/s), the focus of this test campaign, it was experienced that large amount of grains are detected, underlining that MicroMED has overcome expectations. For intermediate wind speeds, a lesser availability of grains was experienced. This reduction detected by MicroMED has been confirmed by the LDA measurements, implying that the instrument might have similar detecting efficiency for all velocities tested, as well as throughout its measurement range. Actually, in opposition with the expectations, the acquisition rate is stable with velocity and increases for high wind speed, which is a very positive outcome. This peculiar trend, that indicates intermediate wind speed cases as the ones with the minimum grain availability, highlighted the possible influence of the dust injection system on the results. The analysis of such influence is already planned, as a series of CFD runs will try to shed light on this aspect. As for the quantification of the instrument sampling efficiency, it will be possible to quantitatively compare such results with LDA data (the quantitative analysis of the LDA data is currently ongoing). The tests described herein show that MicroMED is able to collect a sufficient sample of grains and

throughout its sampling range even in presence of strong winds, showing that the instrument has outperformed expectations.

3.2.6 Dust concentration as measured by MicroMED

An important aspect of the analysis of tests on MicroMED has been the development of reliable methods to evaluate dust concentration from MicroMED's measures. In order to develop a method for the calculation, results coming from tests have been integrated with CFD simulations to provide a complete scheme. The following sections will provide an overview of the method developed for the evaluation of MicroMED's volumetric flow rate. My role in this part of the work has been of co-responsible of the work (with PoliMI) and of both developing the method and perform the CFD analysis.

A key aspect of the analysis has been the determination of the relationship between two different Δp values, here labeled as "Δp1" and "Δp2". Labeling as "p_a" the ambient pressure (outside of MicroMED), as "p1" the pressure value inside MicroMED's optical head and as "p2" the pressure value at the outlet section of MicroMED, which coincides to the inlet section of MicroMED's pump, the two Δp values are the following:

- Δp1 is the pressure difference between the outside of the instrument and the inside of MicroMED's optical head: $\Delta p1 = p1 - p_a$;
- Δp2 is the pressure difference between the outside of the instrument and the inlet section of the pump: $\Delta p2 = p2 - p_a$.

Figure 3.92 shows a section of MicroMED and clarifies at which pressures p_a, p1 and p2 refer to. The P Ratio = Δp1/Δp2 is extremely important because, while Δp2 is the parameter used in the CFD simulations to vary the operating conditions of the pump, Δp1 is instead the only Δp value that can be directly measured in MicroMED. Figure 3.92 indeed shows that the pressure sensor of MicroMED, which in the figure is highlighted in red, is a differential pressure sensor exposed to the pressure in MicroMED's outer box, which is equal to ambient pressure, and to the pressure inside MicroMED's optical head (p1). In synthesis, MicroMED's pressure sensor measures Δp1 while simulations vary Δp2, thus their relationship is key in order to correctly relate and compare results of simulations and of laboratory tests in order to develop a solid estimation of MicroMED's volumetric flow rate.

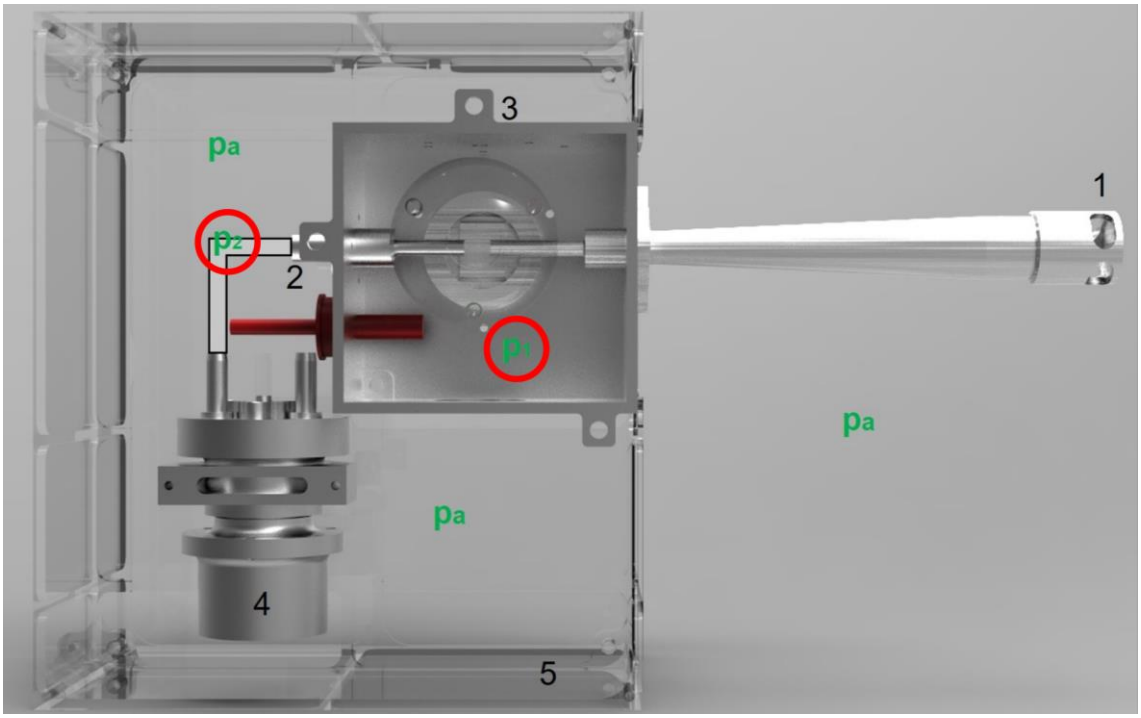

Figure 3.92 MicroMED section. In the figure, the most important components of MicroMED are shown: (1) Sampling head, (2) Outlet section of MicroMED, which coincides with the inlet section of the pump, (3) Optical head (internal box), (4) Pump, (5) External box. The MicroMED pressure sensor is highlighted in red. Here can be noted which region of MicroMED p_a, p1 and p2 refer to.

The forthcoming sections will show how this parameter is key in the evaluation of MicroMED's volumetric flow rate and thus for the measurement of dust concentration.

3.2.6.1 CFD evaluation of the effect of environmental parameters on volumetric flow rate

CFD runs at different values of the main environmental parameters have been performed with the purpose of determining the influence of each parameter on the flow rate. Three main influential parameters have been individuated (ambient pressure p_a, instrument temperature T_i, the aforementioned $\Delta p2$). Ambient temperature (T_a) has been considered in the analysis; however, the effect of ambient temperature on MicroMED performances, as already evidenced by the analyses of Sections 2.1 and 2.2, is negligible. Runs have then considered a constant ambient temperature value of 20°C, while p_a has been varied from 6 to 15 mbar, T_i from -15°C to +35°C, in accordance with MicroMED's operating conditions, and $\Delta p2$ from 1 to 5 mbar.

Figure 3.93 shows the effect of ambient pressure on volumetric flow rate. Variations are significant for high values of the pump generated Δp ($\Delta p2$). For the values of interest (that range from $\Delta p2 = 2$ mbar to $\Delta p2 = 3$ mbar, which are the values that are usually found during MicroMED's tests) such variations go from ~ 2% to ~ 7%. It has to be underlined that, in order to obtain a good measurement of dust concentration in the chamber (See Section 3.2.1.6), it is

preferable to perform a single injection and a single test so that the sample taken for the analysis of the chamber dust concentration is not contaminated. This means that, since tests always begin at ~ 6 mbar, the real effect of ambient pressure on tests should be negligible (ambient pressure at the end of tests is usually around 7 mbar, for which variations of ~ 1% of the volume flow rate are expected).

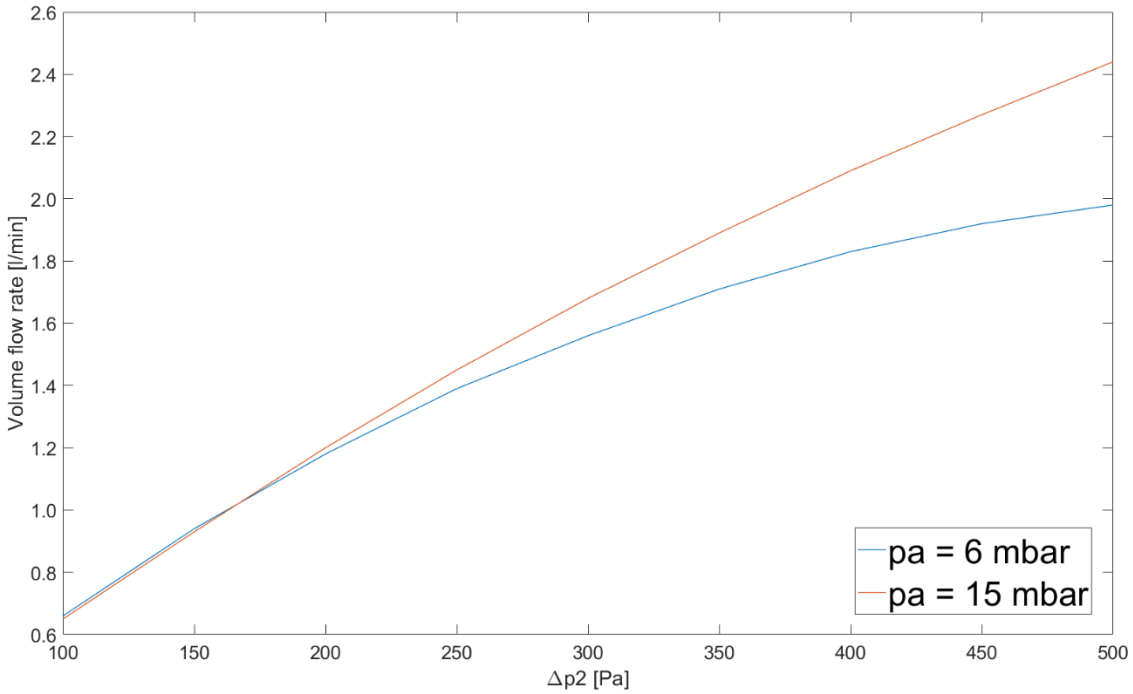

Figure 3.93 Effect on ambient pressure on volumetric flow rate. Variations are more significant for higher values of the pump generated Δp (Δp2).

Figure 3.94 shows the effect of instrument temperature on the volume flow rate. The effect is evaluated at different values of Δp2, even though the effect of instrument temperature is mostly independent from such parameter: for a 50°C difference in instrument temperatures, variations are ~21%, ~20%, ~19% for Δp2 = 2, 3, 4 mbar respectively. Instrument temperature is an influential parameter in the analysis. Anyway, its value is measured through dedicated temperature sensors (PT) and stored in the housekeeping data.

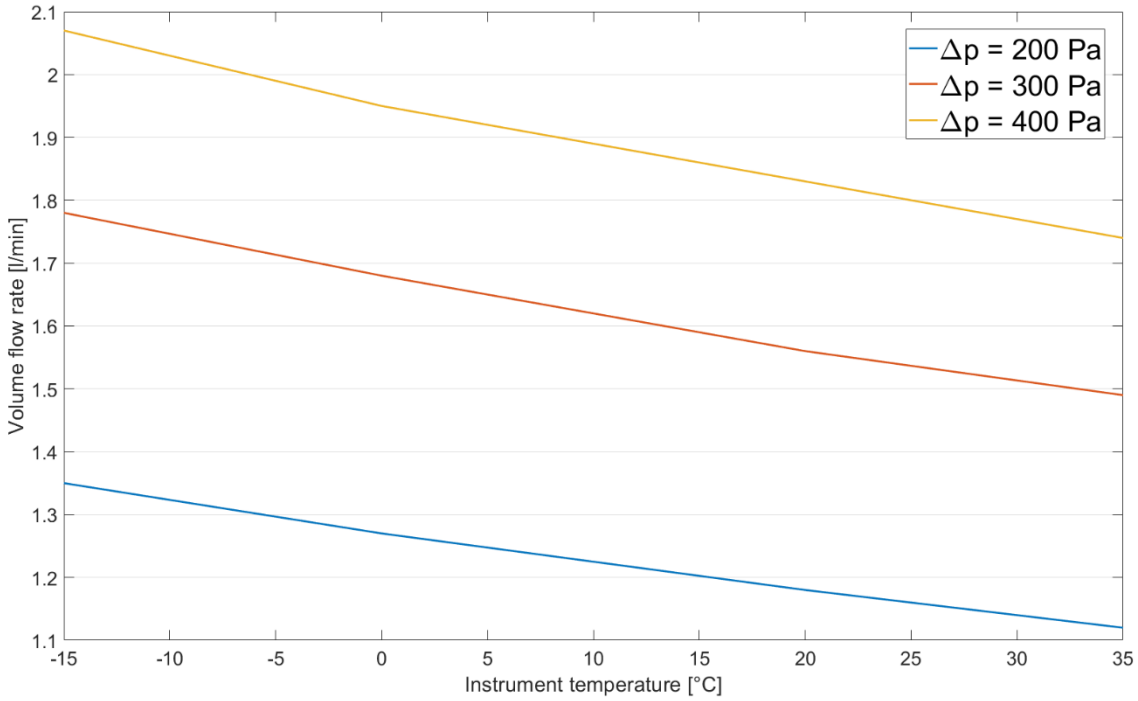

Figure 3.94 Effect of instrument temperature on volumetric flow rate.

3.2.6.2 Comparison with volume flow rate measurements made by PoliMI

Saggin et al. 2020 have developed a method to measure volume flow rate in low pressure conditions. The method can be tailored to suit MicroMED. However, the method relates the instrument volume flow rate to the pressure difference (Δp2) between the inlet and outlet sections of MicroMED, which is generated by the instrument's pump. Thus, a differential pressure measurement is needed in order to accurately estimate the volume flow rate. Due to mission constraints, it was only possible to install a differential pressure sensor in MicroMED's optical head (Figure 3.92), and it was experienced that the Δp between outer atmosphere and MicroMED's optical head (Δp1) is different from that needed for the evaluation of the volume flow rate (i.e. the Δp between the outside environment and the outlet section of the instrument, here labeled as Δp2, as said before). The method developed by Saggin et al. implies a different dynamics than what physically happens on MicroMED: in essence the measurement is performed by means of a bellow, which means that in the case of the measurement, which have been performed at the MetroSpaceLab premises in Lecco (which includes the thermal vacuum and the vibration facilities that will be described in Section 3.3), the pressure difference between the inlet and the outlet sections of MicroMED is actually an over-pressure rather than a depression (Please refer to Saggin et al. 2020 for a complete description of the methods adopted). Given the different conditions in which tests have been made with respect to the actual MicroMED operating conditions, only a few points allow a direct comparison between the CFD runs performed on MicroMED and the tests performed in Lecco. Such points have been reported in Table 2.1. We can notice that there is

good agreement between tests and CFD simulations, especially considering the approximations needed to compare the two results. There are only few percentage points of difference and the sign of those variations are coherent. Overall, these results validate the CFD model, therefore in the following parts of the analysis the CFD runs have been used to fill the voids and provide a complete method for the derivation of the volume flow rate of MicroMED.

Case	p inlet* [mbar]	p outlet* [mbar]	Q [l/min]	Difference [%]
#1 CFD	6	3	1.68	
#1 PoliMI	3	6	1.77	+5.1%
#2 CFD	8	5	2.28	
#2 PoliMI	5	8	2.43	+6.2%

Table 3.8 Comparison between results obtained from tests performed at the MetroSpaceLab premises in Lecco and the CFD simulations. Such results allowed the validation of the CFD model. Notice that, since the method developed by Saggin et al. 2020 requires the presence of a bellow which generates an over-pressure rather than a depression, inlet and outlet pressure values are inverted in the two cases, but the cases themselves are directly relatable.

3.2.6.3 Determination of the ratio of pressures P

As already discussed in this work, an evaluation of the instrument volume flow rate is needed in order to derive dust concentration. However, such estimation is quite challenging, since the classic instrumentation used at ambient conditions on Earth cannot be used, as the instrument is designed to work in Martian atmospheric conditions, i.e. very low atmospheric pressure and density (0.6-0.8% and 1.4-1.8% of Earth's, respectively, Gómez-Elvira, J. et al., 2014). Such issue leads to the necessity to develop a custom method for the estimation of volume flow rate.

As said before, Saggin et al. 2020 have developed a method for the evaluation of MicroMED's volume flow rate; however, this method relates the volume flow rate with the $\Delta p2$, while MicroMED's pressure sensor measures $\Delta p1$. This aspect highlights the need for an investigation of the relation between $\Delta p1$ and $\Delta p2$. Knowing the value of this ratio for every combination of environmental conditions would provide the information needed to use the results obtained by Saggin et al. 2020 and derive volume flow rate values for every test performed on MicroMED. In order to have a preliminary estimation of this ratio ($P = \Delta p1/ \Delta p2$), the CFD simulation, that has been designed and discussed in Section 3.2.6.1, has been analyzed considering the main influencing factors on the instrument's volume rate, which have been identified as:

- Atmospheric temperature (T_a);
- Atmospheric pressure (p_a);

- Instrument temperature (T_i, which can be different from Ta since the instrument will be installed on the ExoMars Surface Platform under a thermal cover, limiting its temperature range).

In the framework of this evaluation, the 2^k factorial model can be used to provide, starting from a limited number of CFD simulations, an estimation of the effect of environmental parameters on the P ratio.

3.2.6.3.1 CFD Model and Evaluation of the influential parameters on the P ratio

Given that the simulations describe laboratory conditions, Earth gravity was considered instead of Mars' one. Ambient temperature was considered constant at 20°C given that temperature is controlled in the laboratory. Because of the ability to control ambient temperature, its effect on the results of the analysis can be neglected. Instrument temperature has been considered in the MicroMED operative temperature range (-20°C, +40°C) with a 5°C margin, as usually considered during laboratory tests. The ambient pressure values are comparable with the expected atmospheric values for Mars and are reproduced inside a Martian Chamber, also able to reproduce the Martian atmospheric composition (Cozzolino et al., 2020).

The parameters considered for the 2^k factorial design are, as already stated, T_a, p_a and T_i whose limit values are described in Table 3.9. It has to be underlined that only single measurements are performed in the dust concentration analysis of MicroMED. This means that both injections and tests are not repeated consecutive times. As a consequence, the range of ambient pressure considered has been reduced to 6-10 mbar instead of 6-15 mbar, since the injection, which is responsible for the growth of the value of pressure in the chamber (given that a CO_2 is responsible for the injection itself, see Section 3.2.1.4), is performed only once in such tests.

Parameter	Min Value (-1)	Max Value (+1)
Δp2 (A)	1 mbar	5 mbar
Ti (B)	-15°C	+35°C
pa (C)	6 mbar	10 mbar

Table 3.9 Input limit values for the 2k factorial design analysis performed.

3.2.6.3.2 Setting the 2^k factorial design

The 2^k factorial design is useful to quantify the impact of different parameters on the P ratio. It allows to only consider the limit values of parameters, and differently to a simple screening design, it takes into account the interaction among parameters which is expected

to have an impact. Given that the data considered in this report comes from CFD simulations, whose results are deterministic, there are no repetition for each case, meaning that $2^k r$ factorial model is not needed. This aspect also leads to the impossibility to perform a related ANOVA. Table 3.10 reports the values of the P ratio of pressures as function of the factors of interest considered in the analysis.

Δp2	**1 mbar**		**5 mbar**	
Ti/pa	**6 mbar**	**10 mbar**	**6 mbar**	**10 mbar**
-15°C	0.498387	0.513237	0.371729	0.491095
35°C	0.496763	0.507198	0.367598	0.467009

Table 3.10 Values of the P ratio for the limit values of the considered factors of interest: Δp2 (A), Ti (B) and pa (C).

3.2.6.3.3 Results of the 2^k factorial design analysis

Results can be synthetically expressed by means of the following Signs Table (Table 3.11). The average value of the P ratio is found to be 0.464127 (highlighted in red). The values corresponding to each case can be found in the column "Y" (values are highlighted in green), while the coefficients needed for the regression model are highlighted in orange.

It can be easily noticed that the factor B (Instrument temperature) and its interactions have significantly smaller coefficients than the other two factors of interest. The effects of each factor have been quantified by means of the allocation of variation.

I	**A**	**B**	**C**	**AB**	**AC**	**BC**	**ABC**	**Y**
1	-1	-1	-1	1	1	1	-1	**0.498387**
1	1	-1	-1	-1	-1	1	1	**0.371729**
1	-1	1	-1	-1	1	-1	1	**0.496763**
1	-1	-1	1	1	-1	-1	1	**0.513237**
1	-1	1	1	-1	-1	1	-1	**0.507198**
1	1	-1	1	-1	1	-1	-1	**0.491095**
1	1	1	-1	1	-1	-1	-1	**0.367598**
1	1	1	1	1	1	1	1	**0.467009**
3.713015	**-0.31815**	**-0.03588**	**0.244062**	**-0.02055**	**0.193493**	**-0.02437**	**-0.01554**	**Total**
0.464127	**-0.03977**	**-0.00449**	**0.030508**	**-0.00257**	**0.024187**	**-0.00305**	**-0.00194**	**Total / 8**

Table 3.11 Signs Table for the case under analysis.

3.2.6.3.4 Allocation of variation

In order to quantify the effect of each factor on the results, the allocation of variation procedure can be performed. It consists of the calculation of the total sum of squares (SST) and of the sum of squares relative to each factor, as well as their interactions. The total sum of squares SST can be computed by means of the following equation (k=3 since we have 3 factors of influence):

$$SST = 2^3(q_a^2 + q_b^2 + q_c^2 + q_{ab}^2 + q_{bc}^2 + q_{ac}^2 + q_{abc}^2) \quad [9]$$

Applying this formula, the sum of squares obtained for our case study are shown in Table 3.12.

SS	Value	% of explained variation
SST	0.025096586	-
SSA	0.012652717	50.42
SSB	0.000160929	0.64
SSC	0.007445761	29.67
SSAB	5.28071E-05	0.21
SSAC	0.004679945	18.65
SSBC	7.42386E-05	0.30
SSABC	3.01897E-05	0.12

Table 3.12 Sum of squares for the case study under consideration and percentage of explained variation for each factor of interest and for their interactions.

It is clear that instrument temperature has basically no effect on the value of P, while Δp2, ambient pressure and their interaction explain 98.74% of the total variation. The large value obtained for the interaction between Δp2 and pa might hint at the presence of an eventual extra factor not considered in this analysis. It is interesting to underline that while instrument temperature has a role in the relation between volume flow rate and Δp2, it has not in the relation between volume flow rate and Δp1 which is actually what is interesting to us since Δp1 is directly measured by MicroMED.

3.2.6.4 Determination of the P- Δp1 relationship – method and flow chart

The 2^k factorial design analysis allowed to eliminate instrument temperature from the influential parameters in the search for the P- $\Delta p1$ relationship. Such relationship characterizes the relation between the $\Delta p1$ measured during tests and the volume flow rate of MicroMED. The analysis has thus been completed only considering the two remaining factors of influence: $\Delta p1$ and p_a. Starting from these parameters, a matrix can be obtained crossing the different possible values of P derived by CFD simulations. Such matrix is reported in Table 3.13.

Δp2/pa	**6 mbar**	**7 mbar**	**8 mbar**	**10 mbar**
100	0.4973	0.5012	0.5045	0.5099
150	0.4873	0.4941	0.4997	0.5062
200	0.4763	0.4864	0.4947	0.5082
250	0.4638	0.4775	0.4886	0.5065
300	0.4494	0.4670	0.4812	0.5037
350	0.4327	0.4548	0.4722	0.4995
400	0.4138	0.4405	0.4615	0.4940
450	0.3926	0.4243	0.4490	0.4869
500	0.3694	0.4061	0.4347	0.4782

Table 3.13 Matrix of the values of the ratio $P = \Delta p1/\Delta p2$ obtained for all the simulated input values of $\Delta p2$ and p_a. Such values have been the starting point for the development of the method deriving the volume flow rate of MicroMED.

Starting form this matrix, the approach described by the flow chart of Figure 3.95 has been followed.

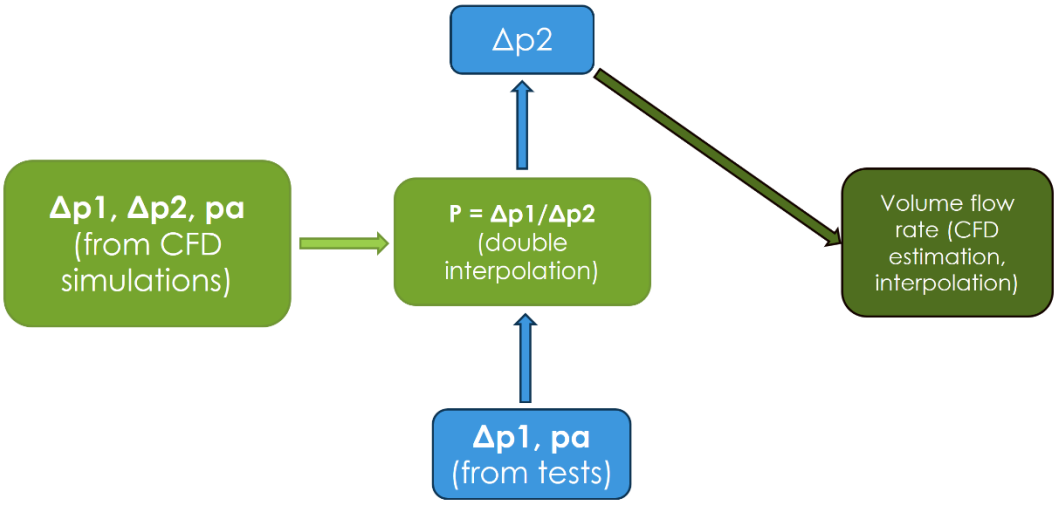

Figure 3.95 Flow chart followed to obtain volume flow rate starting from test results and CFD simulations.

The input data needed are $\Delta p1$ and p_a, which are provided by tests performed on MicroMED. Since, depending on those two values, P can be set considering the inputs coming from the CFD tests, a double interpolation process is set, which provides the value of the P ratio for the specific condition of the ongoing test. Knowing P, it is possible to estimate the real value of $\Delta p2$ which is related to the pump actual operating conditions and that allows to use the CFD simulations to derive with a good approximation an estimation of the volume flow rate of MicroMED.

This algorithm has been implemented in a Matlab code. The development of this method and of the code has been a part of my Ph.D. work. The routine has then been implemented in the MicroMED SW by the part of the team responsible for the SW development and management.

The Matlab code allowed to derive the relationship between the measured $\Delta p1$ and $\Delta p2$ which is needed for the estimation of the volume flow rate. The code is structured as follows:

- $\Delta p1$ and p_a are directly measured during the test, while the matrix of the values of P comes from CFD simulations and provides 36 different values coming from 9 different $\Delta p2$ values (from 100 to 500 Pa, which is the usual range 1-5 mbar, with a 50 Pa step) and 4 different ambient pressure values (6, 7, 8 and 10 mbar); the matrix has already be shown in Table 3.13;
- We interpolate for each of the 4 values of p_a the column of the matrix in Table 3.13 in order to obtain the 4 curves of Figure 3.96, since $\Delta p1$ is measured during tests and the ratio can be derived from the interpolation (one value for each of the 4 ambient pressures considered);
- A column containing a direct relationship between volume flow rate and $\Delta p2$ is introduced. It is an input of CFD simulations and it is mediated among different values of instrument temperature. This procedure simplifies the calculation and

gives marginal variations to the results, in the matter of few percentage points. A curve is derived, by which volume flow rate is related to Δp2;

- Once p_a is fixed (it is a direct output of the test), we perform a second interpolation among the coefficients of the third degree polynomial interpolation curves obtained previously in the code, so that entering with the correct ambient pressure value it is possible to derive only one curve rather than 4 (1 for each pressure), and this curve is directly related to the measured ambient pressure. Inputting Δp1 in this polynomial equation, the exact value of P, hence of Δp2 is derived. This value is the input needed for the previously calculated volume flow rate polynomial expression, so that a value of volume flow rate can be derived.

Figure 3.96 reports the aforementioned P curves, one for each p_a value considered. Such curves show the interpolation provides values that are not realistic for extreme values of Δp1; however, Δp1 has never been under 50 Pa and has never exceeded 150 Pa in tests. The curves are tuned for this stricter range of Δp1 values, and the Δp2 values obtained are realistic.

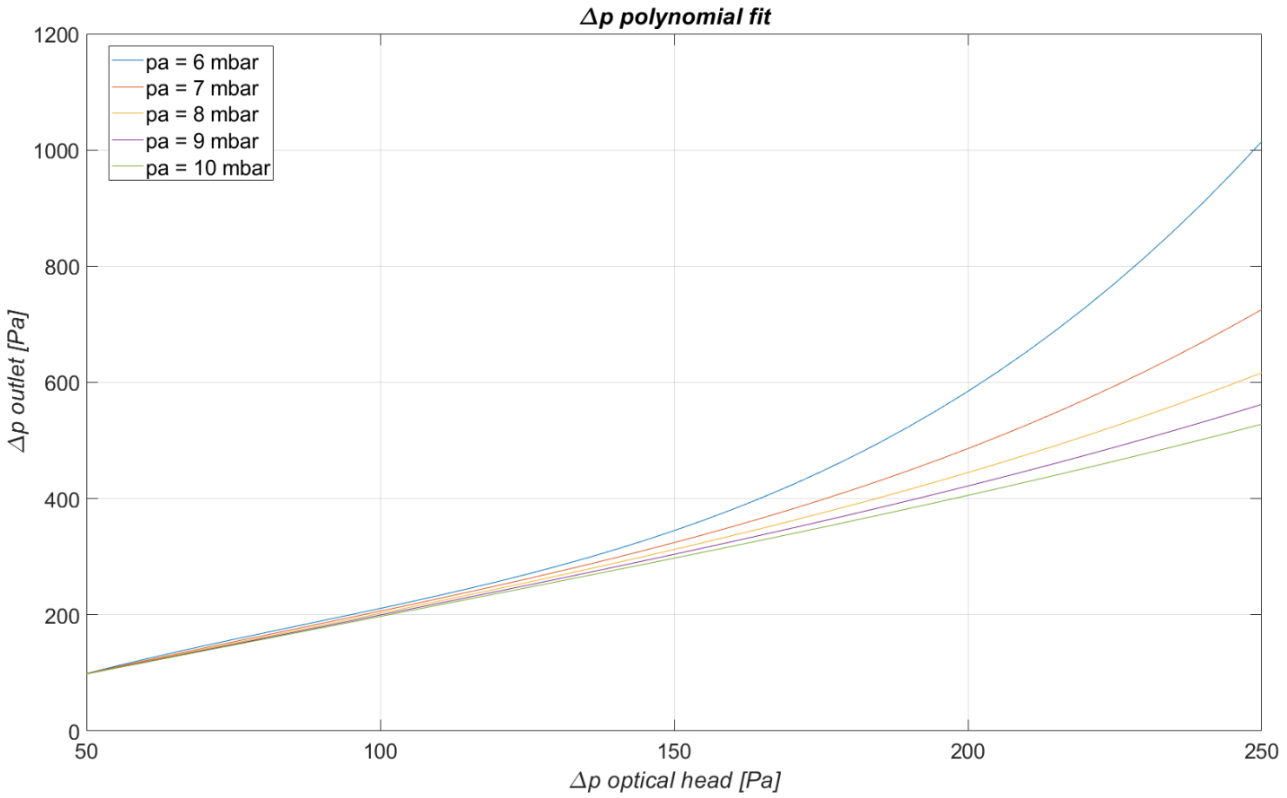

Figure 3.96 Curves relating Δp1 and Δp2 for different values of ambient pressure.

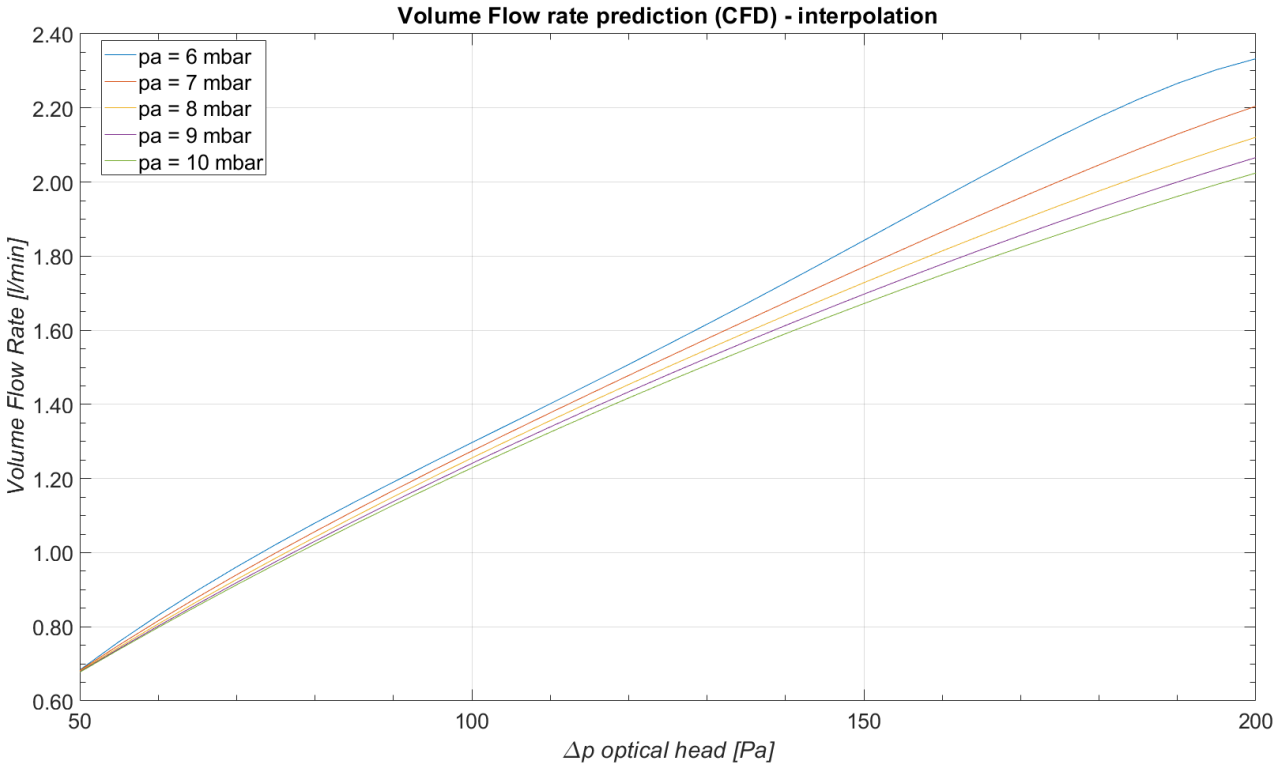

Figure 3.97 Relation between Δp1, which is here labeled as "Δp Optical head" since it is the pressure difference between MicroMED's optical head and the outside of the instrument, and the instrument's volume flow rate.

As previously explained, as a result of the double interpolation, a direct relation between the measured Δp1 and the volume flow rate of MicroMED has been obtained, as shown in Figure 3.97. Such relation has been used during tests on MicroMED to retrieve the instrument's flow rate during each test and measure the dust concentration through the ratio between the number of detected grains and the sampled volume of air, estimated from the flow rate and the total duration of the measurement.

3.2.7 Test campaigns in terrestrial desert

The main purpose of our research is the characterization of airborne Martian dust. Such characterization, and that of dusty phenomena, such as dust storms and dust devils, would dramatically improve our knowledge of Martian climate. Indeed, the abundance and the granulometry of dust present in the atmosphere are directly related to the dust injection mechanism active on Mars and its characterization would be pivotal in the comprehension of the climate of the red planet. However, no mission up to now was able to provide enough data to completely characterize Martian dusty phenomena and Aeolian processes.

Several indirect evidences suggest that saltation is an active mechanism on Mars. Active dunes and ripples (Silvestro et al., 2010; Silvestro et al., 2020) and wind-abraded landforms are common on Mas as well as dust devils and dust storms and saltation is a likely

mechanism of raising dust in these phenomena (Greeley 2002, Kok 2010), although other plausible dust emission mechanisms have been suggested (Sullivan et al 2008, Wurm et al 2008). Anyway, wind intensity measured from some landers, as well as predictions from atmospheric models, suggest that wind rarely exceed the threshold needed to initiate the saltation process in the low pressure Martian atmosphere. Several models and hypotheses have been suggested to explain these contradictory observations. Only direct, on site measurement would allow to shed light on this topic.
In the same time, the dust lifting mechanisms and the structure, rise and evolution of dusty phenomena, are not completely clear and are a subject of study also on Earth. Hence, it is important to deeply characterize these phenomena on the Earth in order to compare and understand data that will be acquired on Mars.

For this reason, a number of test campaigns in the Moroccan Sahara desert have been performed by the MicroMED team. The first two twin campaigns were performed in 2013 and 2014 and lasted around three months each (from June to September), as a meteorological station, including a Grimm ® OPC, anemometers, dust impactors, and an innovative sensor able to measure the local electrical field, was installed in Moroccan desert. A similar but shorter campaign (2 week long) followed in 2017, then two others in 2019 that lasted 2 and 1 week respectively. The purpose of the latter campaigns has been to complement the previous campaigns that as just said used the Grimm ® OPC. Such campaigns can help shed light on the analysis of previous data, in the wait of a campaign with a terrestrial version of MicroMED (Section 4). A detailed description of such campaign can be found in Franzese, G. 2020. My role in this part of the work of the MicroMED team is related to the last Moroccan mission that took place in July 2019. I was part of the mission and contributed to the data gathering. The following section will provide a brief description of the test campaign I was part of and an overview of the results obtained by the various campaigns.

3.2.7.1 Test campaign setup

The Moroccan desert has been chosen as a solid Martian equivalent for a number of reasons. In order for the tests to be successful, the location of the meteorological station is extremely important and has to be chosen accurately. A location that is a solid Martian equivalent has to be with no or sparse vegetation, no buildings or human infrastructures and with moderate surface roughness. Obviously, the surface has to be covered by dust. Sahara desert checks all the boxes and it is the largest dust source of the planet, therefore it is a good Martian equivalent. The equivalence cannot be extended to dust composition or either atmospheric composition or density, however the dynamics of dust lifting are similar and can be successfully compared. For our campaign, the Tafilalt region in Morocco has been chosen. The station was installed in the desert nearby the small town of Merzouga.

The campaigns have been carried out as part of the development process of the DREAMS station (Esposito et al. 2018) and of MicroMED (Mongelluzzo et al. 2019a, 2019b and 2020; Cozzolino et al., 2020). Results shown are relative to the two Moroccan field campaigns of

2014 and 2017; however, similar but upgraded data and results are expected from the following field campaigns, included the 2019 one.

During the 2014 mission a meteorological station was mounted on two separated masts (for a full review of the mission and instrumentation see Esposito et al. 2016 and Aguirre et al. 2017). Horizontal wind data were acquired by a Campbell Scientific CSAT3 anemometer, mounted at 4.5 m height with a sampling rate of 20 Hz. During the 2017 campaign the wind speed and direction was monitored using three 2D anemometers (Gill WindSonic) placed at 0.7 m, 2.0 m and 3.35 m, using a sample rate of 0.5 Hz. The 2017 meteorological station has been coupled with a camera, in order to record the passing dust lifting events.

Figure 3.98 shows instead the setup of the meteorological station for the July 2019 campaign. On the left, a small rod sustains the dust impactor sensor. The higher pole sustains the anemometers, one on the top and one at a lesser height measuring wind velocity on a different axis, and the electrical field sensor (the white sensor installed at mid height on the central pole). The white box under the central pole is the data logger, which is connected to all the instruments, managing their operations and the data acquisition and storage. The pole on the right has a solar panel, which provides the instruments with the required power. A camera is also installed, filming a fixed region around the station to capture dust devils passage, and the reference marks that were placed on the ground. These have been placed at fixed distance each other in order to help estimating the dimensions and the speed of the dust devil. LED lights were also present, aiming at helping the camera see nocturnal dust devils. Such phenomena have been theorized but never filmed before.

Figure 3.98 The meteorological station of the 2019 Moroccan desert mission.

By means of a complex image processing and data analysis (Franzese, G. et al., 2020) it has been possible to derive information about dust phenomena like dust devils and the characteristics of their forward motion.

For example, in Franzese, G. et al. 2020 we proposed a method to derive the translational speed and direction of the dust devils by monitoring the horizontal wind velocity. The possibility to study the dust devils motion from the wind time series is crucial for the understanding of their physics, allowing a direct comparison with the environmental wind conditions. We tested our technique using the data acquired in the aforementioned Sahara Desert campaigns, where the dust devils activity was monitored acquiring both the wind speed time series and the image sequences of vortex passage. The results confirm that, despite the simplicity of the methods and its assumptions, with this methodology we are able to consistently retrieve the forward motion parameters of the observed events.

Using this method, we deeply analyzed the 2014 Saharan survey, where we monitored the local dust devils population without the aid of a camera. We evaluated the translational speed and direction for 338 events, comparing the results with the measurements of the local wind regime. Our data not only indicated that the vortices consistently translate along the direction of the prevailing wind, as already expected in the literature, but they also shed light on the open questions regarding the magnitude at different height of this speed. Indeed, we observed how the forward velocity closely matches the one of the near ground wind, indicating how both follow a similar vertical profile. Small deviations from the environmental wind have been observed, relatable to the local fluctuation of the wind regime. The increase of the wind speed and the decrease of its circular standard deviation minimize these deviations. Our results bear out the utility of the dust devils as a probe of the environmental wind condition. The technique proposed is of particular interest in the frame of both the currently ongoing and the upcoming Martian missions, that deploy or will deploy on the surface sensors capable of the meteorological monitoring of the dust lifting events, like the MEDA (Mars Environmental Dynamics Analyzer) suite on board of the NASA Mars 2020 mission or the METEO package on board of the ESA/Roscosmos ExoMars 2022. Our method will allow to fully characterize the dynamics of the observed dust devils, resolving their translational and rotational motion component. The METEO package in particular will work alongside the MicroMED instruments and the other sensors belonging to the Dust Complex, allowing to characterize the dust devils also from an electric and dust load point of view. Results like this one show how valuable terrestrial field campaigns can be to the positive outcome and the scientific retrieval of Martian missions in general and of MicroMED in particular. Data gathered in 2019 are currently under analysis and will provide further evidence of the developed theories and help generate upgraded ones that will help shed light on dust phenomena.

3.3MicroMED's space qualification

After integration, the instrument has been characterized through functional and performance tests, able to verify the functionality of all subsystems and the capability to sample and correctly characterize the grains injected in simulated Martian atmospheres both at our facility in Capodimonte and in other specialized facilities (like the AWTS II). However, after this phase, space qualification of the instrument had to be guaranteed. MicroMED, which has been assembled using space qualified components, has to demonstrate that it is able to survive the extreme conditions of deep space and the harshness of the take off. To this purpose, Thermal Vacuum and Vibration test procedures have been designed for MicroMED and approved duringthe Test Readiness Review (TRR). MicroMED successfully passed the qualification process, confirming its ability to withstand extreme thermal and mechanical loads with no deterioration of performances. This section provides an insight of the space qualification procedures. My role in this phase was to take part to the design of the tests and to redact the corresponding official reports, that are part of MicroMED's official documentation.

3.3.1 Vibration test procedure

3.3.1.1 Introduction to the procedure

The vibration procedure has been performed at the vibration facility in PoliMI (Politecnico di Milano, Polo Territoriale di Lecco, Lecco). The procedure aims at simulating the extreme conditions the instrument will face during take-off and in critical portions of the mission, verifying that it is able to withstand such extreme loads. This section provides a brief description of such procedure and of the activities performed.

As the PoliMI facility did not assure the compliance with Planetary Protection (PP) requirements, MicroMED was integrated inside a metallic vessel provided with a HEPA filter. A complete electrical interface allows connection to MicroMED and the possibility to test MicroMED while it is inside the vessel, preserving its PP status.

Figure 3.99 shows MicroMED's accommodation inside the vessel, where three monoaxial accelerometers are already present (mounted during instrument integration), one for each measurement axis. The mounting position of the accelerometers is on the top edge of the MicroMED, as shown in Figure 3.100. This position would allow for identification of first mechanical resonances of the MicroMED structure.

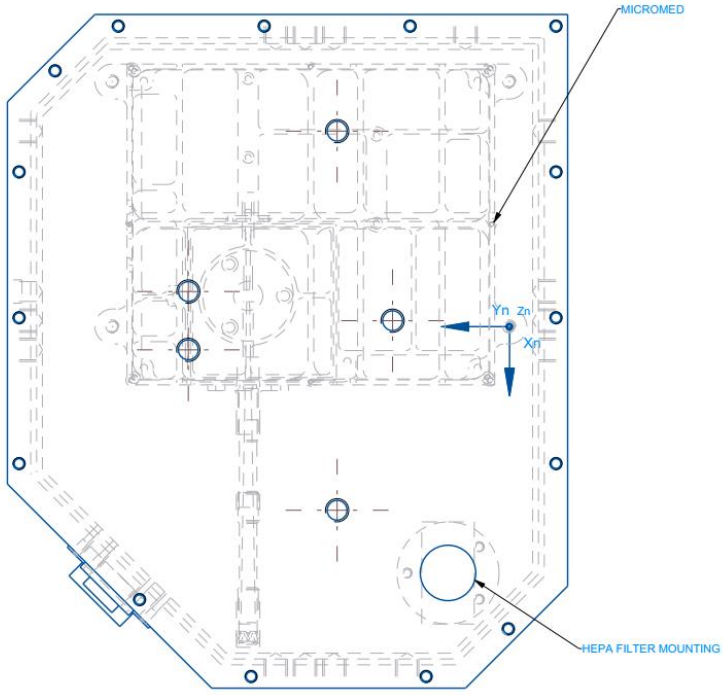

Figure 3.99 MicroMED mounting within the instrument vessel.

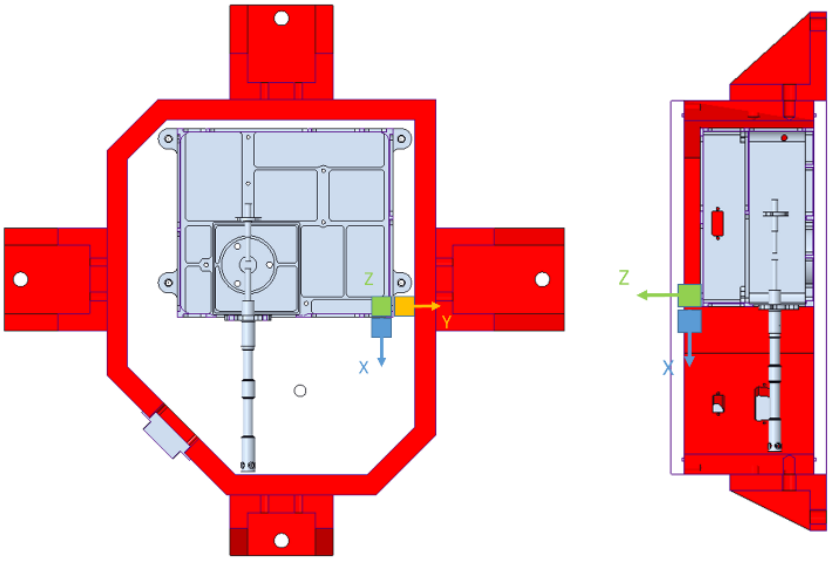

Figure 3.100 Mounting of three monoaxial accelerometers, for X, Y and Z directions.

The test facility is based on the LDS V830 SPA-16 electro-dynamic shaker, with LMS SCADAS III controller for sine, random and shock excitation. The performances of the vibration facility (335 mm armature diameter model) are reported in the following figure (Figure 3.101) .

Armature diameter		185 mm (7.28 in)	335 mm (13.2 in)
Sine force, peak (Note 1)	SPA8K	6.78 kN (1524 lbf)	6.54 kN (1470 lbf)
	SPA16K	8.90 kN (2000 lbf)	8.90 kN (2205 lbf)
Random force, rms (Note 2)	SPA8K	5.77 kN (1298 lbf)	7.60 kN (1709 lbf)
	SPA16K	5.78 kN (1300 lbf)	9.81 kN (2205 lbf)
Half sine peak bump force (Note 3)		17.3 kN (3900 lbf)	29.4 kN (6615 lbf)
Armature resonance (f_n), nominal		3100 Hz	2250 Hz
Useable frequency range		d.c. to 3500 Hz	d.c. to 3000 Hz
Effective mass of moving element	Flush inserts	6.98 kg (15.39 lb)	12.05 kg (26.57 lb)
	Raised (hex) inserts	7.48 kg (16.49 lb)	12.83 kg (28.28 lb)
Velocity, sine, peak (Note 1)		2.0 m/s (78.7 in/s)	2.0 m/s (78.7 in/s)
Acceleration, sine, peak, flush inserts		1176.7 m/s² (120 g_n)	735.4 m/s² (75 g_n)
Acceleration, random, rms		735.4 m/s² (75 g_n)	588.4 m/s² (60 g_n)
Degauss: (Note 4)	Stray magnetic field	< 0.5 mT (<5 gauss)	< 0.5 mT (<5 gauss)
Armature suspension stiffness:			
Axial (nominal)		zero	
Cross-axial at insert level		5250 N/mm (30000 lbf/in)	
Rotational		41.8 kN m/radian (370000 lbf in/radian)	67.8 kN m/radian (600000 lbf in/radian)

Figure 3.101 Vibration facility characteristics.

Tests have been performed at different stress levels, in accordance with what reported in Table 3.14-Table 3.16.

Parameter	Value
Amplitude [g]	0.5
Sweep rate [Oct/min]	4
Frequency range [Hz]	20-2000

Table 3.14 Vibration level, sweep sine, X, Y and Z axes.

Frequency [Hz]	Level [g]
20	1
40	1.5
80	2

160	4
320	7
640	9
2000	9

Table 3.15 Vibration level, qualification power sweep sine, X, Y and Z axes, rate 4 oct/min.

Frequency [Hz]	Level [g^2/Hz]	Duration [s]
20	0.02	60
50	0.02	
100	0.02	
200	0.05	
500	0.05	
1000	0.025	
2000	0.013	

Table 3.16 Random test qualification level, X, Y and Z axes.

3.3.1.2 Execution and successful outcome of the vibration tests

Before starting mechanical test, full functional tests have been performed to verify that handling and transportation had not altered the instrument's correct functionality. A quick visual inspection has also been made to verify eventual damage to the vessel. After these preliminary operations, accelerometers have been places on the outside of MicroMED's vessel as shown in Figure 3.102, with the monoaxial accelerometer positioned at the shaker base mounted as close as possible to the shaker axis.

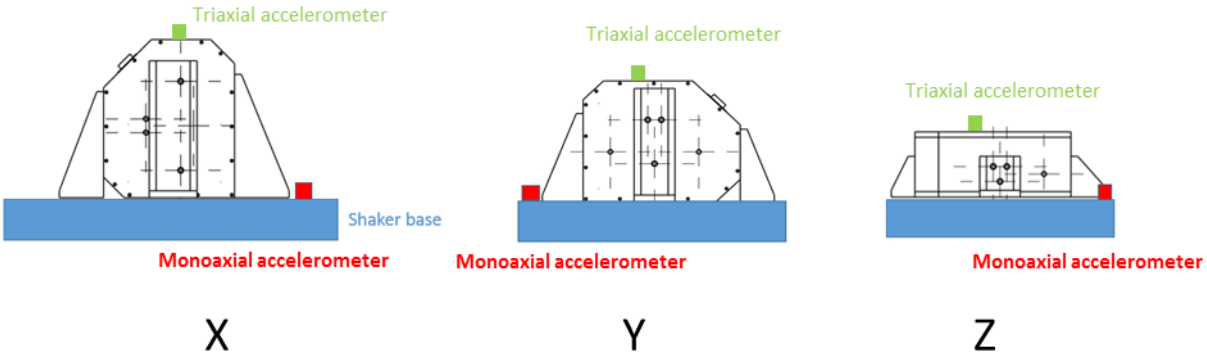

Figure 3.102 Positioning of the reference accelerometers on the shaker base for the mechanical testing.

A triaxial accelerometer has also been placed on the MicroMED Vessel top, to monitor movements on the structure during testing.

Before installation of the Vessel on the shaker platform, a sweep sine test run has been made to verify that the first eigenfrequency of shaker interface is above 2000 Hz, which is the

maximum frequency tested during random tests as shown in Table 3.16. After a successful verification, MicroMED Vessel has been mounted on the shaker platform. Each direction has been tested with values and procedures in accordance with the requirements set by the ECSS.

MicroMED has been mounted on the shaker for monoaxial testing. The procedure described hereafter has been repeated three times, for tests on the X, Y, and Z directions as for Figure 3.100. Between each monoaxial test, the vessel has been dismounted from the shaker to change the solicitation axis. The instrument has undergone the following sequence of tests along each axis:

- Sweep sine test, to identify the main modes and amplification factors. Sweep sine test values are reported in Table 3.14;
- A new sweep sine test with qualification levels, as reported in Table 3.15, after the successful completion of the review of the low level sweep sine test results;
- A power sweep sine test at low level sweep sine test, to verify that no structural change has happened during test. The values of tests are still the ones reported in Table 3.14;
- A random test phase considering values as reported in Table 3.16;
- A low level sweep sine test, to verify that no structural change has happened during tests;
- Functional tests, to verify MicroMED's correct functionality after mechanical testing.

Mechanical tests success criteria are the following:

- No structural failures;
- Post vibration resonance frequency shift < 5%;
- Post-vibration functional test is successful.

Tests performed verified that MicroMED has been able to meet all such criteria, therefore vibration test procedure has been successfully passed by MicroMED.

3.3.2 Thermal Vacuum test procedure

MicroMED has also undergone a procedure called Thermal Vacuum Test. Such procedure aims at verifying that an instrument is able to withstand the extreme stresses that come from an exposition to extremely low pressure environment, like deep space during the course of the travel toward Mars, and to extreme thermal loads, which could happen in various phases of the mission. In order to control the microbiological contamination of MicroMED, just like the vibration tests, MicroMED has been tested inside its Vessel box also

during the thermal vacuum test. The following sections will provide a brief description of the test setup and of the obtained results.

3.3.2.1 Thermal Vacuum Test setup

MicroMED with its vessel has been positioned in a Thermal Vacuum (TV) Chamber and mounted on a dedicated fixture attached to the chamber cold-plate. The Electrical Test set up is shown in Figure 3.103.

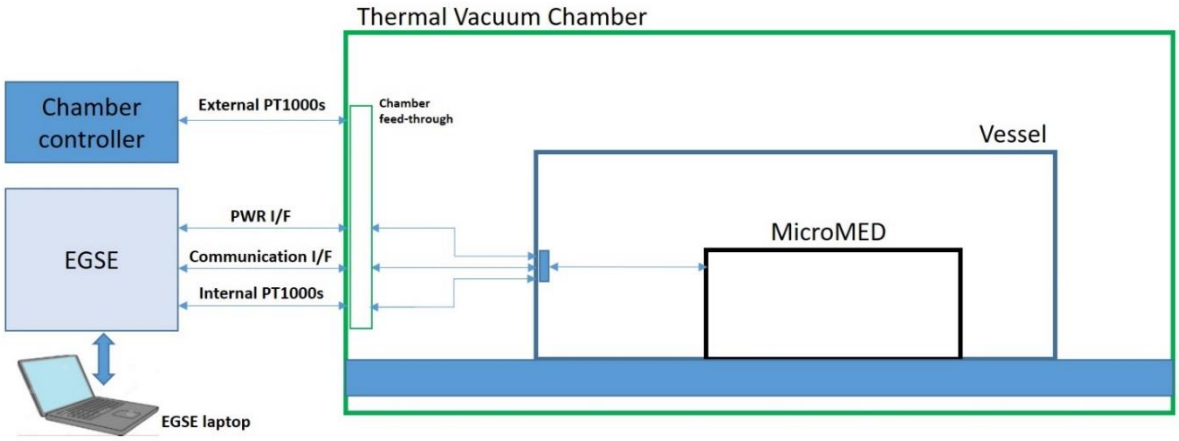

Figure 3.103 Test setup for TV cycling.

Data and power lines of MicroMED have been transmitted between internal and external of the test chamber via a dedicated cable that is connected to the thermal vacuum chamber flange connectors. Moreover, four PT1000s have been installed on MicroMED to measure the temperature during the test. Figure 3.104 shows the location of the external sensors.

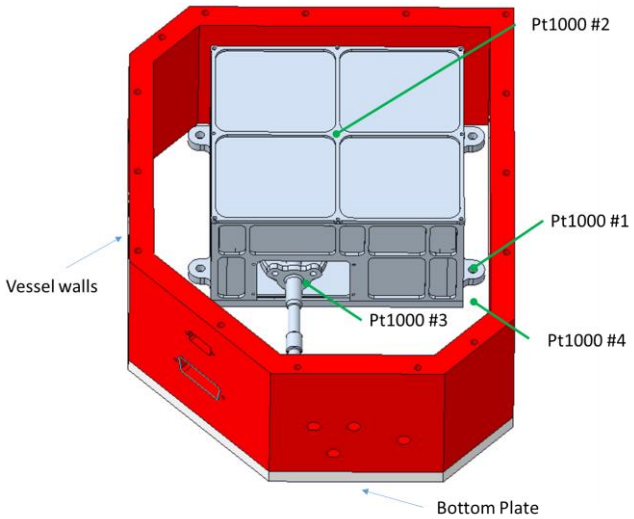

Figure 3.104 External PT1000 sensors positioning.

The cables are built with low-outgassing flight-like material in order to avoid chamber contamination. Overall, outgassing is a key issue in performing such tests and has been monitored and studied throughout the various phases of the procedure.

Heat exchange for MicroMED has been guaranteed by means of conduction through the base plate of the vessel, that resembles the mechanical interface on the lander. No intermediate interfaces have been used. The cooling system was based on copper base plate with liquid nitrogen cooling. Apiezon L grease has been used between cooling plate and bottom plate to enhance conduction. The scheme of such testing setup is shown in Figure 3.105.

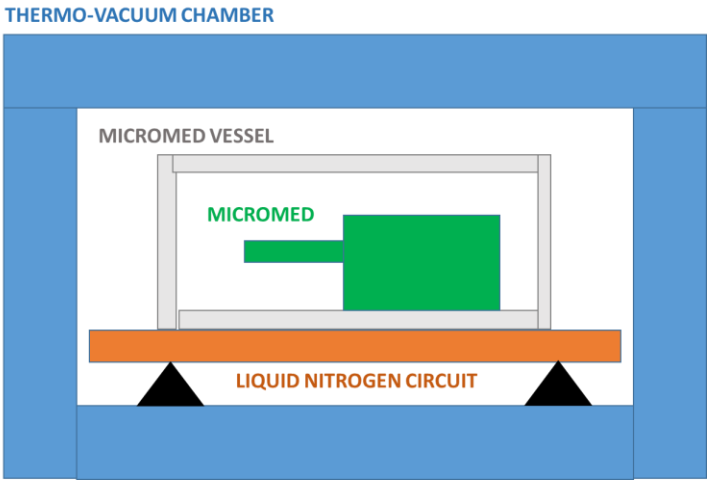

Figure 3.105 TV setup scheme.

The Radiative interface temperature for the vessel has been provided by MLI insulator facing the TV chamber. The vessel panels have provided the radiative interface temperature for MicroMED.

The Temperature monitoring has been provided by considering a Temperature Reference Point (TRP) located on a mounting foot of MicroMED (see Figure 3.106). The external temperature of MicroMED has been monitored by means of test sensors (resistance temperature sensors PT1000s), whose outcome has been managed by the thermal vacuum chamber test equipment. Their positions on MicroMED is shown in Figure 3.106.

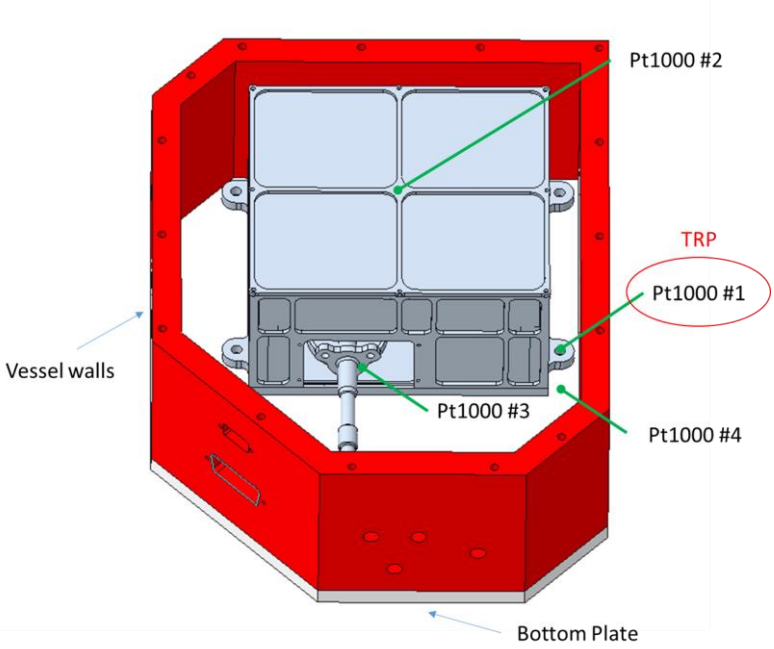

Figure 3.106 TRP and temperature sensors positions.

In addition to the external test sensors, installed outside MicroMED via the vessel, there is a set of 5 flight sensors (also these 5 sensors are PT1000 temperature sensors) whose output has been acquired during the test execution, and has been constantly monitored to check the good health status of the unit during cycling.

MicroMED's telemetry has also been periodically acquired to monitor its health status. In this way, in case of a temperature exceeding its set threshold value, the contingency management procedure would have been executed. This feature however has not been necessary as MicroMED has not registered any of those issues.

All tests have been performed at the PoliMI Thermal Vacuum facility, which is briefly described in the following section.

3.3.2.2 The PoliMI Thermal Vacuum Facility

A brief description of the PoliMI Thermal Vacuum facility is provided in this section. The Thermal Vacuum chamber is based on a cylindrical stainless-steel vessel, 300 mm in diameter and 400 mm in length. Both ends of the cylinder are removable flanges. Inside the vessel a LiN_2 cooled plate can be placed on one of the ends allowing to cool down to -180°C. Film heaters are available for fine thermal control. The TV system is provided with mechanical (translational, 25mm travel) optical and IR windows and electrical feed-through. Different pressure gauges allow measurement of the pressure in the range from 1 bar to 10^{-4} Pa. Varian DS 402 rotary vane pump and T-Station 85 turbomolecular pumping station are used to achieve required low pressure level in the vacuum chamber. The TV chamber, in the configuration for a combined thermal and mechanical test is shown in Figure 3.107.

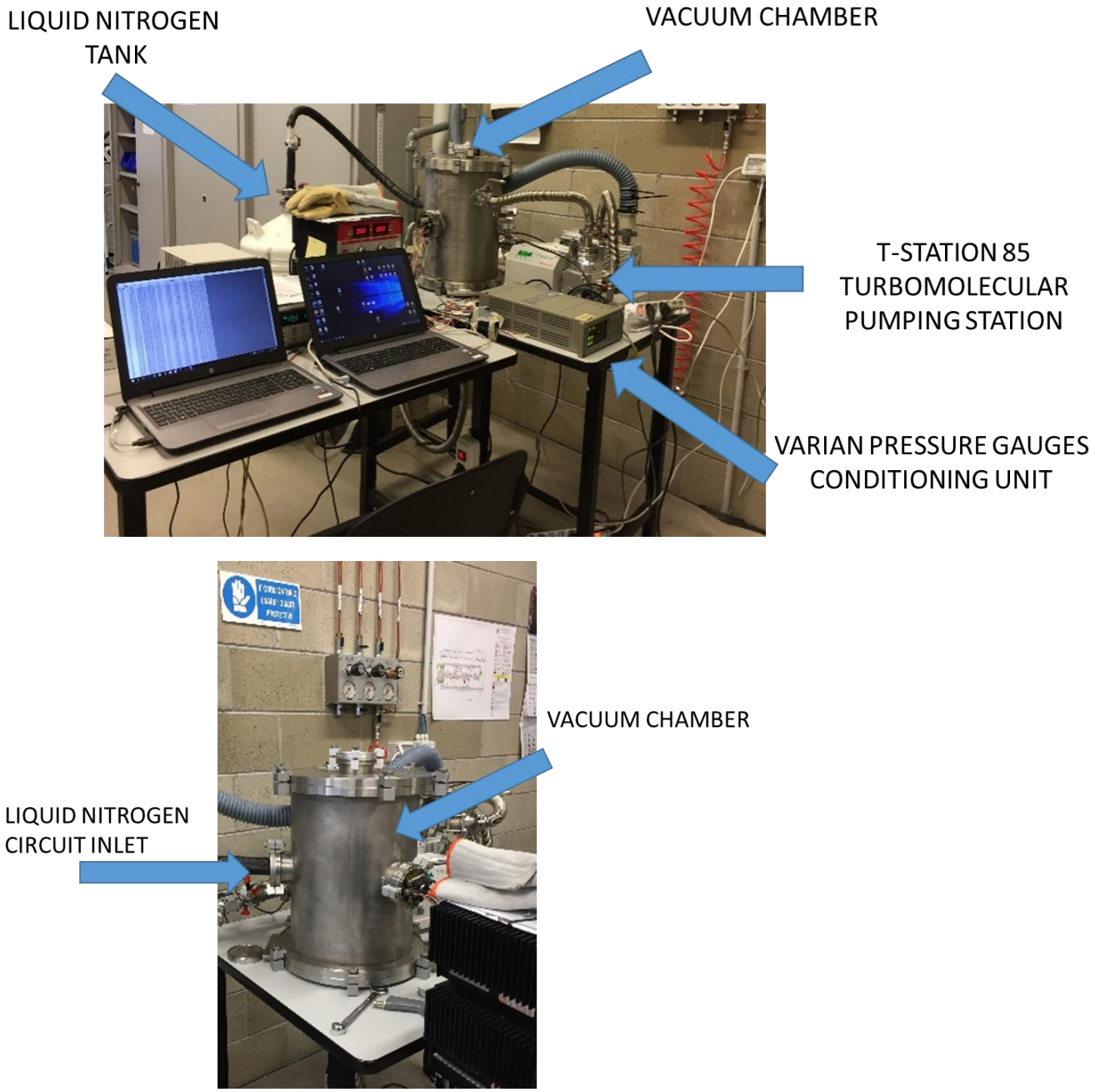

Figure 3.107 PoliMI TV Facility description.

3.3.2.3 Execution and successful outcome of the Thermal Vacuum Test procedure

The TV test is considered successful if the results of the Functional Tests performed in various phases of the TV test result nominal.

The TV test procedure requires six different Functional Tests. Such tests have been performed with the usual scheme, using the MicroMED EGSE that allows to switch MicroMED's laser and pump on and to check the proper functioning of such subsystems. For a detailed description of these tests, their execution and the criteria used to evaluate their

results, please refer to Section 3.2.2. During the TV test, a total of six Reduced Functional Tests have been performed:

- Two tests before and after the TV cycles;
- Four tests in different steps of the cycles and at two different operating temperatures.

In order to satisfy the thermal vacuum test objectives, the TRP temperature have been set to test MicroMED at its foreseen working temperature by means of properly setting base-plate and shroud temperatures along four thermal cycles. Being the unit a Proto Flight Model (PFM), the following test philosophy has been implemented, according to standard ECSS approach:

- Number of temperature cycles: 4
  - one cycle in mixed operational/non-operational mode (1st cycle)
  - three cycles in operational mode (from 2nd to 4th cycle)
- Temperature levels: Qualification temperatures (i.e., considering 10 °C qualification margin at both ends, with respect to the design operational temperatures, see Table 3.17);
- Temperature gradient: The temperature gradient has been set at around 2 K/min, well below the limit rate of change of 20 K/minute imposed by the standards;

- Dwell time: the dwell time has been set to 2 hours in accordance with the requirements imposed by the standards.

The temperature requirements referred to TRP for MicroMED are shown in Table 3.17.

Operating temperature		**Non-operating temperature**	
T_{min}[°C]	**T_{max}[°C]**	**T_{min}[°C]**	**T_{max}[°C]**
-20	40	-40	50

Table 3.17 Minimum and maximum temperature over time of MicroMED thermal model nodes.

Considering the Proto Flight approach adopted for MicroMED, all the temperature levels must be extended by 10°C at both ends, resulting in the following test temperature range (qualification levels) of Table 3.18.

	Qualification test levels	
	T_{min}[°C]	T_{max}[°C]
Operating	-30	50
Non Operating	-50	60

Table 3.18 Qualification test levels.

Considering limitations of laser working temperature range, selected temperatures for functional testing are the ones shown in Table 3.19.

Selected temperatures for functional tests	
$T_{S,min}$[°C]	$T_{S,max}$[°C]
-15	35

Table 3.19 Selected temperatures for functional tests.

The pressure inside the chamber during the test should be equal or less than 10^{-5} hPa (equivalent to 10^{-5} mbar).

A representative test profile of the TRP is indicated in Figure 3.108.

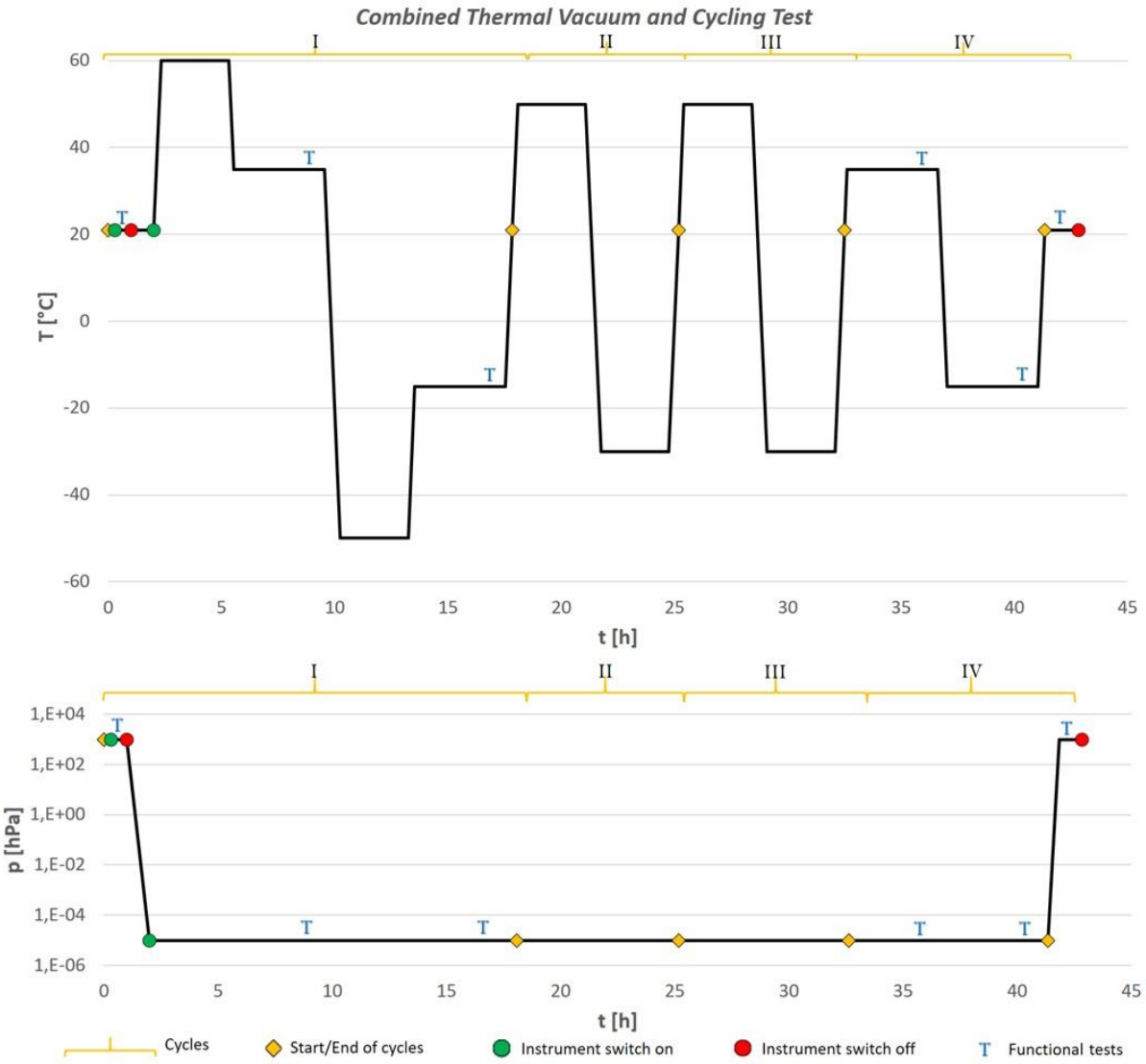

Figure 3.108 Representative TRP TV test temperature and pressure profile.

The procedure is set for a total duration of 43 hours, with four cycles and a total of six different functional test sessions performed. Functional Tests are to be performed at ambient temperature before and after the TV testing and at T_{Smin} and T_{Smax} during the first and fourth operative cycle. Such tests have been performed in their Reduced form (See Section 3.2.2, Reduced Functional Tests are indicated by the acronym RFT).

The following constraint had to be followed during the test execution:

- Laser and Pump operating conditions:

In order to guarantee the instrument integrity, both the laser and the pump had to be switched on only during Functional Tests. This condition still provides a realistic simulation of the actual operating conditions of the instrument, given that during the mission MicroMED will be switched on only during the measurements (8 times max per day for 120 seconds each time).

- RFT temperature:

Given the impossibility to switch the laser on at the minimum and maximum operating temperatures ($T_{op,min}$ = -30°C and $T_{op,max}$ = +50°C), RFTs planned during the TV cycles shall be performed at two different operating temperatures (T_{Smin} = -15°C and T_{Smax} = +35°C) in order to preserve the laser integrity while still allowing verification of the laser during the TV test.

3.3.2.4 Positive outcome of the TV procedure

The Thermal Vacuum procedure has been performed on MicroMED's PFM model, which was able to keep its functionality both during and after the cycling. Functional tests have been successfully performed, guaranteeing the positive outcome of the qualification campaign. Performance tests such as those described in Section 3.2.3 have then been repeated, showing identical results to the ones already described there. This outcome indicates that the thermal vacuum procedure had no influence on the instrument's performances.

3.4MicroMED's calibration procedure

After verification of MicroMED's performances and after space qualification, the MicroMED OPC has undergone the scientific calibration procedure. This procedure allows the retrieval of the calibration curve needed to derive physical quantities (dust size) from engineering output data (photodiode current). The procedure adopted for such calibration process is described hereafter.

3.4.1 Test conditions

The campaign has been performed inside the Martian simulation Chamber at the INAF-OAC premises in Capodimonte (for a description of the facility see Section 3.2.1).

Test conditions and setup have been set in accordance with what already described in Section 3.2.1. Given that the Martian Chamber was sterilized before testing, the vessel was not used and MicroMED has been installed inside the ATS thermal chamber as described in Section 3.2.1.

3.4.2 Test results and discussion

Tests with grains of various sizes were performed as shown in Table 3.20. Calibrated spherical grains have been used as they are the only calibrated particles commercially available.

Diameter [μm]	NumRun [#]	NumSignal [#]	Current [nA]	σ [nA]
0.78	84	8422	$1.1 \cdot 10^{-7}$	$3 \cdot 10^{-8}$
1.00	65	9463	$2.4 \cdot 10^{-7}$	$6 \cdot 10^{-8}$
1.93	21	2008	$6.2 \cdot 10^{-7}$	$10 \cdot 10^{-8}$
4.28	98	11811	$1.5 \cdot 10^{-6}$	$2 \cdot 10^{-7}$
6.13	22	2540	$3.3 \cdot 10^{-6}$	$2 \cdot 10^{-7}$
7.87	65	9695	$5.3 \cdot 10^{-6}$	$5 \cdot 10^{-7}$
10.07	19	1693	$9.8 \cdot 10^{-6}$	$1 \cdot 10^{-6}$
10.85	78	7579	$1.0 \cdot 10^{-5}$	$1 \cdot 10^{-6}$
16.02	46	4951	$2.4 \cdot 10^{-5}$	$2 \cdot 10^{-6}$

18.12	149	15937	$2.7 \cdot 10^{-5}$	$4 \cdot 10^{-6}$
19.70	41	4249	$3.0 \cdot 10^{-5}$	$2 \cdot 10^{-6}$

Table 3.20 Acquisitions used forMicroMED's PFM calibration.

The grain size in Table 3.20 is expressed in diameter. Tests at different laser currents are conceived to perform a sensitivity analysis versus the power of the laser.

For each set of monodisperse grains, a set of output voltages are obtained from MicroMED electronics. These are converted in currents through the gain factor related to the specific amplification channel used to get the measurement. Data are then processed in order to identify and eliminate possible false events. Finally, they are averaged to obtain a single current value for each size of the used monodisperse set of grains. We obtained the set of experimental points represented in Figure 3.108. These points have been used in a least-squares minimization procedure to obtain the best fitting calibration curve, also shown in Figure (continuous line).

The calibration curve has only one free parameter and has been obtained by applying the exact Mie's scattering theory (Bohren and Huffman, 1983) to the description of the light scattered by the grains and collected by the mirrors embedded in the Optical System.

The steps followed are described hereafter:

- The Mie theory requires grain size, refraction index of the grain material as well as the size of the sensing region and its effective optical laser power as input data. The effective optical power has been left as a free parameter in the least-squares procedure. Starting from such data, the Mie theory allows to obtain physical quantities like the scattering coefficient of grains, among others;
- The obtained quantities obtained allow to derive an integral of the energy collected by the mirrors, given the collecting angles in play;
- From these calculations, it is possible to derive an expected value of current related to each grain size.
- The expected value of current is compared iteratively with the value actually obtained from test so that a proper tuning of the free parameter can be performed in order to obtain the best fitting curve.

As a result of such procedure, a curve can be obtained, describing the expected response of MicroMED when facing grains of each size in the measurement range. Such curve is shown in Figure 3.109. Tests have then been performed to verify that the process was successful. Figure 3.110-Figure 3.112 show, as an example, the histograms obtained in tests for grains of small, intermediate and large size. Such histograms show that the outcome of the calibration procedure can be considered successful.

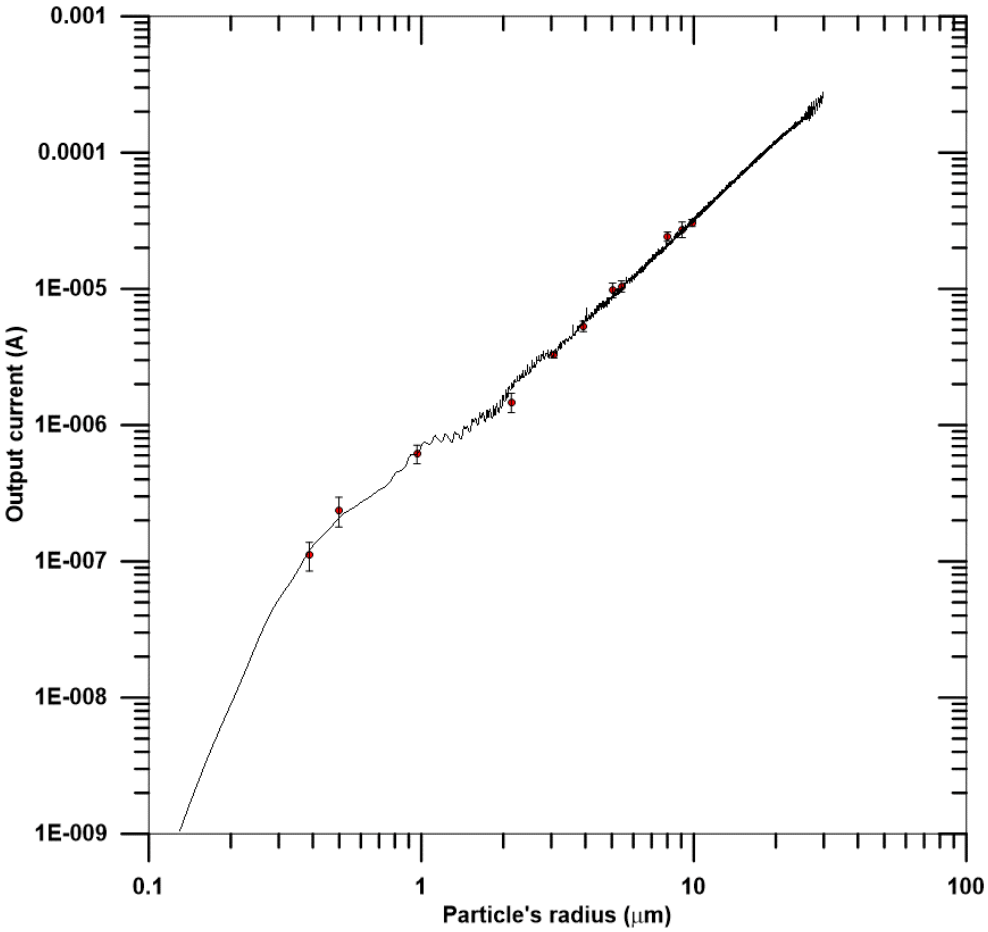

Figure 3.109 Comparison between experimental results and the calculated calibration curve.

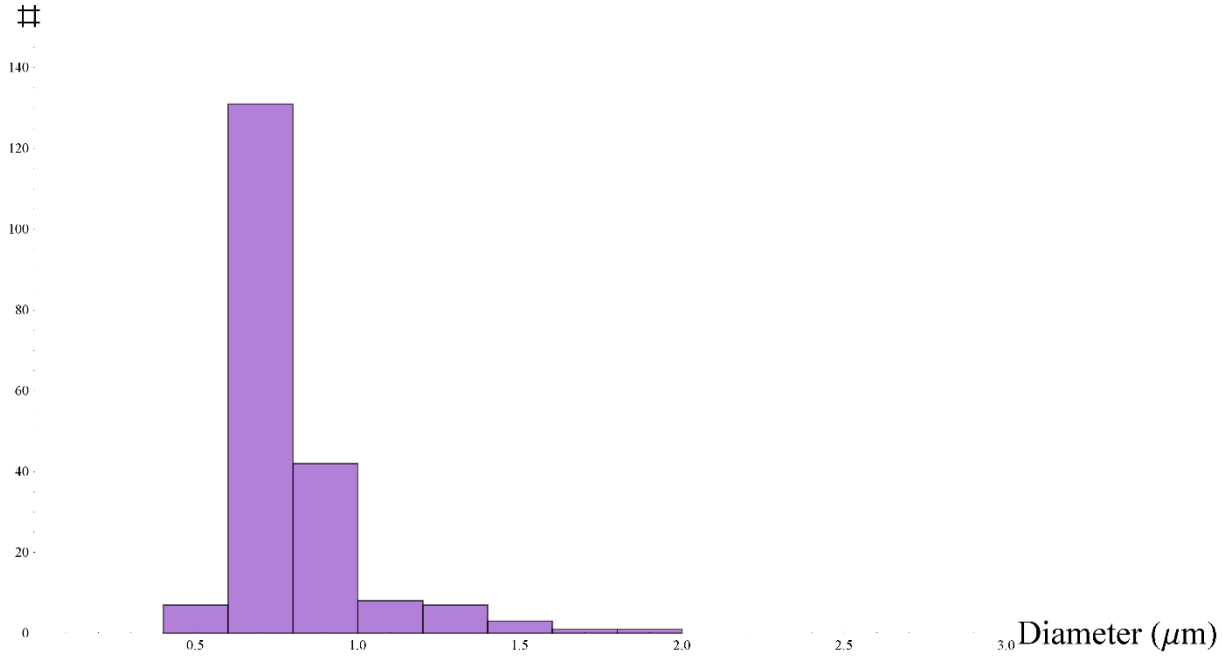

Figure 3.110 Histogram acquired during calibration tests with 0.776 μm grains.

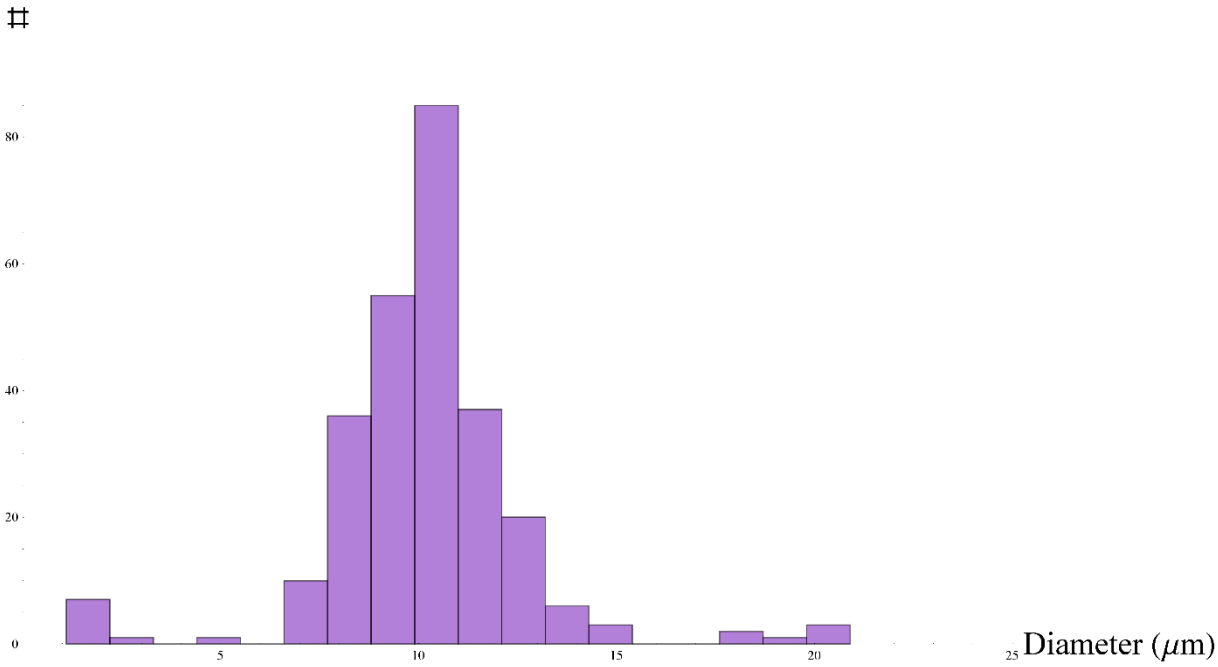

Figure 3.111 Histogram acquired during calibration tests with 10.07 μm grains.

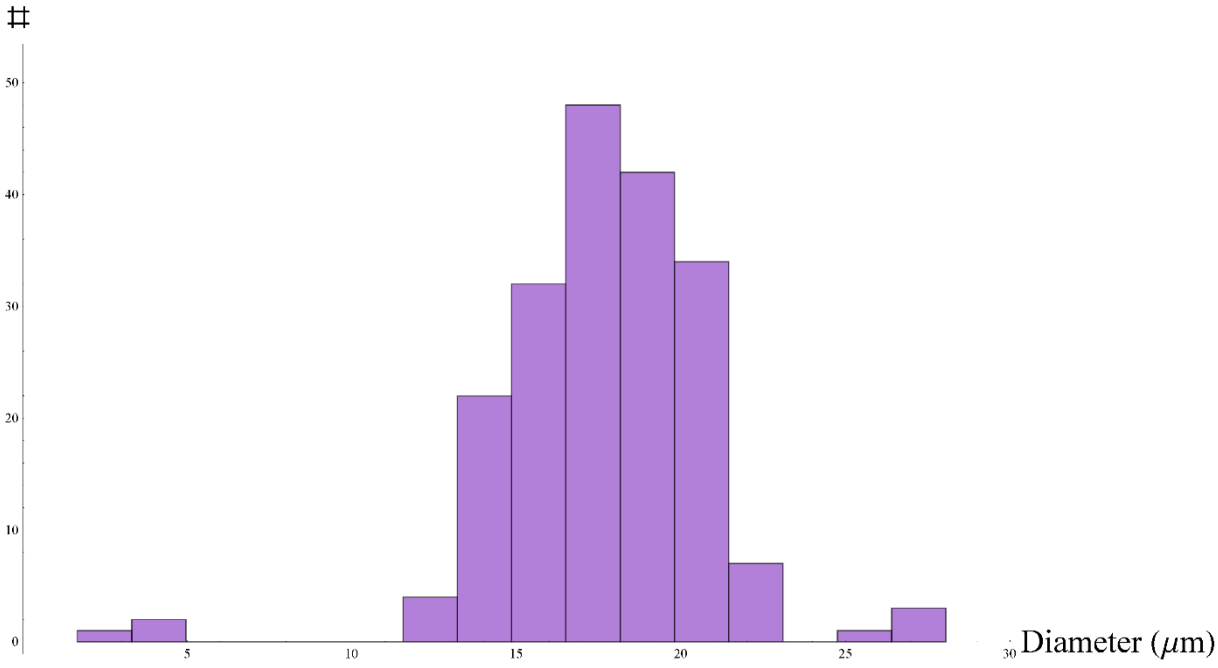

Figure 3.112 Histogram acquired during calibration tests with 19.70 μm grains.

4.The terrestrial version of MicroMED

During my Ph.D. work at the INAF – OAC, the development of a terrestrial version of MicroMED has been investigated and then realized. A terrestrial instrument would allow to test the instrument operations in a field environment and during real dust storm and dust devil events.

This section provides an overview of the performed work (CFD analysis, characterization and design) aimed at the development of such a model. A partial re-design of the instrument was deemed necessary since the operating conditions of a terrestrial instrument are dramatically different from the Martian MicroMED, and a complete analysis of the instrument's fluid dynamic was performed. MicroMED's terrestrial version is planned to be integrated in 2022. This section provides an overview of the work performed aimed at the realization of such instrument.

4.1 The design of MicroMED's terrestrial version

Because of the different conditions faced in Earth atmosphere, MicroMED internal flow would significantly change if the instrument's PFM was used on Earth. The flow could become turbulent, since density and pressure are higher by two and three orders of magnitude, respectively, and the atmosphere has a different composition. Moreover, the same pump operating conditions would generate a larger pressure difference (a difference of about one order of magnitude) because of the denser atmosphere. These variables imply high fluid velocities, which are detrimental to MicroMED both in terms of its sampling efficiency and for the quality of its measurements. The main affecting factors to these two characteristics are the fluid velocity and the creation of potential eddies. The modified fluid velocity could induce turbulence that could deflect the particle trajectories outside the laser illuminated spot, resulting in a count underestimation. The potential presence of eddies could instead produce counting overestimations, since a single dust grain could pass through the measurement spot more than once. Moreover, turbulence in the inlet duct could increase the number of dust grains that may interact with the duct walls. In agreement with previous analyses (Mongelluzzo, G. et al., 2018, 2019a, 2019b, 2019c, 2020), it is expected that dust grains that hit the walls get stuck, given that they have comparable size to the duct mean surface roughness, resulting in a failed detection of such grains. On the other hand, especially at high fluid speed, it is possible that grains could be reflected by the walls, becoming unpredictable both in terms of position and trajectory. Both possibilities are detrimental to the instrument efficiency. Reflected grains may also settle on the optics. As a consequence of these considerations, the eventual impact of grains on MicroMED inner walls was one of the aspects considered in the re-design of the ducts.

The specific design of the instrument is potentially adaptable to successfully operate in other planetary environments (e.g., Earth and Titan). Thus, in order to test MicroMED on Earth, the original design had to be adapted to terrestrial atmospheric conditions (i.e. pressure, density, composition and temperature). In this section, the re-design process of MicroMED's inlet duct is presented, which is removable and can therefore be substituted, allowing us to operate the instrument both in terrestrial and Martian conditions.

In order to obtain an efficient re-design, a CFD analysis of the PFM has been performed considering terrestrial atmospheric conditions. The analysis was aimed at understanding the dynamics of dust grains inside MicroMED's PFM (when used in Earth environment) and to provide tips about the adjustments needed to guarantee efficient performances in terrestrial conditions. The modifications indicated by this analysis have allowed the development of a terrestrial model. This kind of approach is common among planetary missions and was also utilized for the case of the DREAMS instrument, the meteorological station on board of the ExoMars 2016 mission (See Section 1.2).

4.1.1 CFD Model

The CFD modelling has been performed using Ansys Fluent® v18.1 and the approach considered was similar to the one used in Section 2.1.1. Given the size of MicroMED, the flow is expected to become turbulent for fluid speed over 35 m/s, which is achievable in terrestrial conditions. Therefore, turbulent models have been used. More specifically, simulations would have to be able to describe a potentially turbulent flow, with Re still not very high (Re < 5000 in our application). To such purpose, the SST (Shear Stress Transport) transition model has been chosen, given its ability to describe the transition, low Reynolds turbulent flows and to consider the surface roughness of walls. The mean surface roughness of inner walls was indeed set to 23 μm, in agreement with what already considered for the analysis of the PFM design, which is described in Section 2.2. Dust grains of 25 different sizes have been simulated in the 0.4-20 μm diameter range, which is the instrument nominal measuring range. Grain trajectories and behavior have then been analyzed using the particle tracking tool provided by Fluent. Both steady state and transient simulations have been performed in order to correctly evaluate the fluid dynamic phenomena and hypothesize the characteristics of the fluid flow. Default values of the residuals needed for convergence of the runs have been set in the simulations; however, there have been cases, especially the ones with low pressure difference generated by the pump, in which the default residual dimensions for the continuity equation were not obtained. In such runs, it was still verified that all residuals had a 10^{-4} order of magnitude or lower, that the energy residual was smaller than 10^{-15} and that the net flux imbalance for both mass and volume flow rates in/out of the instrument was less than 0.05%. Therefore, those results, being physically reasonable, have still been considered during the analysis.

4.1.2 Input data for runs

Simulations were performed considering an atmospheric pressure range between 950 and 1050 mbar and a temperature range between 273 and 323 K. Differently to what happened for the analysis in Martian conditions, ambient and instrument temperature were set to be equal, given the lack of a thermal cover on the instrument on Earth. Special emphasis was given to high temperature runs, given the interest in testing MicroMED in desert environment. In agreement with previous analyses, the effect of the pump was simulated by means of the pressure difference (Δp) generated by its rotation, setting "pressure inlet" and "pressure outlet" as boundary conditions, respectively related to the outside and to the outlet section of MicroMED. Δp values were varied between 2.5 and 30 mbar, in accordance with

the experimental results obtained during tests performed on MicroMED pump during the PFM integration.

The "sampling efficiency" parameter, defined as the ratio of the number of grains detected to the total number of grains entering the instrument (See Section 2.1), was used in order to evaluate the efficiency of MicroMED's PFM in terrestrial conditions. The analysis assumes ideal behavior by the other components of the instrument, so every grain that crosses the sensing spot is considered detected. The sampling efficiency parameter is especially important and is considered a driving parameter for the analysis of the results, just like in the Martian analysis. Table 4.21 reports a summary of the input parameters set for the performed simulations.

Parameter	Min value	Max value	Nr. of values
p_a	950 mbar	1050 mbar	3
T	273 K	323 K	5
Δp	2.5 mbar	20 mbar	6

Table 4.21 Input parameters for simulations. The table indicates the considered minimum and maximum values, as well as the number of different values of other parameter considered in the simulations.

4.1.3 Results and discussion

4.1.3.1 Proto Flight Model performances in Earth atmosphere

A detailed description of the PFM's fluid dynamic design has already been provided in Section 1.2.5.2. As a quick reminder, the inlet duct is a 111 mm long simply conical duct, going from a 4 mm internal diameter after the sampling head to 1 mm of internal diameter in proximity of the sensing spot of the instrument, that is inside MicroMED main box. The sampling head is a cylinder with an 8 mm external diameter, with 4 circular holes separated by 90 degrees, conceived for the sampling of fluid with embedded particles from the surrounding environment. The complete description of the PFM geometry is provided in Section 1.2.5. MicroMED's PFM was tested in the environmental conditions discussed in Section 4.1.2 (Table 4.21). The pump operating condition that provided the best results (in terms of sampling efficiency) is the one generating an inlet-outlet Δp of 30 mbar. Figure 4.113 shows the sampling efficiency plot for such design. It reports a direct comparison of the sampling efficiency obtained in terrestrial and Martian conditions when using the PFM geometry, considering for both cases the pump operating conditions that optimize performances (that are $\Delta p = 30$ mbar in Earth conditions, $\Delta p = 2$ mbar in Martian conditions). The instrument is able to achieve a sampling efficiency over 0.95 for the whole sampling

range in Martian conditions. However, due to the different fluid dynamics, the instrument is partially unable to properly collect dust grains in terrestrial atmospheric conditions, especially for grains under 7 μm in diameter. The worsening of the instrument efficiency limits the possibility to test MicroMED in terrestrial environment when using the PFM geometry.

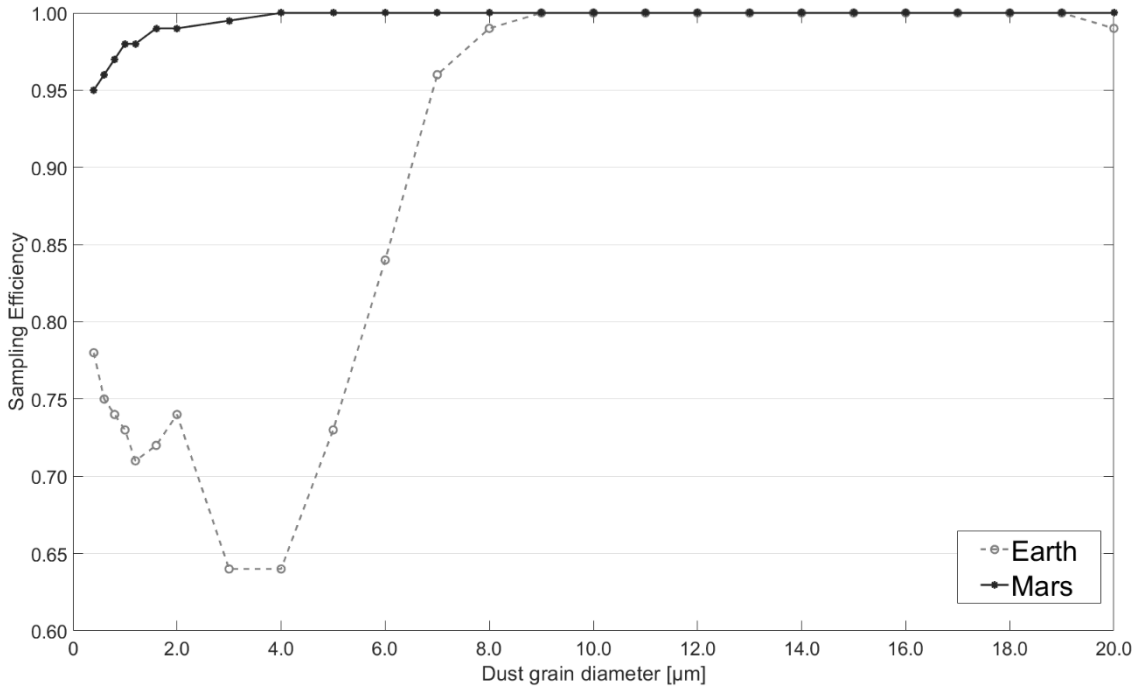

Figure 4.113 Comparison between typical MicroMED sampling efficiency curves in Mars (pressure = 8 mbar, temperature = 280 K, instrument temperature = 253 K, Δp = 2 mbar) and Earth conditions (pressure = 950 mbar, ambient temperature = instrument temperature = 273 K, Δp = 30 mbar).

Particular attention was dedicated to the fluid dynamics of the inlet duct and of the sampling head, as well as to the fluid streamlines and the particle trajectories along MicroMED's PFM. It was possible to identify some potential causes of the experienced efficiency loss. In particular, pressure gradients (Figure 4.114) are present inside MicroMED sampling head, altering grain trajectories. The particle tracking tool by Ansys Fluent allows to verify such influence (Figure 4.115-Figure 4.116). Undetected grains are mainly lost in the inlet duct. In this duct, flow is laminar since Re is in the 800-1600 range. Hence, the efficiency loss is not directly related to turbulence, but rather to the greater density of the fluid. In the rarefied Martian atmosphere, dust grains can be better centered in the duct section, meaning they can be closer, on average, to the duct longitudinal axis and hence to the center of the laser illuminated spot. Conversely, terrestrial environment implies higher dispersion of grains. Such behavior is depicted in Figure 4.117, where it is also shown that dust grains velocity is higher in terrestrial conditions. This is due to the better performances of the pump in the denser Earth atmosphere, generating a stronger suction and consequently a larger

acceleration of the fluid. However, grains that are able to reach the internal box of MicroMED's PFM tend to cross the laser illuminated spot in very high percentages, similarly to what happens in Martian conditions. This means that, while the fluid dynamic behavior in the head and inlet duct of MicroMED is worse in Earth condition, there is little difference inside the instrument box, if the flow is kept laminar.

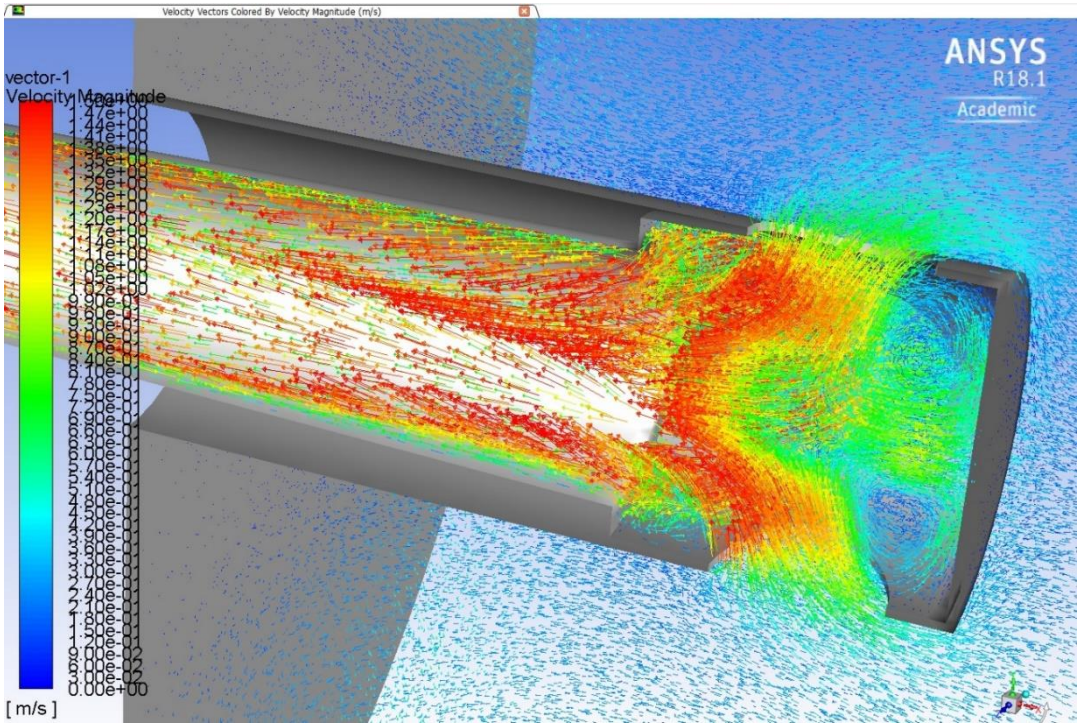

Figure 4.114 Fluid flow inside MicroMED Proto Flight Model sampling head. In all figures showing either fluid velocity vectors (like this one) or particle trajectories (like Figure 4.115), the different colors represent grain velocity [m/s] according to the scale shown in each figure.

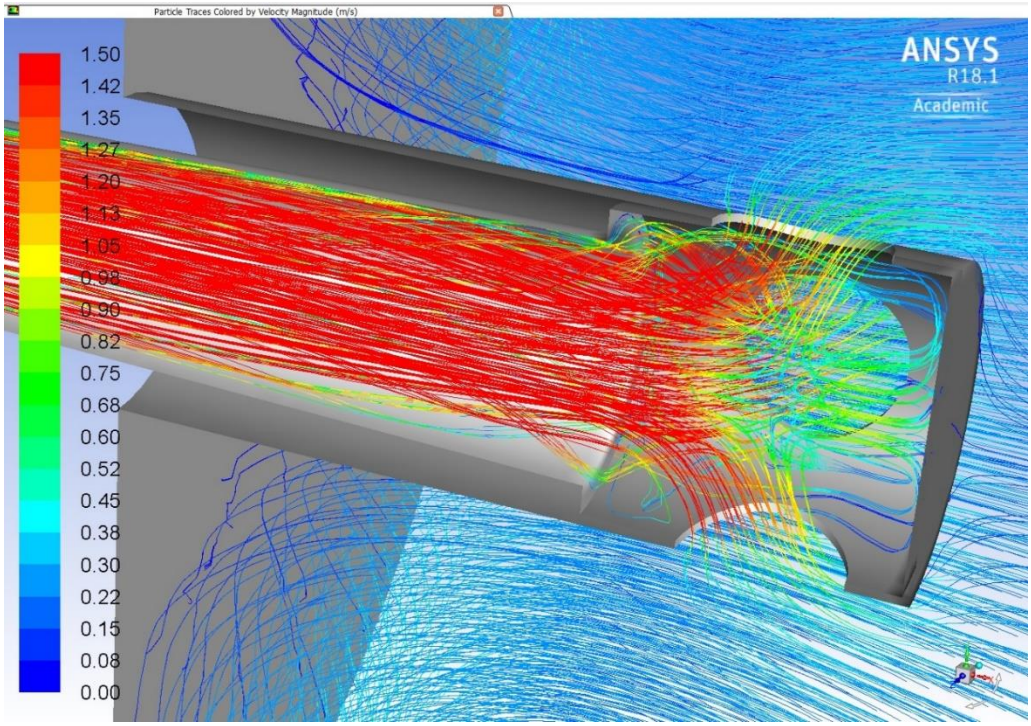

Figure 4.115 Particle tracks for small (0-1 µm diameter) grains inside MicroMED Proto Flight Model sampling head when used in Earth atmosphere.

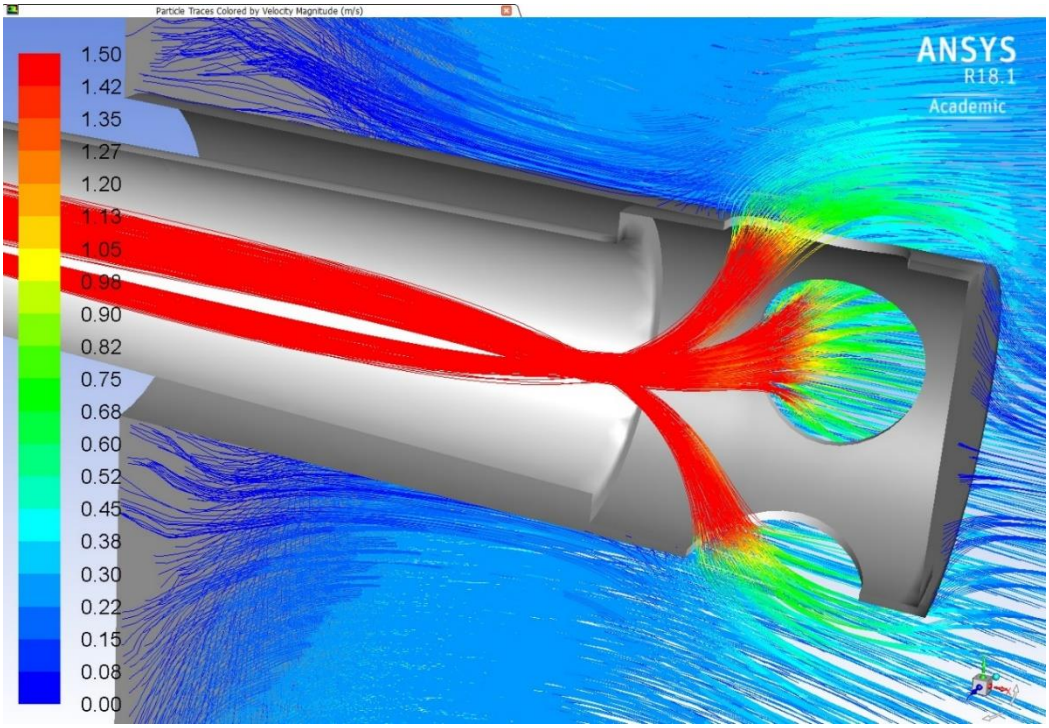

Figure 4.116 Particle tracks for large (15-20 µm diameter) grains inside MicroMED Proto Flight Model sampling head when used in Earth atmosphere.

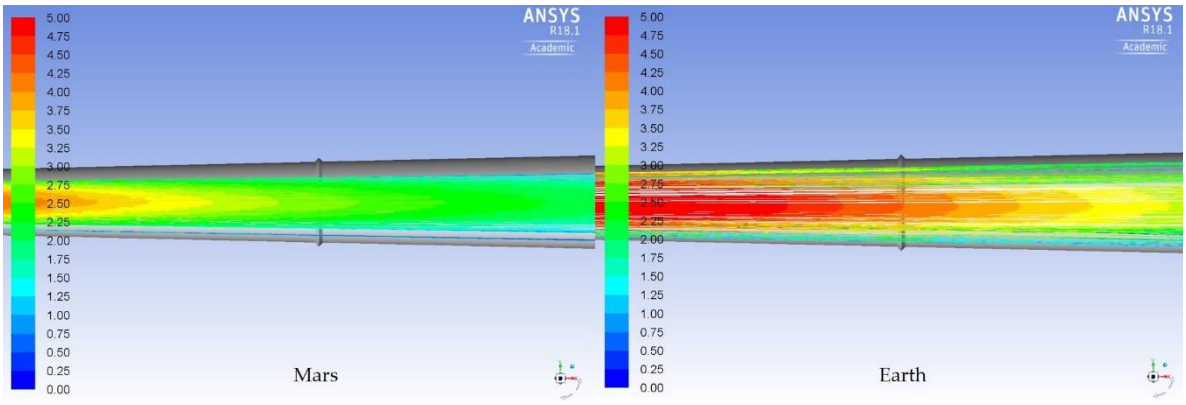

Figure 4.117 Direct comparison of dust grains trajectories in Martian and Earth conditions along MicroMED Proto Flight Model inlet duct (Martian conditions: ambient pressure = 8 mbar, ambient temperature = 280 K, instrument temperature = 253 K, Δp = 2 mbar; Earth conditions: ambient pressure = 1050 mbar, ambient temperature = instrument temperature = 303 K, Δp = 30 mbar).

4.1.3.2 Effects of environmental parameters on MicroMED PFM in terrestrial atmosphere

MicroMED's PFM behavior in Martian conditions is influenced by the environmental parameters (Section 2.2). In particular, the instrument temperature was found to be the most influential parameter on efficiency. A similar analysis has been performed in terrestrial environment, showing that, in this case, there is no dependence of the instrument efficiency on pressure and temperature (Figure 4.118-Figure 4.119). The influence of pressure on Earth is slightly stronger; however, average variations are under 1% for most dust grain sizes with peaks around 5-7%.

The pressure difference generated by the pump is obviously an influential parameter. Both in terrestrial and Martian conditions, within a reasonable range of values, an increase of the pump generated Δp (which is related to a higher pump rotating speed, thus to higher fluid speed) produces an increase of the sampling efficiency for large grains (i.e. diameter > 10 μm) but conversely a slight reduction of the sampling efficiency for small grains (diameter < 1 μm) (Figure 4.120).

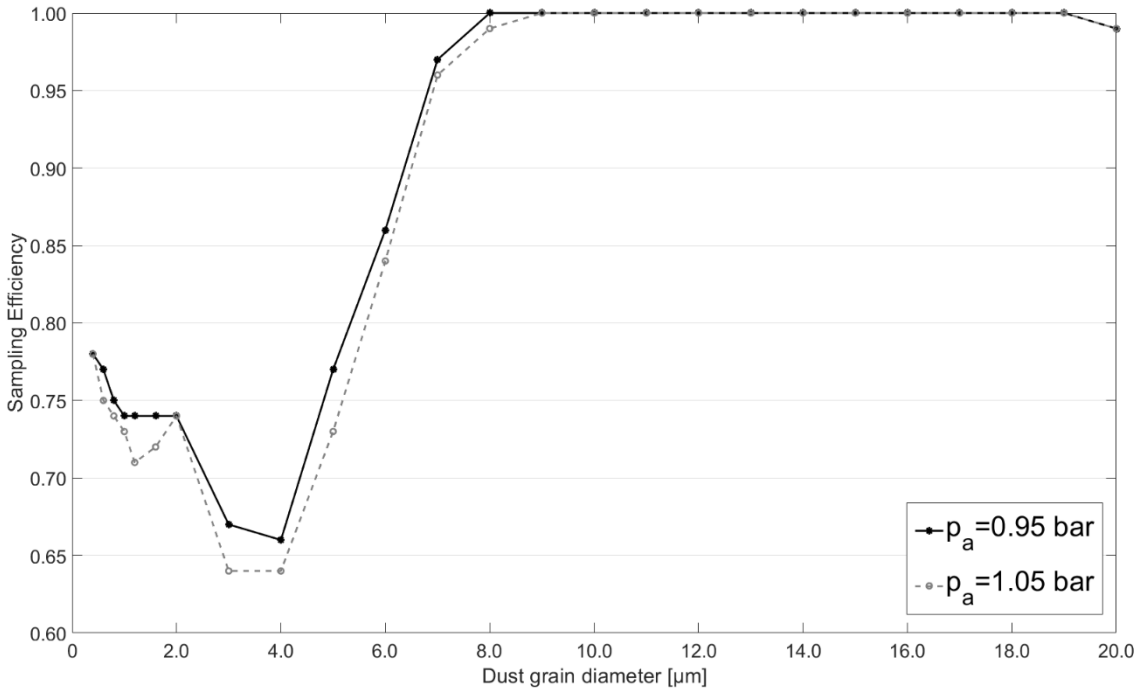

Figure 4.118 Effect of atmospheric pressure on sampling efficiency in Earth conditions (Δp = 30 mbar, Ambient temperature = 303 K).

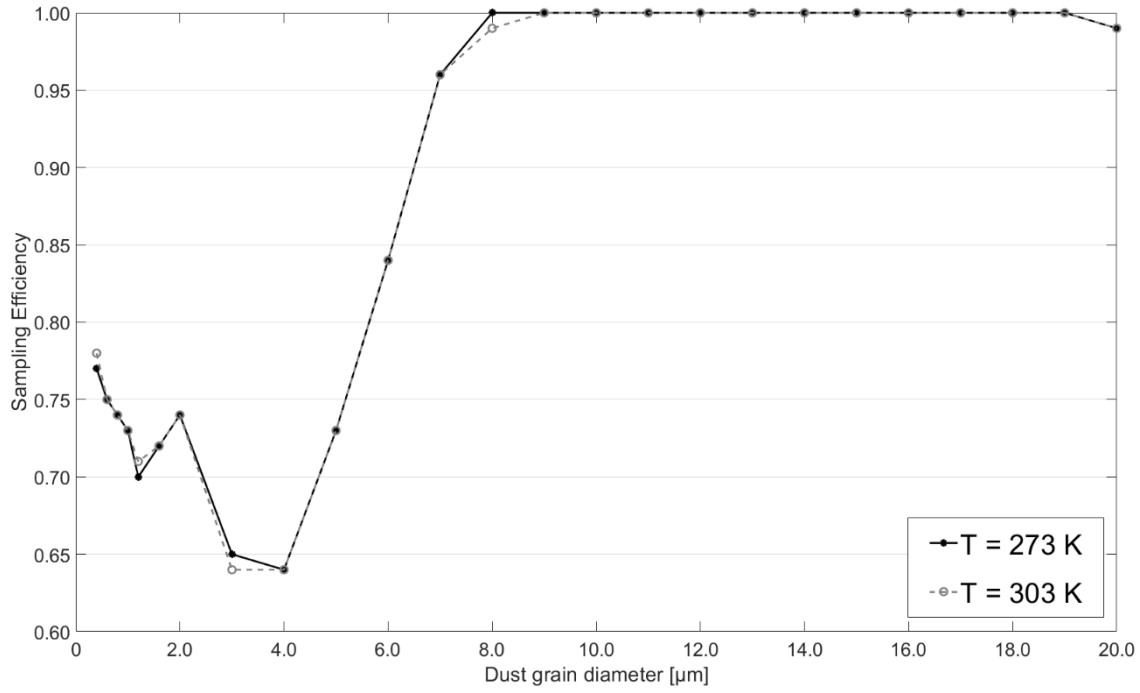

Figure 4.119 Effect of atmospheric temperature (or instrument temperature) on sampling efficiency in Earth conditions (Δp = 30 mbar, ambient pressure = 1050 mbar).

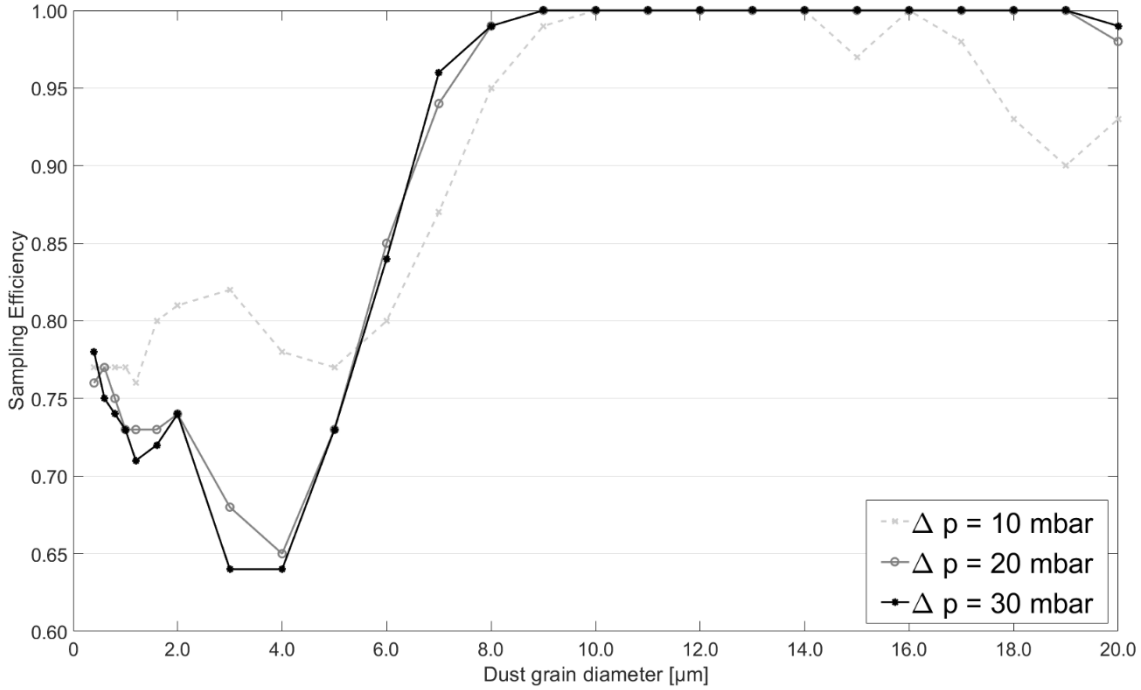

Figure 4.120 Effect of pump induced Δp on sampling efficiency in Earth conditions (Ambient pressure = 1050 mbar, ambient temperature = 303 K).

4.2Proposed MicroMED terrestrial adaptations / designs

The possibility of adapting MicroMED to Earth conditions is favored by the accessibility of its inlet duct. The duct is constituted by three threaded elements (see Section 1.2.5), and it is placed outside the instrument main box. It is thus possible to substitute the current inlet duct, designed for Martian conditions, with a newly designed version conceived for Earth usage.

Results in Section 4.1.3.1 show that, with the PFM design, dust grains up to 7 μm are detected with less accuracy in Earth conditions. Deflections of grains are less sharp in Earth atmosphere; the adapted geometry has thus to ease the particle deflection. A couple of possible new designs were proposed and are described in the following subsections.

4.2.1 First design solution

A first possible design was developed, consisting of a sampling head with a grid replacing the holes (Figure 4.121). The sampling head has the same diameter of the PFM geometry (8 mm). The analysis was performed considering different lengths of the conic duct going from 111 to 141 mm. Variations of the duct length were made with the intent of finding the right trade-off between the ability to generate a pressure force on outside grains (the force is stronger for a shorter duct) and the ability to smooth the flow field in the duct, providing dust grains more space to adjust their trajectories toward the sensing spot. The duct diameter is the same had for the PFM geometry, namely 4 mm of internal diameter in proximity of the sampling head, 1 mm at the end of the duct (inside MicroMED box).

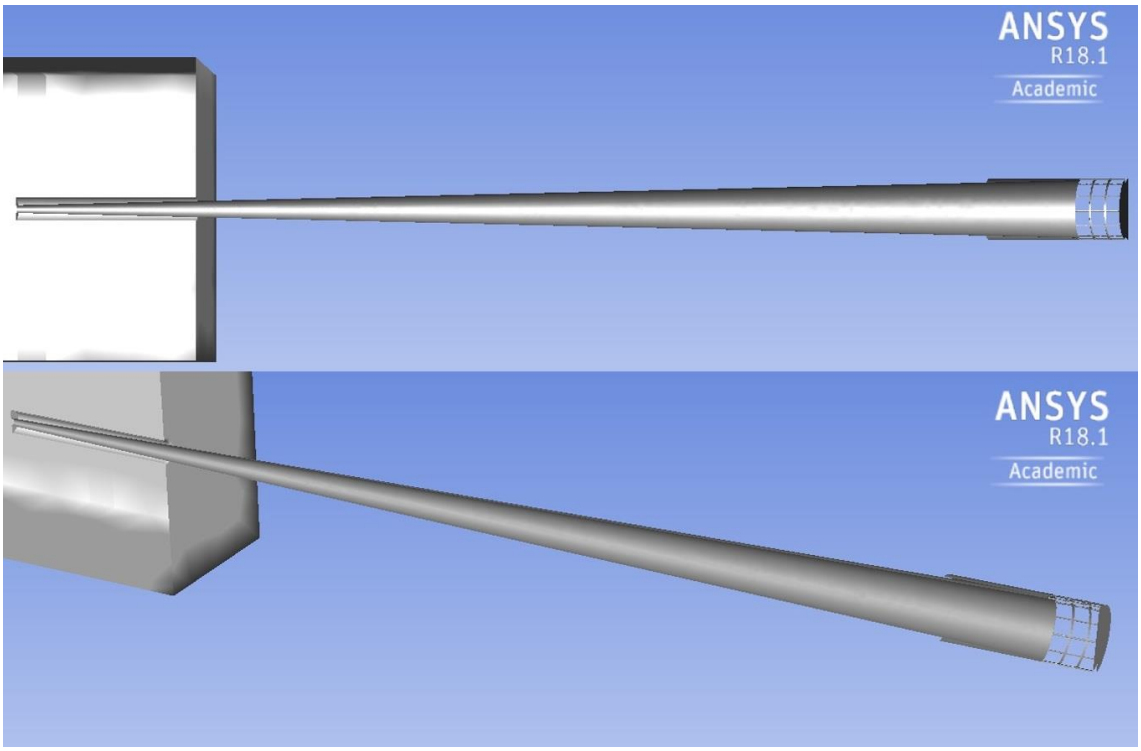

Figure 4.121 Possible solution with a grid substituting inlet holes in the sampling head. Figure only shows the internal surfaces of ducts, since the Fluent® input mesh that was generated is representative of the fluid domain, namely the fluid inside the ducts, so the figure has not to be interpreted as an actual geometry representation.

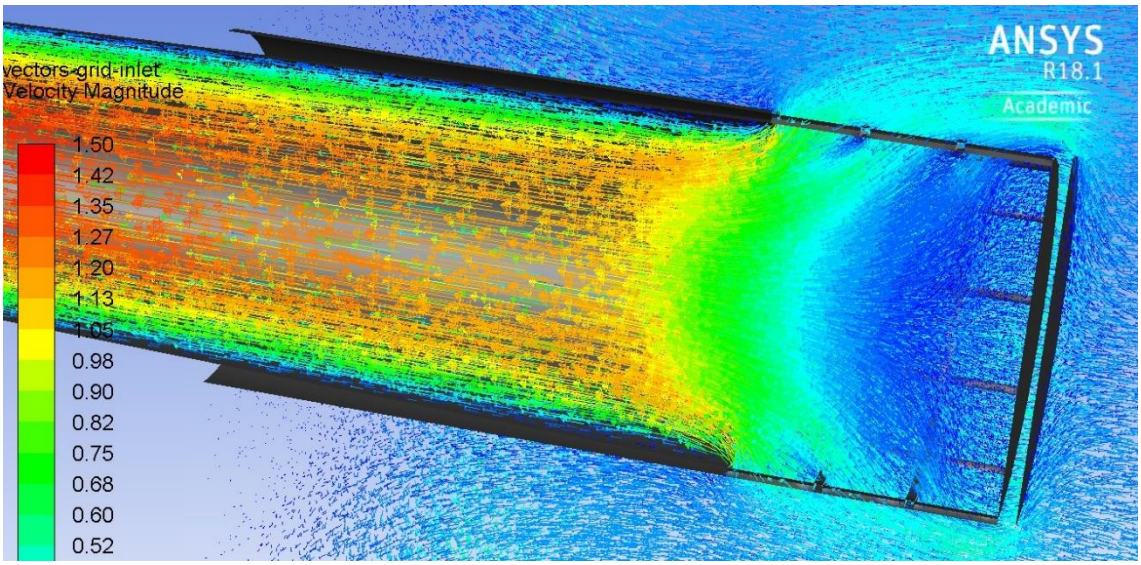

Figure 4.122 Fluid flow inside MicroMED sampling head with a grid in place of the inlet holes.

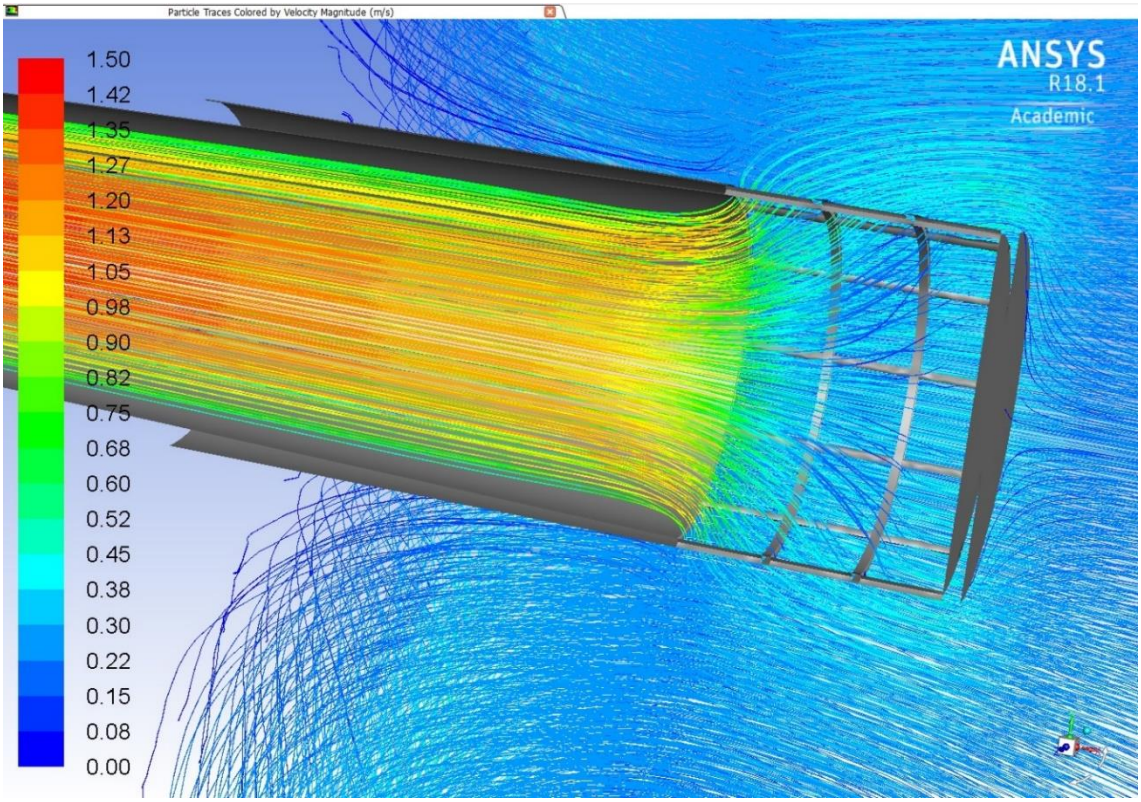

Figure 4.123. Particle tracks for small (0-1 μm diameter) grains inside MicroMED Grid Inlet

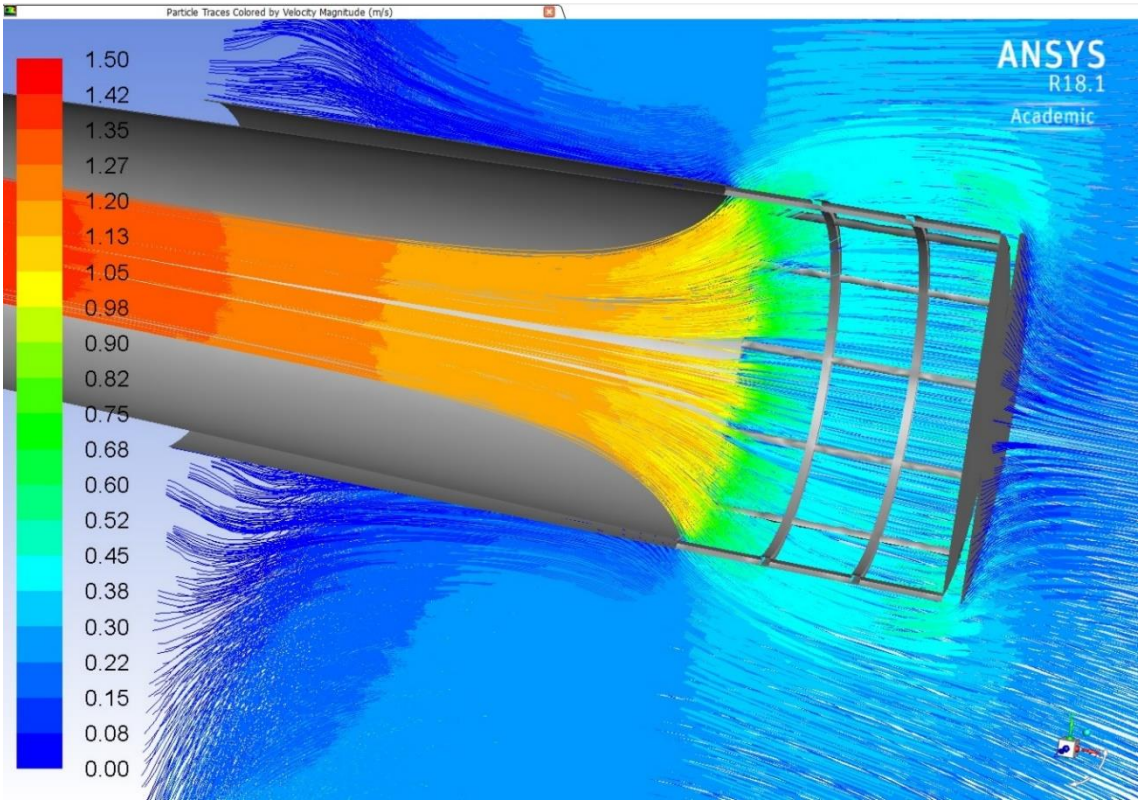

Figure 4.124 Particle tracks for large (15-20 μm diameter) grains inside MicroMED Grid Inlet.

As shown in Figure 4.122, this design removes pressure gradients inside the sampling head and the particle trajectories appear to be much improved with respect to the PFM geometry both for small and large dust grains (Figure 4.123-Figure 4.124). The lack of side walls on the head, though, makes it tougher to generate a significant pressure force on the flowing grains, thus suction of large dust grains is only possible for large pump induced pressure differences. The analysis showed that for anything less than Δp = 15 mbar, the instrument is unable to properly detect large dust grains (diameter > 14 μm, see Table 4.22) with this sampling head. All simulations were performed considering the same dust concentration in the atmosphere surrounding MicroMED. Thus, if MicroMED could sample all grain sizes in the sampling range with the same efficiency, it would reproduce the input dust grain distribution. In such case, the distribution obtained would have about 18% of grains of at least 14 μm in diameter (the expected value is 17.8%). Table 4.22 shows that with this design and for low pressure differences, the instrument is not able to sample large dust grains in good percentages and the size distribution obtained is significantly altered. As for the input grain size distribution, it has to be underlined that values in Table 4.22 are relative to the input size distribution used for simulations and not for the expected size distribution in terrestrial deserts. The discrepancy is due to the need for the simulation to provide a statistically valid number of grains of each size. Runs with a more realistic distribution led to a small sample of large grains, which is expected for both Earth and Mars atmospheres (under 1% of large grains is expected considering both Pollack and Dickinson distributions, Pollack, J.B. et al., 1995; Wolff, M.J. et al., 2009; Dickinson, C. et al., 2011). This aspect furtherly highlights the need for an efficient sampling of large grains, since, given the small percentages of such grains in the atmosphere, the sample obtained from tests could be extremely small.

Δp [mbar]	**Pct. %**
2.5	1.6%
10.0	13.0%
15.0	17.0%
20.0	18.3%
Expected value	**17.8%**

Table 4.22 Percentage of large dust grains (diameter > 14 μm) among detected grains for Grid Inlet runs

Given its inability to sample large grain sizes at low pump speed, the usage of the Grid Inlet design would increase the risk of turbulence inside the ducts. On the other hand, there is still an improvement to the instrument sampling efficiency with respect to the Martian design (Figure 4.125).

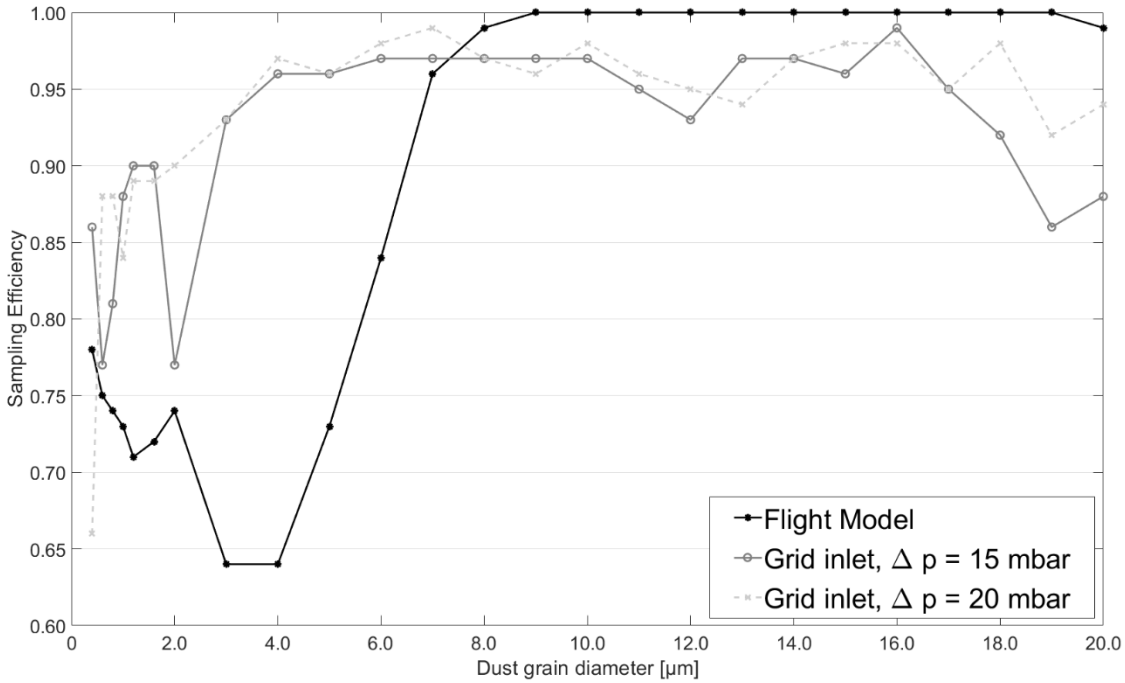

Figure 4.125 Comparison between sampling efficiency in Earth conditions for MicroMED Proto Flight Model and Grid inlet versions (For Grid inlet runs: ambient pressure = 1050 mbar, ambient temperature = 313 K; for Proto Flight Model runs: ambient pressure = 1050 mbar, ambient temperature = 303 K, Δp = 30 mbar).

4.2.2 Second design solution

Figure 4.126 shows a second possible design for MicroMED's "terrestrial" inlet. The inlet duct was elongated and an additional fifth hole (with respect to the PFM design) was added on the top of the sampling head, with the idea of reducing pressure gradients inside the head and trying to smooth the fluid streamlines along the fluid's path toward the sensing region.

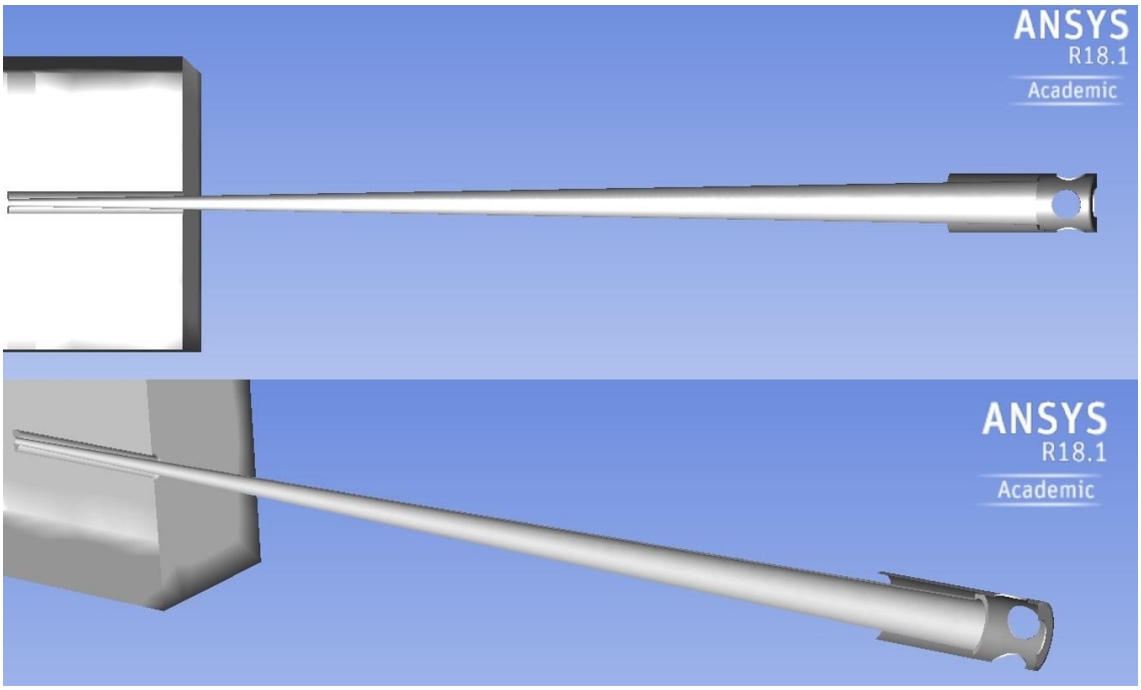

Figure 4.126 Possible solution with a 5th hole on the top of the sampling head. Like in Figure 4.121, only the internal surfaces of ducts are shown here, as the Fluent® input mesh that was generated is representative of the fluid domain, namely the fluid inside the ducts, so the figure has not to be interpreted as an actual geometry representation.

This solution gave good results in reducing the vorticity regions in the sampling head (Figure 4.127). The improvement of the fluid dynamic behavior can be better appreciated by observing the particle trajectories (Figure 4.128-Figure 4.129) that are smoother for both small and large dust grains. Such improvements are reflected by the efficiency curves that have been obtained (Figure 4.130). The design allows the detection of dust grains with good efficiency (0.89 or higher) throughout the sampling range. Curves shown in Figure 4.130 are relative to different pump speeds. For the PFM geometry, the curve is relative to an inlet-outlet Δp of 30 mbar, which optimizes performances for such design. Curves for the 5-Hole Inlet design correspond to pressure differences that range from 2.5 to 20 mbar, hinting on the evolution of the performances with the increase of the pump speed. Similarly to what happened for the PFM design (results already discussed and shown in Figure 4.119), it is clear that a growth of the pump speed increases the pressure forces exercised on the particles flowing around MicroMED's sampling head, which is positive for the sampling of large dust grains. Higher samples of such grains are indeed provided. On the other hand, higher pump speeds could alter the instrument's ability to concentrate small dust grains in the 1 mm^2 sensing area.

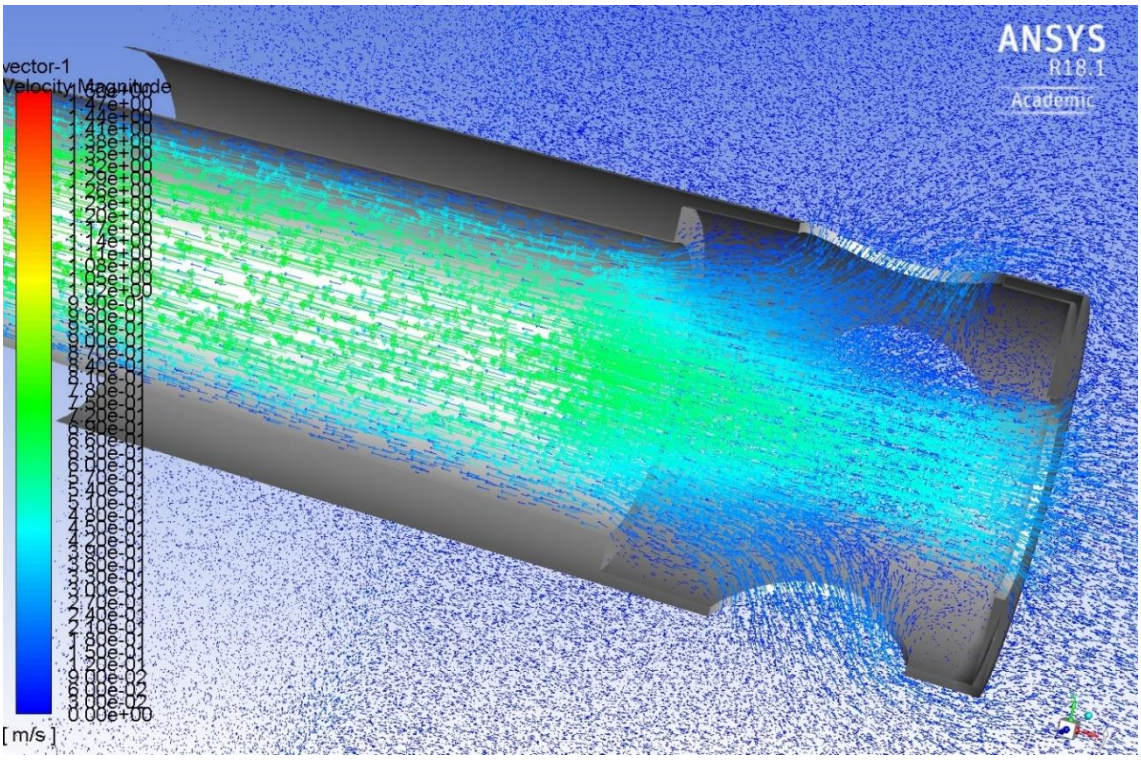

Figure 4.127 Fluid flow inside MicroMED 5-Hole sampling head (color scale is related to fluid speed).

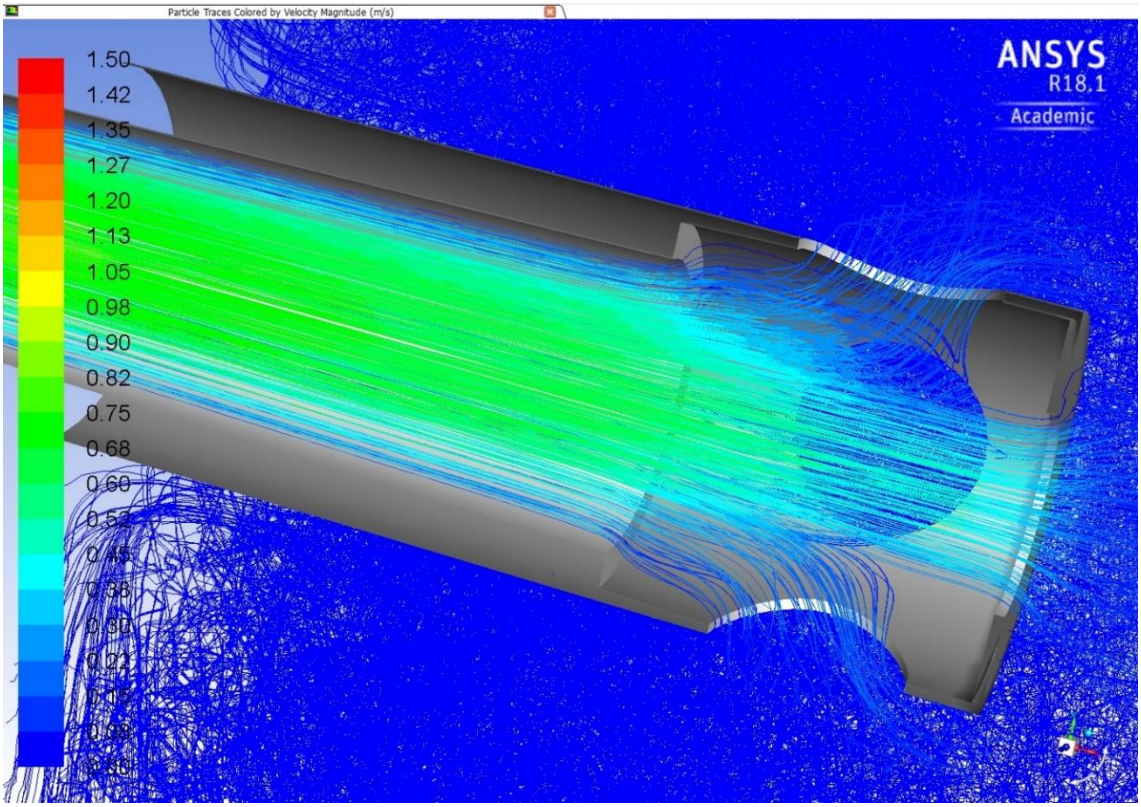

Figure 4.128 Particle tracks for small (0-1 μm diameter) grains inside MicroMED 5-Hole Inlet.

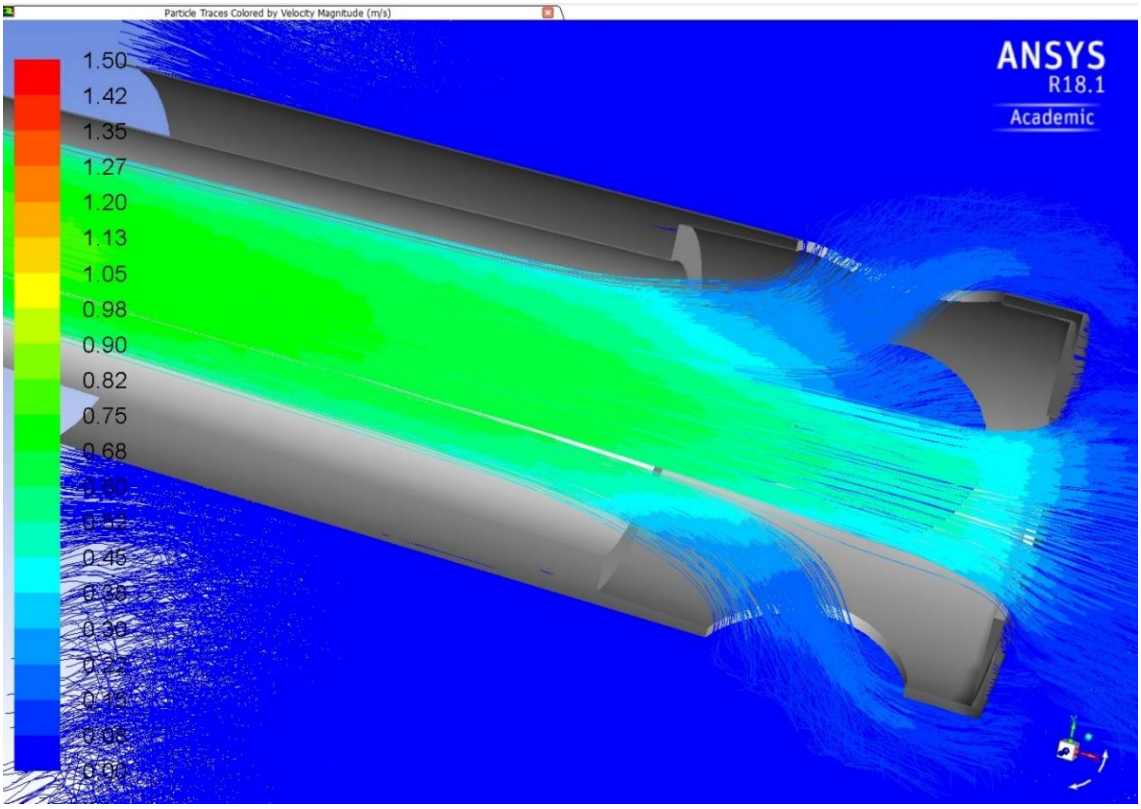

Figure 4.129 Particle tracks for large (15-20 μm diameter) grains inside MicroMED 5-Hole Inlet.

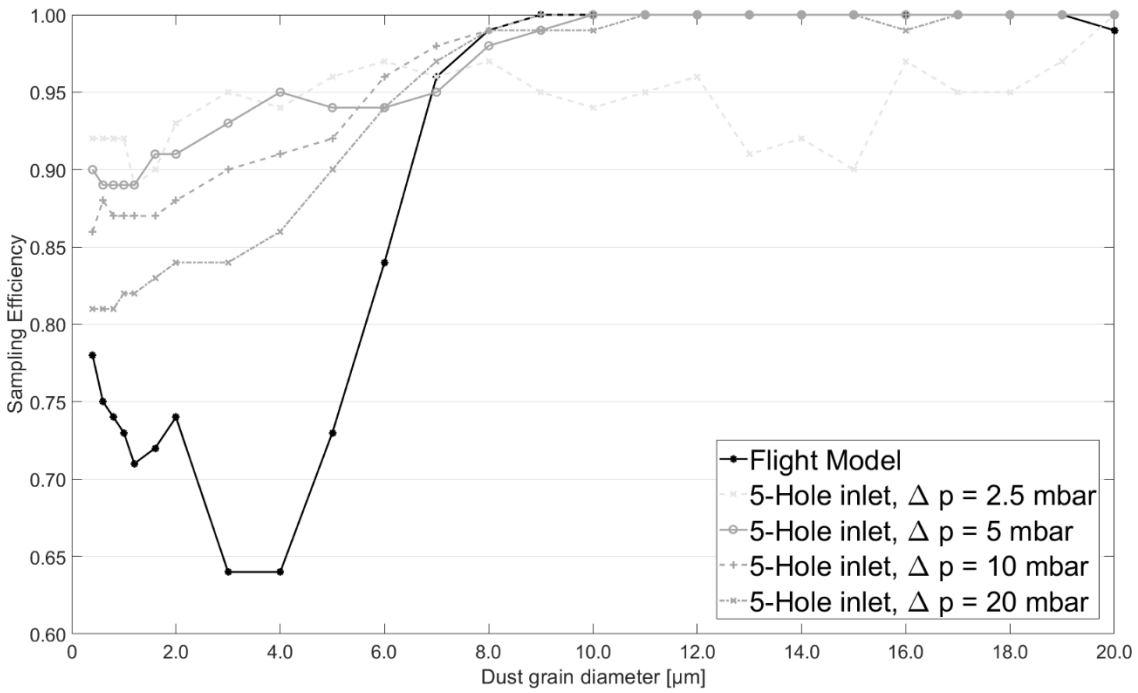

Figure 4.130 Comparison between sampling efficiency in Earth conditions for MicroMED Proto Flight Model geometry and 5-Inlet Hole versions (For 5-Hole inlet runs: ambient pressure = 1050 mbar, ambient temperature = 303 K; for Proto Flight Model runs: ambient pressure = 1050 mbar, ambient temperature = 303 K, Δp = 30 mbar).

Overall, the second proposed design shows better performances for low values of Δp (Figure 4.130, the best result is obtained for Δp = 5 mbar) and this is relevant since it guarantees good performances for significantly lower pump rotational speeds. This implies laminar flow along the instrument, as well as a reduction of the power consumption of the instrument. As already stated, laminar flow is a favorable feature in order to improve MicroMED's efficiency and has to be treated as a design parameter. The improvement in performances can be also appreciated by Table 4.23, which similarly to Table 4.22 aims at evaluating the ability, using this design, to sample large grains. The results presented show that the instrument is always able to sample large grains and reproduce the input size distribution, with optimized sampling efficiency in the Δp range between 5 and 10 mbar.

Δp [mbar]	Pct. %
2.5	15.2%
5.0	16.3%
10.0	18.5%
Expected value	**17.8%**

Table 4.23 Percentage of large dust grains (diameter > 14 μm) among detected grains for 5-Hole Inlet runs.

4.2.3 Comparison between the two proposed designs

The results obtained for the two proposed designs were compared in order to finalize a trade-off analysis. Figure 4.131 shows a comparison in terms of sampling efficiency. The second proposed design provides the best performances. Results are comparable for the two designs for most of MicroMED detection range, however for the first design it is impossible to either provide good performances for small dust grains when the pump speed is high or to sample large dust grains when the pump speed is low.

In terms of power consumption, the second design is also the best choice. This is due to the possibility to operate at very low pump rotational speeds. At the same time, it has to be underlined that the choice of the actual operating condition has to be a compromise between the optimal fluid dynamic behavior and the mechanical issues related to the pump, that could become unstable and get stuck for rotational speeds under 1000 rpm. A Δp of 5 mbar could indeed be related to similar pump speeds. However, if this Δp value can be mechanically afforded, the pump consumption could be reduced from 1.5 W to roughly 0.4 W (a ~ 70% reduction).

In terms of fluid speed, the second design is definitely the best choice as laminarity of the flow is needed inside MicroMED. Considering that MicroMED characteristic length is 1 mm, laminar flow can be obtained for fluid speed of less than 35 m/s. In the case of the first design, the highest efficiency is achieved at Δp of ~ 20 mbar. However, the maximum fluid velocity in MicroMED box is already ~ 35 m/s for a Δp of 9 mbar. In contrast, the second design has optimal behavior at Δp ~ 5 mbar, and fluid speed inside MicroMED reaches a maximum value of 20 m/s in this case. Critical conditions that could lead to a transition of the flow are not met until Δp is well over 10 mbar.

A comparison between the two proposed designs can also be made in terms of position histograms in the sampling spot. Given the ability to track grains trajectories along the instrument, it is possible to evaluate the tendency of grains of each size to cross the sensing spot close to the longitudinal axis of the ducts. This is relevant, because light is more uniform and intense at the center of the laser illuminated spot, therefore grains that cross the central spot are evaluated with better accuracy. It is possible to build histograms that show the distance of passing grains from the center of the laser spot. Figure 4.132 and Figure 4.133 show a comparison between the position histograms obtained for the two designs. The extremes of MicroMED sampling range (0.4 and 20 μm in diameter) are taken as an example. The Grid Inlet design optimizes the detection of large dust grains for a Δp of 20 mbar, which is considered in the histograms even though, for such design, a maximum Δp of only 9 mbar can be afforded because of flow laminarity constraints. Both cases with Δp = 9 and 20 mbar are reported, just to show that one optimizes the collecting ability for large grains, the other for small grains. Figure 4.132 shows the position histograms for 0.4 μm grains. For such grains, the 5-Hole Inlet design provides a reduced percentage of undetected grains (11% compared with 19% and 39% for the Grid Inlet design with 9 and 20 mbar of Δp, respectively). Both designs appear to have a distribution of grains centered at a distance between 350 and 400 μm from the center of the spot. In the case of 20 μm dust grains (Figure 4.133), the 5-Hole Inlet is able to concentrate all grains inside the sensing spot, while the Grid Inlet would need high pump speeds to optimize their detection. However, a Δp of 20 mbar, as stated above, would lead to a turbulent flow. Moreover, the sample obtained, especially for a Δp of 9 mbar, is significantly lower, as Table 4.22 and Table 4.23 already showed (the 20 μm bar plot for Grid Inlet and a Δp of 9 mbar is indeed related to a very small sample).

As a consequence of this analysis, the second design was chosen to be the definitive one for the terrestrial version of MicroMED. The newly designed inlet is currently under construction, and the terrestrial version of MicroMED is currently in realization. Once it is integrated, the instrument is then going to be tested in desert terrestrial environments, hopefully as soon as 2022.

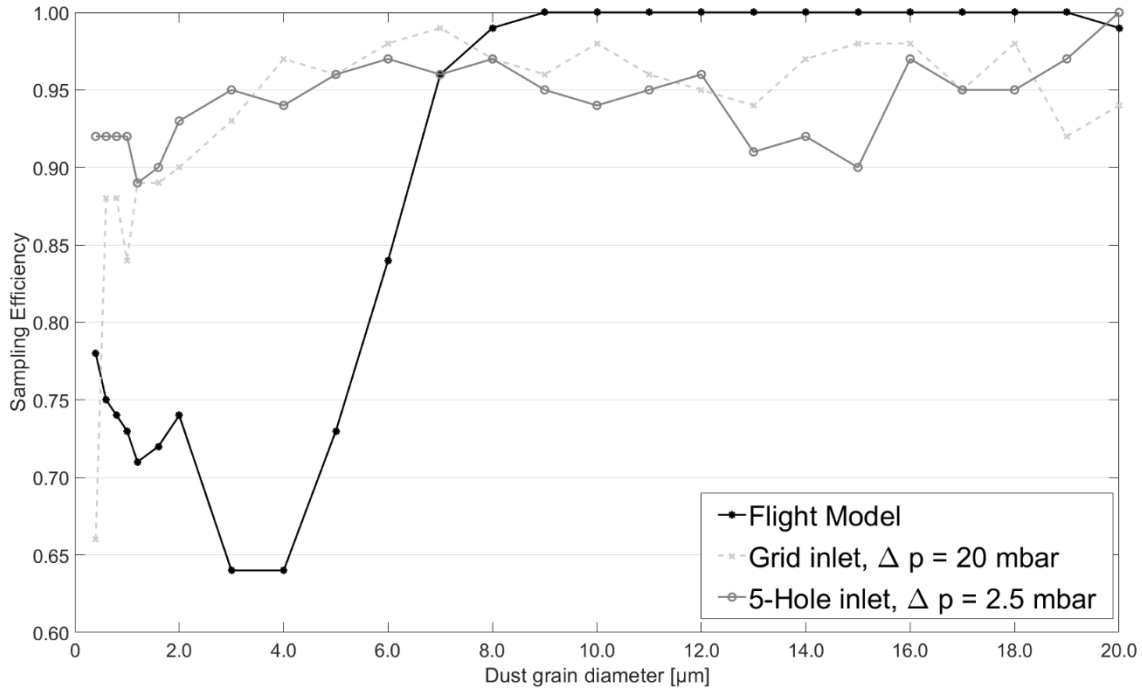

Figure 4.131 Comparison between sampling efficiency in Earth conditions for MicroMED Proto Flight Model, 5-Hole inlet and Grid inlet versions (operating conditions are the conditions that optimize the performances for the three geometries, namely: for Proto Flight Model runs ambient pressure = 1050 mbar, ambient temperature = 313 K, Δp = 30 mbar; for Grid inlet runs ambient pressure = 1050 mbar, ambient temperature = 313 K; for 5-Hole inlet runs ambient pressure = 1050 mbar, ambient temperature = 303 K).

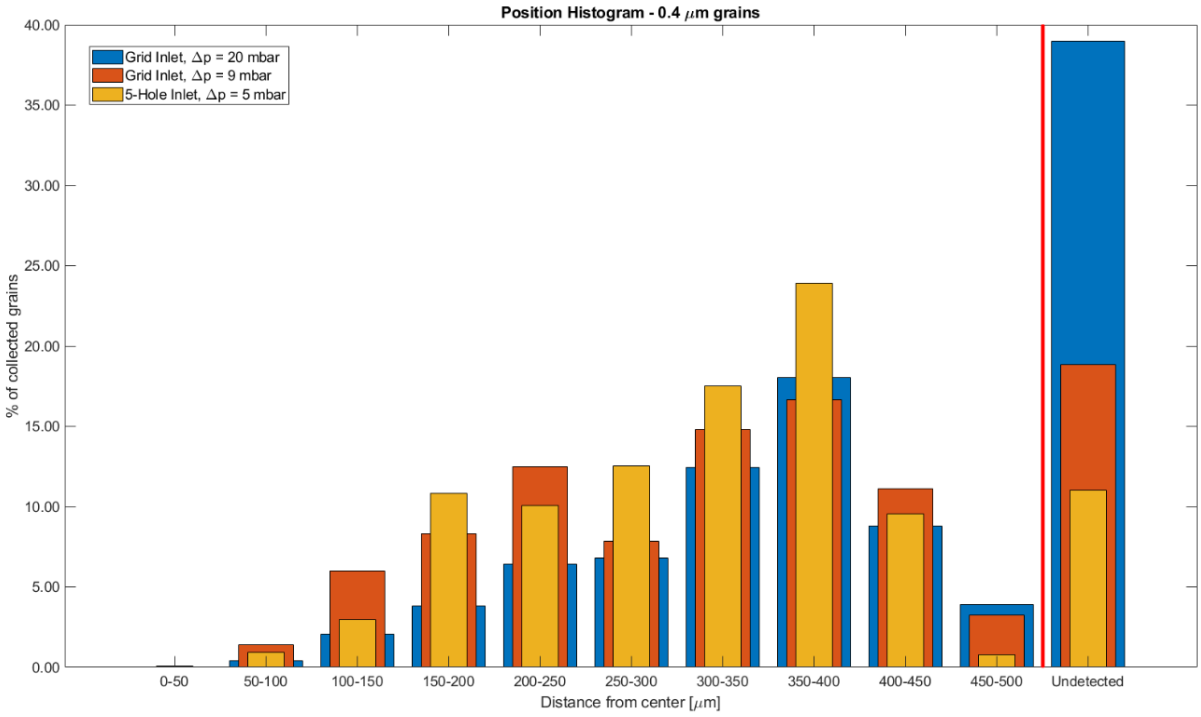

Figure 4.132 Position Histograms for 0.4 μm grains.

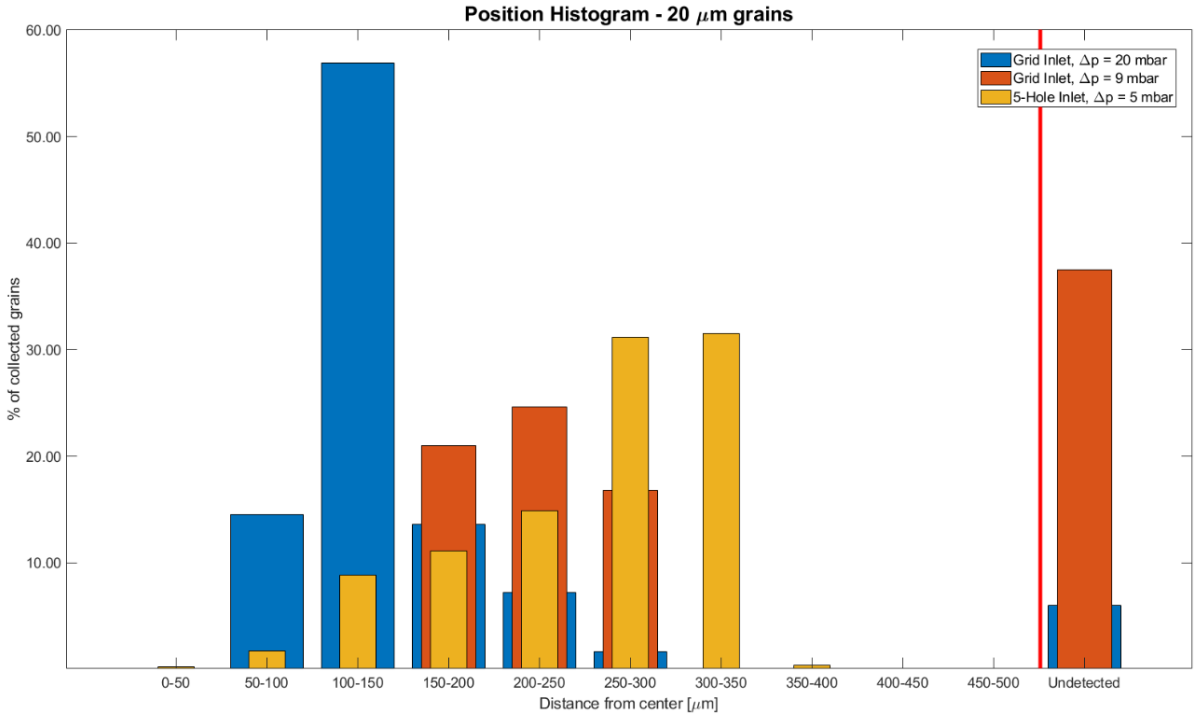

Figure 4.133 Position Histograms for 20 μm grains.

4.2.4 Quick summary of the results of the re-design of MicroMED for terrestrial applications

MicroMED's design has been developed for optimal efficiency in Martian environment. However, besides testing the instrument in Martian environment, significant contribution is expected from tests in terrestrial deserts where, despite a different atmospheric and fluid dynamic environment, Mars-like dust lifting phenomena are expected. In order to operate MicroMED in terrestrial conditions, the design of its sampling system required modification. To this purpose, an in-depth CFD analysis of MicroMED PFM behavior in terrestrial environment was performed. The aim of such analysis was to evaluate the performances of the current Mars-optimized design in Earth conditions and then to individuate possible adjustments to properly re-design MicroMED's inlet duct for terrestrial usage. This would allow to test the instrument in Earth atmosphere and also to potentially alternate tests in Earth and Mars conditions.

In this section, the process of re-design of MicroMED's inlet with the purpose of using it on Earth is described. The updated geometry derived from the CFD analysis, that is expected to optimize the instrument behavior in terrestrial conditions with minimal instrument modification. The effect of environmental parameters on the instrument efficiency and the

adjustments needed to improve the performances have been quantified. Two new possible designs have been proposed. The two designs have been compared in terms of a number of parameters. Results show that the second design, with 5 holes on the sampling head, is the best one, given its ability to guarantee high sampling efficiency throughout the instrument's sampling range (at least 0.89 for all sizes). Moreover, such a new design shows its optimal performances at very low pump speed, an operating condition that allows a reduction of power consumption and assures flow laminarity inside the instrument, a mandatory condition for MicroMED's scientific retrieval. With its new fluid dynamic design being set, the inlet duct of MicroMED's terrestrial version is set for realization, pending the instrument integration that is currently ongoing.

5.The Safeair® instrument

The current Covid-19 pandemic has sparked an explosion of the research activities aimed at detecting the presence of pathogens (namely the coronavirus responsible for the SARS-CoV-2 disease), in order to contribute to the battle against the spreading of the virus and provide an efficient monitoring of the health and safety of shared environments. To this purpose, and in the framework of a larger INAF initiative aimed at adapting already existing technologies for the usage in the battle against Covid-19, our group has developed an adaptation of the MicroMED OPC aimed not at the sampling of dust grains, but at the sampling and capture of environmental aerosol, potentially contaminated by Sars-Cov-2 virus. The idea is to use this instrument, called Safeair ®, in hospital rooms and/or in closed venues (offices, supermarket, etc.) to scan the aerosol coming from people breathe in the environment. The instrument is then able, by means of lab on chip technology, to capture the aerosol in a liquid solution and convey it toward the lab on chip, which analyzes the liquid and, in case of detection of Covid-19 in the sample, triggers a warning signal. Safeair is currently undergoing the international patent procedure, to be recognized as an original invention. As part of the group of inventors that has developed the Safeair instrument, I own 2% of the intellectual property of the invention (Patent n° 102020000018409 filed on 29th July 2020), and my role has been to adapt the fluid dynamic sampling system of the instrument, which resembles MicroMED (from which it originates) to the sampling and capture of aerosol. The following sections will describe such work, even though, for copyright purposes related to the patent procedure currently ongoing, the description will lack a number of details that have been considered covered by copyright.

5.1Safeair ® description

Safeair® (Figure 5.134) is an instrument able to sample and individuate pathogens in the surrounding air. The main foreseen application is to use it in closed venues, hospital rooms, subway trains, supermarkets, etc. as well as a direct receiver of the breath of patients in hospitals with the aim of sampling aerosol with embedded pathogens. The instrument is able to detect the presence of pathogens, included the virus of SARS-CoV-2. This section refers to the sampling of the latter, however the method can be used for any other pathogen, making the instrument extremely flexible to various usages. Currently, the ongoing pandemic requires detection and prevention methods able to protect the population from the exposition to the virus. In this framework, we know very well that a 1 m social distancing is advised to prevent the spreading of the contagion, however, as reported in L. Bourouiba, 2020, such recommendations are based on reports from the early 1900s that consider as contagious only the droplets emitted by breath or talking which are large enough to deposit in the surroundings of the infected individual before evaporating. However, Bourouiba shows that, along the large droplets following a semi-ballistic trajectory, a turbulent cloud is generated during emissions like a sneeze of a cough, which remains in suspension for as long as minutes or hours, depending on the size of the droplets. Overall, a continuum of sizes is emitted, with droplets going from hundreds of μm to some nm. Warm and wet climate can contribute to the duration of the cloud. In this case, a 7-8 m distance could be considered enough for safety. Droplets depositing along the trajectory can deposit the virus on surfaces and objects, while smaller ones that are trapped in the turbulent cloud stay suspended until the cloud loses momentum and evaporation happens. These nuclei of droplets can thus remain in suspension for hours. The evidence of such clouds has been shown in works like N. van Doremalen et al., 2020, that indicates that the SARS-CoV-2 virus stays in suspension for as long as 3 hours. Even simple breath can emit SARS-CoV-2 in the surrounding air. Moreover, the virus is able to survive for hours on objects and in ventilation apparatuses. A further mode of contamination can be atmospheric particulate matter. A number of studies have shown a direct correlation between atmospheric pollution and diffusion of the SARS-CoV-2 epidemic.

These considerations lead to the need of a system able to sample and analyze both particulate matter and aerosol in the atmosphere. In case of detection of the virus, strict measures can be adopted to prevent the spreading of the contagion. Given the possibility of using the device to directly sample the breath of patients, Safeair can also be thought as a potential aid to swabs or antigen tests.

Devices able to sample and capture viruses are already known in literature (Andersen impactors, all-glass impingers - AGIs and so on). Methods for the sampling of viruses utilizing spectroscopy and recently lab-on-chip technology are also known. The latter is able to provide complex analysis of small DNA samples by means of amplification using the so called Polymerase Chain Reaction (PCR). However, already known technologies all have

limitations and are realized by different devices in different phases, meaning that large amounts of time and resources are needed for a complete analysis, which actually forces a delayed analysis of the samples. This separated sequence of operations also requires an operator physically taking the sample from the first segment to the second for the completion of the procedure. Moreover, the sample often needs to be treated before analysis, to isolate either the RNA or the DNA of interest. Safeair aims at solving all those issues. The instrument is conceived as a simple instrument made of different stages, so that the analysis can be automated, on-site and in real time. The instrument is also conceived to be portable, compact and small. This reduces times, costs, and allows the usage without the need for a specialized operator. Safeair is made of three main modules, the first one able to sample fluid with embedded aerosol and particulate, the second one able to isolate biological matter from sampled air and a third module which analyzes the obtained biological sample. The development of this first module has been the part of the work that I have been involved into. A CFD analysis was performed in order to design a tentative geometry starting from the known MicroMED BB's, then a Safeair BB has been realized and tested, verifying the ability to sample good amounts of aerosols. The module, after development, is expected to be able to sample aerosol droplets in a range that goes from 100 nm and 40 μm. This interval includes PM2.5 and PM10 particulate as well as aerosol coming from breath, sneezes and cough. The fluid dynamic sampling system has been developed starting from MicroMED's BB geometry, and it is made of an inlet duct able to sample fluid, no sampling head and a collector inside the instrument, whose shape has been developed as a trade-off between an efficient sampling of aerosol and particulate from the sampled air and geometric and mechanical constraints. The geometric details of these ducts and of the collector are here omitted for copyright reasons. Safeair is currently able to have a volume flow rate of about 3 l/min. A second part of the analysis has been focused on increasing this flow rate to values closer to the average flow rate of the human lungs (a person breaths on average 60 l/min). The analysis showed that the flow rate can be increased to values up to 100-120 l/min but a re-design of the collector is needed in such case. This second part of the analysis is currently only a theoretical study and it will be described in the later sections of this work, that describe my contribution to this project.

Figure 5.134 Safeair inside its protective metal box. Here Safeair is connected to a tube producing aerosol containing pathogens in order to perform a test.

5.1.1 CFD Model and input data for runs

The CFD Analysis has started from MicroMED's BB geometry (See Section 2.1). The model is similar to what has been used for MicroMED's terrestrial version (Section 4.1). Simulations have been performed by means of the SST Transition model like for the terrestrial model, however runs with the k-ε realizable model with enhanced wall treatment have also been performed to complete the analysis. Most runs have been performed at ambient conditions, simulating the environment of closed venues like a hospital room, for example. This means pressure has been kept constant at 1 atm, while temperature has been set to 20°C (293 K). Small variations of these values have been considered, but the bulk of the work has been performed at such ambient conditions. Since the actual goal of the instrument is to sample droplets, no matter the flow condition, little attention has been given to keeping the flow laminar, differently to what happens for MicroMED in both its terrestrial and Martian versions, where laminarity of the flow is a design requirement. Values of Δp generated by the pump has been varied from 10 to 30 mbar, as such values have been considered realistic as already described in Section 4.1. Aerosol has been simulated similarly to what has been made for dust grains. Characteristics like density and specific heat have

been set to values of water droplets, however the flow has been simulated as fluid inseminated with droplets using the injection tool by Fluent. This approach has already been used in literature (Vuorinen, V. et al., 2020; Worth Longest, P. et al., 2007 among others) for the simulation of aerosol droplets. Such droplets have been simulated at a vast variety of sizes, going from 0.1 to 200 μm in diameter. In order to evaluate the efficiency, a parameter similar to the sampling efficiency has been defined similarly to the one used for MicroMED. However, the definition here is different. The boundary conditions have been set to *reflect* everywhere except for the bottom of the collector, where the boundary condition is *trap*. This means that if a droplet touches the collector surface, it is considered captured by it and the calculation of its trajectory stops there. If it hits any other surface, the droplet bounces and then keeps flowing along Safeair toward its outlet. The model is thus able to predict eventual rebounding of droplets but not the splashing of them, with the creation of smaller ones. Further investigation on the matter is currently ongoing, aimed at a possible introduction of this aspect in the model. Given these assumptions, the sampling efficiency is then defined as the ratio of the number of droplets that get captured by the collector to the total number of droplets that flow through Safeair.

As for the geometry, various different designs have been tested with a number of purposes:

- Optimize the geometry of the collector so that Safeair is able to efficiently sample pathogens with the current duct geometry, which is mostly taken from MicroMED's BB;
- Evaluate the possibility to increase the instrument's volume flow rate (making it closer to the flow rate of an average human respiratory system, which is 60 l/min) without losing sampling efficiency;
- Evaluate the correct position of the subsystems inside the instrument's main box so that they have minimum impact on Safeair's fluid dynamics.

The following sections will show an overview of the obtained results.

5.1.2 Results of the analysis on the original geometry

The first phase of the analysis has been performed on MicroMED's BB. A study of the effect of environmental parameters on performances has not been performed in detail as only small temperature and pressure variations have been considered (Safeair is conceived to work in controlled environments) which led to limited variations, never more than a few percentage points of results.

The bulk of the work has been to evaluate the dynamics of the aerosol inside Safeair and the efficiency of the collector that has been designed to collect droplets and allow for the extraction of pathogens. A couple of possibilities have been explored in terms of the sampling system, namely MicroMED's BB has been simulated both with and without the sampling

head with 4 holes. In the end, the solution without sampling head has been chosen, with a simple circular hole at the top of the inlet duct. Figure 5.135 shows an example of trajectory tracks for aerosol inside Safeair for such configuration. Droplets dynamics is such that they finish inside the collector in very high percentages for all tested conditions. Figure 5.136 shows indeed the collector sampling efficiency (as just defined) for a 10 mm diameter collector and three different values of the pump generated Δp. It can be noted that droplets over 1 μm are detected with excellent accuracy, and even under such diameter droplets are collected with an efficiency ~ 90%.

A potential issue is the droplet velocity, since droplets could splash while hitting the collector or other surfaces of the instrument. This aspect leads to a trade-off analysis: higher sampling capability of the instrument requires stronger suction by the pump, but stronger pressure forces generated inside the instrument imply the risk of splashes and of losing efficiency. Moreover, high pressure forces increase the volume flow rate, which is positive because it allows to retrieve a larger sample of pathogens as well as have a more reliable comparison with the human breath in terms of volume flow rate. The possibility of increasing the volume flow rate has also been explored by means of a re-design of the ducts, as we will see in the upcoming sections.

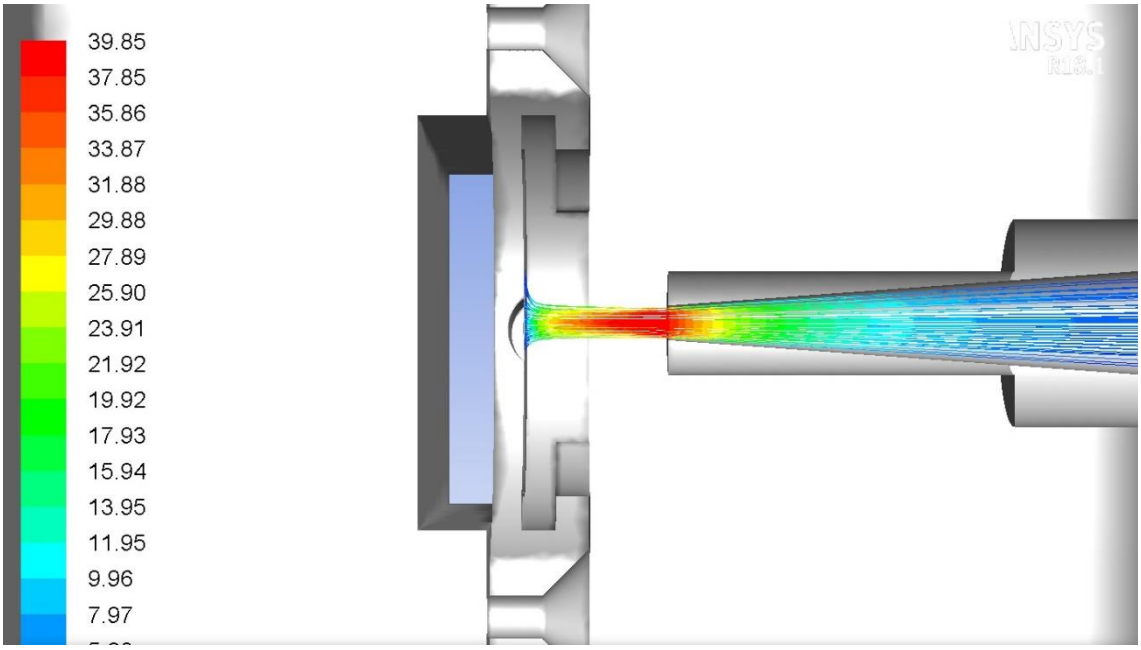

Figure 5.135 Example of aerosol trajectories inside Safeair. The example corresponds to 1.2 μm droplets and a pump generated Δp of 10 mbar. It can be noted that droplets speed (droplets are colored based on their speed [m/s]) may be an issue as values are quite high and may cause splashes of liquid around the instrument's main box.

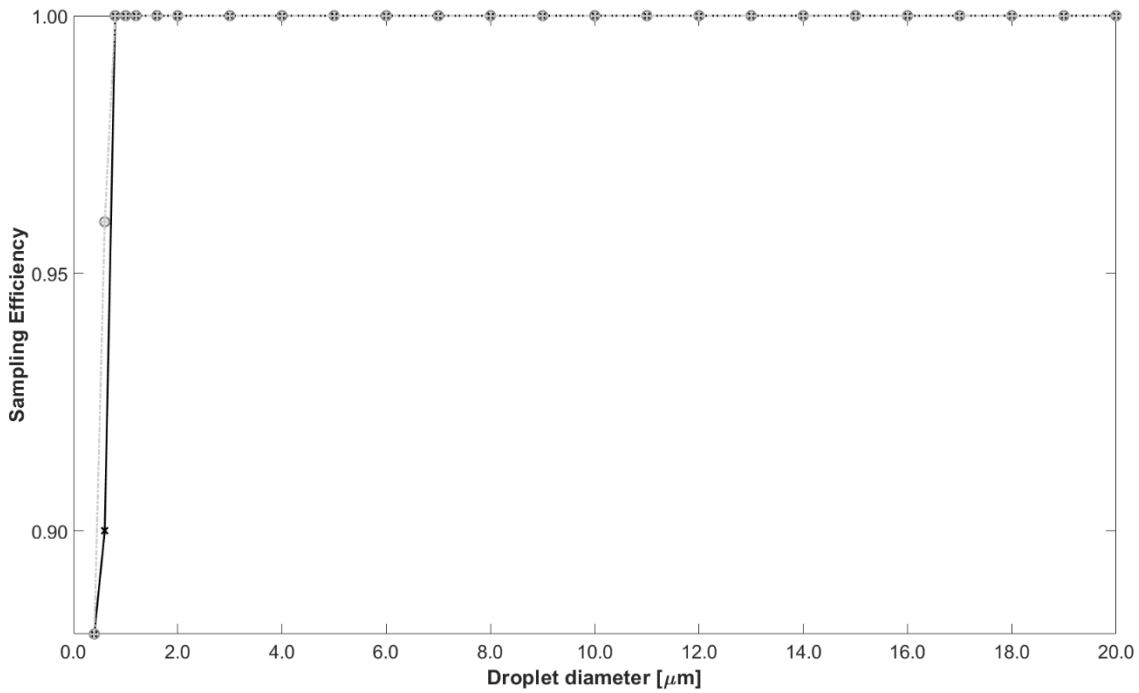

Figure 5.136 Sampling efficiency for a 10 mm diameter collector and a sampling head with no holes. Efficiency over 0.88 is guaranteed for a large range of droplet sizes.

Overall, the analysis on Safeair's BB version (which is inspired by MicroMED's BB as already underlined) has shown that it is able to collect droplets up to 100 μm in diameter. These characteristics have been verified by tests performed at our premises in Capodimonte. Such tests have verified the instrument's ability to collect large amounts of droplets.

The design of Safeair is currently ongoing an engineering process led by TransTech ®, which is aimed at tuning all the geometric elements. Details are omitted for copyright purposes; however, the fluid dynamic sampling system has been mostly maintained equal to MicroMED's BB inlet duct. In order to optimize the volume distribution inside the instrument, the systems extracting the liquid from the collector has been positioned underneath the collector itself, avoiding interference with the main flow of Safeair. This modification required CFD investigation since it meant that the outlet duct had to be positioned asymmetrically, causing misalignment with the inlet duct. Such aspect would have been an issue for MicroMED; however, for the operational needs of Safeair, this variation can be accepted as Figure 5.137 shows. The figure shows indeed a sampling efficiency plot which compares results for symmetric and asymmetric positioning of the outlet duct, and it can be noted that there is little impact on the collecting ability. Figure 5.138 shows that droplets trajectories are not influenced by the repositioning of the outlet. which is probably due to the high Stokes (Stk) number of the droplets. Droplets in this range are however collected with good efficiency as Figure 5.136 already showed.

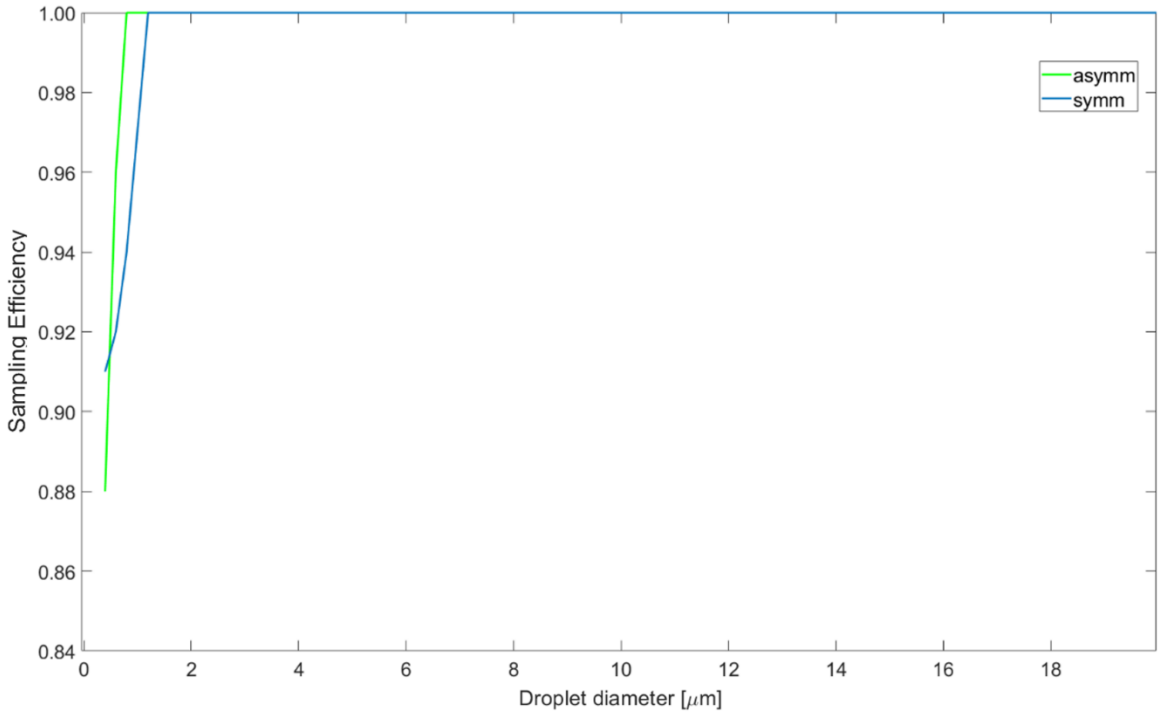

Figure 5.137 Comparison between the sampling efficiency of Safeair in symmetric and asymmetric configuration. This example plot is relative to ambient conditions and pump generated Δp of 20 mbar, but comparable results have been obtained for all other cases.

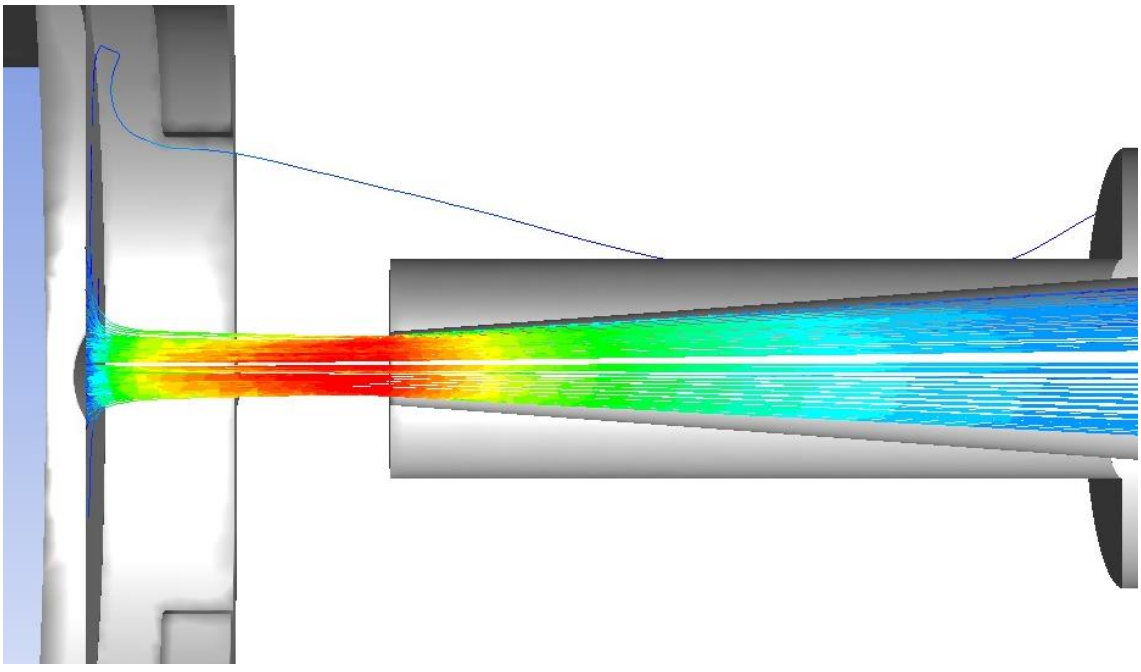

Figure 5.138 Droplet trajectories for the case of misalignment between the inlet and outlet duct. It can be noted that little interference is evidenced.

5.1.3 Possible flow rate increase

Safeair currently has a volume flow rate ~ 2-3 l/min. There is strong interest in the ability to increase its flow rate to make it at least comparable to the volume flow rate of human breath (~ 60 l/min). To perform such increase without losing sampling efficiency, a deep CFD analysis has been performed. The idea has been to develop a feasibility analysis and a first optimization phase aiming at a future realization of a high flow rate version of the instrument. The analysis has been carried out considering a number of possible different geometries, operating mostly on:

- Inlet duct length;
- Inlet duct diameter and structure;
- Collector diameter;
- Outlet diameter.

Varying all of this parameters among values that have been considered reasonable, a total of 45 different geometry designs have been proposed and tested, with progressive corrections to fluid dynamic issues. A synthesis of the results obtained is presented here.

First of all, it has to be underlined that it has appeared clear that, in order to increase the instrument volume flow rate while also trying to reduce the droplet velocity, the diameter of both the inlet and the outlet duct had to be significantly increased. Table 5.24 reports some of the simulated geometries with the related values of obtained volume flow rate, as well as average velocity by droplets when approaching the collector. It has to be underlined that the inlet ducts has been developed with at least one conical section, meaning that the table had to indicate two values of inlet diameter (initial and final). The table shows some cases with a 15 mm initial internal diameter for the inlet duct, which has been chosen as a possibility for the future, high flow rate version of Safeair. The pump generated Δp has been limited to a maximum of 20 mbar in an effort to limit the speed of incoming droplets. In such cases, the volume flow rate can be increased up to ~ 100 l/min. Options that guaranteed about ~ 120 l/min have also been developed, but they have been excluded because of the third pivotal parameter of the trade-off analysis, that is the collector efficiency.

The analysis shows indeed that such an increase of the diameters causes a dramatic reduction of the sampling efficiency for the current geometry of the collector. Figure 5.139 shows an example of droplet trajectories for such geometries. It can be noted that there is plenty of splashes and overall only a small percentage of the droplets are collected (~ 30-40% of droplets are collected especially for small diameter droplets).

Φ Inlet [mm]	**Φ Outlet [mm]**	**Δp [Pa]**	**Q [l/min]**	**Velocity [m/s]**
15+6	10	10	40	25
15+6	10	20	58	34

15+10	10	10	70	22
15+10	10	20	103	33

Table 5.24 Volume flow rate values obtained for some of the simulated geometry configurations. Cases with inlet dimensions indicated as "a + b" are relative to a conic duct in which a is the initial internal diameter, b is the final internal diameter.

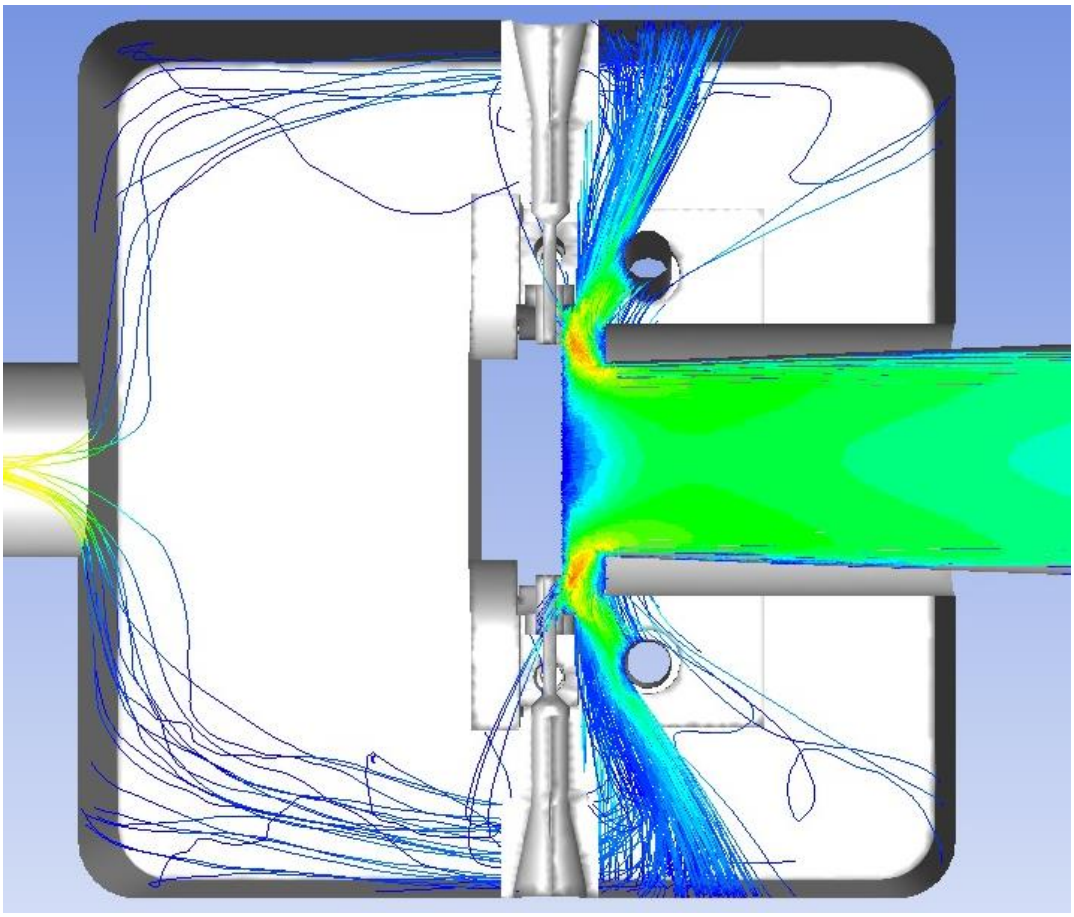

Figure 5.139 Droplet trajectories for the high flow rate version of Safeair. Droplets tend to splash and move chaotically after rebounding on the collector. This has highlighted the need to either reduce droplet speed or change the geometry of the collector.

In the framework of this study, the possibility of developing an updated design of the collector has been investigated. This part of the study is still ongoing, however preliminary results can be shown for a couple of proposed collector designs. Figure 5.140 and Figure 5.141 show droplet trajectories for such designs. The first proposed design is basically a bowl shaped collector with an inclined cover, which is thought to redirect rebounding droplets toward the inside of the collector. Such design gives improved results for droplets over 1 μm in diameter, however its particular shape causes increased turbulence, which overall is not a critical issue but adds to the chaotic nature of the flow inside this high flow rate version of Safeair. The second design is similar to the first but with a conical nose inspired to the nose intakes of military planes. The idea is to avoid a direct return of the flow toward the inlet duct, which has caused chaotic flow in the previous version of the collector. The inclined walls of the conical nose guide the flow toward the bottom of the collector, a dull corner is

present between the bottom and the nose of the collector. This leads the flow smoothly toward the walls of the collector. This solution has proved to guarantee a solid value of sampling efficiency (Figure 5.142), however this solution is just preliminary and it is still under study.

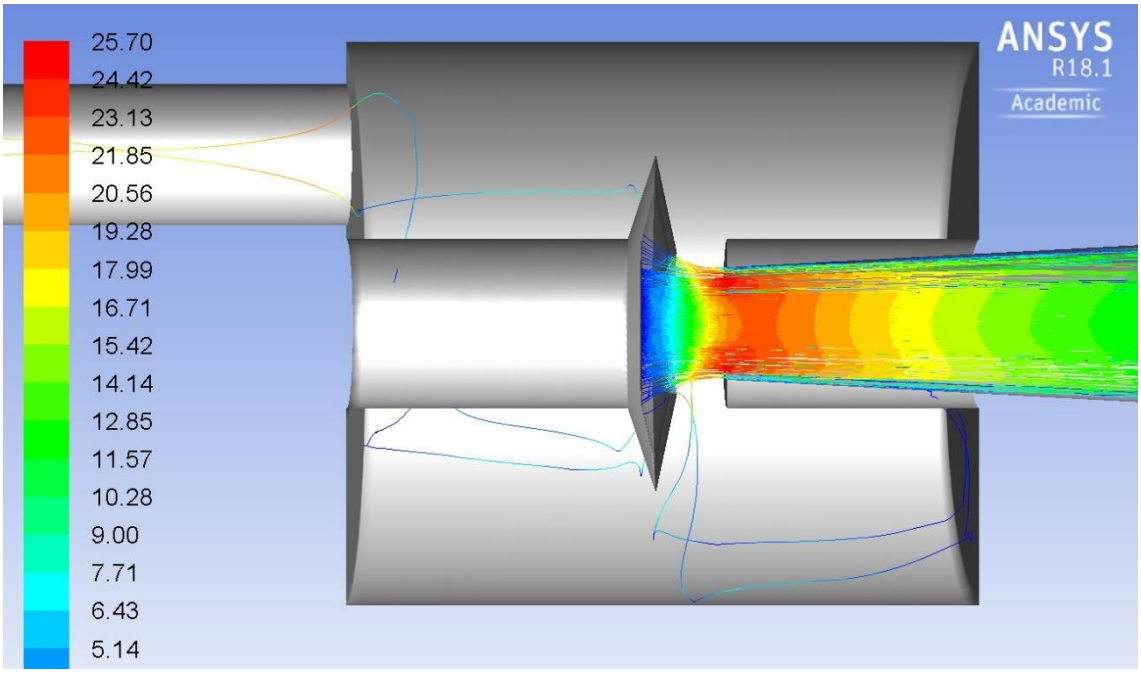

Figure 5.140 Droplet trajectories for the high flow rate version of Safeair with the first proposed geometry for the collector. Droplets over 1 μm are collected with good efficiency. Smaller ones tend to splash or rebound elsewhere, and overall the flow streamlines can become jagged.

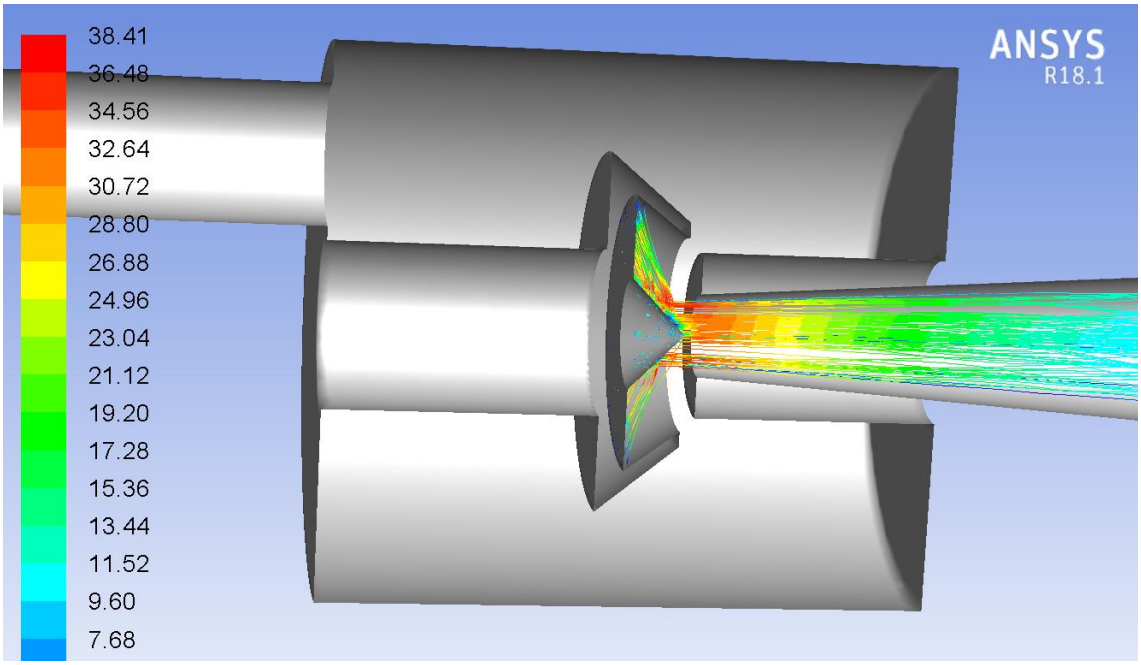

Figure 5.141 Droplet trajectories for the high flow rate version of Safeair with the second proposed geometry for the collector. Droplets in the range of our interest are collected with good efficiency, even smaller ones.

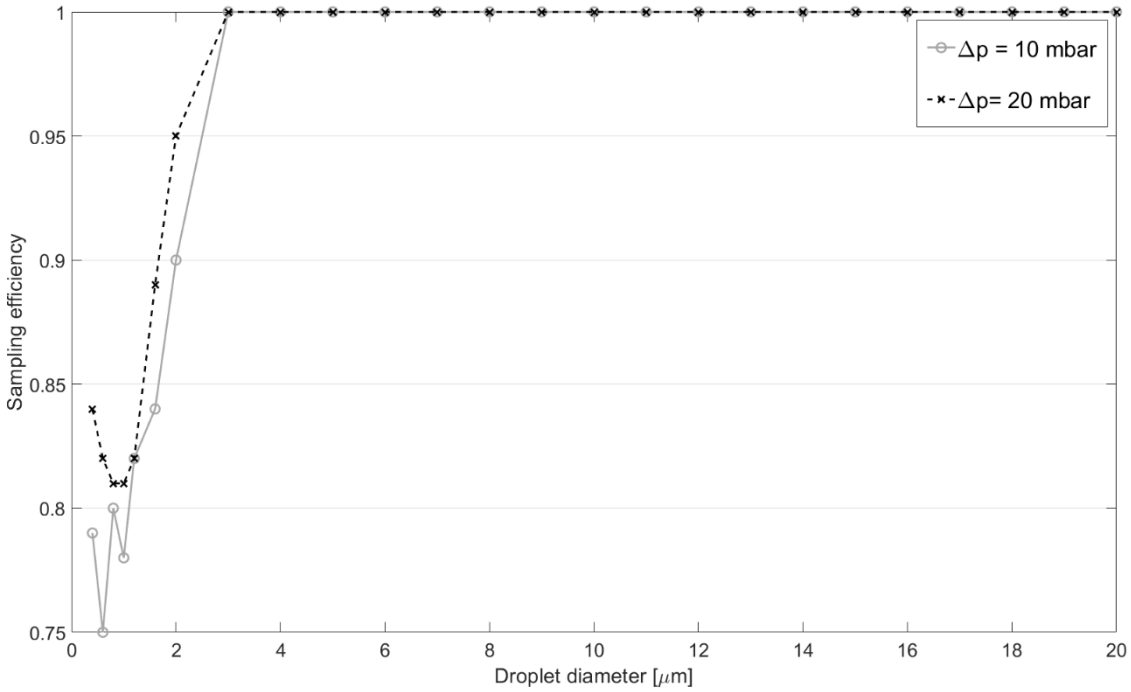

Figure 5.142 Sampling efficiency for the high flow rate version of Safeair with the second proposed geometry for the collector. Sampling efficiency is good in the entire measurement range of the instrument. The two cases in the figure are relative to pump generated Δp of 10 and 20 mbar, which correspond to 40 and 58 l/min flow rates, respectively (with the 15 + 6 mm conical inlet).

5.1.4 Solution with a metal grid as the droplet collector

In the current version of Safeair, the possibility of using a metal grid in place of the current collector has been investigated. Results for this configuration are currently under analysis, however preliminary information obtained are extremely positive and hint at the possibility to vastly improve the collecting ability of Safeair, which could also lead to the possibility to increase the instrument's flow rate with a smaller impact on the sampling efficiency.

The grid could be chosen as a substitute to the collector considered in the initial analysis; in such case results should be updated to the actual design.

5.1.5 Proposed inlet adaptment to test constraints

Safeair has to be tested by means of a direct comparison with an aerosol sampler in order to verify its efficiency. However, it has been difficult to directly compare results with instruments that have significantly different flow rates. The reference aerosol sampler is indeed able to sample 9 l/min of air, versus 3 l/min of Safeair. In section 5.1.3 it has already been underlined that a volume flow rate increase would be desirable, but an increase up to ~ 60 l/min would require extensive modifications to the design of Safeair, which cannot be afforded because of time constraints. However, an increase to 9 l/min could be obtained

without significant variations to the geometry and would allow direct comparison with the reference aerosol sampler. To this purpose, a CFD simulation campaign has been performed, obtaining that, with a small variation of the inlet duct (the final diameter of the inlet should be increased), such flow rates can be obtained. Table 5.25 shows that, even for low Δp induced by the pump, it is possible to obtain huge increases of volume flow rate by increasing the inlet final diameter. At the same time, such increase in diameter reduces the inlet outflow fluid speed, which is positive because it reduces the risk of splashes. Conversely, it obviously causes a larger spread of the droplets in the collector plane, meaning that it could be necessary to also increase the dimensions of the collector. Figure 5.143 shows indeed that for small droplets (d < 1 μm) the distance from center increases with the increase of the inlet final diameter. This aspect is currently under development; however, it is expected that such variations will be introduced into the design of Safeair.

	Φ4 in, Φ1 fin		**Φ4 in, Φ3 fin**		**Φ4 in, Φ4 fin**	
Δp [mbar]	**Q [l/min]**	**Max Velocity [m/s]**	**Q [l/min]**	**Max Velocity [m/s]**	**Q [l/min]**	**Max Velocity [m/s]**
5	**1.4**	24	**10**	27	**12**	25

Table 5.25 Influence of the increase of the final diameter of the inlet duct on Safeair's volume flow rate and maximum fluid speed. The configuration with a 4 mm initial diameter and 1 mm final diameter is the current configuration.

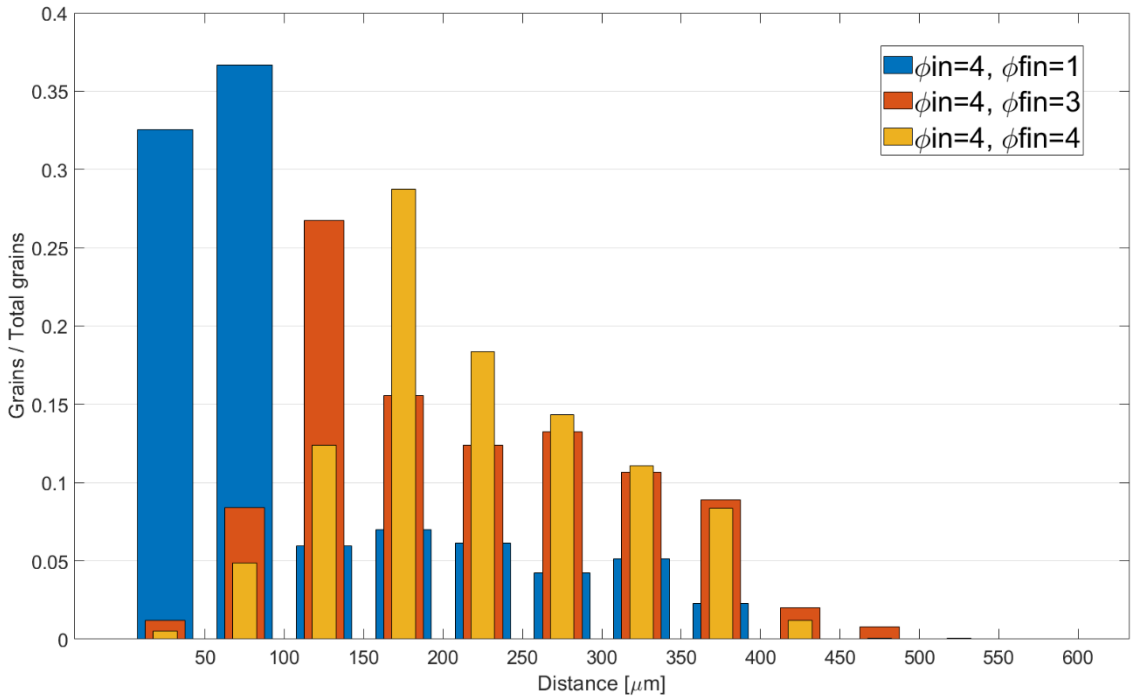

Figure 5.143 Influence of the increase of the final diameter of the inlet duct on the distance of small grains (d < 1 μm) from the axis of the ducts. An increase of the final diameter predictably induces an enlargement of the flow; however, given that the distance stays smaller than the internal diameter of the collector, it should not reduce the instrument's efficiency. However, following a conservative approach, it has been decided to increase the dimension of the collector anyway.

6. Conclusions

This work provides a detailed overview of my Ph.D. work, that has been carried out at the INAF – Astronomical Observatory of Capodimonte in Naples, Italy, in co-operation with the Department of Industrial Engineering at the University of Naples "Federico II". Most of the work has been focused on the development of a completely novel space instrument: A Martian OPC, aimed at the characterization of airborne Martian dust. Such OPC, named "MicroMED", is part of the ESA/Roscosmos ExoMars 2022 mission and will perform the first ever direct measurement of airborne Martian dust close to its source, which is the Martian soil. MicroMED has been accommodated on the ExoMars lander. Its scientific retrieval will provide a significant contribution to the characterization of airborne dust and its related phenomena in the atmosphere, and consequently to the overall understanding of Martian climate.

MicroMED is a complex instrument, made of a number of subsystems which are all described in detail in this work. Its functionality is based on optical methods and it is vastly described. In the framework of the instrument's design and development phases, a CFD analysis of MicroMED's BB has been performed. Such version of the instrument had already been realized by my arrival in Capodimonte; however, the instrument's fluid dynamic design had to be improved for optimal performance in the range of interest of the instrument, which is related to the dust grain size and corresponds to 0.4-20 μm in dust grain diameter. The analysis involved hundreds of CFD simulations, providing a complete sensitivity analysis with respect to each environmental parameter, as well as an evaluation of the instrument's sampling efficiency in each different environmental condition that the instrument could face. This parameter, the "sampling efficiency", has been defined in the work and has been extensively used in order to quantify the design quality from a fluid dynamic standpoint. The CFD model used for the simulations strongly differs from the "classical" methods used in Earth atmosphere, since the peculiar conditions that will be faced by MicroMED in Martian atmosphere require some adjustments to the model, especially when it comes to a prediction of the dust grain trajectories inside the instrument. On Mars surface, the flow is laminar for MicroMED, and the atmosphere has extremely low density, pressure and temperature. The analysis in question indicated that ambient pressure and temperature don't have a significant impact on MicroMED's behavior, which is probably due to the fact MicroMED will be positioned under a thermal cover which limits the range of temperature (to the range -20°C, +40°C). On the other hand, instrument temperature proved to be the most influential parameter. Instrument temperature, which influences MicroMED's sampling efficiency in the entire range of the instrument (up to 8% variations in the 0.4-15 μm range) is actually enormously significant for large grains ($d > 15$ μm). It has been indeed noted that the BB design has issues in detecting large grains when instrument temperature is close to the lower end of the instrument temperature range. MicroMED is able to detect almost 100% of large grains when the instrument is "hot" ($T_i \sim +40$°C) while it could have an

efficiency as low as ~ 30% when the instrument is "cold" (T_i ~ -20°C). This huge variation (also the effect on smaller grains is not positive) is related to a couple of undesired phenomena that have been individuated thanks to the CFD analysis. The first phenomenon is an expansion of the flow in the 4 mm gap between the inlet and outlet sections of MicroMED, which drags small grains outside of the laser illuminated spot, preventing their detection. This expansion cannot be avoided, since it is simply due to the exit of the flow from the inlet duct, but it can be made unharmful by means of a proper duct design, able to concentrate grains inside the laser spot front area even for such an expanding flow. The second phenomenon is instead related to the dynamics of the dust sampling: large grains, which have high inertia, are deflected less sharply toward the inside of the instrument (a deflection of ~ 90° is indeed imposed to grains for a correct sampling with the BB geometry) which means that they hit the inlet duct walls, which is detrimental to the efficiency both in case of grains getting stuck on the walls (which has been the assumption in the analysis) and in case of grains rebounding on them.

As a result of such analysis, a complete re-design of the MicroMED ducts has been performed with the aim of eliminating or at least reducing the effect of the aforementioned phenomena on performances. By means of CFD, the re-design has been completed. The inlet duct has been changed in shape, helping the deflection of sampled grains toward the inside of the instrument, and the outlet duct has been reshaped. Such variations had obviously to be in accordance with the geometrical constraints due to the position of MicroMED on the ExoMars lander. After re-design, a CFD analysis has been performed to verify the improvements due to the re-design. The new design, which has then been chosen as the PFM design of MicroMED, has provided an extremely high efficiency (> 90% in all cases, with many cases providing an efficiency over 95% for the entire measurement range) in all simulated environmental conditions.

Once the design phase was concluded, MicroMED's PFM was integrated and tested. The integration was performed at OAC premises in Capodimonte in 2019. As a result, MicroMED's PFM and its FS counterpart were realized. The integration phase has been successful and has been described in this work. Both instruments have been tested to verify their functionality. Tests in all their different forms have been described both in terms of their execution and of their aims. First of all, functional tests have been performed, verifying that all subsystems of the instruments worked nominally. After that, performance tests have been made, verifying that MicroMED is actually able to detect grain size with good accuracy and in accordance with the Mie model (grains used for such tests were spherical, and the scattering law of spherical grains is ruled by the Mie theory). Both functional and performance tests have been quite successful. The performance tests have then been completed at the AWTS II facility at the University of Aarhus, Denmark, where tests also in presence of winds up to 15 m/s were performed. Such tests verified that MicroMED is able to sample grains also in presence of wind, even for the maximum wind speed tested during the test campaign (15 m/s) and for the largest grains used (d = 20 μm). The test campaign, which was the first part of a 2 campaigns test session at the AWTS II facility, was financed by the Europlanet project and I own the PI-ship for both campaigns. During performance tests, an issue related to the presence of some bimodal histograms has been individuated,

and has been studied in detail in order to understand its origin. A number of hypothesis have been proposed, and the cause for such phenomenon has possibly been individuated in the deposition of grains inside the instrument's ducts. Such deposition is unharmful for the actual Martian campaign as it only happens for strong concentrations of large grains, which is something that never happens on Mars but that happened during some tests at our premises at INAF – OAC.

A section about dust concentration in the chamber and inside MicroMED is present. The determination of dust concentration inside the Martian chamber is pivotal to our purposes, and there are currently no methods nor instruments available able to determine dust concentration in an environment with such a low pressure such as the Martian one. This means that custom methods had to be developed. The methods used for such determination are provided in the section. Such methods are based on measurements in the chamber, by means of custom systems like the CMS (which I designed) for the evaluation of dust concentration in the chamber, and by post processing analysis, by means of a Matlab code for the evaluation of the flow rate of MicroMED. This code has been derived starting from a hybrid database coming both from indirect measurements during tests and by CFD simulations. All methods in this section are original and I have been responsible for the determination of such measurement.

Tests in terrestrial deserts have also been performed, aimed at advancing in the study of the dust lifting mechanisms and the structure, rise and evolution of dusty phenomena on Earth. The logics of such campaigns are described in the corresponding section of this work.

Various field campaigns have been performed by our team at INAF – OAC in the Tafilalt region in the Moroccan Sahara Desert. As part of my Ph.D. work, I have personally been a part of one of those campaigns, in July 2019.

Tests on MicroMED have not only been focused on performances. Space qualification tests were also needed, and MicroMED has been subject to Vibrational and Thermal Vacuum qualification campaigns. My role in this part of the work was to contribute to the design of tests and to the redaction of the official documentation. Tests were successful and MicroMED was space qualified, as it proved to keep its nominal behavior in harsh conditions.

Before being delivered to TAS-I for the integration on the Surface Platform, MicroMED was calibrated by means of tests with both polydisperse and monodisperse samples, as well as a combination of spherical and aspherical grains, so that its response to dust grains is correctly characterized. A long and detailed procedure of calibration has been performed and described in the work, and the calibration curve is provided.

In order to verify the performances of the instrument in a natural dusty environment, we have also developed a terrestrial version of MicroMED. Such adaptation has been designed by means of a CFD analysis, determining MicroMED's PFM behavior in Earth conditions. For grains under 7 μm in diameter, the sampling efficiency drops if the Martian design is used on Earth. The CFD analysis has individuated some phenomena that cause the worsening of performances, and with a similar approach to what was utilized for the PFM design (albeit with a different CFD model, given the completely different conditions), slight modifications of MicroMED's design have been proposed and tested. In the end, a design featuring a fifth hole on the top of MicroMED's sampling head has been adopted for the

terrestrial design. Such geometry provides good performances also on Earth with minimal modifications needed, hence reduced impact of the intervention (and reduced cost). MicroMED's terrestrial version is currently in realization and could be tested in terrestrial deserts as soon as 2022.

In the framework of the battle against the Sars-CoV-2 pandemic, INAF has launched an initiative that aimed at adapting already existing technologies to battle the Coronavirus outbreak. In this contest, MicroMED has been adapted as an aerosol sampler. The Safeair instrument has been invented, and it provides a single instrument able to sample, analyze and detect the presence of pathogens in the atmosphere (the instrument can also be adapted to other viruses/pathogens). A CFD design phase of the instrument has been faced, resulting in an original instrument able to sample aerosol in a vast range of droplet sizes. A study of the shape of the collector inside the instrument has also been performed. Safeair is currently ongoing an international patent procedure, and I am personally owner of 2% of the intellectual property of the invention (Patent n° 102020000018409 filed on 29th July 2020). Because of the patent procedure, some details have been omitted for copyright reasons.

References

Alvarez, M., et al. (2015) "Low Dose Rate testing of ADXL327 Accelerometer for a Mars Mission." 2015 IEEE Radiation Effects Data Workshop (REDW), IEEE.

Aguirre, C. et al. “Signal-adapted tomography as a tool for dust devil detection”. Aeolian Research, 29, 12-22 (2017).

Anderson, E., and Leovy, C. “Mariner 9 Television Limb Observations of Dust and Ice Hazes on Mars”, Journal of Atmospheric Sciences, 35(4), 723-734. Retrieved Oct 20, 2021, from https://journals.ametsoc.org/view/journals/atsc/35/4/1520-0469_1978_035_0723_mtlood_2_0_co_2.xml (1978).

Arruego, I. et al. (2015a) "Practical application of the Optical Wireless communication technology (OWLS) in extreme environments." 2015 IEEE International Conference on Wireless for Space and Extreme Environments (WiSEE), IEEE.

Arruego, I. et al. (2015b) "A roadmap for the development of miniature scientific instruments for planetary landers." European Planetary Science Congress. Vol. 10.

Arruego, I. et al. (2018) “InMARS: a comprehensive program for the development of keytechnologies for miniature Martian probes.” International Planetary Probe Workshop (IPPW), Colorado.

Baddeley, M. D. “Whirlwinds and Dust-storms of India: An Investigation into the Law of Wind”. (1860)

Bagnold, R. A., “The Physics of Blown Sand and Desert Dunes”. London: Methuen & Co. (1941).

Balme, M. R., et al. "Field measurements of horizontal forward motion velocities of terrestrial dust devils: towards a proxy for ambient winds on Mars and Earth." Icarus 221.2 (2012): 632-645.

Balme, M. and Hagermann, A. “Particle Lifting at the Soil–Air Interface by Atmospheric Pressure Excursions in Dust Devils” - Geophysical Research Letters, Vol. 33 (2006).

Banfield et al. “The atmosphere of Mars as observed by InSight." *Nature Geoscience* 13.3 (2020): 190-198.

Bell III, J. F. et al. "Chromaticity of the Martian Sky as Observed by the Mars Exploration Rover Pancam Instruments" - Journal of Geophysical Research, Vol. 111, N. E12S05. (2006).

Bettanini, C., et al. "The DREAMS experiment on the ExoMars 2016 mission for the study of Martian environment during the dust storm season", IEEE Metrology for Aerospace (MetroAeroSpace), 167-173. (2014).

Bettanini, C., et al. "The DREAMS experiment flown on the ExoMars 2016 mission for the study of Martian environment during the dust storm season", Measurement, Volume 122, 484-493. (2018).

Biener, K. K. et al "Observations of Dust Devils in MOC Wide Angle Camera Images" - Lunar Planetary Science XXXIII, Abstract N. 2004. 2002.

Bila, Tetyana, et al. "Lifting grains by the transient low pressure in a martian dust devil." Icarus 339 (2020): 113569.

Bohren, C. F. and Huffman D. R. (1983) "Absorption and Scattering of Light by Small Particles". "John Wiley and Sons, Inc. Press".

Bourouiba, L. "Turbulent Gas Clouds and Respiratory Pathogen Emissions", JAMA Insight. (2020).

Bridges, N. T. et al. "Planet-Wide Sand Motion on Mars. Geology", 40(1), 31–34. (2012).

Cantor, Bruce A., Katharine M. Kanak, and Kenneth S. Edgett. "Mars Orbiter Camera observations of Martian dust devils and their tracks (September 1997 to January 2006) and evaluation of theoretical vortex models." Journal of Geophysical Research: Planets 111.E12 (2006).

Chojnacki, Matthew, et al. "Ancient Martian aeolian sand dune deposits recorded in the stratigraphy of Valles Marineris and implications for past climates." Journal of Geophysical Research: Planets 125.9 (2020): e2020JE006510.

Colangeli, L. et al. "GIADA: The Grain Impact Analyser and Dust Accumulator for the Rosetta space mission", Advances in Space Research, Volume 39, Issue 3, p. 446-450. (2007).

Colangeli, L. et al. "MEDUSA: The ExoMars experiment for in-situ monitoring of dust and water vapour", Planetary and Space Science, Volume 57, Issue 8, p. 1043-1049. (2009).

Colburn, D. S., J. B. Pollack, and R. M. Haberle. "Diurnal variations in optical depth at Mars." Icarus 79.1 (1989): 159-189.

Conrath, Barney J. "Thermal structure of the Martian atmosphere during the dissipation of the dust storm of 1971." Icarus 24.1 (1975): 36-46.

Cozzolino, F. "Progettazione e Sviluppo di un sistema di GSE per il controllo di sensori per applicazioni spaziali. Test e analisi di un rivelatore compatto di polveri per l'ambiente Marziano", Ph.D. thesis. (2015).

Cozzolino, F. "Martian environment chamber: Dust systems injections", Planetary Space Science 104971. DOI: 10.1016/j.pss.2020.104971. (2020).

Cunningham, Emma. "On the velocity of steady fall of spherical particles through fluid medium." Proceedings of the Royal Society of London. Series A, Containing Papers of a Mathematical and Physical Character 83.563 (1910): 357-365.

Della Corte, V. et al. "67P/C-G inner coma dust properties from 2.2 au inbound to 2.0 auoutbound to the Sun", Monthly Notices of the Royal Astronomical Society, Volume 462, Issue Suppl_1. (2016). Pages S210–S219, DOI:https://doi.org/10.1093/mnras/stw2529

Dickinson, C. et al. "Lidar atmospheric measurements on Mars and Earth", Planetary and Space Science, 59, pp. 942-951. DOI: 10.1016/j.pss.2010.03.004 (2011).

Drossart, P., et al., Martian Aerosol Properties from the Phobos/ISM Experiment - Annales Geophysicae, Vol. 9, pp. 754-760, 1991.

Eden, H. Frank, and Bernard Vonnegut. "Electrical breakdown caused by dust motion in low-pressure atmospheres: Considerations for Mars." Science 180.4089 (1973): 962-963.

Edgett, Kenneth S., and Michael C. Malin. "New views of Mars eolian activity, materials, and surface properties: Three vignettes from the Mars Global Surveyor Mars Orbiter Camera." Journal of Geophysical Research: Planets 105.E1 (2000): 1623-1650.

Esposito, F. et al. "Physical aspect of an "impact sensor" for the detection of cometary dust momentum onboard the "Rosetta" space mission." Advances in Space Research 29.8 (2002): 1159-1163.

Esposito, F. et al. "MEDUSA: Observation of atmospheric dust and water vapor close to the surface of Mars", International Journal of Mars Science and Exploration, Vol. 6, p. 1-12. (2011).

Esposito, F. et al. "The role of the atmospheric electric field in the dust-lifting process". Geophysical Research Letters, 43(10), 5501-5508. (2016).

Esposito, F. et al. "The DREAMS experiment onboard the Schiaparelli module of the ExoMars 2016 mission: design, performances and expected results". Space Science Reviews, 214(6), 103. (2018).

Farrell, W. M., et al. "Electric and magnetic signatures of dust devils from the 2000–2001 MATADOR desert tests." Journal of Geophysical Research: Planets 109.E3 (2004).

Fedorova, A.A., et al., Solar Infrared Occultation Observations by SPICAM Experiment on Mars-Express: Simultaneous Measurements of the Vertical Distributions of H2O, CO2 and Aerosol - Icarus, Vol. 200, pp. 96–117, 2009.

Ferri, F., Smith, P. H., Lemmon, M., & Renno, N. O. (2003). Dust devils as observed by Mars Pathfinder. Journal of Geophysical Research: Planets, 108(E12).

Fisher, J. A., Richardson, M. I., Newman, C. E., Szwast, M. A., Graf, C., Basu, S., ... & Wilson, R. J. (2005). A survey of Martian dust devil activity using Mars Global Surveyor Mars Orbiter Camera images. Journal of Geophysical Research: Planets, 110(E3).

Forget, F., Costard, F., Lagnonné, F., Planet Mars - Story of Another World - Springer, 2006.

Forward, Keith M., Daniel J. Lacks, and R. Mohan Sankaran. "Particle-size dependent bipolar charging of Martian regolith simulant." Geophysical Research Letters 36.13 (2009).

Franzese, G. et al., "Electric properties of dust devils", Earth and Planetary Science Letters, Volume 493, 2018, Pages 71-81, ISSN 0012-821X, https://doi.org/10.1016/j.epsl.2018.04.023.

Franzese, G. "Characterisation of dust events on Earth and Mars the ExoMars/DREAMS experiment and the field campaigns in the Sahara desert", Ph.D. thesis, 2020.

Franzese, G. et al., "Dust devils: Characteristics of the forward motion from a Saharan survey", Aeolian Research, 50, 2021a, doi =10.1016/j.aeolia.2021.100678.

Franzese, G. et al., "MicroMED: study of the relation between signal durations and grain diameters," 2021 IEEE 8th International Workshop on Metrology for AeroSpace (MetroAeroSpace), pp. 247-252, doi: 10.1109/MetroAeroSpace51421.2021.9511713 (2021b).

Geissler, Paul E., et al. "Gone with the Wind: Eolian erasure of the Mars Rover tracks." *Journal of Geophysical Research: Planets* 115.E7 (2010).

Geissler, P. E. "The birth and death of transverse aeolian ridges on Mars." Journal of Geophysical Research: Planets 119.12 (2014): 2583-2599.

Gómez-Elvira, Javier, et al. "Curiosity's rover environmental monitoring station: Overview of the first 100 sols." Journal of Geophysical Research: Planets 119.7 (2014): 1680-1688.

Grant, CC, Dust devils in the subattic, Weather, 4, 402-403, 1949.

Greeley, R., Leach, R., White, B.R., Threshold Windspeeds for Sand on Mars: Wind Tunnel Simulations - Geophysical Research Letters, Vol. 7, pp. 121-124, 1980.

Greeley, R., & Iversen, J. D. (1987). Wind as a geological process: on Earth, Mars, Venus and Titan (Vol. 4). CUP Archive.

Greeley, R. "Saltation impact as a means for raising dust on Mars." Planetary and Space Science 50.2 (2002): 151-155.

Greeley, R, et al. "Martian dust devils: Laboratory simulations of particle threshold." Journal of Geophysical Research: Planets 108.E5 (2003).

Greeley, Ronald, Patrick L. Whelley, and Lynn DV Neakrase. "Martian dust devils: Directions of movement inferred from their tracks." Geophysical research letters 31.24 (2004).

Greeley, Ronald, et al. "Active dust devils in Gusev crater, Mars: observations from the Mars exploration rover spirit." Journal of Geophysical Research: Planets 111.E12 (2006).

Guzewich, Scott D., et al. "Mars Orbiter Camera climatology of textured dust storms." Icarus 258 (2015): 1-13.

Haberle, R. M., and R. Greeley. "Sand and dust on Mars." NASA Conf. Publ. Vol. 10074. 1991.

Harrison, R. Giles, et al. "Applications of electrified dust and dust devil electrodynamics to Martian atmospheric electricity." Space Science Reviews 203.1 (2016): 299-345.

Holstein-Rathlou, C. et al., An Environmental Wind Tunnel Facility for Testing Meteorological Sensor Systems, Journal of Atmospheric and Oceanic Technology 2014, Volume 31, Issue 1, p. 447-457. DOI: 10.1175/JTECH-D-13-00141.1

Iversen, James D., and Bruce R. White. "Saltation threshold on earth, mars and venus." Sedimentology 29.1 (1982): 111-119.

Ives, Ronald L. "Behavior of dust devils." Bulletin of the American Meteorological Society 28.4 (1947): 168-174.

Jakosky, B.M., Haberle, R.M., The Seasonal Behaviour of Water on Mars - The University of Arizona Press, pp. 969-1016, 1992.

Jakosky, Bruce M., and Terry Z. Martin. "Mars: North-polar atmospheric warming during dust storms." Icarus 72.3 (1987): 528-534.

James, Philip B., et al. "Monitoring mars with the hubble space telescope: 1990-1991 observations." Icarus 109.1 (1994): 79-101.

Jaquin, Fred, Peter Gierasch, and Ralph Kahn. "The vertical structure of limb hazes in the Martian atmosphere." Icarus 68.3 (1986): 442-461.

Kahn, R.A., Ice Haze, Snow, and the Mars Water Cycle - Journal of Geophysical Research, Vol. 95, pp. 14677-14693, 1990.

Kahn, R.A., et al., The Martian Dust Cycle - The University of Arizona Press, pp. 1017-1053, 1992.

Kahre, Melinda A., Murphy, James R. Haberle, Robert M., E06008, "Modeling the Martian dust cycle and surface dust reservoirs with the NASA Ames general circulation model", Journal of Geophysical Research: Planets J. Geophys. Res. 111 E6 0148-0227, https://doi.org/10.1029/2005JE002588, 2006.

Kok, J.F., Difference in the Wind Speeds Required for Initiation versus Continuation of Sand Transport on Mars: Implications for Dunes and Dust Storms - Physical Review Letters, Vol. 104, Issue 7, 2010.

Kok, Jasper F., et al. "The physics of wind-blown sand and dust." Reports on progress in Physics 75.10 (2012): 106901.

Kok, J.F. Renno, N.O., Electrification of wind-blown sand on Mars and its implications for atmospheric chemistry - Geophysical Research Letters, Vol. 36, L05202, 2009.

Korablev, O. I., et al. "Vertical structure of Martian dust measured by solar infrared occultations from the PHOBOS spacecraft." Icarus 102.1 (1993): 76-87.

Malin, Michael C., and Kenneth S. Edgett. "Mars global surveyor Mars orbiter camera: interplanetary cruise through primary mission." Journal of Geophysical Research: Planets 106.E10 (2001): 23429-23570.

Mars climate database v 5.3, developed by Forget and his team and available online at: http://www-mars.lmd.jussieu.fr/mcd_python/

Martin, Terry Z. "Mean thermal and albedo behavior of the Mars surface and atmosphere over a Martian year." Icarus 45.2 (1981): 427-446.

Martin, Terry Z., and Hugh H. Kieffer. "Thermal infrared properties of the Martian atmosphere: 2. The 15-μm band measurements." Journal of Geophysical Research: Solid Earth 84.B6 (1979): 2843-2852.

Martin-Ortega, A. et al. (2008) "Radiation hardening of FPGA-based SoCs through self-reconfiguration and XTMR techniques." 2008 4th Southern Conference on Programmable Logic, IEEE.

Martín-Ortega, A. et al. (2017) "Micro-Processor Qualification for Planetary Exploration." International Planetary Probe Workshop (IPPW). The Hague.

Martín-Ortega, A. et al. (2019) "Early SEU sensitivity assessment for collaborative hardening techniques: A case study of OPTOS processing architecture." Microelectronics Reliability 95, p. 36-47.

Merrison, J. P. "Environmental Wind Tunnels", Wind Tunnels, IntechOpen, 2011, 1, doi = 10.5772/15019

Metzger, S.M., et al., Dust Devil Vortices Seen by the Mars Pathfinder Camera - Geophysical Research Letters, Vol. 26, pp. 2781, 1999.

Metzger, S.M., Feeding the Mars Dust Cycle: Surface Dust Storage and Dust Devil Entrainment - 30th Annual Lunar and Planetary Science Conference, 1999.

Mongelluzzo, G. et al. "Optimization of the fluid dynamic design of the Dust Suite-MicroMED sensor for the ExoMars 2020 mission, IEEE Metrology for Aerospace (MetroAeroSpace), Rome, Italy, 2018, p. 134-139. DOI: 10.1109/metroaerospace.2018.8453505.

Mongelluzzo, G. et al., CFD analysis and optimization of the sensor "MicroMED" for the ExoMars 2020 mission. Measurement, Volume 147, 106824.
DOI: 10.1016/j.measurement.2019.07.052 (2019a).

Mongelluzzo, G. et al. "Design and CFD analysis of the fluid dynamic sampling system of the "MicroMED" Optical Particle Counter". Sensors 19(22). pii: E5037. DOI: 10.3390/s19225037. (2019b).

Mongelluzzo, G. et al., Optimization of the sensor "MicroMED" for the ExoMars 2020 mission: the Flight Model design, IEEE Metrology for Aerospace (MetroAeroSpace), Turin, Italy, 2019, p. 749-753. DOI: 10.1109/MetroAeroSpace.2019.8869610 (2019c).

Mongelluzzo, G. et al., "CFD analysis of the "MicroMED" Optical Particle Counter in various planetary environments," 2020 IEEE 7th International Workshop on Metrology for AeroSpace (MetroAeroSpace), 2020, pp. 356-36.
doi: 10.1109/MetroAeroSpace48742.2020.9160139.

Montabone, Luca, Stephen R. Lewis, and Peter L. Read. "Interannual variability of Martian dust storms in assimilation of several years of Mars global surveyor observations." Advances in Space Research 36.11 (2005): 2146-2155.

Moroz, V. I., E. V. Petrova, and L. V. Ksanfomality. "Spectrophotometry of Mars in the KRFM experiment of the PHOBOS mission: Some properties of the particles of atmospheric aerosols and the surface." Planetary and space science 41.8 (1993): 569-585.

Murphy, Jim, et al. "Field measurements of terrestrial and martian dust devils." Space Science Reviews 203.1 (2016): 39-87.

Murphy, J. R., and Nelly, S. (2002). Mars Pathfinder convective vortices: Frequency of occurrence. Geophysical research letters, 29(23).

Neakrase, L. D. V., et al. "Particle lifting processes in dust devils." Space Science Reviews 203.1 (2016): 347-376.

Neubauer, F. M. "Thermal convection in the Martian atmosphere." Journal of Geophysical Research 71.10 (1966): 2419-2426.

Newman, Claire E., et al. "Modeling the Martian dust cycle, 1. Representations of dust transport processes." Journal of Geophysical Research: Planets 107.E12 (2002a): 6-1.

Newman, Claire E., et al. "Modeling the Martian dust cycle 2. Multiannual radiatively active dust transport simulations." Journal of Geophysical Research: Planets 107.E12 (2002b): 7-1.

Pollack, James B., et al. "Properties of aerosols in the Martian atmosphere, as inferred from Viking Lander imaging data." Journal of Geophysical Research 82.28 (1977): 4479-4496.

Pollack, James B., et al. "Properties and effects of dust particles suspended in the Martian atmosphere." Journal of Geophysical Research: Solid Earth 84.B6 (1979): 2929-2945.

Pollack, James B., Maureen E. Ockert-Bell, and Michael K. Shepard. "Viking Lander image analysis of Martian atmospheric dust." Journal of Geophysical Research: Planets 100.E3 (1995): 5235-5250.

Rasmussen, K. et al. Rasmussen, K.R., J. F. Kok, J.P. Merrison (2009), Enhancement in wind driven sand transport by electric fields, Planetary and Space Science, 57, 804-808.

Reiss, Dennis. "Dust Devils: Stirring Up the Martian Surface." Dynamic Mars. Elsevier, 2018. 295-316.

Ringrose, T. J., M. C. Towner, and J. C. Zarnecki. "Convective vortices on Mars: a reanalysis of Viking Lander 2 meteorological data, sols 1–60." Icarus 163.1 (2003): 78-87.

Rodriguez, S., et al. (2005) "Optical Wireless MIL-STD-1553 and Serial Synchronous buses for intra-spacecraft communications." DASIA 2005-Data Systems in Aerospace. Vol. 602.

Rotundi, A. et al. (2015) "Dust measurements in the coma of comet 67P/Churyumov-Gerasimenko inbound to the sun", Science, 347, Issue 6220, article id. aaa3905.

Ryan, J. A., and R. M. Henry. "Mars atmospheric phenomena during major dust storms, as measured at surface." Journal of Geophysical Research: Solid Earth 84.B6 (1979): 2821-2829.

Ryan, J. A., and R. D. Lucich. "Possible dust devils, vortices on Mars." Journal of Geophysical Research: Oceans 88.C15 (1983): 11005-11011.

Runyon, Kirby D., Christina E. Viviano, and Mackenzie Day. "Abraded pyroclastic linear paleodunes in Syria and Daedalia Plana, Mars." Earth and Planetary Science Letters 557 (2021): 116719.

Russo, G., Pagliocca, G., Esposito, F. et al. Autonomous Thermal Simulator for EXOMARS-MicroMED Calibration. Adv. Astronaut. Sci. Technol. 3, 1–15 (2020). https://doi.org/10.1007/s42423-019-00052-y

Sagan, Carl, and R. A. Bagnold. "Fluid transport on Earth and aeolian transport on Mars." Icarus 26.2 (1975): 209-218.

Saggin, Bortolino, et al. "Development and characterization of a volume flow measurement system for low-pressure gases." Measurement 166 (2020): 108230.

Scaccabarozzi, D., et al., MicroMED, design of a particle analyzer for Mars. Measurement (2018), Volume 122, p. 466-472. DOI: https://doi.org/10.1016/j.measurement.2017.12.041.

Scaccabarozzi, D. et al., Design validation of MicroMED, a particle analyzer for ExoMars 2020, IEEE Metrology for Aerospace (MetroAerospace), Turin, Italy, 2019.
DOI: https://doi.org/10.1109/MetroAeroSpace.2019.8869666.

Scaccabarozzi, D. et al., "MicroMED" optical particle counter: from design to Flight Model, Sensors 2020, Jan 20;20(3). DOI: 10.3390/s19225037.

Silvestro, S., Fenton, L. K., Vaz, D. A., Bridges, N. T., & Ori, G. G. (2010). Ripple migration and dune activity on Mars: Evidence for dynamic wind processes. *Geophysical Research Letters*, *37*(20).

Silvestro S., Vaz D. A., Fenton L. K. and Geissler P. E., 2011, "Active aeolian processes on Mars: a regional study in Arabia and Meridiani Terrae", Geophys. Res. Lett. 38 L20201.

Silvestro, S., et al. "Periodic Bedrock Ridges at the ExoMars 2022 landing site: Evidence for a changing wind regime." Geophysical research letters 48.4 (2021): e2020GL091651.

Sinclair, P. C. (1969). General characteristics of dust devils. Journal of Applied Meteorology, 8(1), 32-45.

Smith, D.E., et al., Mars Orbiter Laser Altimeter (MOLA): Experiment Summary after the First Year of Global Mapping of Mars - Journal of Geophysical Research, Vol. 106, pp. 23,689-23,722, 2001.

Smith, M.D., et al., Compact Reconnaissance Imaging Spectrometer Observations of Water Vapor and Carbon Monoxide - Journal of Geophysical Science, Vol. 114, N. E00D03, 2009.

Stanzel, C., et al., Dust Devil Speeds, Directions of Motion and General Characteristics Observed by the Mars Express High Resolution Stereo Camera - Icarus, Vol. 197, pp. 39–51, 2008.

Sullivan, R., et al., Wind-driven Particle Mobility on Mars: Insights from Mars Exploration Rover Observations at the "El Dorado" and Surroundings at Gusan Crater - Journal of Geophysical Research, Vol. 113, N. E06S07, 2008.

Thomas, P., & Gierasch, P. J. (1985). Dust devils on Mars. Science, 230(4722), 175-177.

Tomasko, M.G., et al., Properties of Dust in the Martian Atmosphere from the Imager on Mars Pathfinder - Journal of Geophysical Research, Vol. 194, pp. 8987-9007, 1999.

Toon, O.B., Pollack, J.B., Sagan, C., Physical Properties of the Particles Composing the Martian Dust Storm of 1971-1972 - Icarus, Vol. 30, pp. 663-696, 1977.

Vago, J., Witasse, O., Svedhem, H. et al. ESA ExoMars program: The next step in exploring Mars. Sol Syst Res 49, 518–528 (2015). https://doi.org/10.1134/S0038094615070199.

N. van Doremalen et al., "Aerosol and Surface Stability of SARS-CoV-2 as Compared with SARS-CoV-1", The New England Journal of Medicine, 2020.

Ventura, S., "The MEDUSA and MicroMED experiments for the ExoMars space programme to perform in situ analysis of Martian dust", Ph. D. thesis, 2011.

Vincente-Retortillo, A., Lifting of Dust on Mars as Observed by the Curiosity Rover. Scientific Reports volume 8(17576), 2018.

Vuorinen, Ville, et al. "Modelling aerosol transport and virus exposure with numerical simulations in relation to SARS-CoV-2 transmission by inhalation indoors." Safety Science 130 (2020): 104866.

Whelley, P. L., & Greeley, R. (2008). The distribution of dust devil activity on Mars. Journal of Geophysical Research: Planets, 113(E7).

White, Bruce R., et al. "Estimated grain saltation in a Martian atmosphere." Journal of Geophysical Research 81.32 (1976): 5643-5650.

White, B.R., Soil transport by winds on Mars – Journal of Geophysical. Research, Vol. 84, pp. 4643-4651, 1979.

Wolff, M.J. et al., Wavelength dependence of dust aerosol single scattering albedo as observed by the Compact Reconnaissance Imaging Spectrometer, J. Geophys. Res. 2009. DOI: 10.1029/2009JE003350.

Worth Longest P, Vinchurkar S. Validating CFD predictions of respiratory aerosol deposition: effects of upstream transition and turbulence. J Biomech. 2007;40(2):305-16. doi: 10.1016/j.jbiomech.2006.01.006. Epub 2006 Mar 14. PMID: 16533511.

Wurm, Gerhard, Jens Teiser, and Dennis Reiss. "Greenhouse and thermophoretic effects in dust layers: The missing link for lifting of dust on Mars." Geophysical research letters 35.10 (2008).

Zhang, W. et al. (2007) "A dsPIC-based Excitation Control System for Synchronous Generator." International Conference on Mechatronics and Automation. Harbin: IEEE. 3844-3848.

Zurek, Richard W., et al. "Dynamics of the atmosphere of Mars." Mars (1992): 835-933.